
Dynamic Calibration of the NASA Ames Rotor Test Apparatus Steady/Dynamic Rotor Balance

Randall L. Peterson and Johannes M. van Aken

April 1996



National Aeronautics and
Space Administration

Dynamic Calibration of the NASA Ames Rotor Test Apparatus Steady/Dynamic Rotor Balance

Randall L. Peterson, Ames Research Center, Moffett Field, California
Johannes M. van Aken, Sterling Federal Systems, Inc., Palo Alto, California

April 1996



National Aeronautics and
Space Administration

Ames Research Center
Moffett Field, California 94035-1000

Dynamic Calibration of the NASA Ames Rotor Test Apparatus Steady/Dynamic Rotor Balance

RANDALL L. PETERSON AND JOHANNES M. VAN AKEN*

Ames Research Center

Summary

The NASA Ames Rotor Test Apparatus was modified to include a Steady/Dynamic Rotor Balance. The dynamic calibration procedures and configurations are discussed. Random excitation was applied at the rotor hub, and vibratory force and moment responses were measured on the steady/dynamic rotor balance. Transfer functions were computed using the load cell data and the vibratory force and moment responses from the rotor balance. Calibration results showing the influence of frequency bandwidth, hub mass, rotor RPM, thrust preload, and dynamic loads through the stationary push rods are presented and discussed.

Introduction

Accurate measurements of the vibratory loading of a rotor system have long been a challenge to the rotorcraft community (refs. 1–4). In 1987, NASA Ames identified the requirement to extend the capability of the Rotor Test Apparatus (RTA) to measure both the steady and vibratory hub forces and moments to thrust levels of 22,000 lb. From this requirement a rotor balance was designed, fabricated, and calibrated to measure both the steady and vibratory thrust, torque, shears, and moments of any rotor system installed on the RTA.

This report documents the procedures and results of the dynamic calibration of the Steady/Dynamic Rotor Balance (S/DRB) on the RTA. Calibration results showing the influence of frequency bandwidth, hub mass, rotor RPM, thrust preload, and dynamic loads through the stationary push rods are presented and discussed. Further results and information regarding the calibration and data processing procedures for the S/DRB are found in references 5 and 6.

Nomenclature

AF	axial force, positive aft, lb
NF	normal force, positive up, lb
NFi	normal force on flexure i, positive up, lb
PM	pitch moment, positive nose up, ft-lb
RM	roll moment, positive right wing down, ft-lb
SF	side force, positive to right, lb
V_X	output voltage for strain gage X, mV

Test Hardware

Rotor Test Apparatus

The NASA Ames RTA is a special-purpose drive and support system for operating helicopter rotors in the 40- by 80- and 80- by 120-Foot Wind Tunnels. The RTA houses two electric drive motors, the hydraulic servomotors of the primary control system, and a dynamic control system capable of introducing dynamic perturbations to the nonrotating swashplate (collective and tilt) at frequencies up to 40 Hz. Installed on the RTA is a five-component S/DRB to measure rotor loads at the hub moment center. The balance was designed and fabricated to measure both the steady and vibratory rotor normal, axial, and side forces, together with rotor pitch and roll moments to rotor thrust levels of 22,000 lb. An instrumented flex-coupling measures rotor torque and residual normal force. The isolated balance natural frequencies are all above 60 Hz.

Steady/Dynamic Rotor Balance

The five-component S/DRB is located between the RTA transmission and the upper housing. The S/DRB consists

*Sterling Federal Systems, Inc., Palo Alto, California.

of two rings with a 28-in. inner diameter and a 32-in. outer diameter, which are connected to each other by four rectangular, instrumented flexures. The centers of the four flexures are located on a 30-in. diameter circle.

Figure 1 shows a schematic top view of the five-component ring balance. The flexures are identified by the numbers 1 through 4. Flexures 1 and 2 are located in the longitudinal plane in the forward and aft locations, respectively. Flexures 3 and 4 are located in the lateral plane at the left and right positions, respectively. The balance flexures are 2.872 in. tall and have a rectangular cross section measuring 0.540 by 1.068 in. The flexures are oriented such that the long side of the rectangular cross section is tangential to the balance circumference. Figure 2 shows the balance. The balance was retrofitted to the existing RTA model and installed on top of the RTA transmission. The presence of an extrusion to accommodate the transmission idler shaft and bearing resulted in a large cutout in the nonmetric side of the balance. This 45 deg pie shape cutout is clearly visible in figure 2 on the lower side of the balance. The cutout is located directly under flexure 2 and resulted in some large balance gage interactions.

The balance static load limits are: 22,000 lb of thrust, 4,400 lb of resultant in-plane shear, and 57,800 ft-lb of resultant moment at the balance moment center. Therefore, the maximum allowable resultant hub moment depends upon the hub height above the balance moment center. The balance shares a common centerline with the rotor shaft. The rotor shaft has an in-line flex-coupling, which is instrumented to measure rotor torque up to a maximum of 36,000 ft-lb and the residual shaft thrust up to a calibration limit of 200 lb.

The vibratory (1/2 peak-to-peak) load limits of the balance are: 5,500 lb of thrust, 1,100 lb of resultant in-plane shear, and 8,920 ft-lb of resultant moment with the balance static load limits listed above as the *do not exceed* limits.

Rotor Control System

Figure 3 shows a schematic of the RTA control system. Static control of the swashplate is provided through the three primary actuators. The three stationary (nonrotating) push rods connect the walking beams to the swashplate. These three push rods are approximately parallel to the rotor shaft and are located on an approximate radius of 8.4 in. at azimuth locations of 120 (push rod number 1), 210 (push rod number 3), and 300 deg (push rod number 2) with zero deg azimuth pointing aft along

the RTA longitudinal axis. The stationary push rods are instrumented to measure the push rod's axial force.

The rotor control system is installed on the actuator baseplate of the RTA, which is mounted to the upper output bearing housing which in turn is installed on top of the steady/dynamic rotor balance. Loading through the stationary push rods results in simultaneous normal force, pitch moment, and roll moment loading. The rotor balance measurements represent the total rotor loading including the loading transferred down from the rotor through primary load path formed by the rotor shaft and the RTA upper output bearing housing, and through the secondary load path formed by the rotating push rods, swashplate, walking beams, stationary push rods, actuator baseplate, and the RTA upper housing output bearing housing. Figure 3 is a schematic of the redundant load path system on the RTA.

Balance Gaging

Each of the four flexures is instrumented with a four-arm active Wheatstone bridge to measure loading in the flexure axial direction (balance normal force direction). These four individual normal force component readings, V_{NF_i} , $i = 1-4$, are summed to provide the balance normal force reading, $V_{NF} = V_{NF1} + V_{NF2} + V_{NF3} + V_{NF4}$. The readings from the opposing flexures are differenced to provide pitch and roll moment readings, $V_{PM} = V_{NF1} - V_{NF2}$ and $V_{RM} = V_{NF3} - V_{NF4}$, respectively.

Each of the four flexures is also instrumented with a four-arm active Wheatstone bending bridge, measuring the shear force along the long side of the flexure cross section. The strain gage outputs of opposing flexures are wired into a Wheatstone bridge to provide the balance axial force reading, V_{AF} (from flexures 3 and 4), and the balance side force reading, V_{SF} (from flexures 1 and 2).

Balance Monitoring

The balance provides six gage readings: NF1, NF2, NF3, NF4, AF, and SF. The summing and differencing of the NF_i gages into the NF, PM, and RM readings are done digitally in the balance data reduction program.

A Balance Analog Monitoring Box (BAMB) is used for on-line monitoring to ensure safe operation of the rotor system and the balance. This box combines the six balance gage outputs into analog signals representing the various forces and moments in both the balance- and the hub-axis systems. This on-line analog process does not

provide for balance gage interaction corrections. The various analog output signals from the BAMB are displayed on an analog bar chart monitor or on an oscilloscope to perform the on-line safety-of-flight monitoring during actual wind tunnel testing. Actual safety-of-flight monitoring limits are test dependent due to hub height above the balance moment center.

The BAMB analog signals for NF, PM, and RM were also acquired during the dynamic calibration test for use in determining the dynamic calibration matrix.

Dynamic Balance Calibration

Test Setup

The RTA was mounted on the three-strut model support system of the 40- by 80-Foot Wind Tunnel. The 8-ft model support struts with 33-in. tips were installed onto a T-frame, which in turn was supported by the wind tunnel scale system. The rotor plane was approximately 22 ft above the tunnel floor. An extensive dynamic calibration test was performed to obtain the balance/stand frequency response (transfer) functions that represent the dynamics of the RTA installation. Figures 4 and 5 show the RTA installed in the test section of the 40- by 80-Foot Wind Tunnel during the dynamic calibration test.

The rotor hub was replaced by special calibration hardware, which allowed for applying loading with and without the rotor shaft rotating. The calibration hardware consisted of a shaft with a radial bearing installed at the appropriate hub height and a thrust bearing at the end of the shaft. These two bearings allow for the application of static or dynamic loads on a rotating shaft: in-plane hub shear load for the radial bearing and thrust load for the thrust bearing. The outer bearing race is prevented from rotating using guy wires secured to a telescoping man-lift as shown in figures 6 and 7.

A calibration fixture was attached to the thrust bearing fixture which allowed for vertical load application at the shaft center and at a radial moment arm. Figure 8 is a schematic showing the vertical calibration configuration in the 40- by 80-Foot Wind Tunnel. The moment carrying capability of the thrust bearing under rotation limited the moment arm to 1 ft. Vertical dynamic loading at the 1-ft moment arm (fig. 6) represented the out-of-plane hub shear (thrust) and dynamic hub moments (pitch and roll). The two bearings allowed for the dynamic in-plane shear load application while applying a steady vertical force at the shaft end, i.e., a thrust force. Figure 9 is a schematic

showing the longitudinal and lateral in-plane calibration configurations in the 40- by 80-Foot Wind Tunnel.

Two circular platters were secured to the shaft just below and above the radial hub bearing (figs. 6 and 7). Semicircular weights of 61.1 lb (half-donuts) were installed onto each of these two platters to simulate the hub and blade weight. By adding or removing weights the total calibration test mass can be varied to represent the mass of different rotor systems. The vertical center of gravity (cg) of the calibration test hardware is located at the radial bearing center, which represents the hub location.

Dynamic calibration of the rotor balance through the stationary push rods was also conducted. To obtain access to the push rods, it was necessary to remove the calibration hardware and acquire the balance gage frequency responses at zero hub and blade mass only. Vibratory loading was applied directly to the free end of one of the stationary push rods.

Test Procedures

A hydraulic actuator was used to excite the model and the support system at the nominal hub height of 6.1 ft above the balance moment center. One end of the hydraulic actuator was attached to a 5-ft long extension arm. The other end of the actuator was attached to the hub. The extension arm was attached to an 11,600-lb reaction mass hung from the gantry crane, as shown in figures 4, 5, and 8. The actuator was aligned with respect to the extension arm, which was in turn aligned parallel to the calibration direction. After achieving rough alignment of the actuator and the extension arm using the gantry crane, finer alignment was achieved by applying tension to the guy wires attached between the reaction mass and the tunnel floor. The guy wires also restrained swinging of the reaction mass during actuator excitation. A load cell located between the hydraulic actuator and the hub measured the applied force.

A random excitation from 0 to 64 Hz at input force levels of up to ± 600 lb was applied at the nominal rotor hub height. A 16-channel GenRad 2515 Computer-Aided Test System was used to acquire and store the Frequency Response Functions (FRFs) or transfer functions of the balance forces and moments with respect to the input force load cell. The FRF data were then transferred to a VAX mainframe computer for further data processing.

Test Envelope

The dynamic calibration test setup did not allow for the application of pure hub moments. Hub moments were obtained by applying a vertical force at a 1-ft radial moment arm from the hub center. This loading results in a hub force (thrust) and a hub moment (pitch or roll). The balance also measures a balance force and a balance moment with respect to the balance moment center. A pure in-plane hub shear does not result in a hub moment, but results in a balance shear and a balance moment due to the vertical separation or offset of the hub and balance moment center. To determine the dynamic calibration matrix for the five-component S/DRB as a result of loading through the primary load path, a total of five loading sequences were used. The five load sequences are identified in table 1. The five unique load sequences are: vertical loading at the shaft center (thrust loading), vertical loading at 1 ft forward of the shaft center (thrust and hub pitch moment loading), vertical loading at 1 ft to the left of the shaft center (thrust and hub roll moment loading), and hub horizontal loading in the RTA longitudinal plane (hub axial force loading) and in the RTA lateral plane (hub side force loading). To determine the dynamic calibration matrix for the five-component S/DRB as a result of loading through the secondary (redundant) load path, a total of three loading sequences were used. The three load sequences are also identified in table 1. The three unique load sequences are: vibratory loading through stationary push rod number 1, vibratory loading through stationary push rod number 2, and vibratory loading through stationary push rod number 3. As discussed previously, loading through the stationary push rods results in simultaneous normal force, pitch moment, and roll moment loading. For each balance loading setup the FRFs for the following balance readings were acquired: NF1, NF2, NF3, NF4, AF, and SF from the balance gages and the resolved NF, PM, and RM signals from the BAMB.

During the calibration test, data for the set of five loading sequences through the primary load path and the three loading sequences through the secondary or redundant load path shown in table 1 were acquired at zero shaft rotation and at zero thrust preload. Data were also acquired during longitudinal and lateral shear force shaking while applying a steady thrust force to the hub. In addition, some data were acquired with shaft rotation at nominal rotor speeds of 315 and 425 RPM, with and without a thrust preload.

A description of the data processing procedures, including the determination of the dynamic calibration matrices, is provided in references 5 and 6. Reference 5 describes the

data processing procedures for the dynamic loading through the primary load path, and reference 6 describes the data processing procedures for the dynamic loading through both the primary load path and the secondary (redundant) load path.

Test Configurations

Dynamic calibration testing of the RTA S/DRB configuration was performed prior to two 40- by 80-Foot Wind Tunnel test entries in which the Sikorsky five-bladed Bearingless Main Rotor (SBMR) (refs. 6 and 7) and the BO105 four-bladed hingeless main rotor (ref. 8) were tested. The RTA was not removed from the tunnel support system between these two tunnel entries. The hub calibration test hardware, however, was reconfigured to represent the hub/blade mass of each of these two rotor systems. The weight difference between the two hub/blade systems is 740 lb. The hub/balance center offset was 6.1 ft in both tests. In general, the lower and upper limits of the RTA test capabilities are represented by the BO105 and SBMR rotor systems, respectively.

Dynamic Calibration Results

Frequency Response Function data were acquired during extensive dynamic calibration testing of the RTA in the 40- by 80-Foot Wind Tunnel. Table 2 shows the test envelope at which these FRFs were obtained for the two test configurations, representing the SBMR and BO105 rotor systems. These FRF data were acquired at a zero deg RTA shaft angle, i.e., at zero model angle of attack. Data were acquired to determine the effects of frequency bandwidth, hub mass, rotor RPM, thrust preload, and dynamic loads through the stationary push rods on the balance response due to the dynamic behavior of the RTA and the wind tunnel support system.

Effects of Frequency Resolution

Figures 10–14 and 16 present comparisons of the balance gage output FRFs for two different data acquisition frequency bandwidth settings (0–32 and 0–64 Hz). These comparisons were performed to evaluate the influence of increased frequency resolution on the measured FRFs. The repeatability of the FRF data from 0 to 32 Hz can also be evaluated from these comparisons. Figure 15 is a comparison of balance gage output FRFs for forward and aft hub (out-of-plane) pitch moment loading. In general, the influence of reduced frequency bandwidth (from 0–64 Hz to 0–32 Hz) in the data acquisition process

showed no significant changes in the FRFs with increased frequency resolution in either the directly loaded balance gages or the interactions.

Figures 10–16 show significant changes in the dynamic response of the balance over the entire frequency bandwidth of either 0–32 Hz or 0–64 Hz. Since the balance flexure design places the balance natural frequencies above 60 Hz, the changes in the dynamic balance response seen in figures 10–16 are attributed to the dynamic structural characteristics of both the wind tunnel support system and the RTA itself. The response/interaction of the balance gages is changed significantly by the balance dynamic response shown in figures 10–16, indicating the necessity of making dynamic corrections to both the gage sensitivity and gage interaction terms in the balance calibration matrix.

Figure 10 presents representative FRFs of the balance gage outputs due to a side force loading at the hub (load sequence 6). The balance moment center is located 6.1 ft below the hub, and a hub side force therefore results in both a balance side force and a balance roll moment loading. The calibration test hub mass for this FRF data set represents the mass of the BO105 hub and blades. The loading, measured by the input force load cell, was converted into the corresponding loading seen by the balance. The FRF magnitude axis dimension is in units of $\text{EU}_{\text{output}}/\text{EU}_{\text{input}}$, where EU represents engineering units of the corresponding balance output. Forces are presented in $\text{lb}_{\text{output}}/\text{lb}_{\text{input}}$, while the moments are presented in $\text{ft-lb}_{\text{output}}/\text{ft-lb}_{\text{input}}$. At low frequencies (<1 Hz) the FRF for the side force (fig. 10(e)) and the roll moment (fig. 10(c)) gages show a ratio of approximately 1 as these are the directly loaded gages. The other three gages, normal force (fig. 10(a)), axial force (fig. 10(d)), and pitch moment (fig. 10(b)), show a ratio of approximately 0 at low frequency (<1 Hz) and indicate the amount of load interaction seen by these gages. The differences in the balance gage FRFs due to side force loading between the 0–32 Hz and 0–64 Hz bandwidths are small and are primarily seen in the balance gage interactions. Small differences in both magnitude and phase are seen in the normal force interaction (fig. 10(a)), the axial force interaction (fig. 10(d)), and the pitch moment interaction (fig. 10(b)).

Figure 11 presents representative FRFs of the balance gage outputs due to an axial force loading at the hub (load sequence 5). As in the case with the side force loading, the balance moment center is located 6.1 ft below the hub, and a hub axial force therefore results in both a balance axial force and a balance pitch moment loading. At low frequencies (<1 Hz) the FRFs for the axial force

(fig. 11(d)) and the pitch moment (fig. 11(b)) gages show a ratio of approximately 1 as these are the directly loaded gages. The other three gages, normal force (fig. 11(a)), side force (fig. 11(e)), and roll moment (fig. 11(c)), show a ratio of approximately 0 at low frequency (<1 Hz) and indicate the amount of load interaction seen by these gages. Again, the differences in the balance gage FRFs due to axial force loading between the 0–32 Hz and 0–64 Hz bandwidths are small and are primarily seen in the balance gage interactions.

Figure 12 presents representative FRFs of the balance gage outputs due to a normal force loading at the hub (load sequence 1). At low frequencies (<1 Hz) the FRF for the normal force (fig. 12(a)) gage shows a ratio of approximately 1 as this is the only directly loaded gage. The other four gages, axial force (fig. 12(d)), side force (fig. 12(e)), pitch moment (fig. 12(b)), and roll moment (fig. 12(c)), show a ratio of approximately 0 at low frequency (<1 Hz) and indicate the amount of load interaction seen by these gages. Again, the differences in the balance gage FRFs due to normal force loading between the 0–32 Hz and 0–64 Hz bandwidths are small and are primarily seen in the balance gage interactions.

Figure 13 presents representative FRFs of the balance gage outputs due to a forward pitch (out-of-plane) moment loading at the hub (load sequence 2). At low frequencies (<1 Hz) the FRFs for the pitch moment (fig. 13(b)) and the normal force (fig. 13(a)) gages show a ratio of approximately 1 as these are the only directly loaded gages. The other three gages, axial force (fig. 13(d)), side force (fig. 13(e)), and roll moment (fig. 13(c)), show a ratio of approximately 0 at low frequency (<1 Hz) and indicate the amount of load interaction seen by these gages. Again, the differences in the balance gage FRFs due to pitch moment loading between the 0–32 Hz and 0–64 Hz bandwidths are small and are primarily seen in the balance gage interactions.

Figure 14 presents representative FRFs of the balance gage outputs due to an aft pitch (out-of-plane) moment loading at the hub (load sequence 3). At low frequencies (<1 Hz) the FRFs for the pitch moment (fig. 14(b)) and the normal force (fig. 14(a)) gages show a ratio of approximately 1 as these are the only directly loaded gages. The other three gages, axial force (fig. 14(d)), side force (fig. 14(e)), and roll moment (fig. 14(c)), show a ratio of approximately 0 at low frequency (<1 Hz) and indicate the amount of load interaction seen by these gages. Again, the differences in the balance gage FRFs due to roll moment loading between the 0–32 Hz and 0–64 Hz bandwidths are small and are primarily seen in the balance gage interactions.

Figure 15 presents a comparison of the balance gage output FRFs for the directly loaded gages shown in figures 13 and 14. Figure 15(a) is a comparison of the normal force response due to a forward (fig. 13(a)) and an aft (fig. 14(a)) hub pitch moment loading. Figure 15(b) is a comparison of the pitch moment response due to the same forward (fig. 13(b)) and an aft (fig. 14(b)) hub pitch moment loading. The primary phase difference (180 deg phase shift) shown in figure 15(b) is due to the positive sign convention of the load cell and balance under a static load. Differences in the FRFs of the directly loaded gages shown in figure 15 and comparisons of the interactions shown figures 13 and 14 are probably caused by the physical cutout in the nonmetric portion of the balance that was discussed previously in this report and shown in figure 2.

Figure 16 presents representative FRFs of the balance gage outputs due to a roll (out-of-plane) moment loading at the hub (load sequence 4). At low frequencies (<1 Hz) the FRFs for the roll moment (fig. 16(c)) and the normal force (fig. 16(a)) gages show a ratio of approximately 1 as these are the only directly loaded gages. The other three gages, axial force (fig. 16(d)), side force (fig. 16(e)), and pitch moment (fig. 16(b)), show a ratio of approximately 0 at low frequency (<1 Hz) and indicate the amount of load interaction seen by these gages. Again, the differences in the balance gage FRFs due to roll moment loading between the 0–32 Hz and 0–64 Hz bandwidths are small and are primarily seen in the balance gage interactions.

In-Plane Versus Out-of-Plane Loading

Figure 10(c) shows the FRF data for the roll moment gage due to a horizontal or in-plane vibratory load at the hub, and figure 11(b) shows the FRF data for the pitch moment gage due to a horizontal or in-plane vibratory load at the hub. During another portion of the calibration test, a balance roll moment and a balance pitch moment were also generated by an out-of-plane force: a vertical vibratory load input was applied 1 ft to the left of the shaft center (fig. 16(c)) and 1 ft forward of the rotor shaft in the longitudinal plane (fig. 13(b)) of the RTA, respectively. In the first case, the balance normal force and roll moment gages are loaded simultaneously, and in the second case the balance normal force and pitch moment gages are loaded simultaneously.

The pitch moment and roll moment FRF data obtained by out-of-plane and in-plane hub force applications are compared in figure 17. Figure 17(a) presents the comparison of the hub pitch moment response, and figure 17(b)

presents the comparison of the hub roll moment response. In both cases, the measured pitch moment and roll moment FRF data are the sum of the response of the PM or RM gage due to a pure moment loading and the interaction response to a force application. Comparisons of the two curves in figure 17 show markedly different balance pitch and roll moment responses due to out-of-plane versus in-plane force loading, especially for frequencies greater than 20 Hz. The difference could be the result of the difference in the magnitude of PM and RM loading, being 500 ft-lb due to the out-of-plane force loading and 3,660 ft-lb due to the in-plane force loading. A second explanation is that the RTA/balance response is considerably different for out-of-plane versus in-plane loading.

Effect of Shaft Rotation

Figures 18–22 present comparisons of the balance gage output FRFs under vibratory in-plane and out-of-plane loading without and with shaft rotation of 315 and 425 RPM. The calibration test configuration again represents the BO105 hub and blade mass. These comparisons were performed to evaluate the influence of shaft rotation on the measured FRFs.

Figure 18 presents representative FRFs of the balance gage outputs due to an axial force loading at the hub (load sequence 5) without and with shaft rotation. The axial force (fig. 18(d)) and the pitch moment (fig. 18(b)) gages are the directly loaded gages in this figure. Figure 18 shows that the effect of rotation is minimal at low frequencies for the directly loaded gages (AF and PM in this case). Differences are noted at the higher frequencies (>30 Hz) for both the magnitude and phase data with the 425 RPM showing the greatest differences. The FRFs for the normal force (fig. 18(a)), side force (fig. 18(e)), and roll moment (fig. 18(c)) interactions show some effect of shaft rotation on magnitude at frequencies greater than 30 Hz, but phase shifts are noticed at frequencies as low as 12 Hz for the normal force interaction (fig. 18(a)). The FRF data of figure 18 show a resonance at approximately 19 Hz, which is also observed in figures 10–17. Review of the FRF data plots shows that rotation influences the magnitude of this resonance for all balance gages.

Figure 19 presents representative FRFs of the balance gage outputs due to a normal force loading at the hub (load sequence 1) without and with shaft rotation. The normal force (fig. 19(a)) gage is the only directly loaded gage in this figure. Figure 19 shows that the effect of rotation is minimal at low frequencies for the directly loaded gage (NF in this case). Again, differences are

noted at the higher frequencies (>19 Hz) for both the magnitude and phase data with the 425 RPM showing the greatest difference. The FRFs for the axial force (fig. 19(d)), side force (fig. 19(e)), pitch moment (fig. 19(b)), and roll moment (fig. 19(c)) interactions show small effects on magnitude and phase due to shaft rotation over the whole frequency range (0–64 Hz).

Figure 20 presents representative FRFs of the balance gage outputs due to a forward pitch (out-of-plane) moment loading at the hub (load sequence 2) without and with shaft rotation. The pitch moment (fig. 20(b)) and the normal force (fig. 20(a)) gages are the only directly loaded gages in this figure. Figure 20 shows that the effect of rotation is minimal at low frequencies for the directly loaded gages (PM and NF in this case). Again, differences are noted at the higher frequencies (>19 Hz) for both the magnitude and phase data. Except for some isolated frequencies in the 5–8 Hz range (due to rotational unbalance), the FRFs for the axial force (fig. 20(d)), side force (fig. 20(e)), and roll moment (fig. 20(c)) interactions show small effects on magnitude and phase due to shaft rotation over the whole frequency range (0–64 Hz).

Figure 21 presents representative FRFs of the balance gage outputs due to an aft pitch (out-of-plane) moment loading at the hub (load sequence 3) without and with shaft rotation. The pitch moment (fig. 21(b)) and the normal force (fig. 21(a)) gages are the only directly loaded gages in this figure. Figure 21 shows that the effect of rotation is minimal at low frequencies for the directly loaded gages (PM and NF in this case). Again, differences are noted at the higher frequencies (>19 Hz) for both the magnitude and phase data. Except for some isolated frequencies in the 5–8 Hz range, the FRF for the axial force (fig. 21(d)) interaction shows small effects on magnitude and phase due to shaft rotation over the whole frequency range (0–64 Hz). The interactions on side force (fig. 21(e)) and roll moment (fig. 21(c)) for both magnitude and phase vary over the whole frequency range (0–64 Hz) due to shaft rotation. Comparison of figures 20 and 21 shows that the aft pitch moment loading with shaft rotation has a much greater effect on the interactions compared with the forward pitch moment loading.

Figure 22 presents representative FRFs of the balance gage outputs due to a roll (out-of-plane) moment loading at the hub (load sequence 4) without and with shaft rotation. The roll moment (fig. 22(c)) and the normal force (fig. 22(a)) gages are the only directly loaded gages in this figure. Figure 22 shows that the effect of rotation is minimal at low frequencies for the directly loaded gages (RM and NF in this case). Again, differences are noted at the higher frequencies (>19 Hz) for both the magnitude

and phase data. The interactions on axial force (fig. 22(d)), side force (fig. 22(e)), and pitch moment (fig. 22(b)) for both magnitude and phase vary over the whole frequency range (0–64 Hz) due to shaft rotation.

Effect of Thrust Preload without and with Shaft Rotation

The effect of rotor thrust preload is shown in figures 23 and 24 with no shaft rotation and in figure 25 with a shaft rotation of 315 RPM. The thrust preload was 4,000 lb (thrust up, $\approx 18\%$ full range). The calibration test mass represents the BO105 rotor system (hub and blade mass). These comparisons were performed to evaluate the influence of rotor thrust preload without and with shaft rotation on the measured FRFs.

Figure 23 presents representative FRFs of the balance gage outputs due to a side force loading at the hub (load sequence 6) without and with a thrust preload of 4,000 lb. At low frequencies (<1 Hz) the FRFs for the side force (fig. 23(e)) and the roll moment (fig. 23(c)) gages show a ratio of approximately 1 as these are the directly loaded gages. The other three gages, normal force (fig. 23(a)), axial force (fig. 23(d)), and pitch moment (fig. 23(b)), show a ratio of approximately 0 at low frequency (<1 Hz) and indicate the amount of load interaction seen by these gages. For the directly loaded balance side force (fig. 23(e)) and roll moment (fig. 23(c)) gages, the effect of thrust load is primarily seen at frequencies above 30 Hz; however, there is also splitting of modes occurring at approximately 16 Hz for both gages. This split may be a result of the boundary conditions and load path created by the thrust preload. Variations in both magnitude and phase over the entire frequency bandwidth are seen in the interaction responses of the normal force (fig. 23(a)), axial force (fig. 23(d)), and pitch moment (fig. 23(b)) gages.

Figure 24 presents representative FRFs of the balance gage outputs due to an axial force loading at the hub (load sequence 5) without and with a thrust preload of 4,000 lb. At low frequencies (<1 Hz) the FRFs for the axial force (fig. 24(d)) and the pitch moment (fig. 24(b)) gages show a ratio of approximately 1 as these are the directly loaded gages. The other three gages, normal force (fig. 24(a)), side force (fig. 24(e)), and roll moment (fig. 24(c)), show a ratio of approximately 0 at low frequency (<1 Hz) and indicate the amount of load interaction seen by these gages. For the directly loaded balance axial force (fig. 24(d)) and pitch moment (fig. 24(b)) gages, the effect of thrust load is primarily seen at frequencies above 30 Hz. Variations in both magnitude and phase over the

entire frequency bandwidth are seen in the interaction responses of the normal force (fig. 24(a)), side force (fig. 24(e)), and roll moment (fig. 24(c)) gages.

Figure 25 presents representative FRFs of the balance gage outputs due to an axial force loading at the hub (load sequence 5) without and with shaft rotation (315 RPM) and a thrust preload of 4,000 lb. At low frequencies (<1 Hz) the FRFs for the axial force (fig. 25(d)) and the pitch moment (fig. 25(b)) gages show a ratio of approximately 1 as these are the directly loaded gages. The other three gages, normal force (fig. 25(a)), side force (fig. 25(e)), and roll moment (fig. 25(c)), show a ratio of approximately 0 at low frequency (<1 Hz) and indicate the amount of load interaction seen by these gages. For the directly loaded balance axial force (fig. 25(d)) and pitch moment (fig. 25(b)) gages, the effect of thrust load is primarily seen at frequencies above 30 Hz. Variations in both magnitude and phase over the entire frequency bandwidth are seen in the interaction responses of the normal force (fig. 25(a)), side force (fig. 25(e)), and roll moment (fig. 25(c)) gages.

Comparisons of figures 24 and 25 indicate that the thrust preload has a greater effect on the magnitude of the resonance at 19 Hz when the shaft is rotating than when not rotating.

Effect of Thrust Inclination

The effect of rotor thrust preload inclined at both 0 and 15 deg is shown in figure 26. The thrust preload was 2,000 lb (thrust up, $\approx 9\%$ full range). Thrust inclination was accomplished by applying the thrust preload in the forward longitudinal direction over the nose of the RTA, resulting in a combined static loading on the balance. The calibration test mass represents the SBMR rotor system (hub and blade mass). These comparisons were performed to evaluate the influence of rotor thrust inclination on the measured FRFs.

Figure 26 presents representative FRFs of the balance gage outputs due to an axial force loading at the hub (load sequence 5) with a thrust preload of 2,000 lb at thrust inclinations of 0 and 15 deg. At low frequencies (<1 Hz) the FRF for the axial force (fig. 26(d)) and the pitch moment (fig. 26(b)) gages show a ratio of approximately 1 as these are the directly loaded gages. The other three gages, normal force (fig. 26(a)), side force (fig. 26(e)), and roll moment (fig. 26(c)), show a ratio of approximately 0 at low frequency (<1 Hz) and indicate the amount of load interaction seen by these gages. For the directly loaded balance axial force (fig. 26(d)) and pitch

moment (fig. 26(b)) gages, the effect of thrust preload inclination is primarily seen at frequencies above 15 Hz. Small variations in both magnitude and phase over the entire frequency bandwidth are seen in the interaction responses of the side force (fig. 26(e)) and roll moment (fig. 26(c)) gages. Thrust inclination has a fairly large effect on the normal force (fig. 26(a)) interaction at frequencies below 5 Hz and small variations at higher frequencies. Thrust inclination also has the effect of shifting the resonance at 19 Hz to a slightly higher frequency (figs. 26(b) and 26(d)).

Combined Effect of Thrust and Shaft Rotation

The effect of rotor thrust variations with shaft rotation (315 RPM) is shown in figure 27. The thrust preload was varied from 2,000 to 4,000 lb (thrust up, 9–18% full range). The calibration test mass represents the SBMR rotor system (hub and blade mass). These comparisons were performed to evaluate the influence of rotor thrust variations with shaft rotation on the measured FRFs.

Figure 27 presents representative FRFs of the balance gage outputs due to an axial force loading at the hub (load sequence 5) with a thrust preload variation from 2,000 to 4,000 lb and a shaft rotation of 315 RPM. At low frequencies (<1 Hz) the FRFs for the axial force (fig. 27(d)) and the pitch moment (fig. 27(b)) gages show a ratio of approximately 1 as these are the directly loaded gages. The other three gages, normal force (fig. 27(a)), side force (fig. 27(e)), and roll moment (fig. 27(c)), show a ratio of approximately 0 at low frequency (<1 Hz) and indicate the amount of load interaction seen by these gages. Small variations in both magnitude and phase over the entire frequency bandwidth are seen in both the directly loaded balance axial force (fig. 27(d)) and pitch moment (fig. 27(b)) gages, as well as in the interaction responses of the normal force (fig. 27(a)), side force (fig. 27(e)), and roll moment (fig. 27(c)) gages.

Comparison of figures 24, 25, and 27 shows that the change in hub mass from the BO105 to the SBMR rotor configuration shifted the resonance frequency at 19 Hz (figs. 24 and 25) to 17 Hz (fig. 27). Figure 27 shows little variation in the magnitude of the resonance with a change in thrust preload.

Effect of Hub Mass without and with Shaft Rotation

The effect of hub mass on the balance frequency response is shown in figures 28–32 with no shaft rotation and in figures 33–36 with a shaft rotation of 315 RPM. The

calibration test masses (hub and blade) of both the BO105 and the SBMR are represented. These comparisons were performed to evaluate the influence of hub mass variations without and with shaft rotation on the measured FRFs.

Figure 28 presents representative FRFs of the balance gage outputs due to a side force loading at the hub (load sequence 6) without shaft rotation. At low frequencies (<1 Hz) the FRFs for the side force (fig. 28(e)) and the roll moment (fig. 28(c)) gages show a ratio of approximately 1 as these are the directly loaded gages. The other three gages, normal force (fig. 28(a)), axial force (fig. 28(d)), and pitch moment (fig. 28(b)), show a ratio of approximately 0 at low frequency (<1 Hz) and indicate the amount of load interaction seen by these gages. For the directly loaded balance side force (fig. 28(e)) and roll moment (fig. 28(c)) gages, the effect of hub mass variations is significant at frequencies above 10 Hz. Variations in both magnitude and phase over the entire frequency bandwidth are seen in the interaction responses of the normal force (fig. 28(a)), axial force (fig. 28(d)), and pitch moment (fig. 28(b)) gages.

Figure 29 presents representative FRFs of the balance gage outputs due to an axial force loading at the hub (load sequence 5) without shaft rotation. At low frequencies (<1 Hz) the FRFs for the axial force (fig. 29(d)) and the pitch moment (fig. 29(b)) gages show a ratio of approximately 1 as these are the directly loaded gages. The other three gages, normal force (fig. 29(a)), side force (fig. 29(e)), and roll moment (fig. 29(c)), show a ratio of approximately 0 at low frequency (<1 Hz) and indicate the amount of load interaction seen by these gages. For the directly loaded balance axial force (fig. 29(d)) and pitch moment (fig. 29(b)) gages, the effect of hub mass variations is significant at frequencies above 15 Hz. Variations in both magnitude and phase over the entire frequency bandwidth are seen in the interaction responses of the normal force (fig. 29(a)), side force (fig. 29(e)), and roll moment (fig. 29(c)) gages.

Figure 30 presents representative FRFs of the balance gage outputs due to a normal force loading at the hub (load sequence 1) without shaft rotation. At low frequencies (<1 Hz) the FRF for the normal force (fig. 30(a)) gage shows a ratio of approximately 1 as this is the only directly loaded gage. The other four gages, axial force (fig. 30(d)), side force (fig. 30(e)), pitch moment (fig. 30(b)), and roll moment (fig. 30(c)), show a ratio of approximately 0 at low frequency (<1 Hz) and indicate the amount of load interaction seen by these gages. For the directly loaded balance normal force (fig. 30(a)) gage, the effect of hub mass variations is small over the entire

frequency bandwidth. Variations in both magnitude and phase over the entire frequency bandwidth are seen in the interaction responses of the axial force (fig. 30(d)), side force (fig. 30(e)), pitch moment (fig. 30(b)), and roll moment (fig. 30(c)) gages.

Figure 31 presents representative FRFs of the balance gage outputs due to a forward pitch (out-of-plane) moment loading at the hub (load sequence 2) without shaft rotation. The pitch moment (fig. 31(b)) and the normal force (fig. 31(a)) gages are the only directly loaded gages in this figure. The other three gages, axial force (fig. 31(d)), side force (fig. 31(e)), and roll moment (fig. 31(c)), show a ratio of approximately 0 at low frequency (<1 Hz) and indicate the amount of load interaction seen by these gages. For the directly loaded balance normal force (fig. 31(a)) and pitch moment (fig. 31(b)) gages, the effect of hub mass variations is significant at frequencies above 15 Hz. Variations in both magnitude and phase over the entire frequency bandwidth are seen in the interaction responses of the axial force (fig. 31(d)), side force (fig. 31(e)), and roll moment (fig. 31(c)) gages.

Figure 32 presents representative FRFs of the balance gage outputs due to a roll (out-of-plane) moment loading at the hub (load sequence 4) without shaft rotation. The roll moment (fig. 32(c)) and the normal force (fig. 32(a)) gages are the only directly loaded gages in this figure. The other three gages, axial force (fig. 32(d)), side force (fig. 32(e)), and pitch moment (fig. 32(b)), show a ratio of approximately 0 at low frequency (<1 Hz) and indicate the amount of load interaction seen by these gages. For the directly loaded balance normal force (fig. 32(a)) gage, the effect of hub mass variation is mostly seen at frequencies above 15 Hz. For the directly loaded balance roll moment (fig. 32(c)) gage, the effect of hub mass variation is significant at frequencies above 6 Hz. Variations in both magnitude and phase over the entire frequency bandwidth are seen in the interaction responses of the axial force (fig. 32(d)), side force (fig. 32(e)), and pitch moment (fig. 32(b)) gages.

Figure 33 presents representative FRFs of the balance gage outputs due to an axial force loading at the hub (load sequence 5) with shaft rotation. At low frequencies (<1 Hz) the FRFs for the axial force (fig. 33(d)) and the pitch moment (fig. 33(b)) gages show a ratio of approximately 1 as these are the directly loaded gages. The other three gages, normal force (fig. 33(a)), side force (fig. 33(e)), and roll moment (fig. 33(c)), show a ratio of approximately 0 at low frequency (<1 Hz) and indicate the amount of load interaction seen by these gages. For the directly loaded balance axial force (fig. 33(d)) and

pitch moment (fig. 33(b)) gages, the effect of hub mass variations with shaft rotation is significant at frequencies above 15 Hz, similar to the results without shaft rotation shown in figure 29. Variations in both magnitude and phase over the entire frequency bandwidth are seen in the interaction responses of the normal force (fig. 33(a)), side force (fig. 33(e)), and roll moment (fig. 33(c)) gages.

Figure 34 presents representative FRFs of the balance gage outputs due to a normal force loading at the hub (load sequence 1) with shaft rotation. At low frequencies (<1 Hz) the FRF for the normal force (fig. 34(a)) gage shows a ratio of approximately 1 as this is the only directly loaded gage. The other four gages, axial force (fig. 34(d)), side force (fig. 34(e)), pitch moment (fig. 34(b)), and roll moment (fig. 34(c)), show a ratio of approximately 0 at low frequency (<1 Hz) and indicate the amount of load interaction seen by these gages. For the directly loaded balance normal force (fig. 34(a)) gage, the effect of hub mass variations with rotation is small over the entire frequency bandwidth, similar to results shown in figure 30 without shaft rotation. Variations in both magnitude and phase over the entire frequency bandwidth are seen in the interaction responses of the axial force (fig. 34(d)), side force (fig. 34(e)), pitch moment (fig. 34(b)), and roll moment (fig. 34(c)) gages.

Figure 35 presents representative FRFs of the balance gage outputs due to a forward pitch (out-of-plane) moment loading at the hub (load sequence 2) with shaft rotation. The pitch moment (fig. 35(b)) and the normal force (fig. 35(a)) gages are the only directly loaded gages in this figure. The other three gages, axial force (fig. 35(d)), side force (fig. 35(e)), and roll moment (fig. 35(c)), show a ratio of approximately 0 at low frequency (<1 Hz) and indicate the amount of load interaction seen by these gages. For the directly loaded balance normal force (fig. 35(a)) and pitch moment (fig. 35(b)) gages, the effect of hub mass variations with shaft rotation is significant at frequencies above 15 Hz, similar to results shown in figure 31 without shaft rotation. Variations in both magnitude and phase over the entire frequency bandwidth are seen in the interaction responses of the axial force (fig. 35(d)), side force (fig. 35(e)), and roll moment (fig. 35(c)) gages.

Figure 36 presents representative FRFs of the balance gage outputs due to a roll (out-of-plane) moment loading at the hub (load sequence 4) with shaft rotation. The roll moment (fig. 36(c)) and the normal force (fig. 36(a)) gages are the only directly loaded gages in this figure. The other three gages, axial force (fig. 36(d)), side force (fig. 36(e)), and pitch moment (fig. 36(b)), show a ratio of approximately 0 at low frequency (<1 Hz) and indicate

the amount of load interaction seen by these gages. For the directly loaded balance normal force (fig. 36(a)) gage, the effect of hub mass variation is mostly seen at frequencies above 15 Hz, also shown in figure 32(a). For the directly loaded balance roll moment (fig. 36(c)) gage, the effect of hub mass variation with shaft rotation is significant at frequencies above 6 Hz, similar to the results as was shown in figure 32(c). Variations in both magnitude and phase over the entire frequency bandwidth are seen in the interaction responses of the axial force (fig. 36(d)), side force (fig. 36(e)), and pitch moment (fig. 36(b)) gages.

Effect of Push Rod Loading

The effect of vibratory loading through the stationary push rods is shown in figures 37–39 with no shaft rotation. The vibratory loading through the push rods was on the order of ± 100 lb. To gain access to the push rods, the calibration hardware was removed and the balance gage FRFs were acquired at zero hub and blade mass. These comparisons were performed to evaluate the influence of the vibratory loading through the stationary push rods on the measured balance FRFs.

Figure 37 presents representative FRFs of the balance gage outputs due to a vibratory loading through stationary push rod number 1 (load sequence 7). The normal force (fig. 37(a)), pitch moment (fig. 37(b)), and the roll moment (fig. 37(c)) gages are the only directly loaded gages in this figure. The other two gages, axial force (fig. 37(d)) and side force (fig. 37(e)), show a ratio of approximately 0 at low frequency (<1 Hz) and indicate the amount of load interaction seen by these gages. Figure 37(f) shows the dynamic load response of push rod number 1 to the load cell attached to the end of the hydraulic actuator.

Figure 38 presents representative FRFs of the balance gage outputs due to a vibratory loading through stationary push rod number 2 (load sequence 8). The normal force (fig. 38(a)), pitch moment (fig. 38(b)), and the roll moment (fig. 38(c)) gages are the only directly loaded gages in this figure. The other two gages, axial force (fig. 38(d)) and side force (fig. 38(e)), show a ratio of approximately 0 at low frequency (<1 Hz) and indicate the amount of load interaction seen by these gages. Figure 38(f) shows the dynamic load response of push rod number 2 to the load cell attached to the end of the hydraulic actuator.

Figure 39 presents representative FRFs of the balance gage outputs due to a vibratory loading through stationary

push rod number 3 (load sequence 9). The normal force (fig. 39(a)), pitch moment (fig. 39(b)), and the roll moment (fig. 39(c)) gages are the only directly loaded gages in this figure. The other two gages, axial force (fig. 39(d)) and side force (fig. 39(e)), show a ratio of approximately 0 at low frequency (<1 Hz) and indicate the amount of load interaction seen by these gages. Figure 39(f) shows the dynamic load response of push rod number 3 to the load cell attached to the end of the hydraulic actuator.

Differences in the dynamic response shown in the phase plots of figure 37(f) (phase variation with frequency) and figure 38(f) (phase oscillation with frequency) relative to figure 39(f) are caused by feedback through the control valves of both the calibration actuator and the primary control actuator push rods on the RTA. Difficulty in introducing vibratory loading at the higher frequencies was noted during the calibration. Time constraints in the wind tunnel schedule precluded a satisfactory solution to this problem. The influence of these phenomena on the balance measurements is not fully known and should be further investigated.

The FRFs presented in figures 37–39 show that significant changes in the dynamic response of the balance exist over the entire frequency bandwidth of 0–64 Hz. These changes in the dynamic response are caused by balance interactions and the dynamic structural characteristics of both the wind tunnel support system and the RTA. The balance gage response due to the dynamic loading through the stationary push rods is significant, indicating the necessity of making dynamic corrections to the dynamic hub loads based on loading through the RTA control system. A description of the procedures used to account for dynamic loading through the stationary push rods is presented in reference 6.

Concluding Remarks

Calibration results showing the influence of frequency bandwidth, hub mass, rotor RPM, thrust preload, and dynamic loads through the stationary push rods were discussed and presented in figures 10–39. The FRFs shown identify the significant changes in the dynamic response of the balance from 0 to 64 Hz. Since the balance flexure design places the isolated balance natural frequencies above 60 Hz, the changes in the dynamic balance response shown are attributed to the dynamic structural characteristics of both the wind tunnel support system and the RTA. Some of the findings from this dynamic calibration effort are identified below.

The influence of reduced frequency bandwidth (from 0–64 Hz to 0–32 Hz) in the data acquisition process showed no significant changes in the FRFs with increased frequency resolution in either the directly loaded balance gages or the interactions.

Out-of-plane versus in-plane force loading resulted in markedly different balance pitch and roll moment responses, which may be the result of the difference in the magnitude of PM and RM loading applied in each case, or that the RTA/balance response is considerably different for out-of-plane versus in-plane loading.

The effects of shaft rotation are mostly seen in the higher frequency range (above 20–30 Hz) and manifest themselves most clearly as a phase shift for both the directly loaded balance gages and the interactions.

The effect of thrust preload without and with shaft rotation primarily influenced the directly loaded gages above 30 Hz and the interactions over the entire frequency bandwidth (0–64 Hz) in both magnitude and phase.

The effect of thrust preload inclination primarily influenced the measured magnitudes of the directly loaded gages above 15 Hz with small variations in both magnitude and phase for the interactions over the entire frequency bandwidth (0–64 Hz).

The influence of thrust preload variations from 2,000 to 4,000 lb (thrust up, 9–18% full range) with shaft rotation showed small variations in both magnitude and phase over the entire frequency bandwidth (0–64 Hz) for both the directly loaded and interaction balance gages.

The effects of hub mass on the measured FRFs with or without shaft rotation were significant in both magnitude and phase for frequencies above 10 Hz for either the directly loaded balance gages or the interactions.

The FRFs for the stationary push rods showed that significant changes in the dynamic response of the balance exist over the entire frequency bandwidth of 0–64 Hz and that the balance gage response due to the dynamic loading through the stationary push rods is significant. These results clearly indicate that corrections to the dynamic hub loads are necessary for oscillatory loading through the RTA control system.

In summary, hub mass variations had the greatest effect on the directly and indirectly loaded balance gages. Shaft rotation had a greater influence on the balance response measurements than the limited thrust preloading that was

applied. Inclination of the thrust preload had a greater influence on the measured balance FRFs than a thrust preloading with no inclination.

Recommendations for Future Work

Future dynamic calibration tests should acquire accelerometer data at the hub in both on-axis and off-axis load directions to aid in determining the hub displacements and the effects of inertial loading on the balance response.

The ability to apply off-axis dynamic calibration loading should be investigated to evaluate the accuracy of the on-axis response measurements and the influence of the interactions. The ability to apply multiple dynamic calibration loadings simultaneously should also be considered.

The ability to apply greater out-of-plane pitch and roll moment loading should be developed and investigated.

Future calibration efforts should include both in-plane and out-of-plane loading sequences from the forward and aft directions, as well as from the left and right sides to further understand the asymmetric response noted in the hub pitch moment response.

Dynamic calibration testing of the RTA tunnel installation at various angles of attack should be performed to investigate the effect of model angle of attack on the balance dynamic response (FRFs). These data can be used to determine whether accurate balance load predictions can be obtained by using a dynamic calibration matrix obtained from the interpolation over model angle of attack of the dynamic calibration matrices, which are determined at only a few model angles of attack.

The accuracy of the balance load predictions was evaluated against the expected loading from an imbalanced hub test in reference 5. This provided only 1/rev balance loading up to 7 Hz. The effects of shaft rotation and especially hub mass on the balance FRFs are most noticeable at frequencies above 15 Hz. An ability to introduce vibratory loading at higher frequencies should be developed to properly evaluate and quantify the balance accuracy at higher frequencies. Such loading should include in-plane and out-of-plane forces and hub moments.

The capability to properly evaluate the accuracy of dynamic corrections to the measured balance forces and moments as a result of vibratory loading through the stationary push rods (control system) should be

developed. Improved procedures for the application of vibratory loading through the stationary push rods should be determined.

References

1. Lehmann, G.; and Fu, K.-H.: Theoretical and Experimental Investigations on a Six-Component Rotor Balance. Eleventh European Rotorcraft Forum, The City University, London, EC1V OHB, England, Sept. 1983.
2. Gabel, R.; Sheffler, M.; Tarzanin, F.; and Hodder, D.: Wind Tunnel Modeling of Vibratory Loads. 38th Annual Forum of the American Helicopter Society, Anaheim, Calif, May 1982.
3. Young, D.; and Tarzanin, F.: Structural Optimization and Mach Scale Test Validation of a Low Vibration Rotor. 47th Annual Forum of the American Helicopter Society, Phoenix, Ariz., May 1991.
4. Staley, J. A.; Matthew, M. B.; and Tarzanin, F.: Wind Tunnel Modeling of High Order Rotor Vibration. 49th Annual Forum of the American Helicopter Society, St. Louis, Mo., May 1993.
5. van Aken, J. M.; Peterson, R. L.; and Freedman, C. J.: Calibration Results of the NASA Ames Rotor Test Apparatus Steady/Dynamic Rotor Balance. American Helicopter Society Aeromechanics Specialists Conference, San Francisco, Calif., Jan. 1994.
6. Wang, J. M.; and van Aken, J. M.: Correlation of Vibratory Hub Loads for a Sikorsky Full-Scale Bearingless Main Rotor. 50th Annual Forum of the American Helicopter Society, Washington, D.C., May 1994.
7. Norman, T. R.; Cooper, C. R.; Fredrickson, C. A.; and Herter, J. R.: Full-Scale Wind Tunnel Evaluation of the Sikorsky Five-Bladed Bearingless Main Rotor. 49th Annual Forum of the American Helicopter Society, St. Louis, Mo., May 1993.
8. Peterson, R. L.; Maier, T.; Langer, H. J.; and Tränapp, N.: Correlation of Wind Tunnel and Flight Test Results of a Full-Scale Hingeless Rotor. American Helicopter Society Aeromechanics Specialists Conference, San Francisco, Calif., Jan. 1994.

Table 1. Identification of the directly loaded balance gages for the various dynamic calibration test load sequences

	NF lb	PM ft-lb	RM ft-lb	AF lb	SF lb
Sequence 1 – Vertical loading at the rotor shaft center ^a	600				
Sequence 2 – Vertical loading at 1 ft forward of the rotor shaft center ^a	500	500			
Sequence 3 – Vertical loading at 1 ft aft of the rotor shaft center	500	500			
Sequence 4 – Vertical loading at 1 ft to the left of the rotor shaft center ^a	500		500		
Sequence 5 – Horizontal loading in longitudinal direction ^a		3,660		600	
Sequence 6 – Horizontal loading in lateral direction ^a			3,660		600
Sequence 7 – Push rod number 1 ^b	100	34	60		
Sequence 8 – Push rod number 2 ^b	100	34	60		
Sequence 9 – Push rod number 3 ^b	100	60	34		

^aUsed to determine dynamic calibration matrix for the rotor balance through primary load path.

^bUsed to determine dynamic calibration matrix for the rotor balance through secondary (redundant) load path.

Table 2. Loading envelope for the BO105 and SBMR dynamic calibration tests

(a) BO105 data set								
RPM	0	315	425	0	–	–	–	315
Thrust (lb)	0	0	0	4000	–	–	–	4000
Thrust Inclination (deg)	0	0	0	0	–	–	–	0
Vertical loading at the rotor shaft center	X	X	X					
Vertical loading at 1 ft forward of the rotor shaft center (longitudinal plane)	X	X	X					
Vertical loading at 1 ft aft of the rotor shaft center (longitudinal plane)	X	X	X					
Vertical loading at 1 ft to the left of the rotor shaft center (lateral plane)	X	X	X					
Horizontal loading in longitudinal direction	X	X	X	X				X
Horizontal loading in lateral direction	X			X				
Stationary push rod (1–3) loading in vertical direction	X							
(b) SBMR data set								
RPM	0	315	–	0	0	315	315	315
Thrust (lb)	0	0	–	2000	2000	2000	3000	4000
Thrust Inclination (deg)	0	0	–	0	15	0	0	0
Vertical loading at the rotor shaft center	X	X						
Vertical loading at 1 ft forward of the rotor shaft center (longitudinal plane)	X	X						
Vertical loading at 1 ft to the left of the rotor shaft center (lateral plane)	X	X						
Horizontal loading in longitudinal direction	X	X		X	X	X	X	X
Horizontal loading in lateral direction	X			X				X

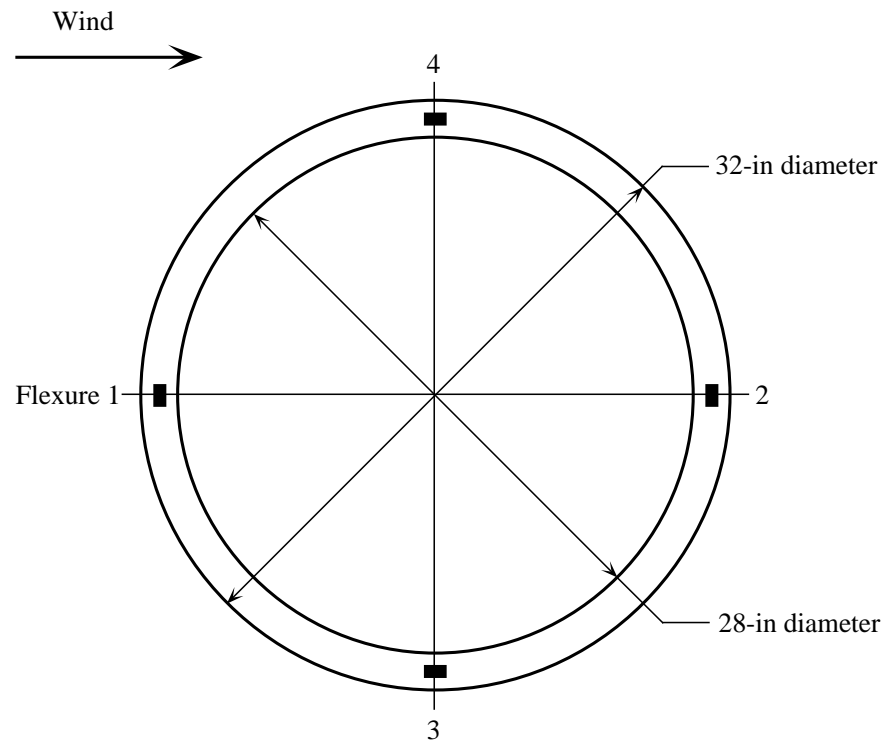


Figure 1. Schematic of top view of the Steady/Dynamic Rotor Balance with flexure identification.

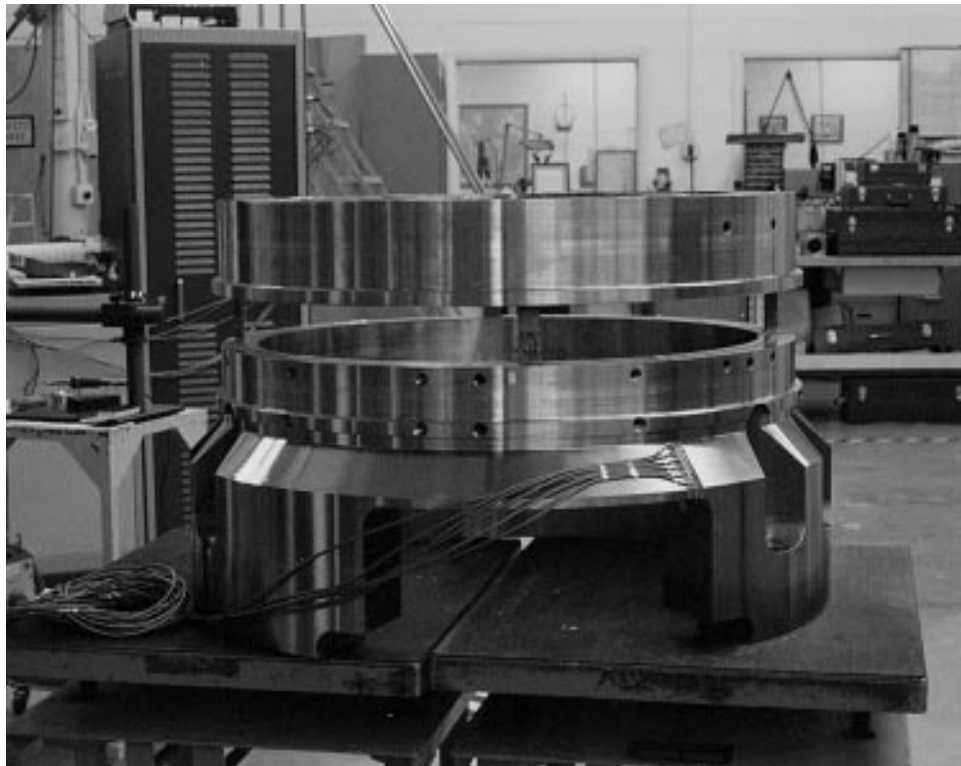


Figure 2. Steady/Dynamic Rotor Balance.

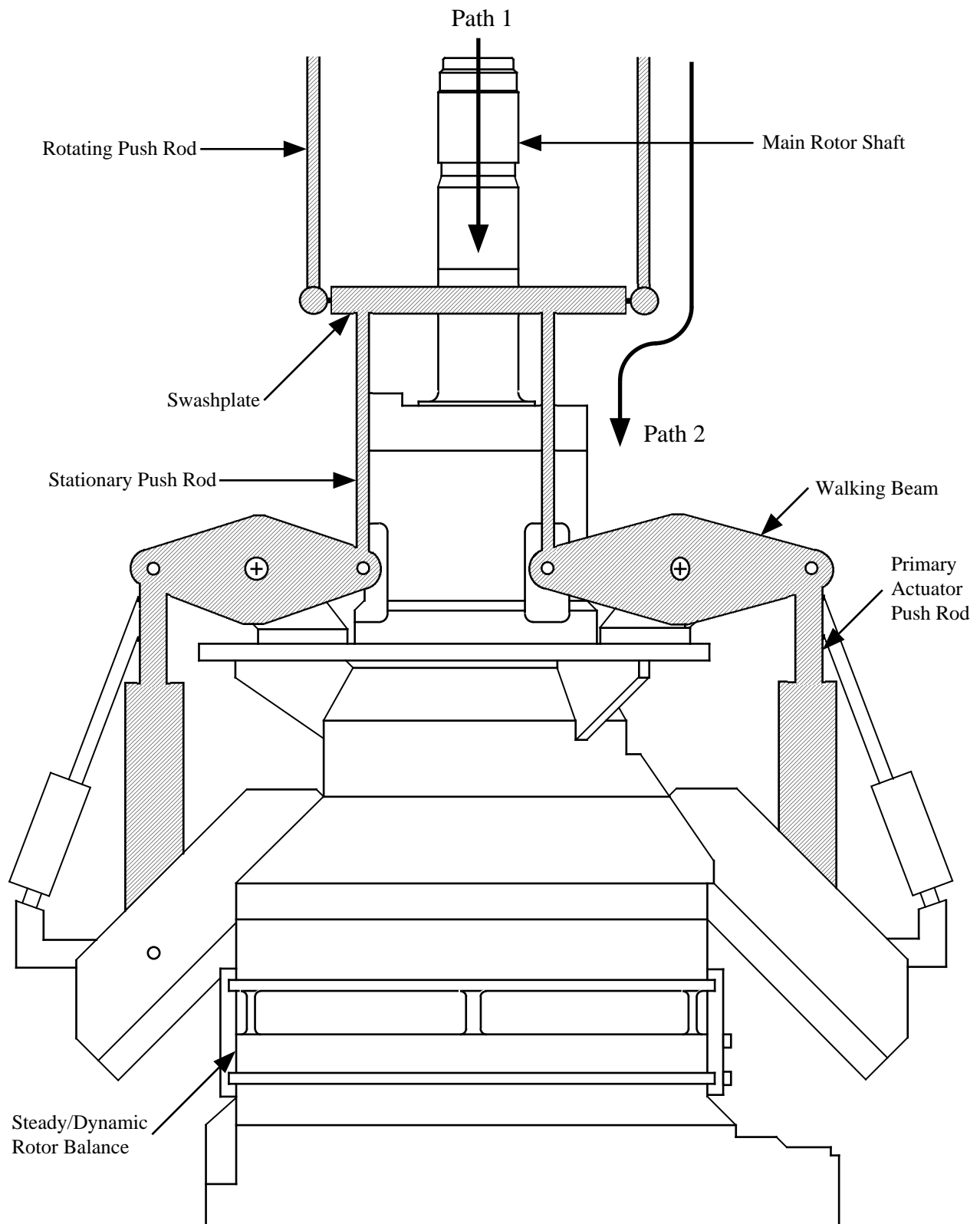


Figure 3. Schematic of the redundant load path system on the RTA.

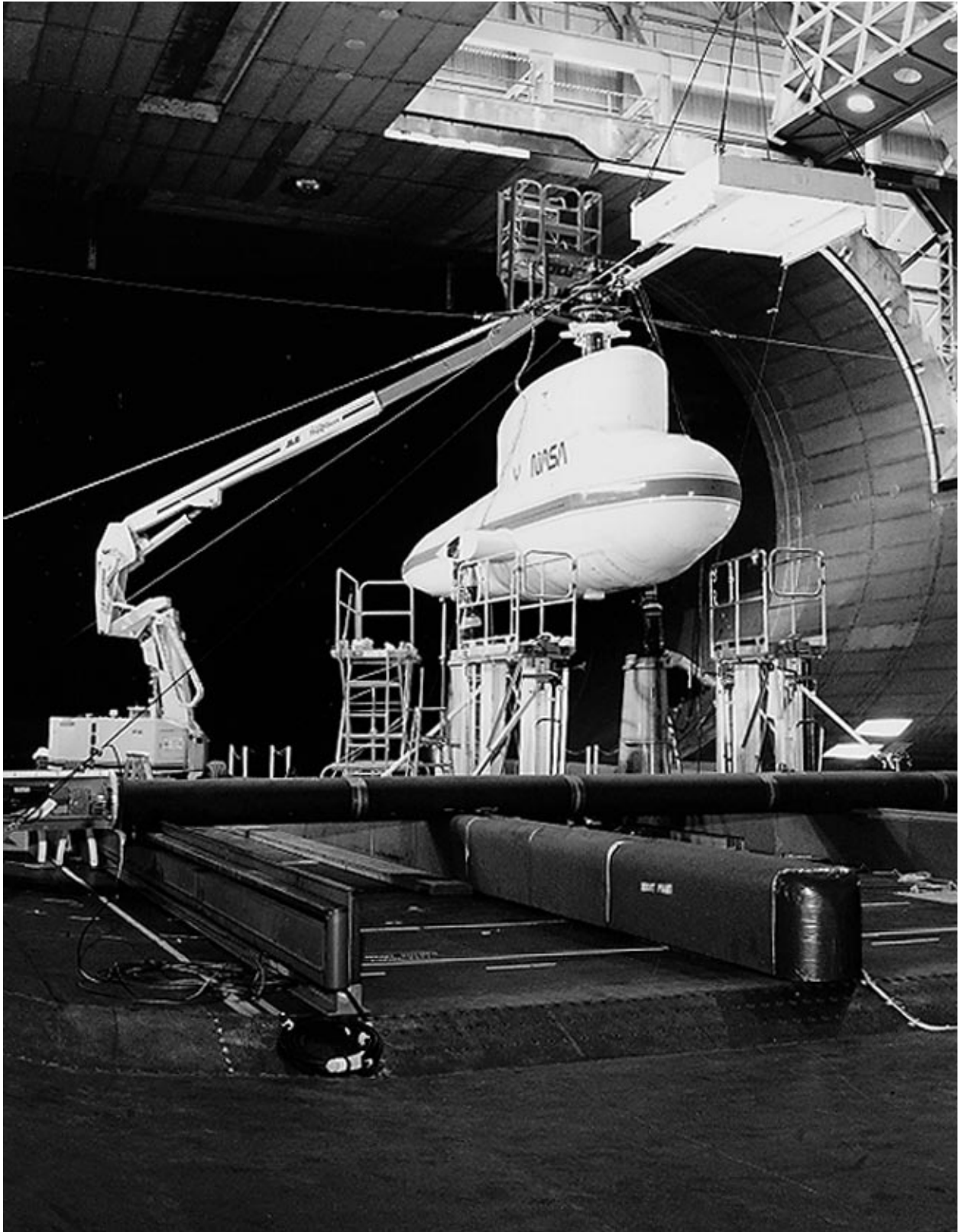


Figure 4. Longitudinal test setup for the installed, dynamic balance calibration in the 40- by 80-Foot Wind Tunnel.

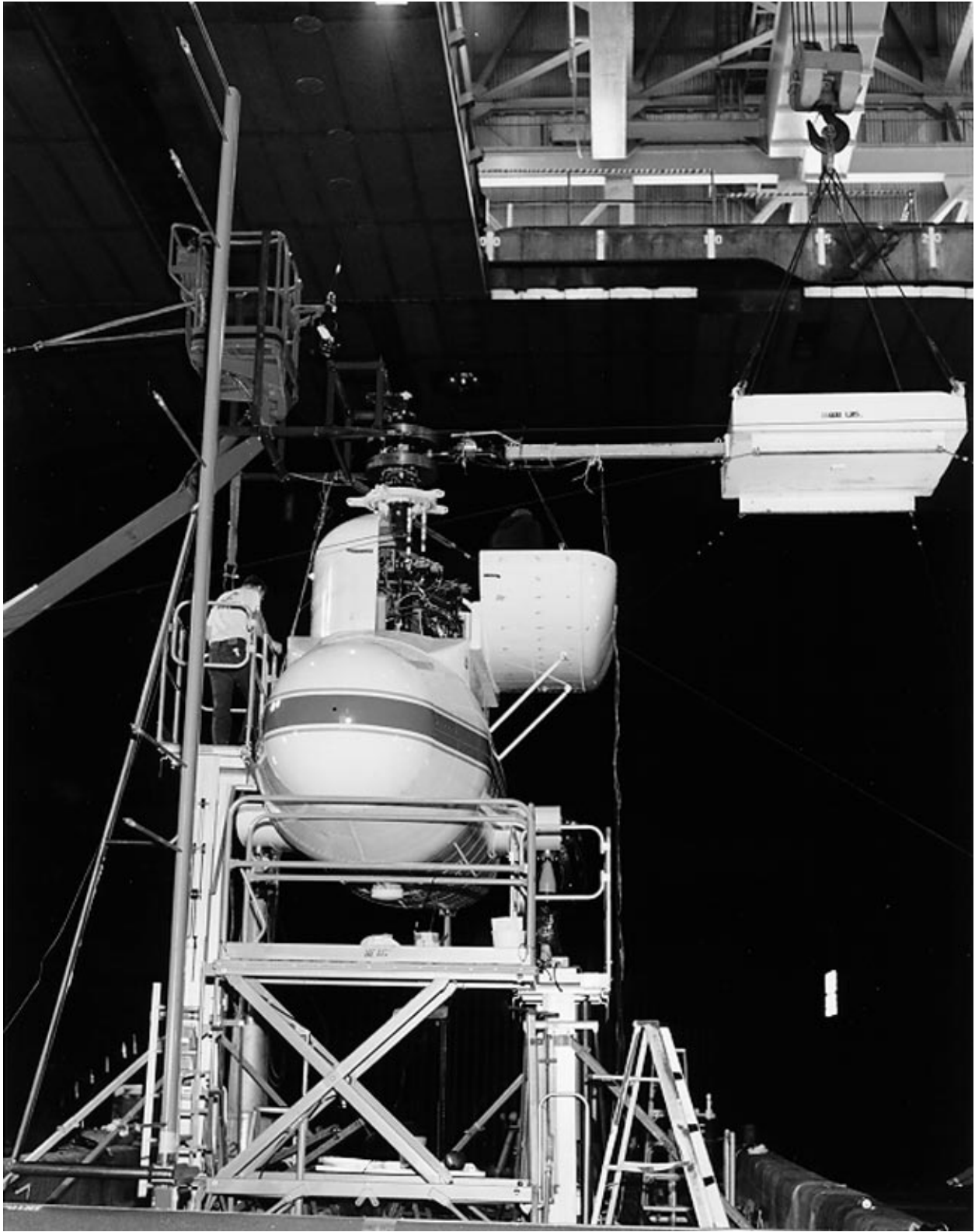


Figure 5. Lateral test setup for the installed, dynamic balance calibration in the 40- by 80-Foot Wind Tunnel.



Figure 6. Vertical moment calibration test setup.

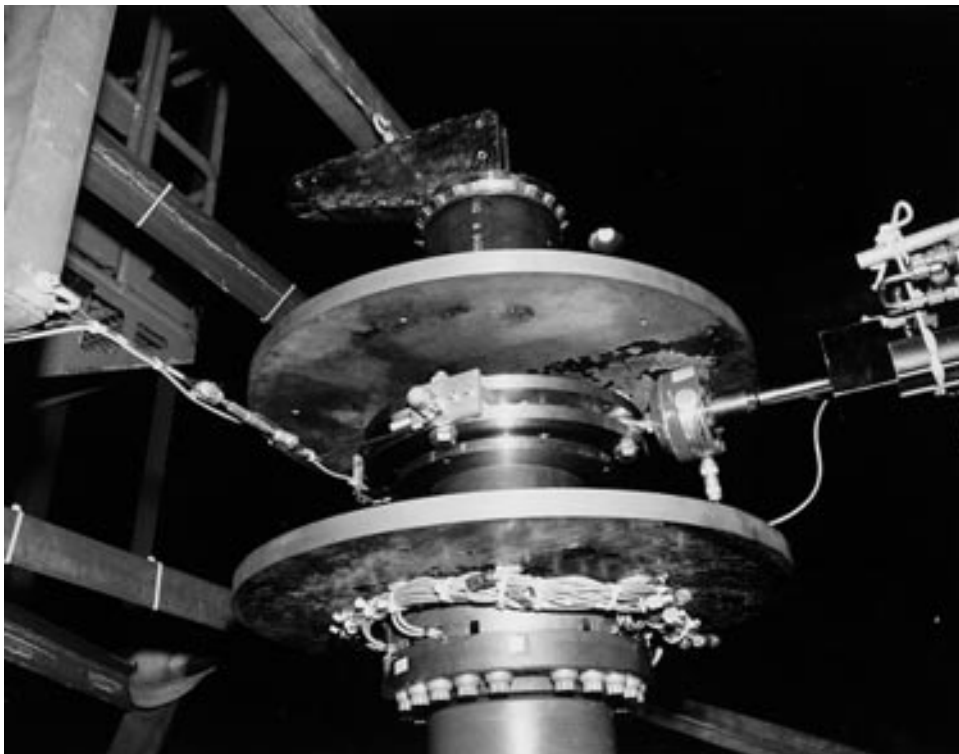


Figure 7. In-plane load calibration test setup.

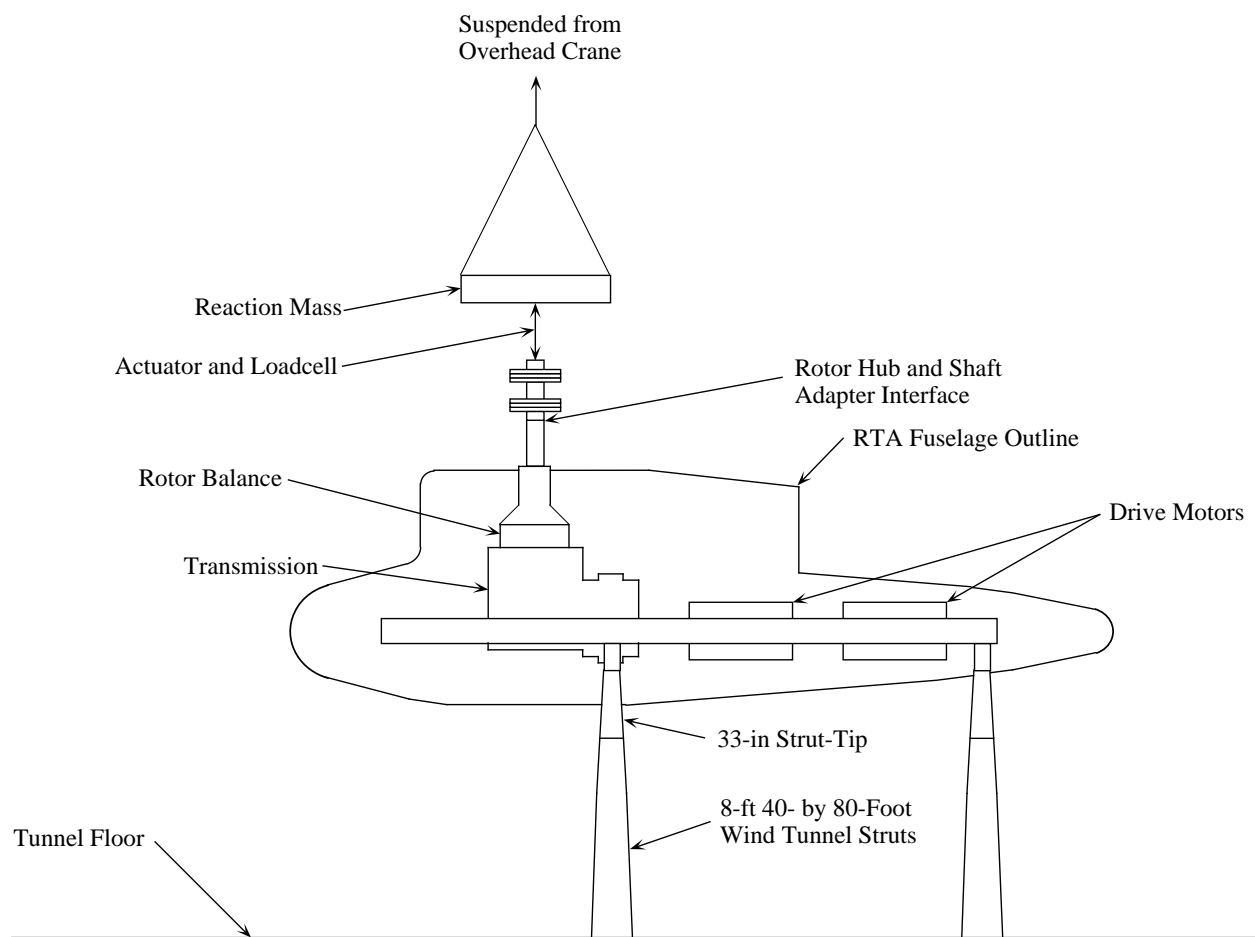


Figure 8. Schematic of side view of RTA vertical calibration configuration in the 40- by 80-Foot Wind Tunnel.

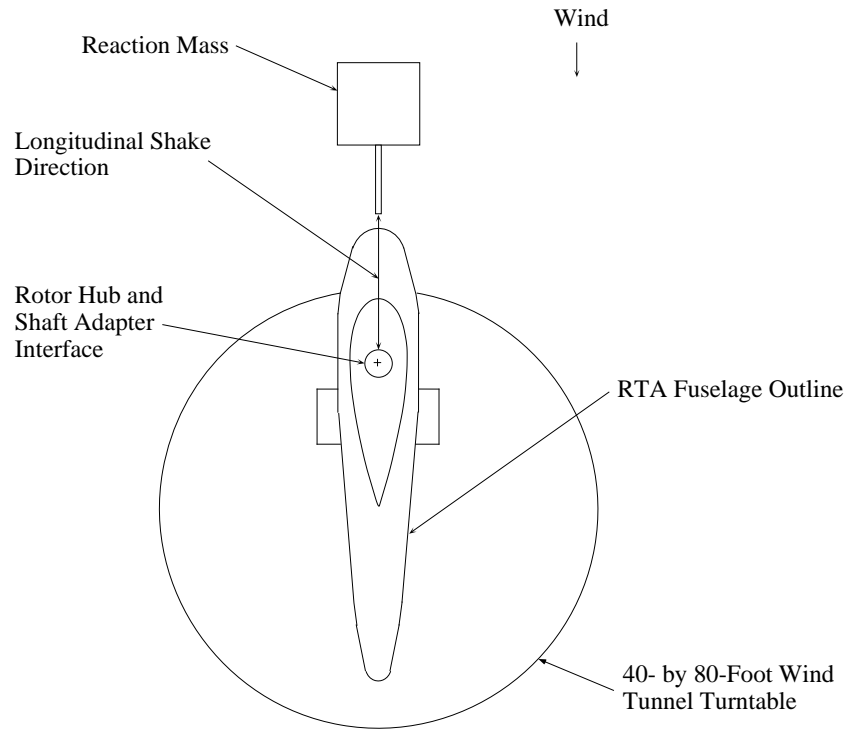


Figure 9(a). Schematic of top view of RTA longitudinal calibration configuration in the 40- by 80-Foot Wind Tunnel.

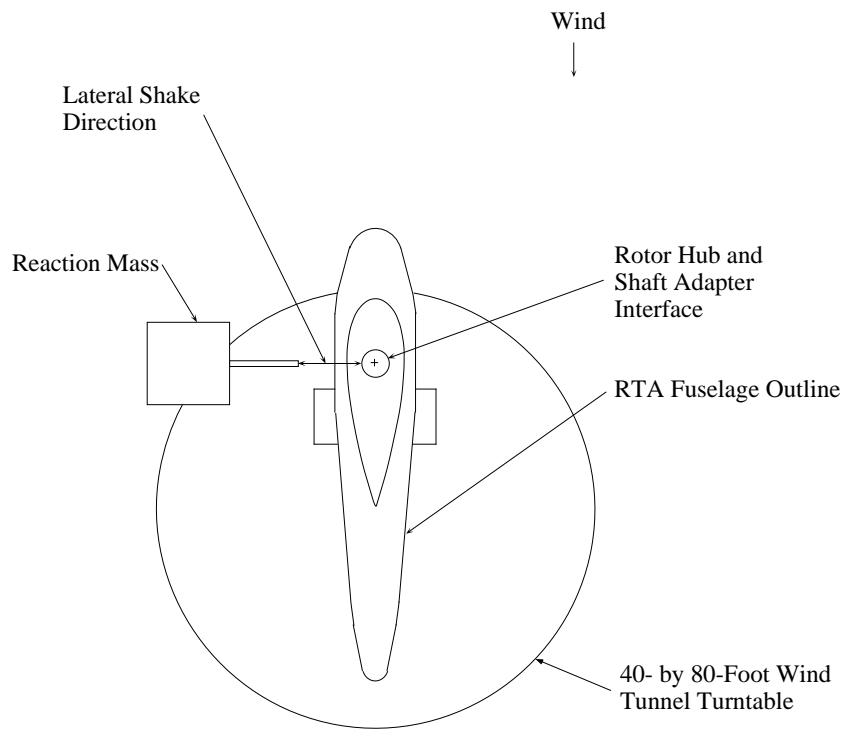


Figure 9(b). Schematic of top view of RTA lateral calibration configuration in the 40- by 80-Foot Wind Tunnel.

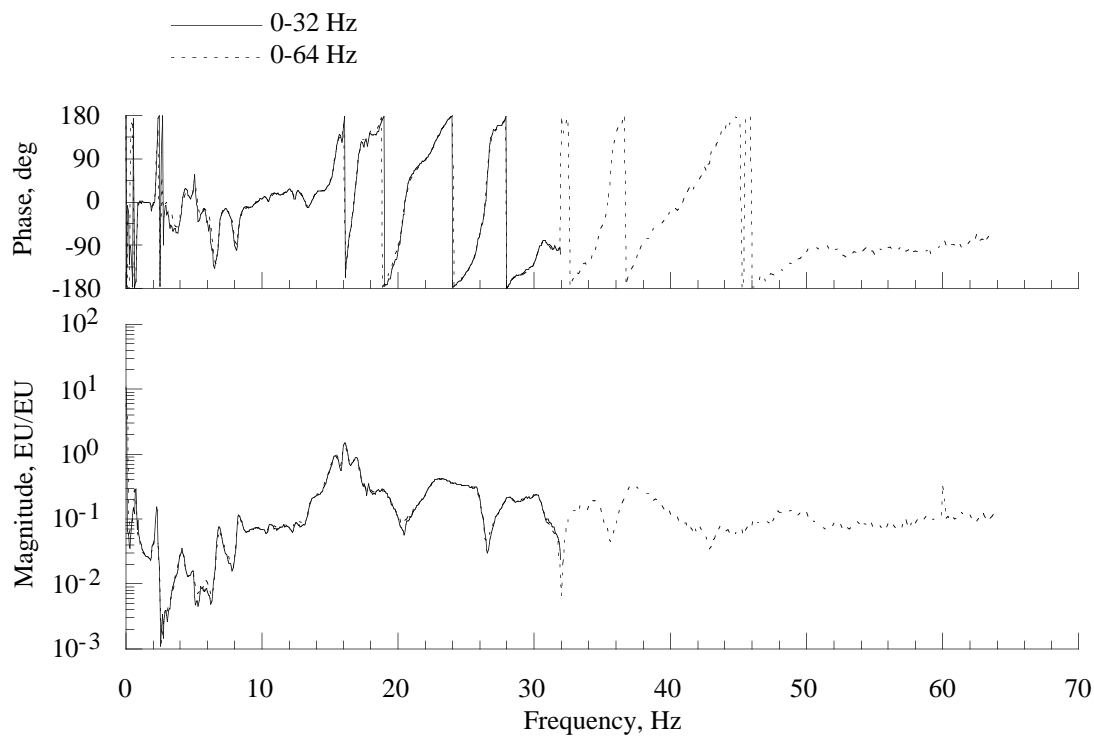


Figure 10(a). Bandwidth comparison of hub normal force balance response due to hub side force loading, simulated BO105 hub mass.

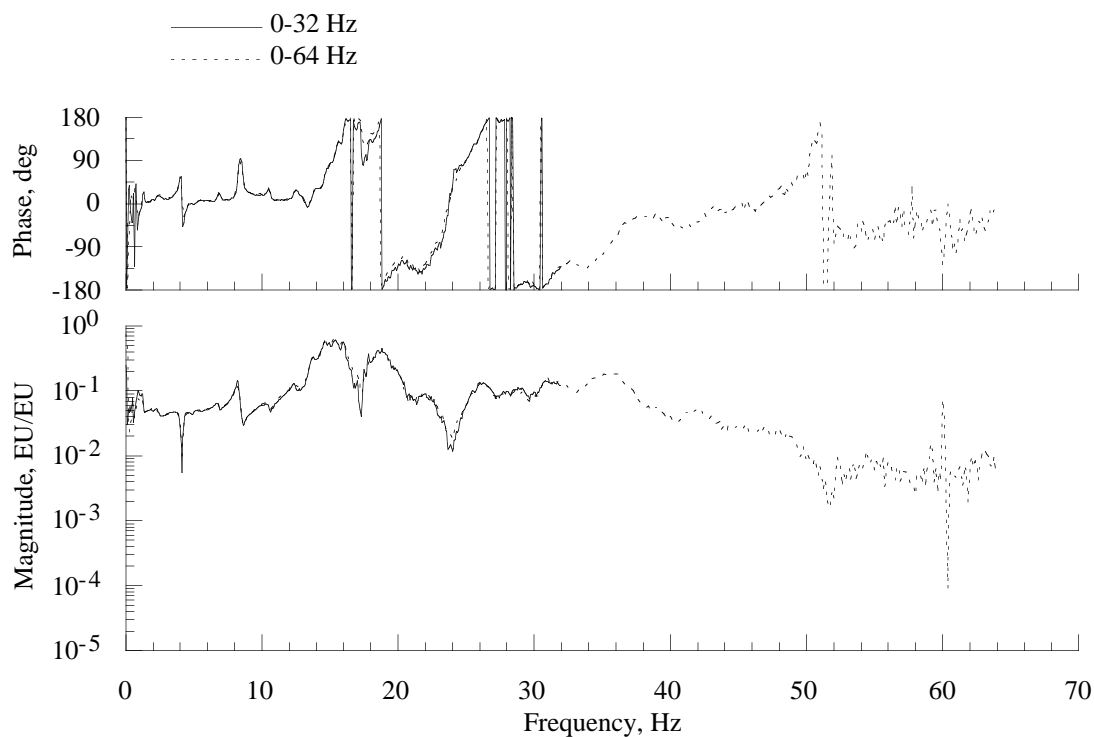


Figure 10(b). Bandwidth comparison of hub pitch moment balance response due to hub side force loading, simulated BO105 hub mass.

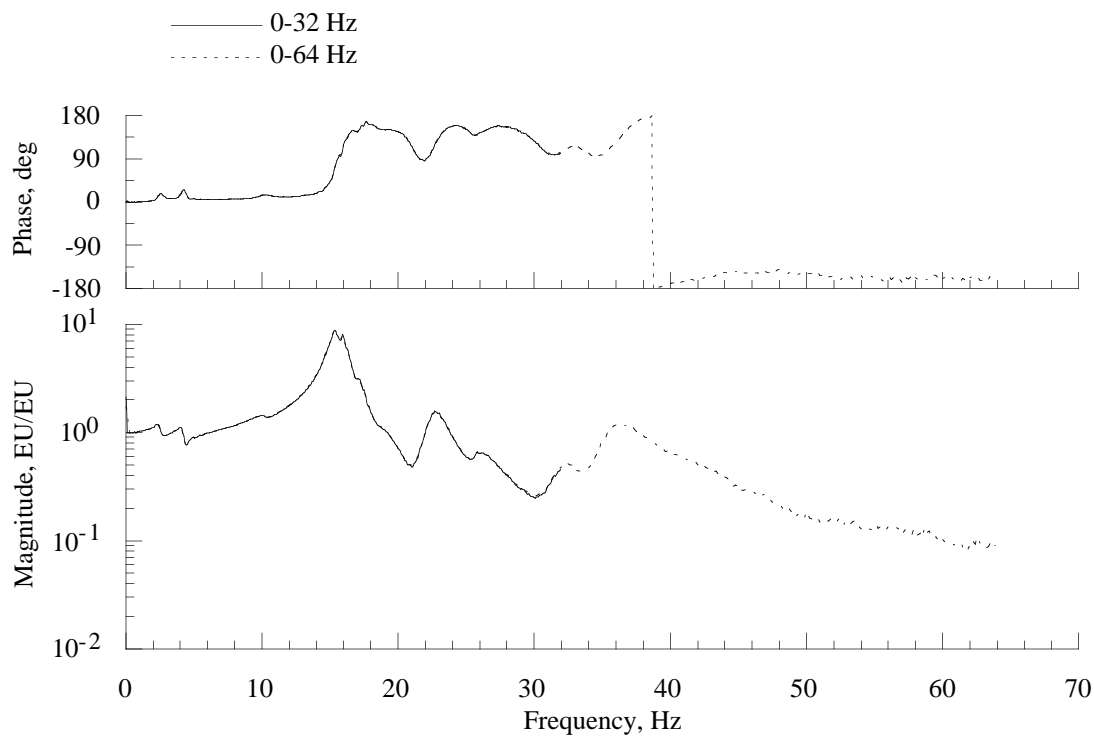


Figure 10(c). Bandwidth comparison of hub roll moment balance response due to hub side force loading, simulated BO105 hub mass.

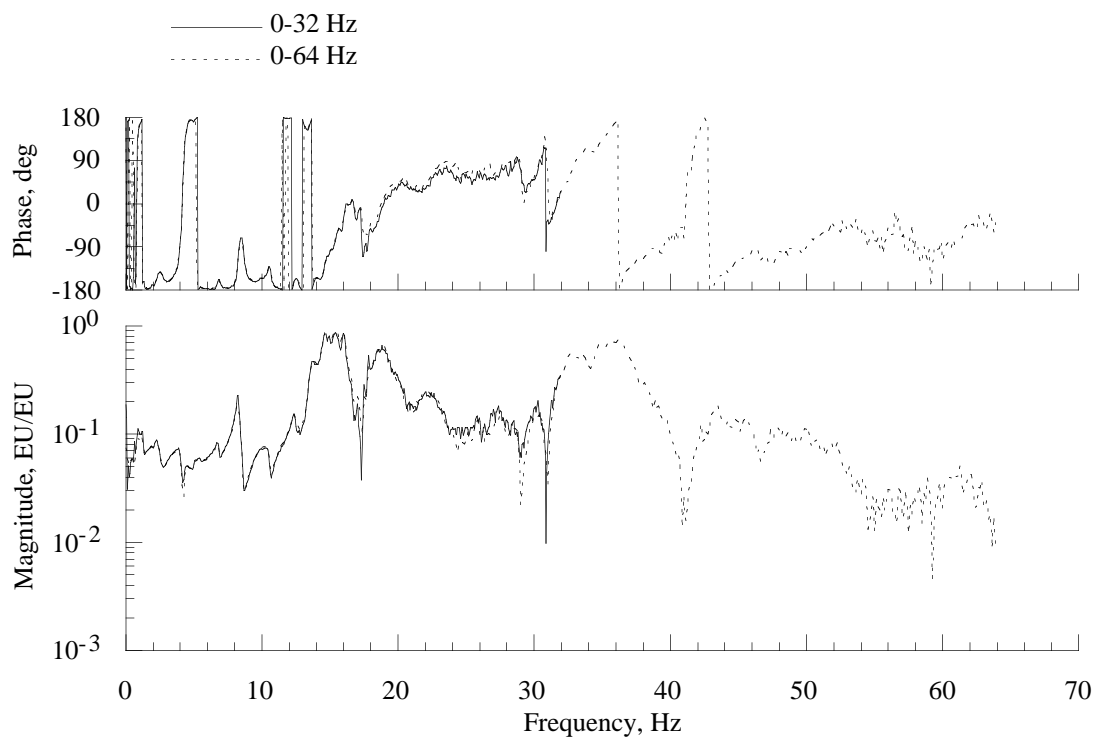


Figure 10(d). Bandwidth comparison of hub axial force balance response due to hub side force loading, simulated BO105 hub mass.

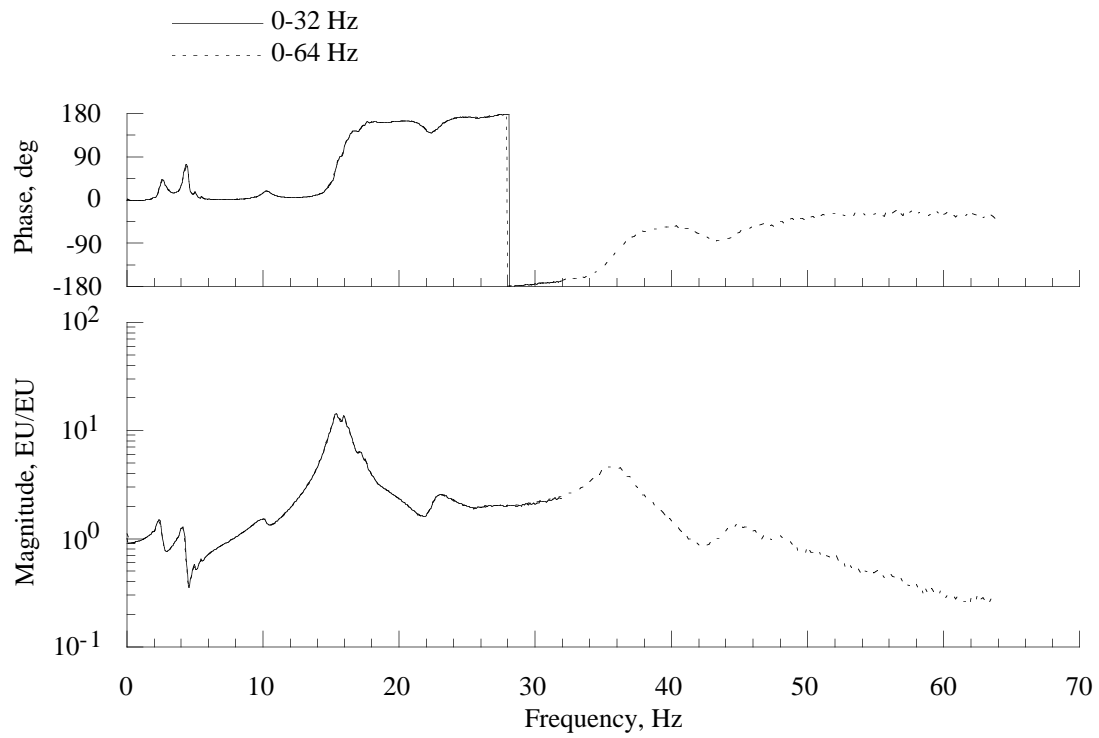


Figure 10(e). Bandwidth comparison of hub side force balance response due to hub side force loading, simulated BO105 hub mass.

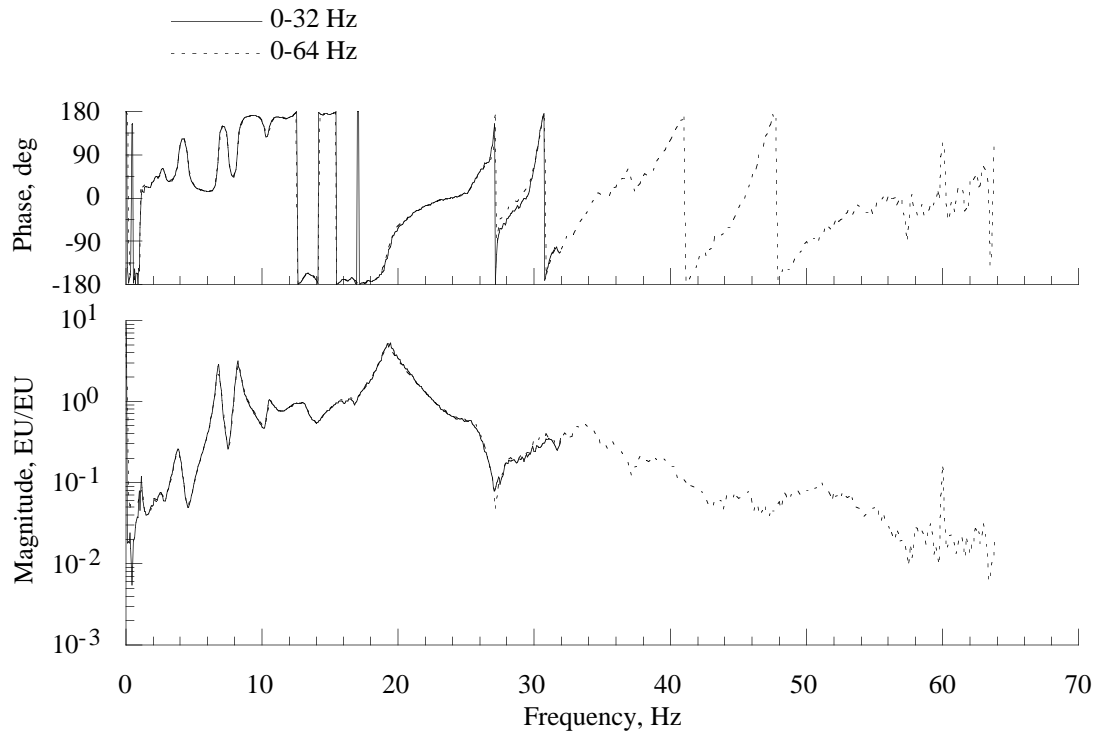


Figure 11(a). Bandwidth comparison of hub normal force balance response due to hub axial force loading, simulated BO105 hub mass.

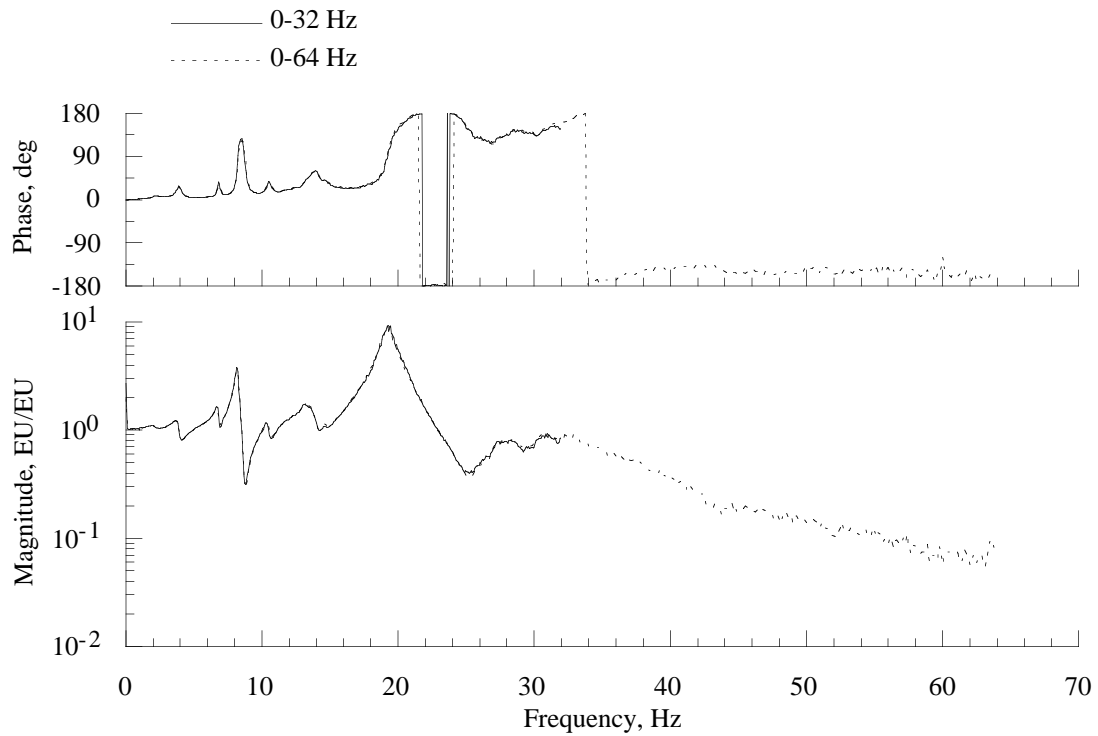


Figure 11(b). Bandwidth comparison of hub pitch moment balance response due to hub axial force loading, simulated BO105 hub mass.

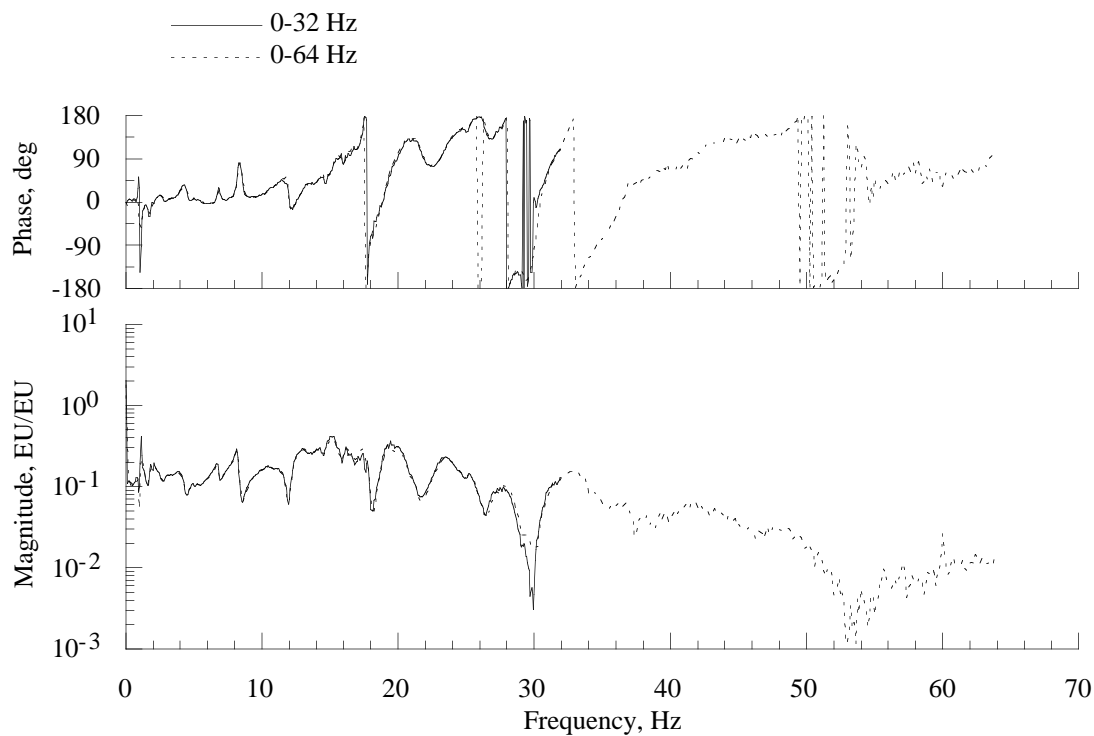


Figure 11(c). Bandwidth comparison of hub roll moment balance response due to hub axial force loading, simulated BO105 hub mass.

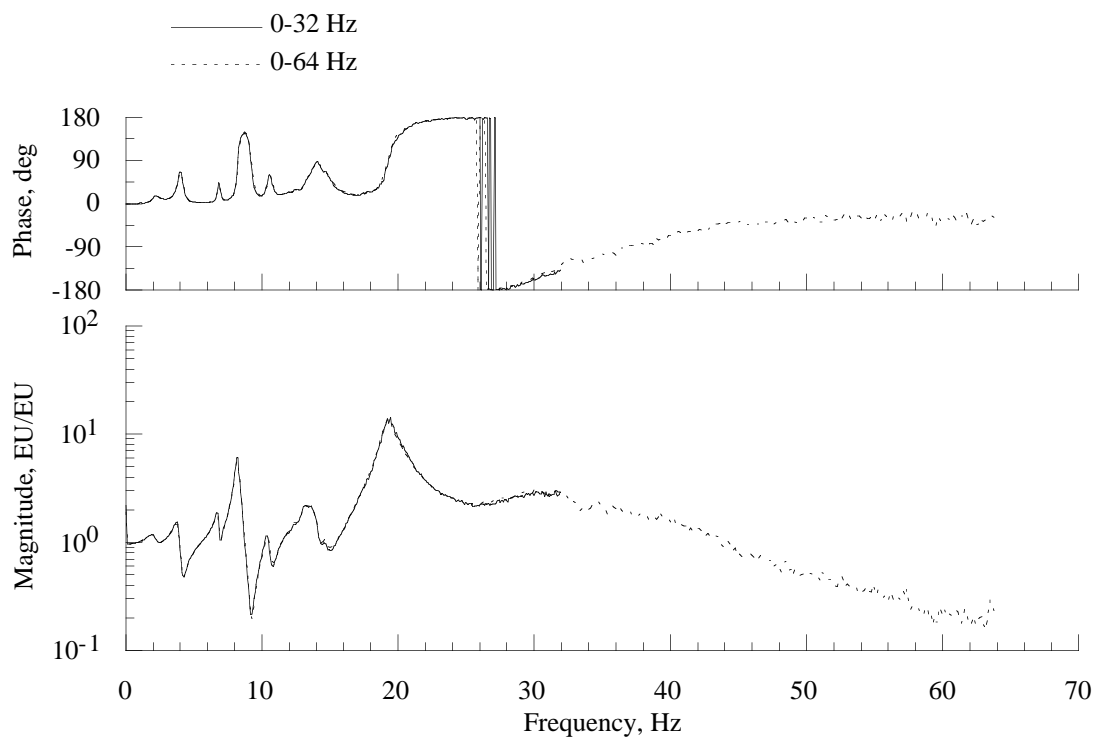


Figure 11(d). Bandwidth comparison of hub axial force balance response due to hub axial force loading, simulated BO105 hub mass.

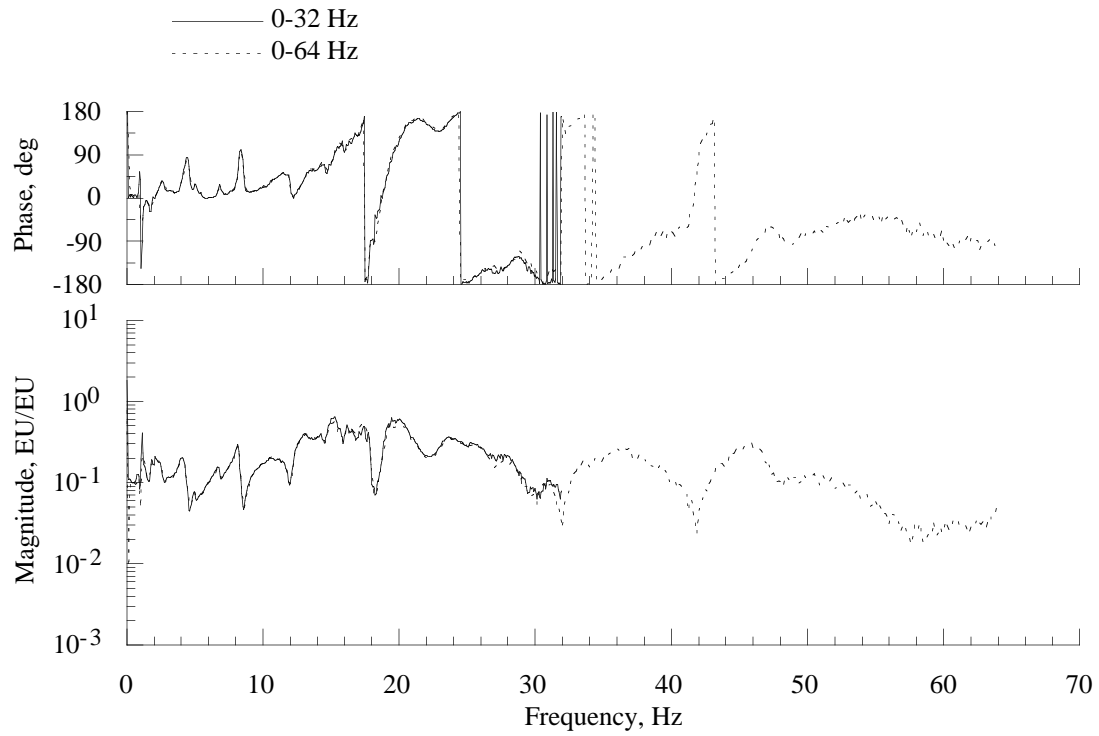


Figure 11(e). Bandwidth comparison of hub side force balance response due to hub axial force loading, simulated BO105 hub mass.

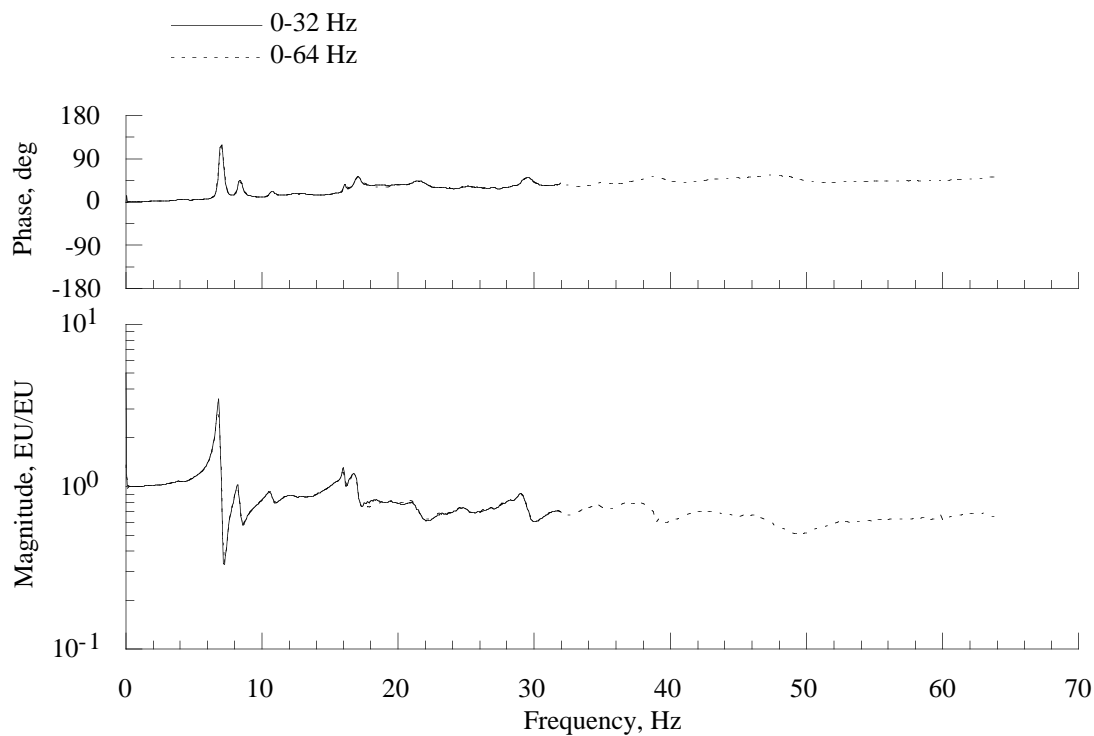


Figure 12(a). Bandwidth comparison of hub normal force balance response due to hub normal force loading, simulated BO105 hub mass.

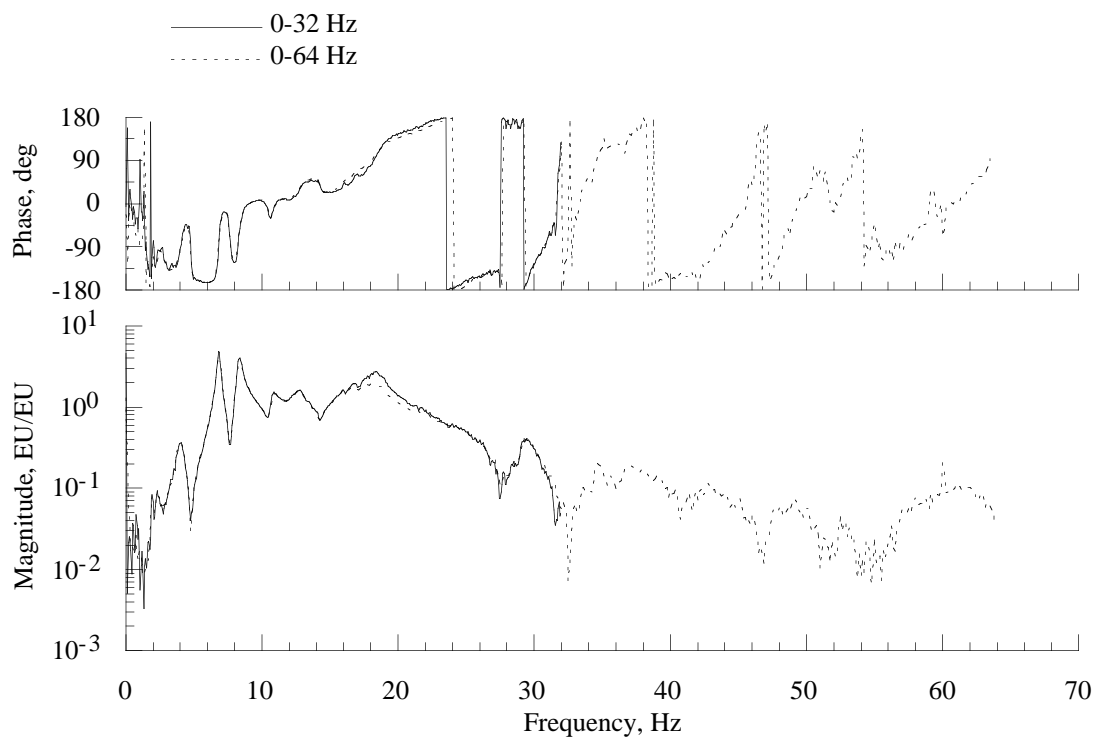


Figure 12(b). Bandwidth comparison of hub pitch moment balance response due to hub normal force loading, simulated BO105 hub mass.

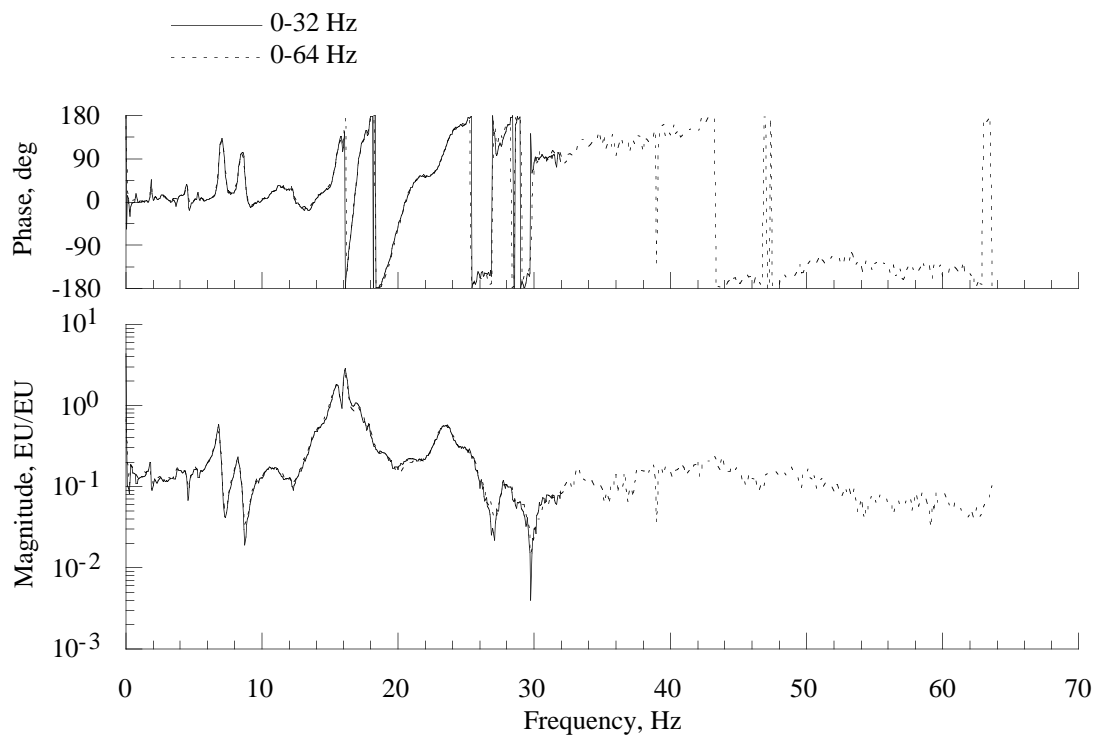


Figure 12(c). Bandwidth comparison of hub roll moment balance response due to hub normal force loading, simulated BO105 hub mass.

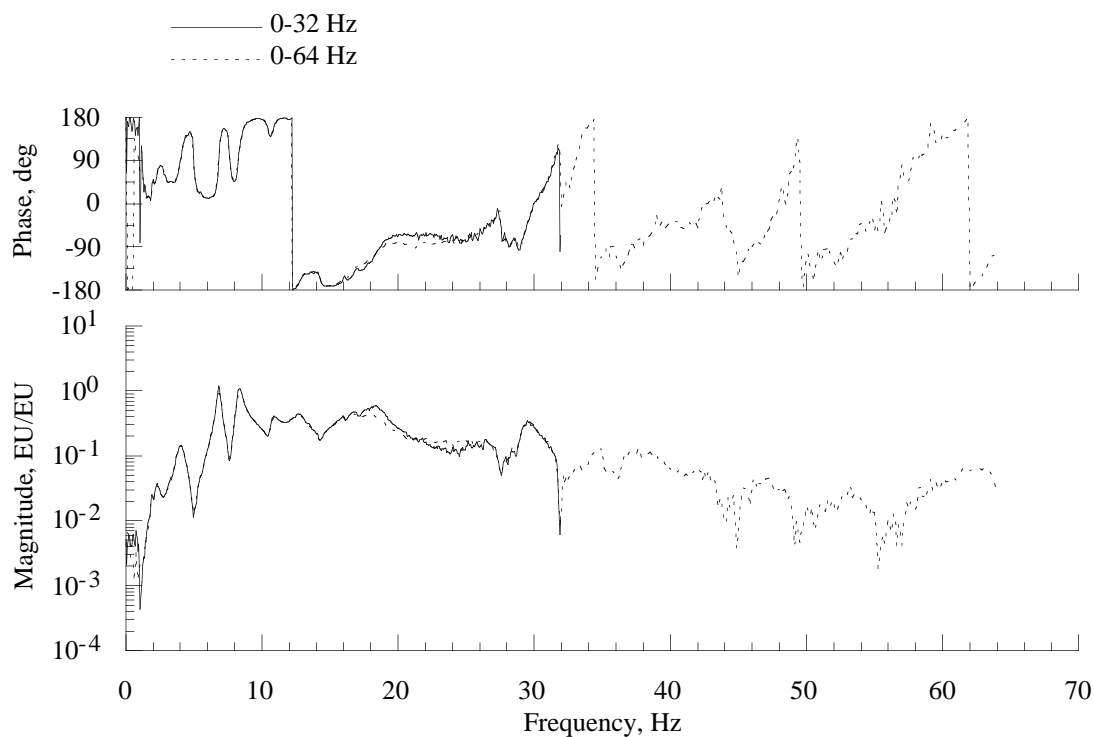


Figure 12(d). Bandwidth comparison of hub axial force balance response due to hub normal force loading, simulated BO105 hub mass.

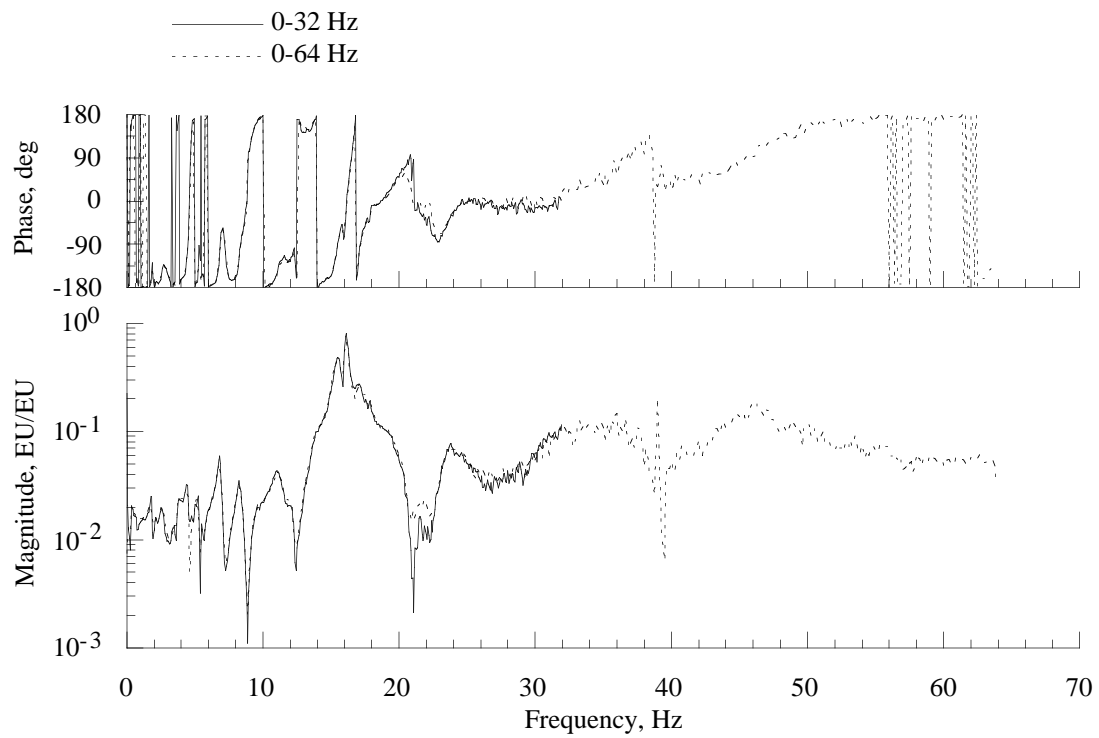


Figure 12(e). Bandwidth comparison of hub side force balance response due to hub normal force loading, simulated BO105 hub mass.

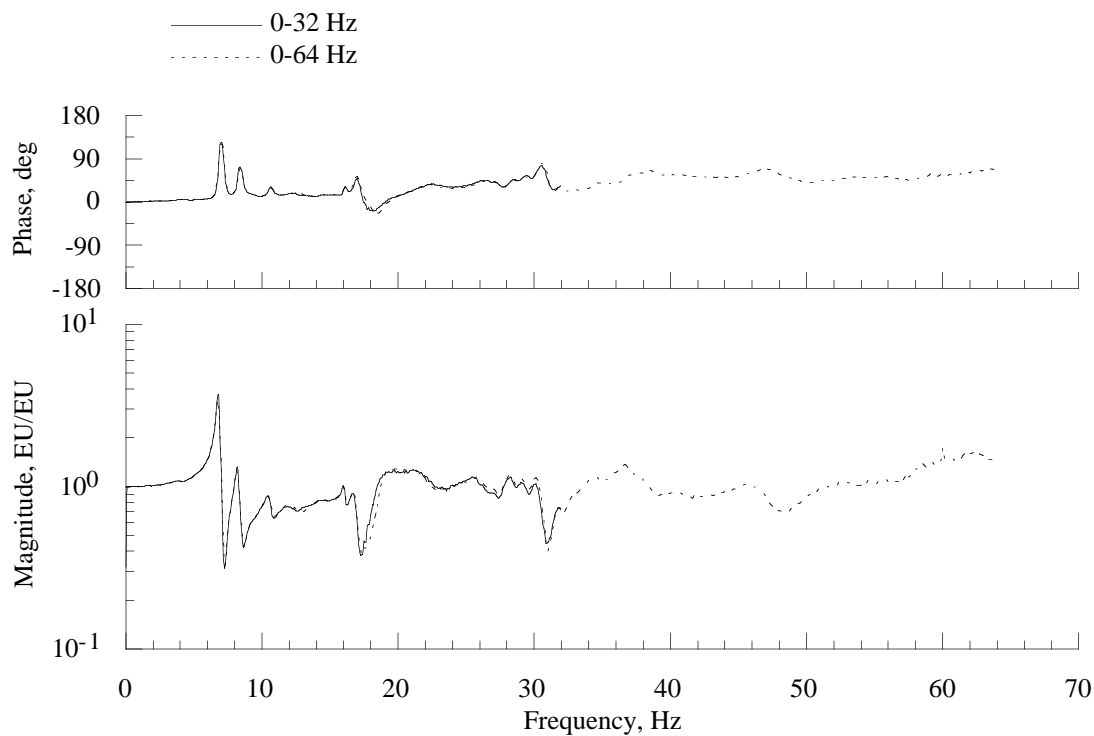


Figure 13(a). Bandwidth comparison of hub normal force balance response due to forward hub pitch moment loading, simulated BO105 hub mass.

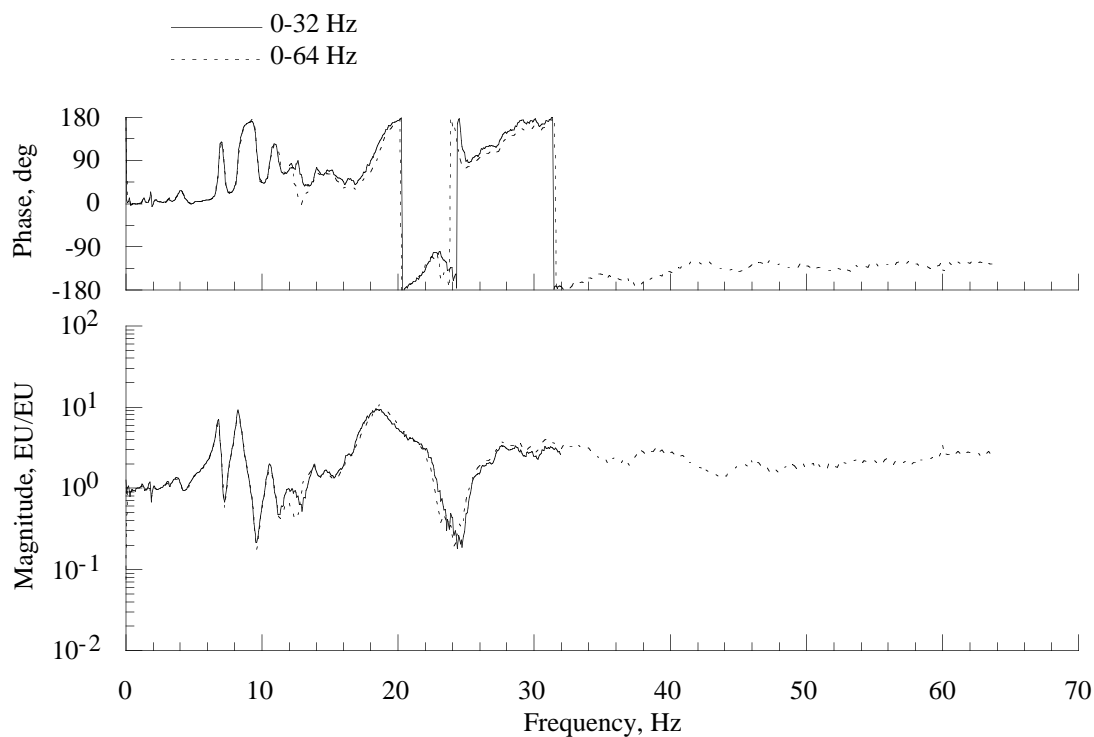


Figure 13(b). Bandwidth comparison of hub pitch moment balance response due to forward hub pitch moment loading, simulated BO105 hub mass.

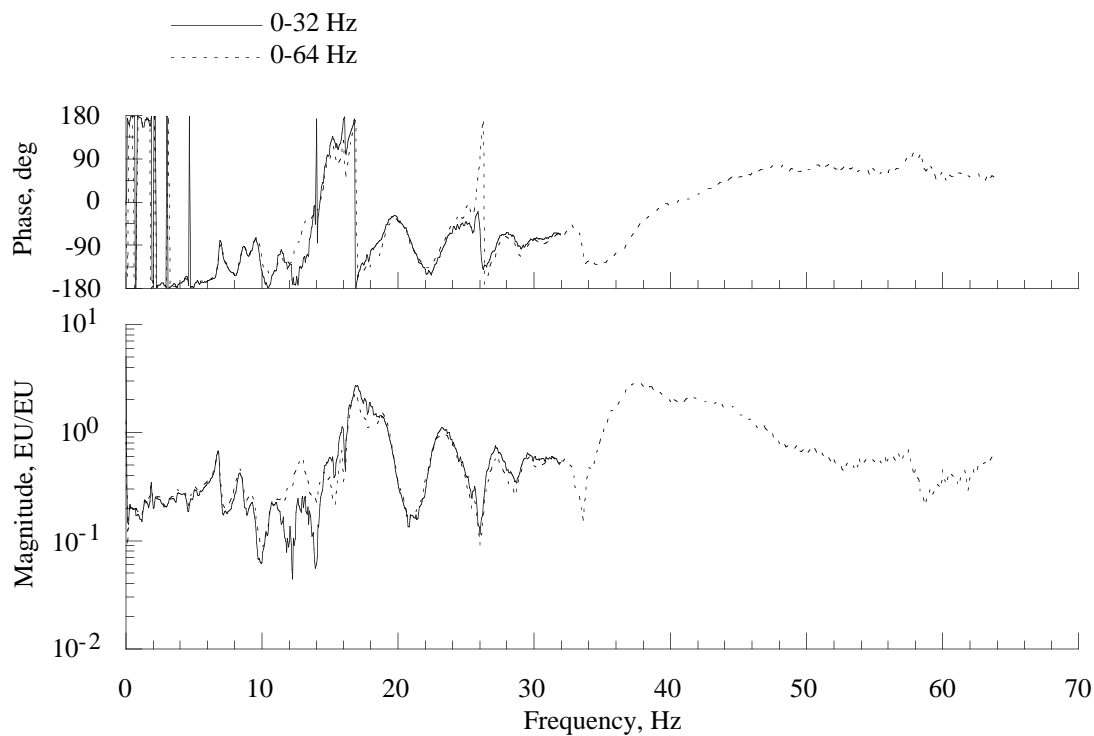


Figure 13(c). Bandwidth comparison of hub roll moment balance response due to forward hub pitch moment loading, simulated BO105 hub mass.

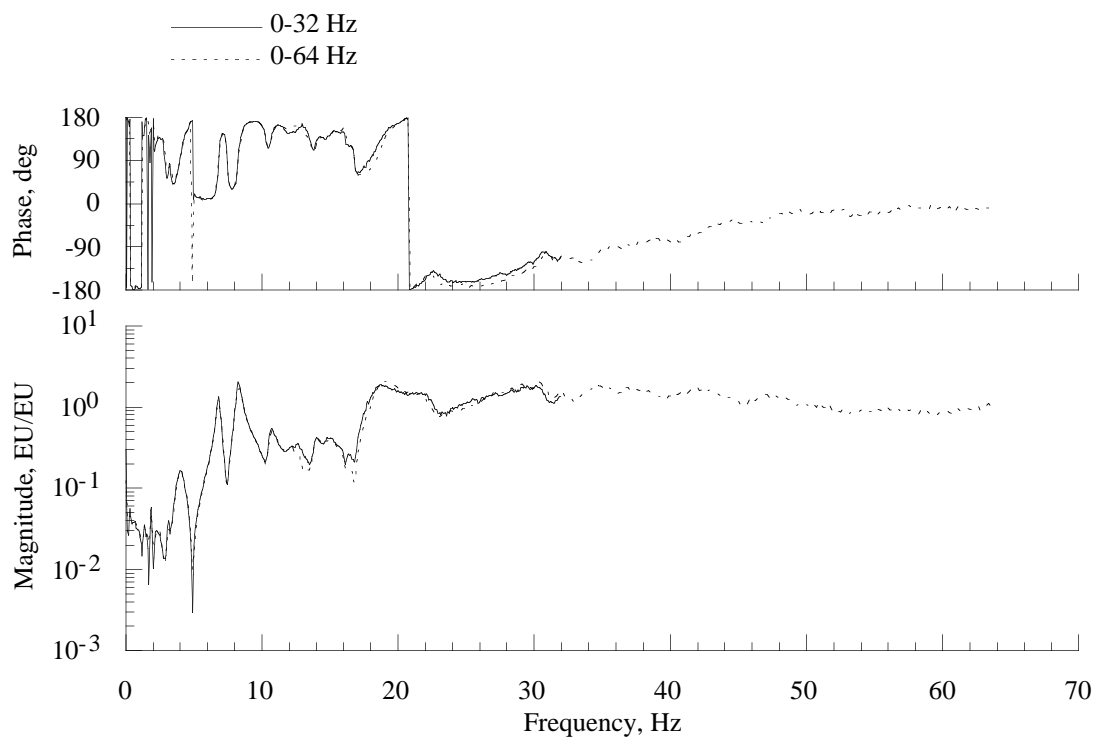


Figure 13(d). Bandwidth comparison of hub axial force balance response due to forward hub pitch moment loading, simulated BO105 hub mass.

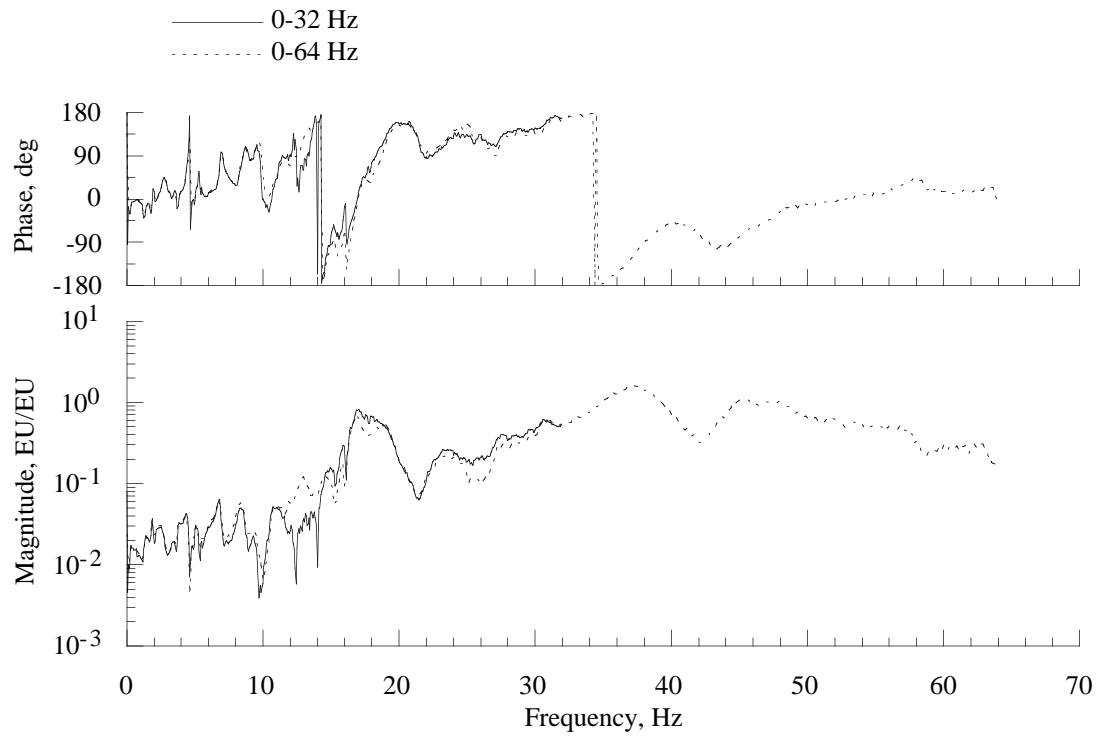


Figure 13(e). Bandwidth comparison of hub side force balance response due to forward hub pitch moment loading, simulated BO105 hub mass.

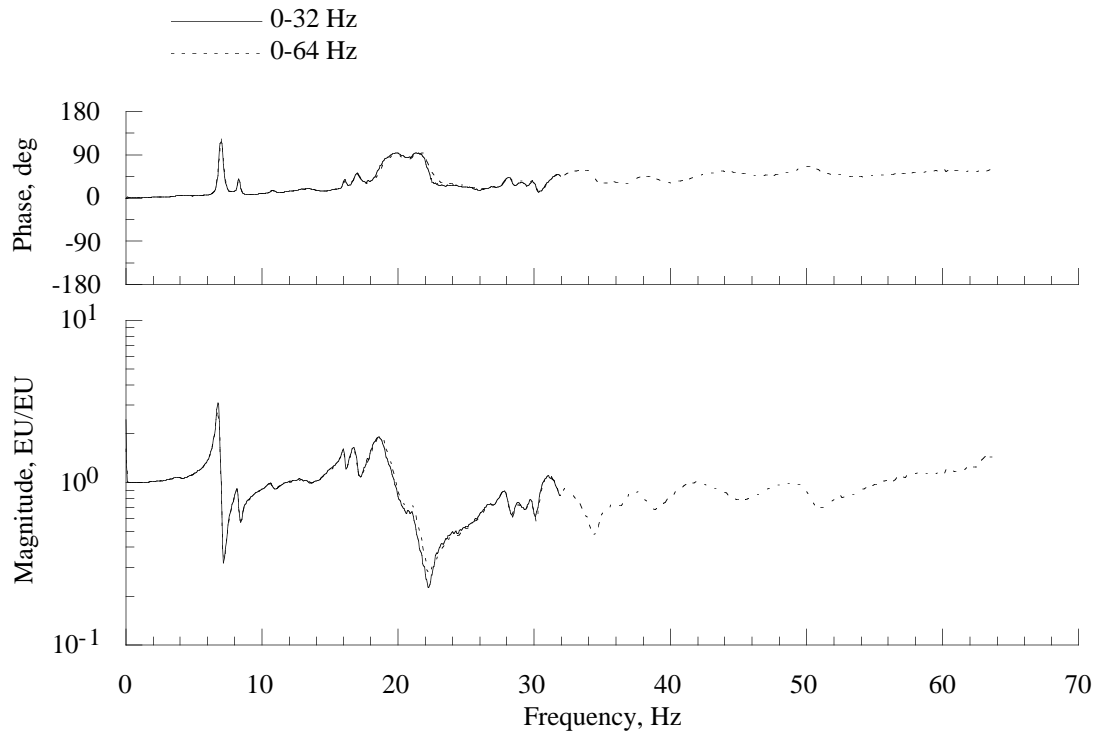


Figure 14(a). Bandwidth comparison of hub normal force balance response due to aft hub pitch moment loading, simulated BO105 hub mass.

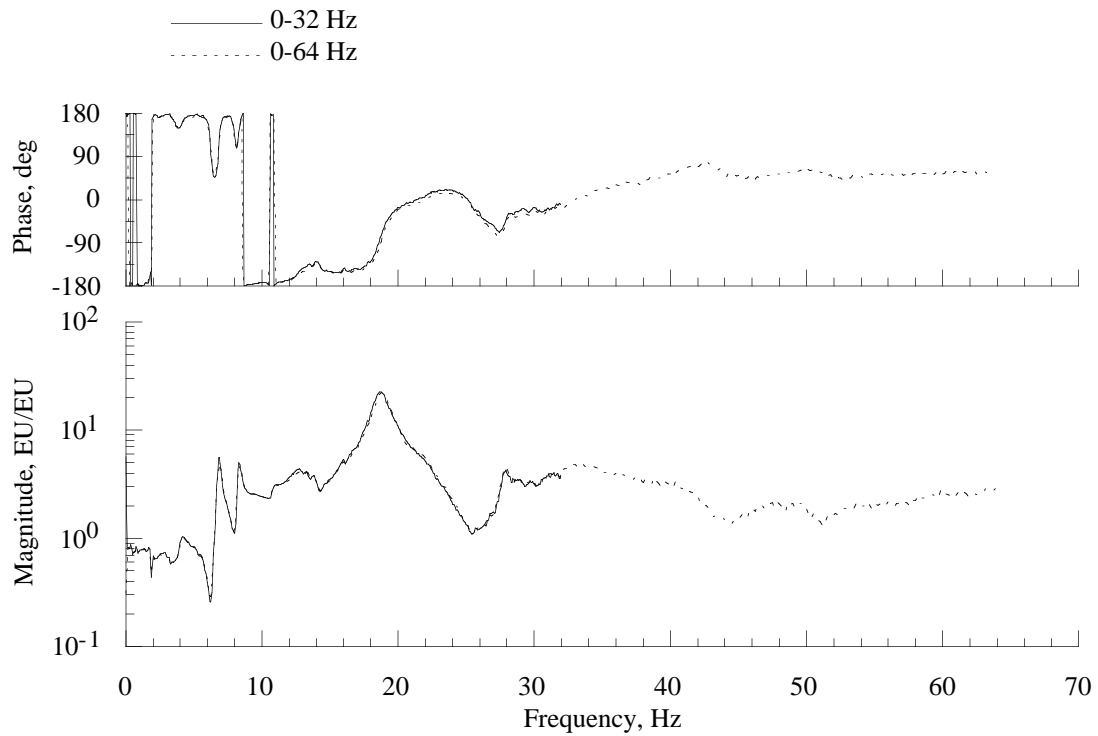


Figure 14(b). Bandwidth comparison of hub pitch moment balance response due to aft hub pitch moment loading, simulated BO105 hub mass.

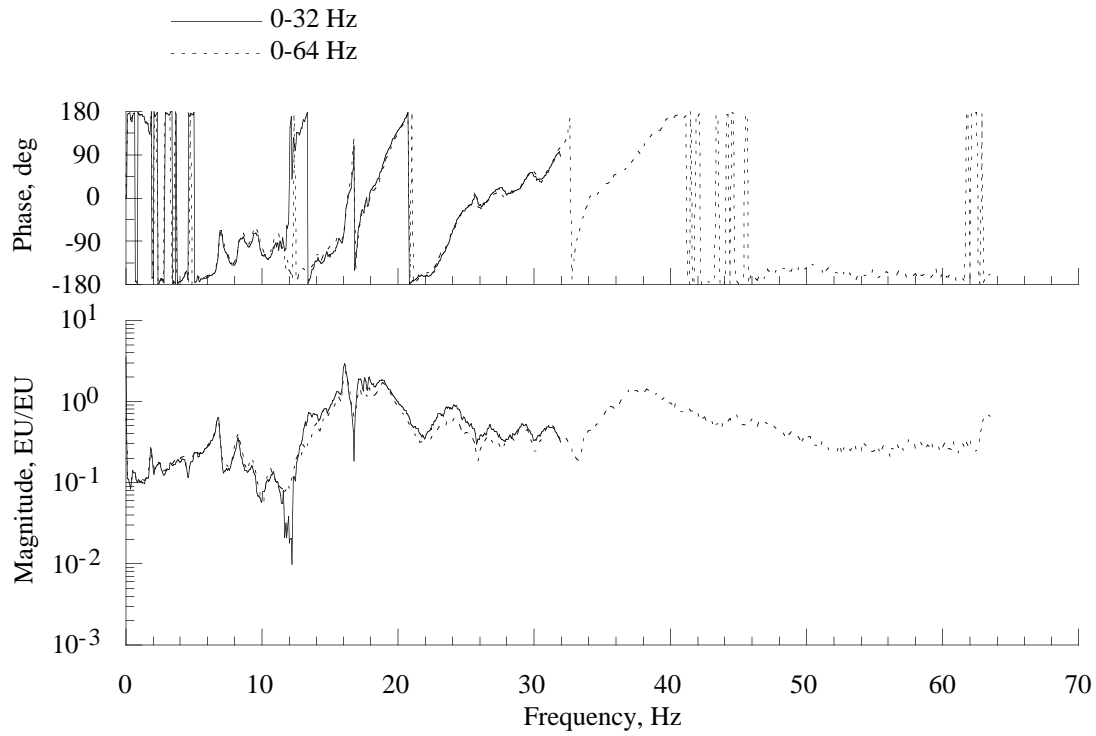


Figure 14(c). Bandwidth comparison of hub roll moment balance response due to aft hub pitch moment loading, simulated BO105 hub mass.

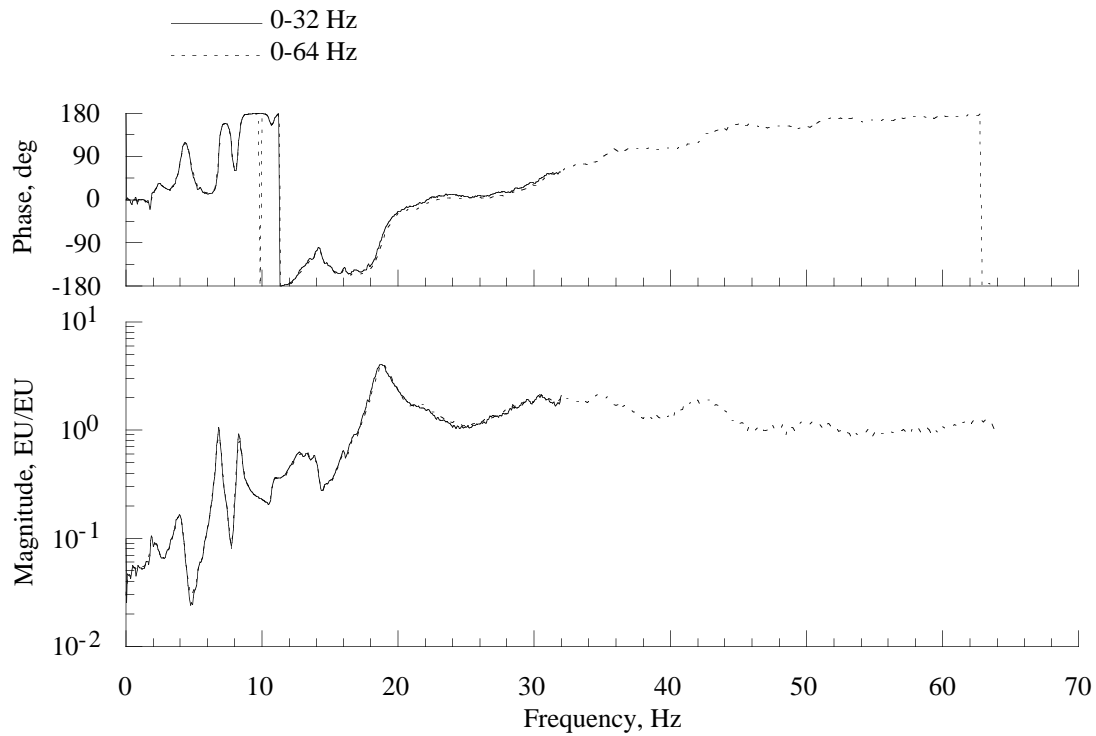


Figure 14(d). Bandwidth comparison of hub axial force balance response due to aft hub pitch moment loading, simulated BO105 hub mass.

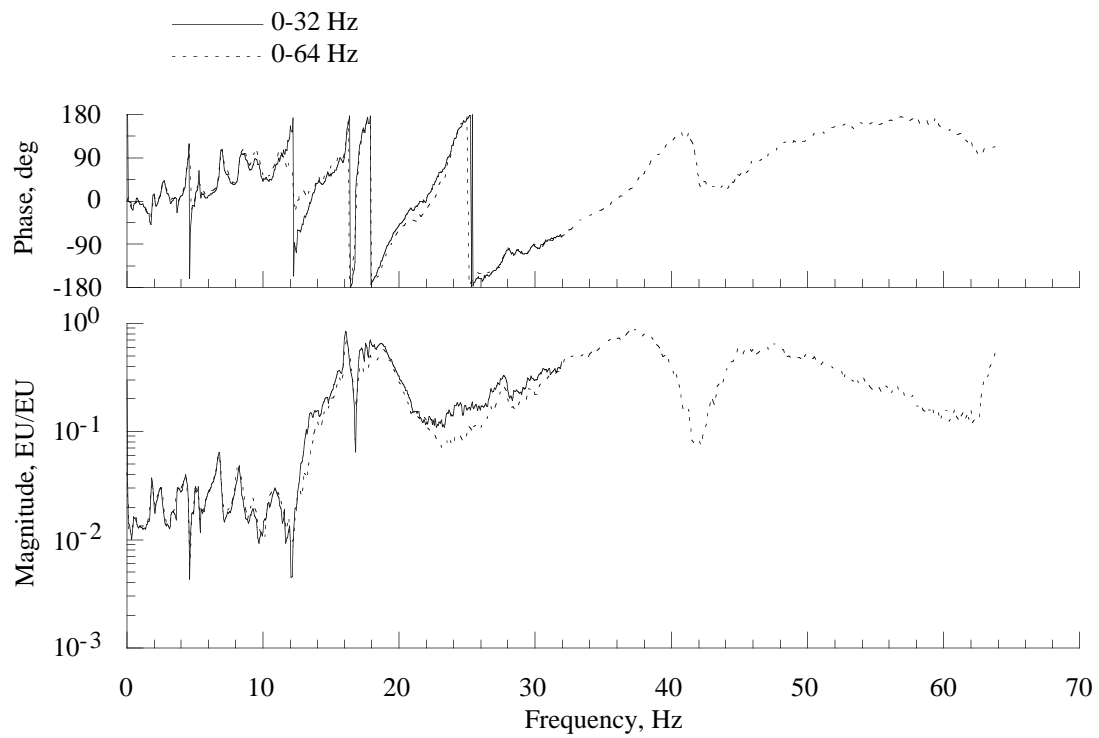


Figure 14(e). Bandwidth comparison of hub side force balance response due to aft hub pitch moment loading, simulated BO105 hub mass.

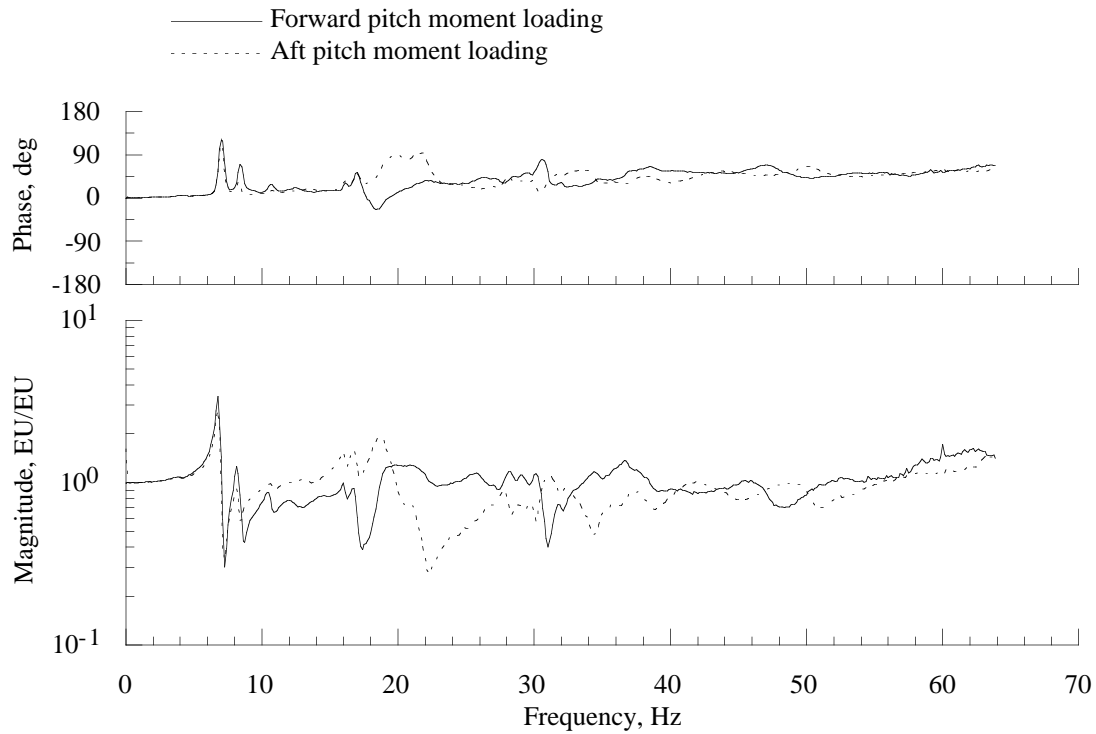


Figure 15(a). Comparison of hub normal force balance response due to forward and aft hub pitch moment loading, simulated BO105 hub mass.

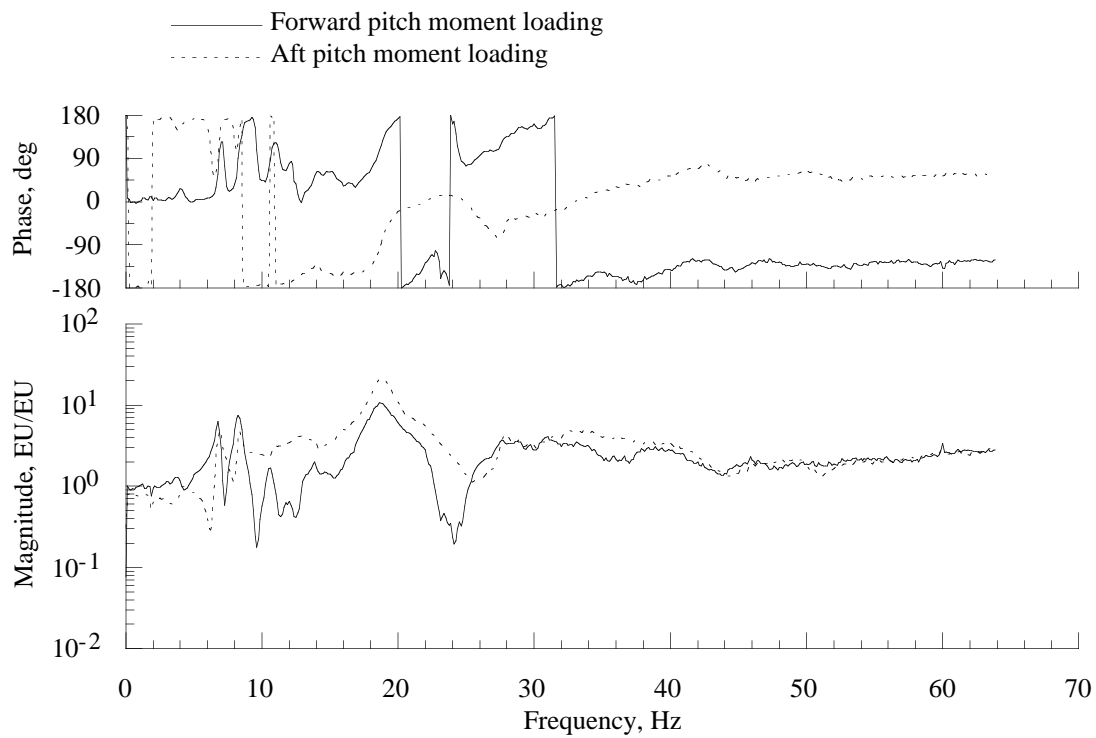


Figure 15(b). Comparison of hub pitch moment balance response due to forward and aft hub pitch moment loading, simulated BO105 hub mass.

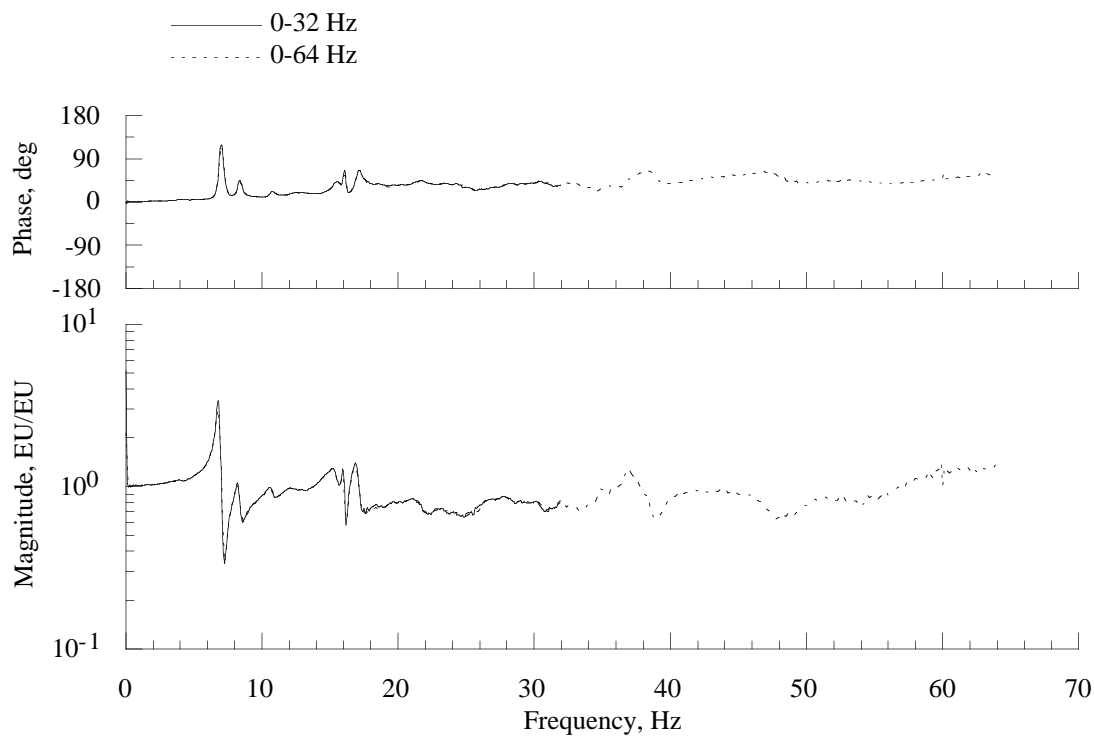


Figure 16(a). Bandwidth comparison of hub normal force balance response due to hub roll moment loading, simulated BO105 hub mass.

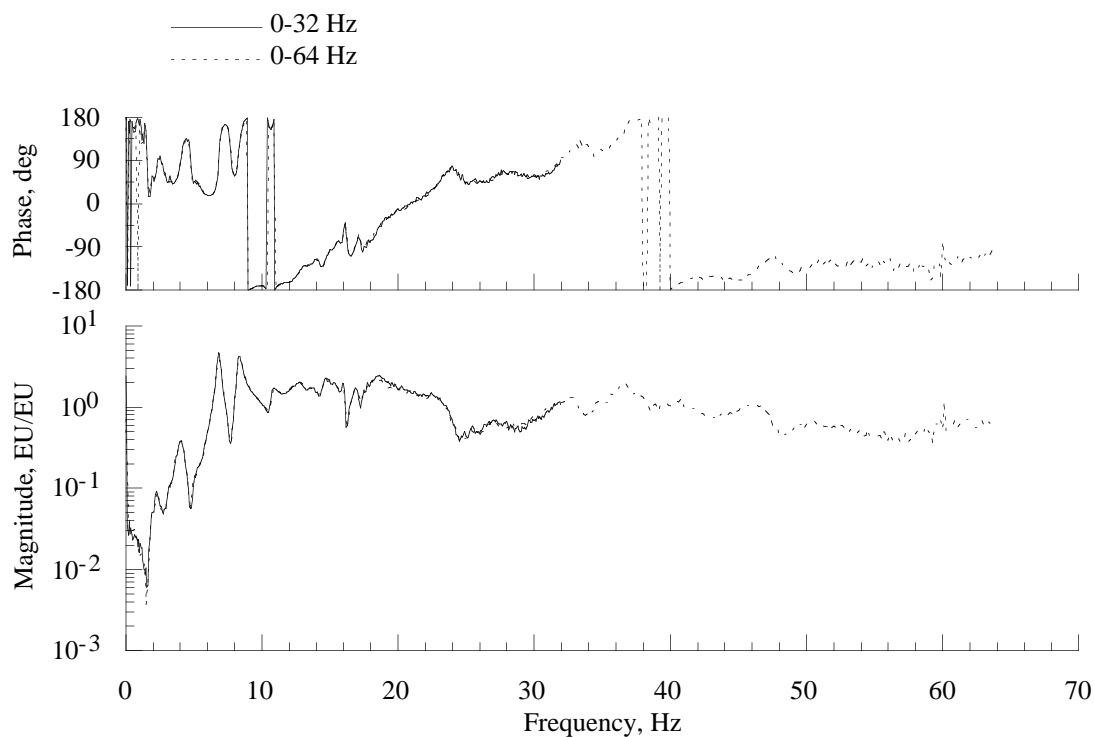


Figure 16(b). Bandwidth comparison of hub pitch moment balance response due to hub roll moment loading, simulated BO105 hub mass.

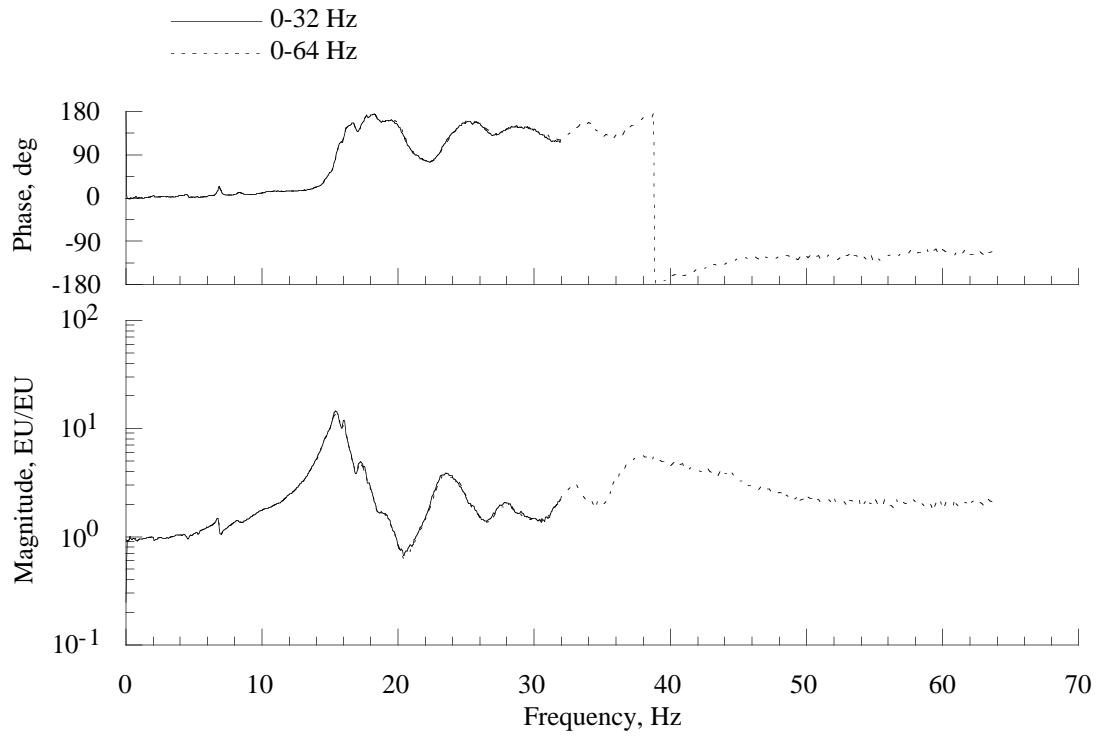


Figure 16(c). Bandwidth comparison of hub roll moment balance response due to hub roll moment loading, simulated BO105 hub mass.

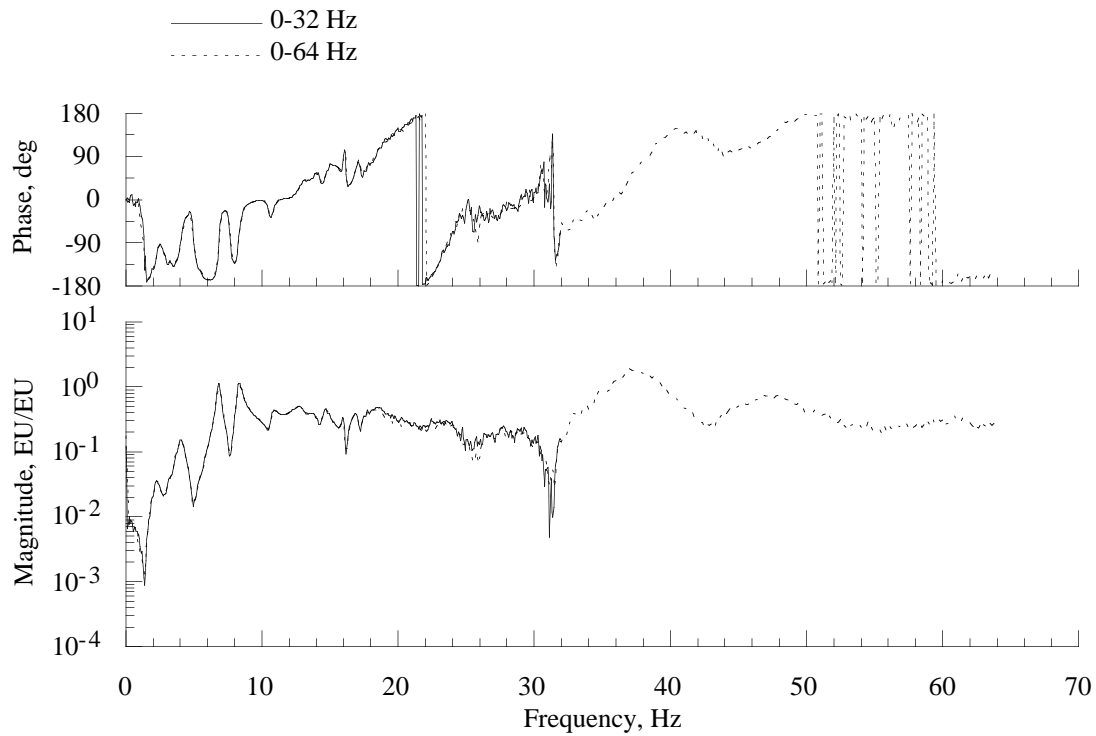


Figure 16(d). Bandwidth comparison of hub axial force balance response due to hub roll moment loading, simulated BO105 hub mass.

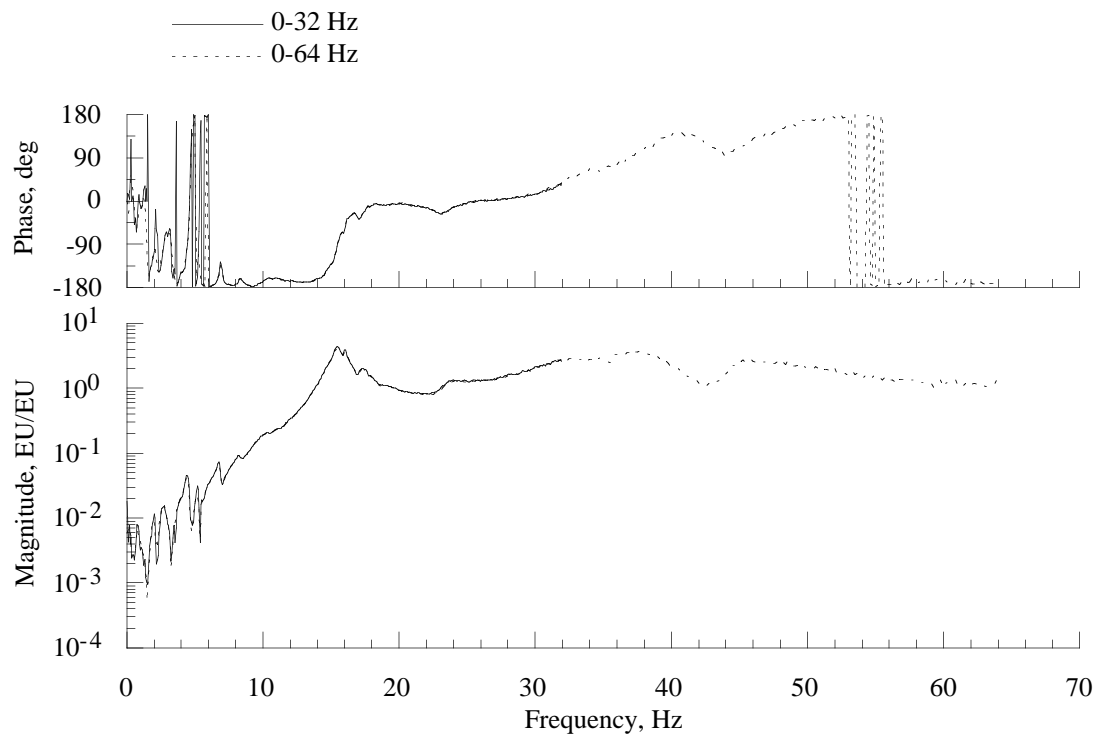


Figure 16(e). Bandwidth comparison of hub side force balance response due to hub roll moment loading, simulated BO105 hub mass.

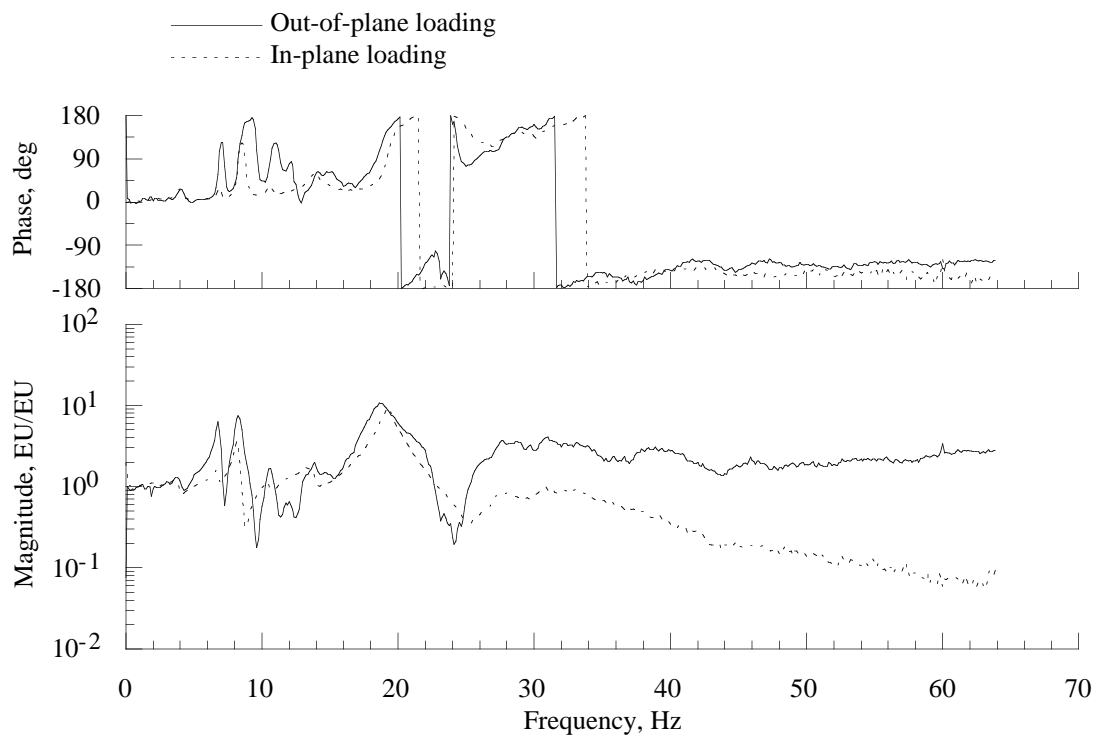


Figure 17(a). Comparison of hub pitch moment response due to out-of-plane and in-plane hub forces, simulated BO105 hub mass.

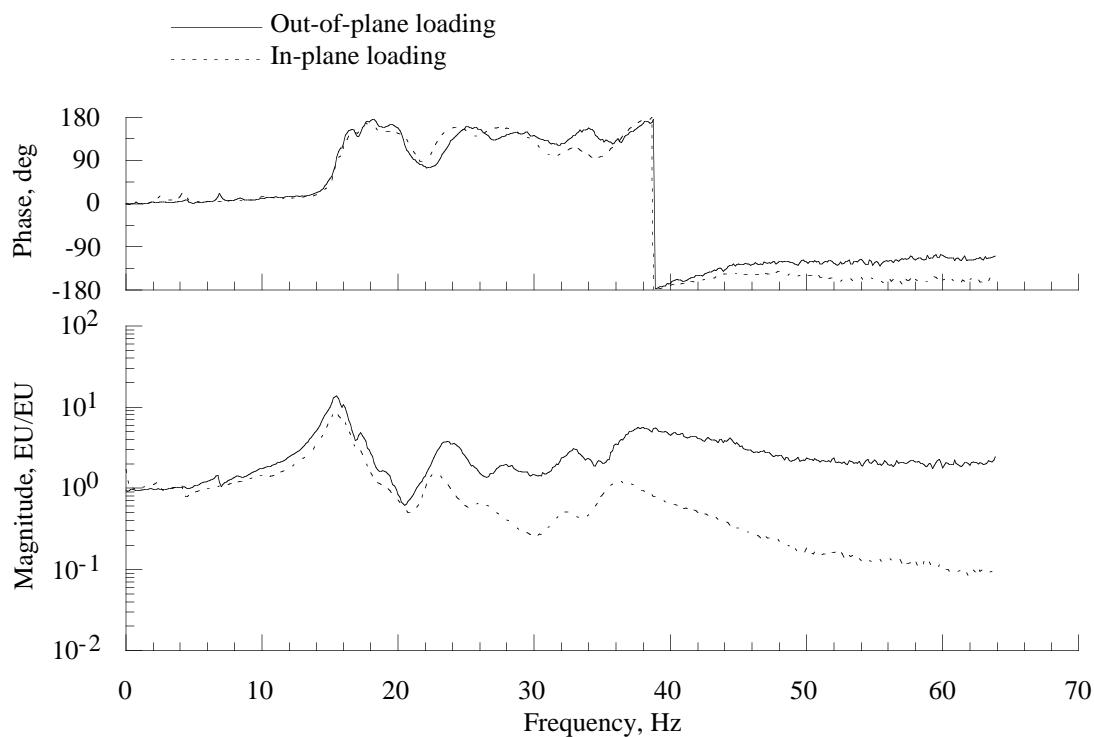


Figure 17(b). Comparison of hub roll moment response due to out-of-plane and in-plane hub forces, simulated BO105 hub mass.

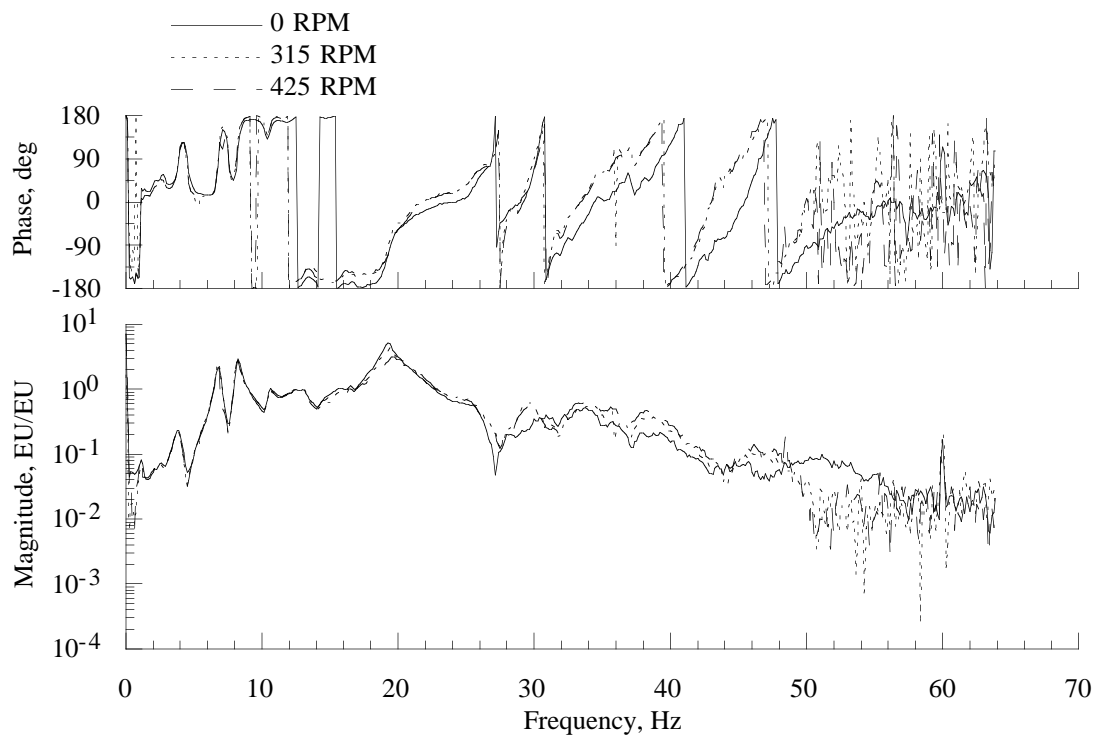


Figure 18(a). Effect of shaft rotation on the hub normal force balance response due to hub axial force loading, simulated BO105 hub mass.

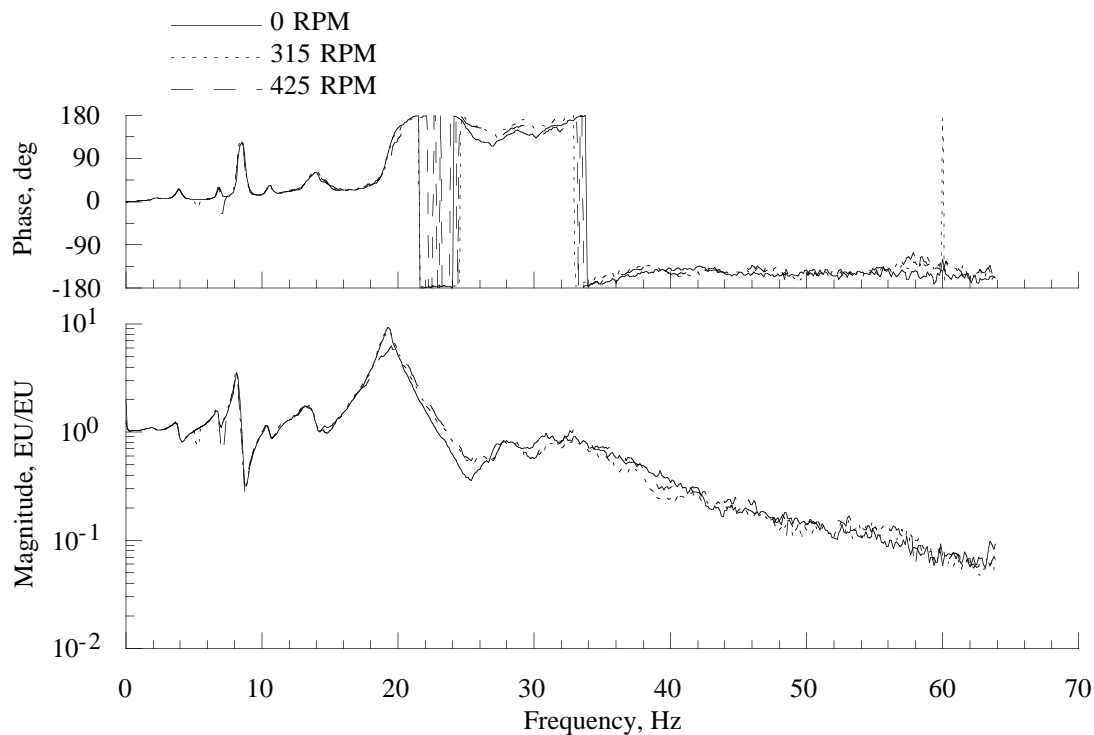


Figure 18(b). Effect of shaft rotation on the hub pitch moment balance response due to hub axial force loading, simulated BO105 hub mass.

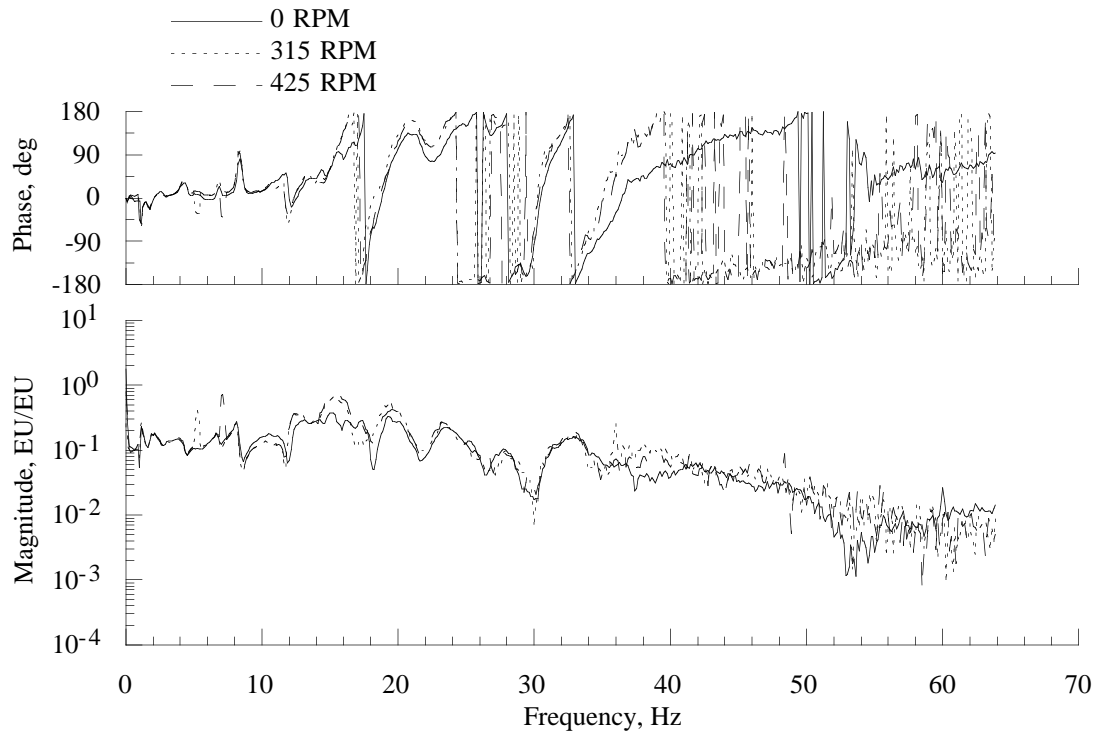


Figure 18(c). Effect of shaft rotation on the hub roll moment balance response due to hub axial force loading, simulated BO105 hub mass.

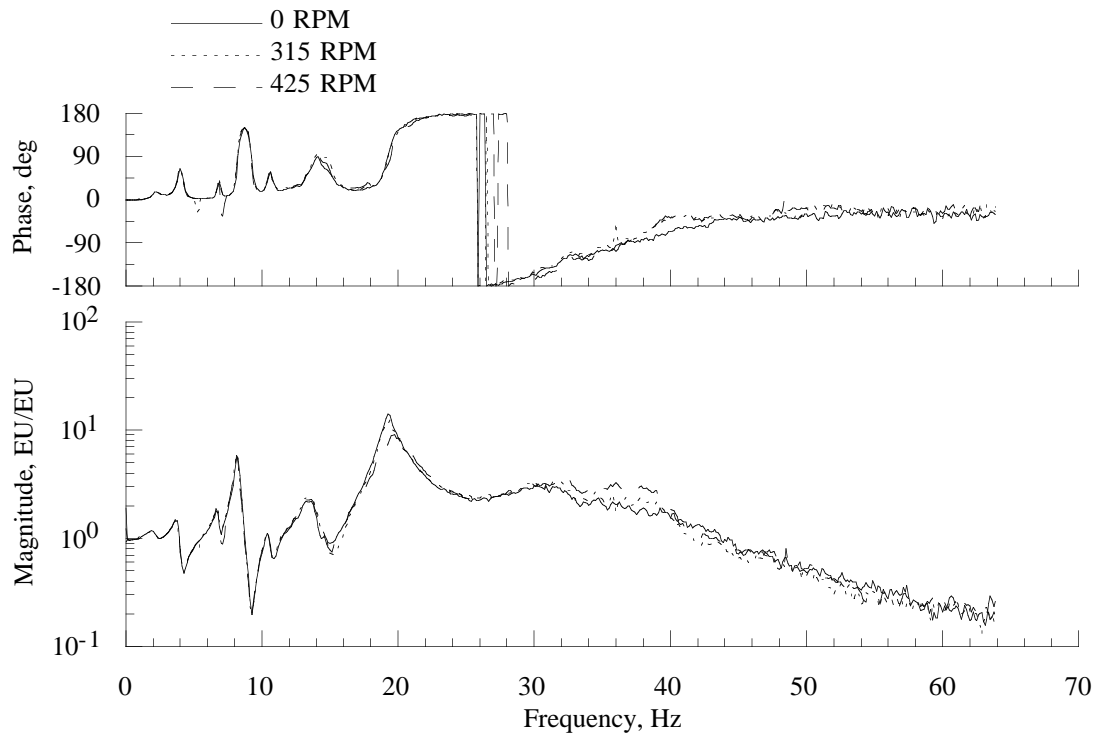


Figure 18(d). Effect of shaft rotation on the hub axial force balance response due to hub axial force loading, simulated BO105 hub mass.

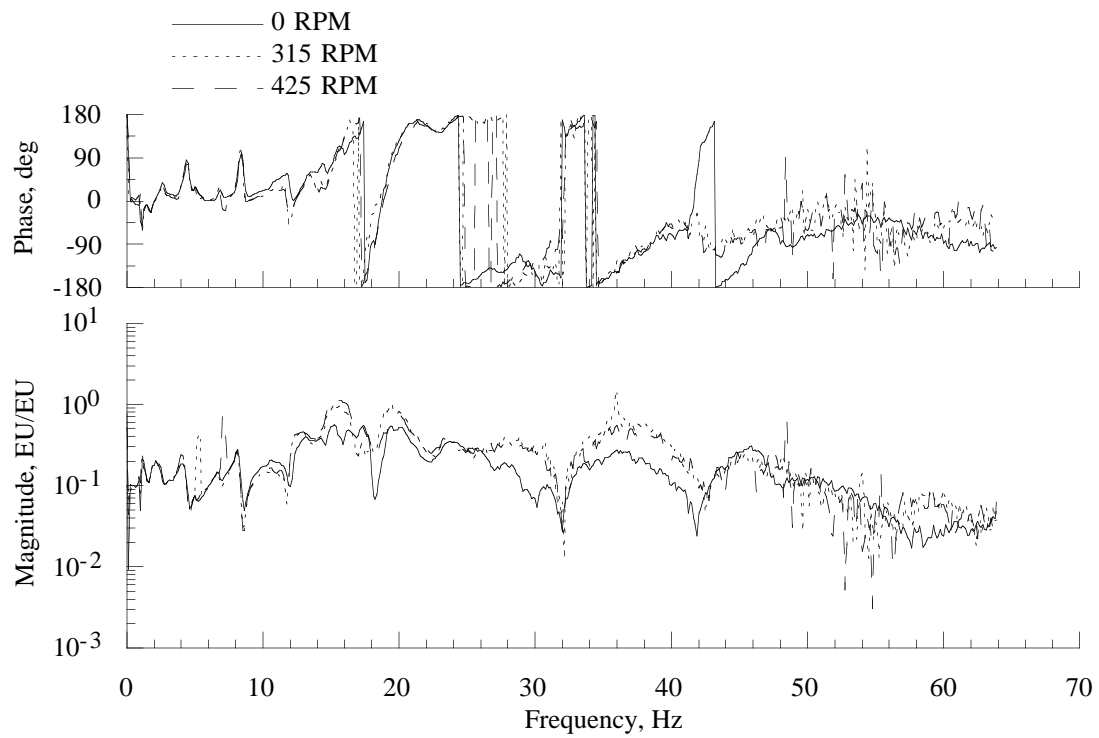


Figure 18(e). Effect of shaft rotation on the hub side force balance response due to hub axial force loading, simulated BO105 hub mass.

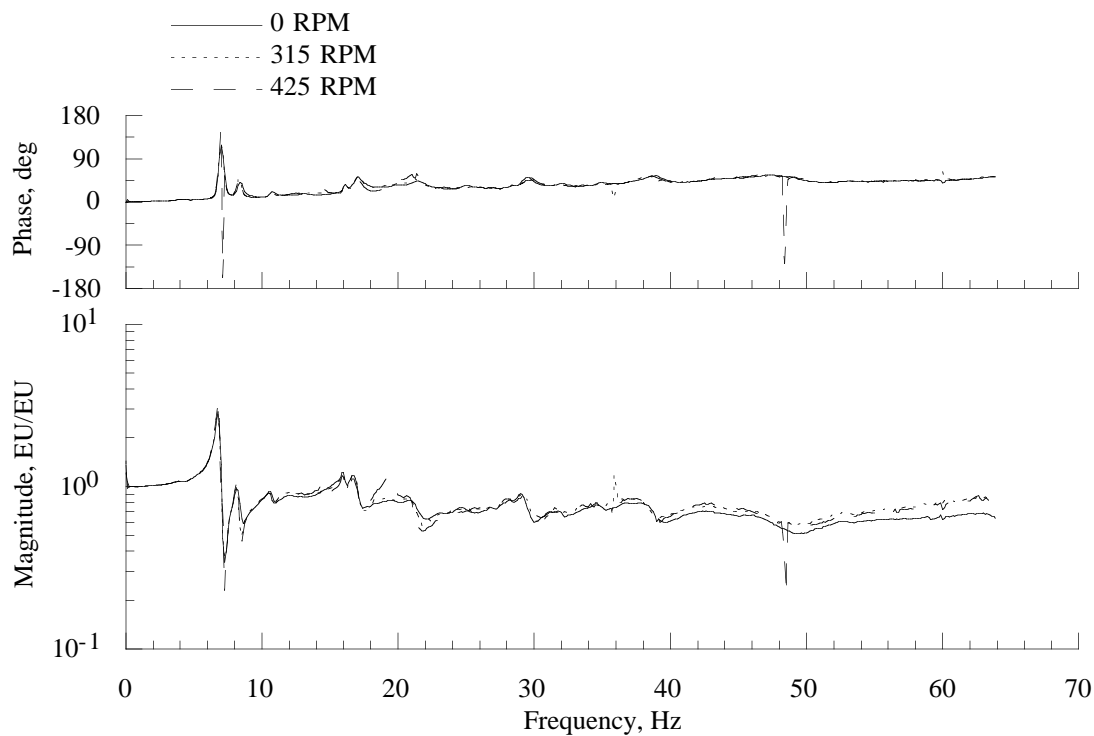


Figure 19(a). Effect of shaft rotation on the hub normal force balance response due to hub normal force loading, simulated BO105 hub mass.

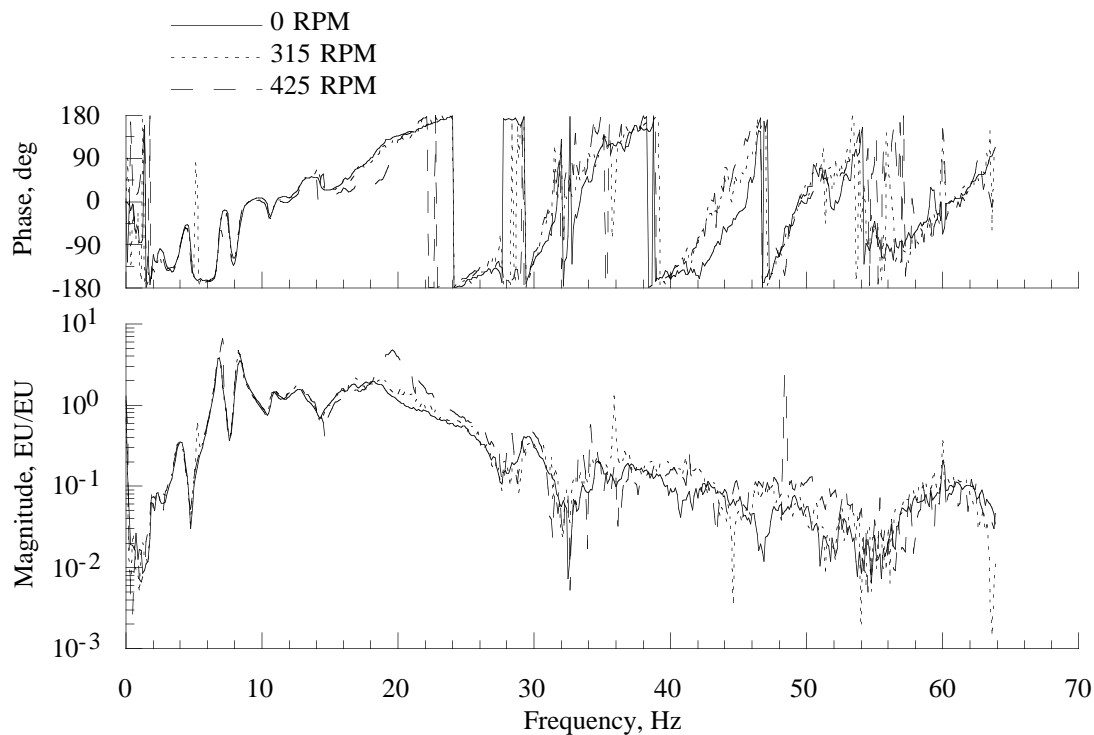


Figure 19(b). Effect of shaft rotation on the hub pitch moment balance response due to hub normal force loading, simulated BO105 hub mass.

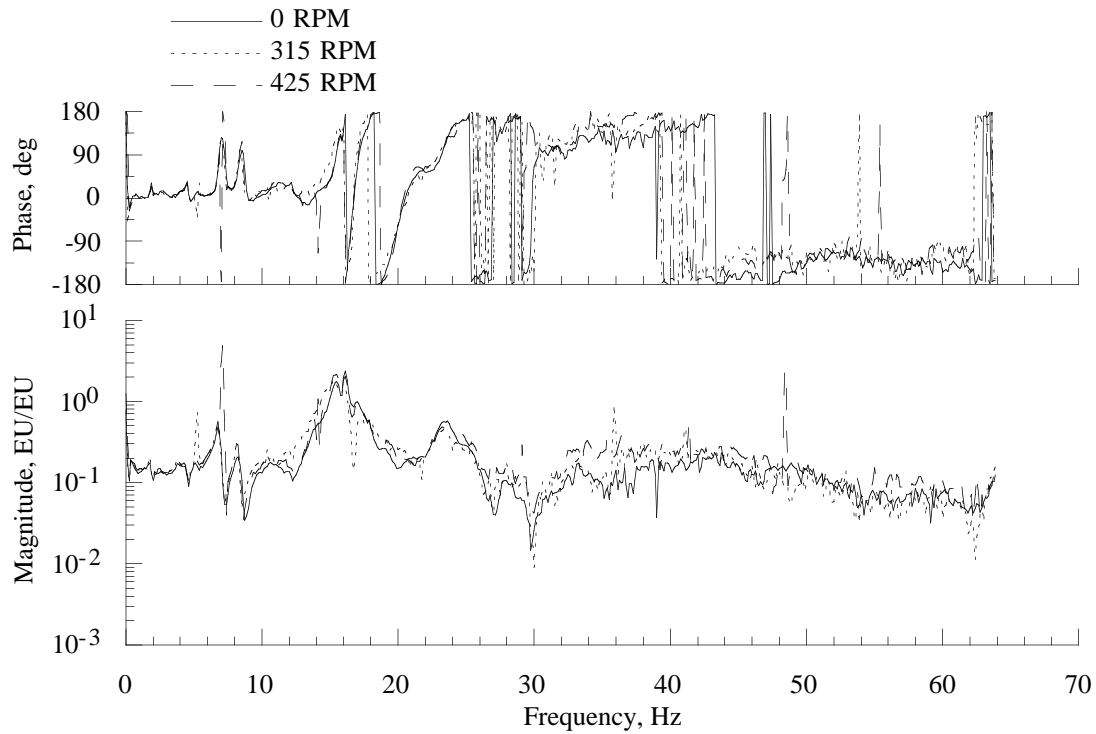


Figure 19(c). Effect of shaft rotation on the hub roll moment balance response due to hub normal force loading, simulated BO105 hub mass.

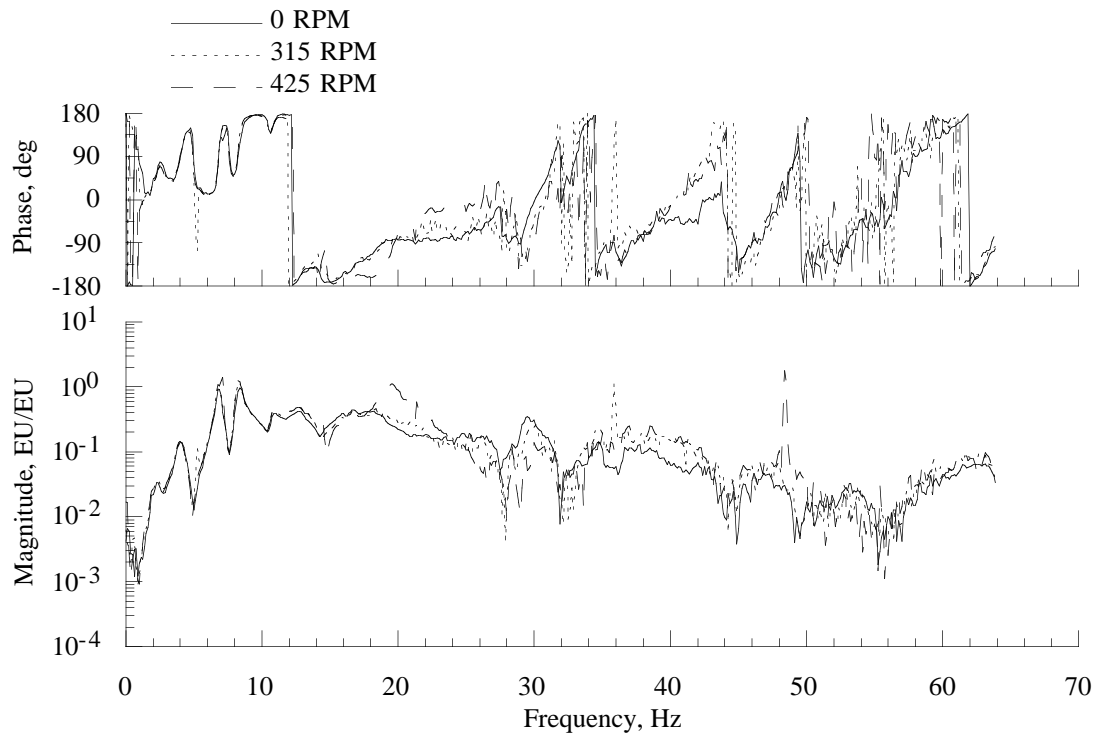


Figure 19(d). Effect of shaft rotation on the hub axial force balance response due to hub normal force loading, simulated BO105 hub mass.

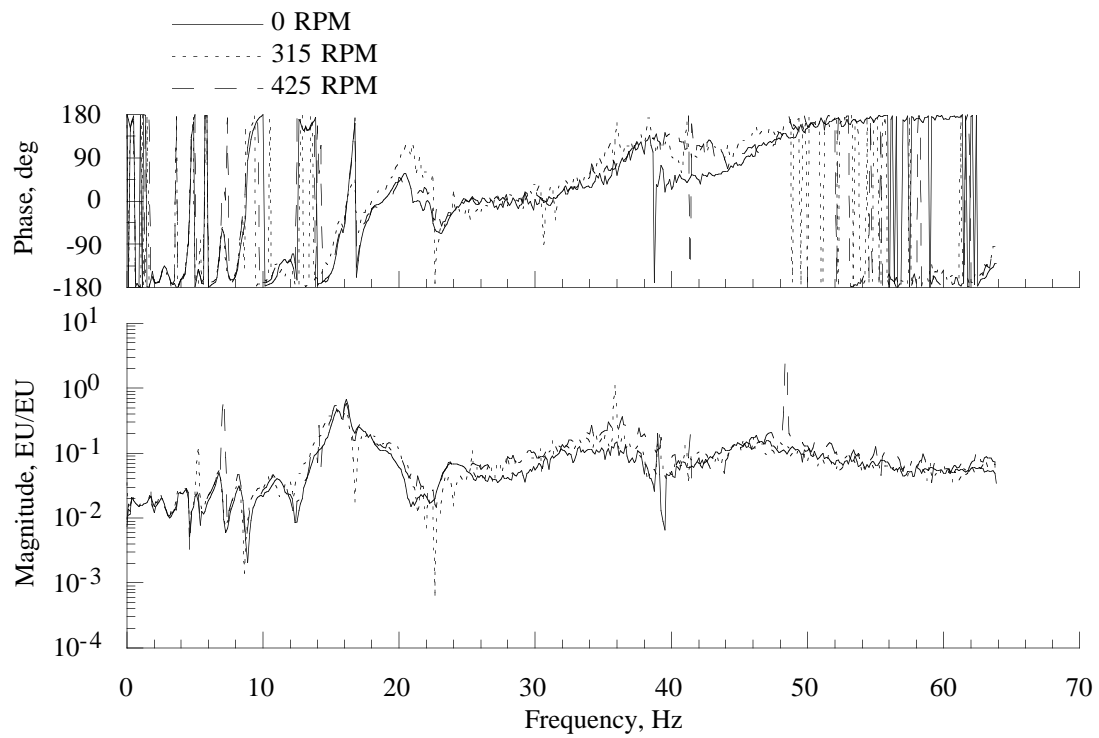


Figure 19(e). Effect of shaft rotation on the hub side force balance response due to hub normal force loading, simulated BO105 hub mass.

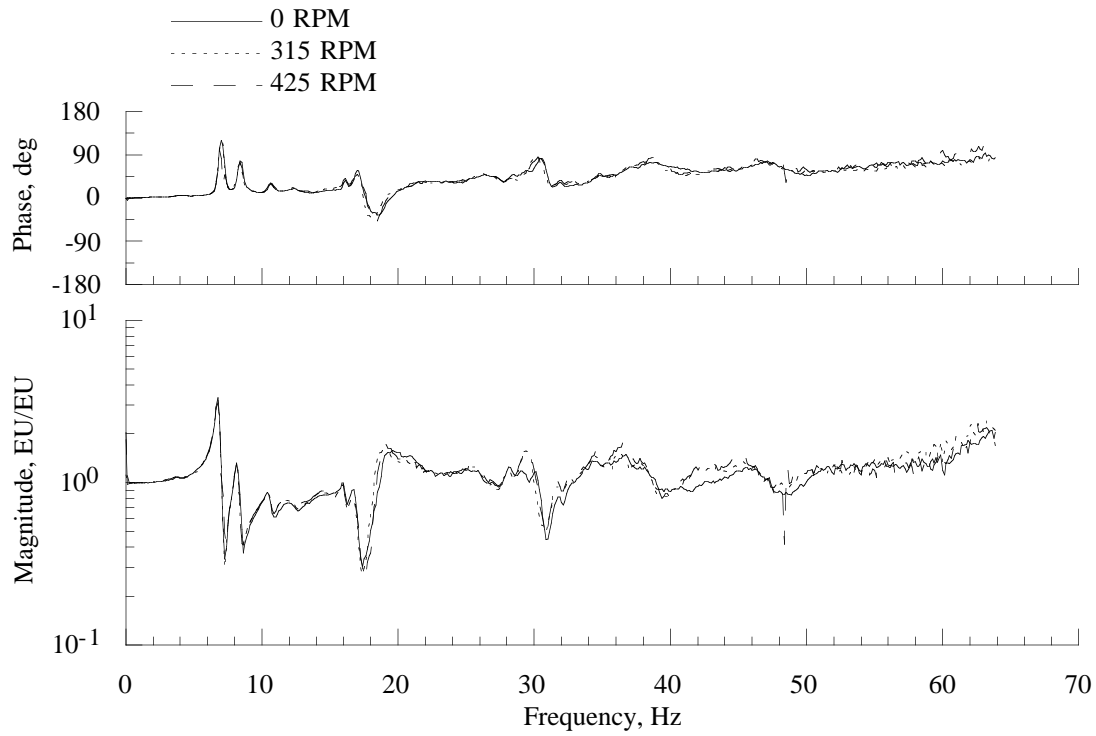


Figure 20(a). Effect of shaft rotation on the hub normal force balance response due to forward hub pitch moment loading, simulated BO105 hub mass.

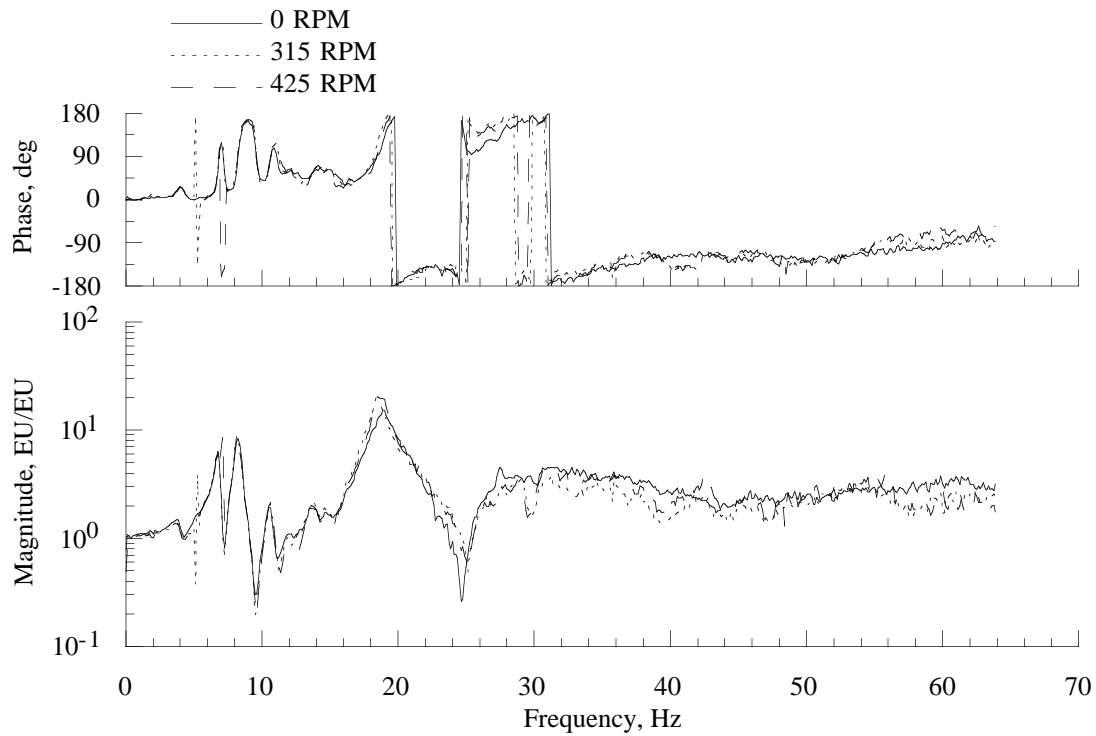


Figure 20(b). Effect of shaft rotation on the hub pitch moment balance response due to forward hub pitch moment loading, simulated BO105 hub mass.

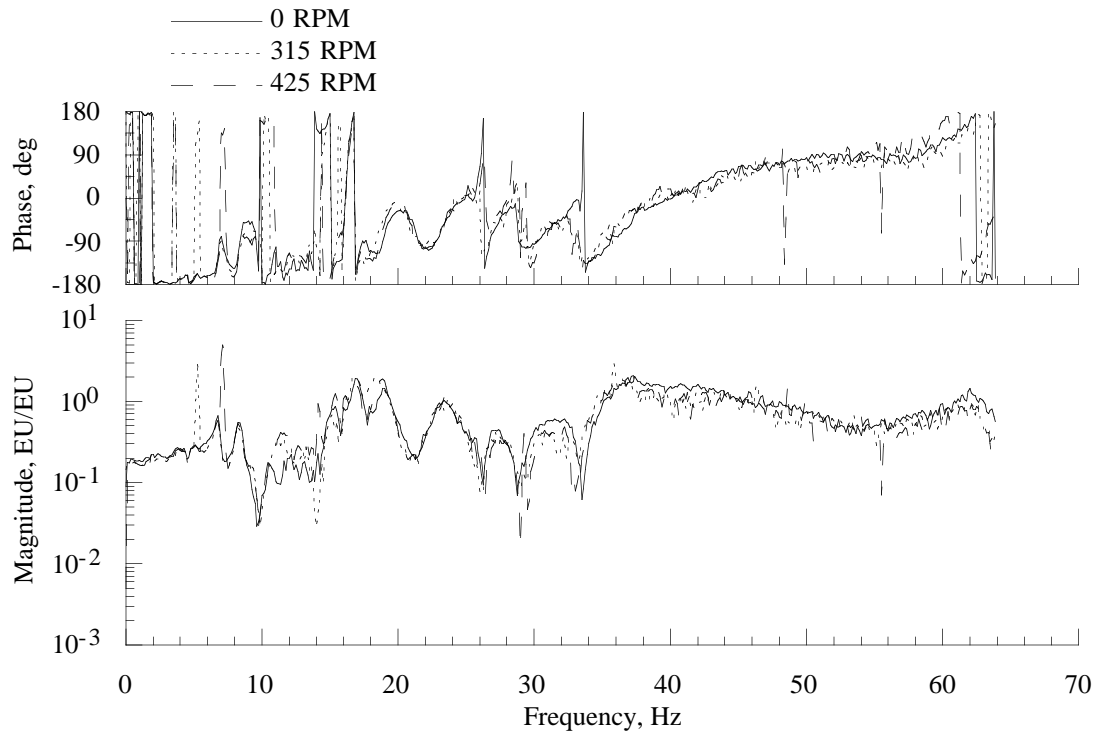


Figure 20(c). Effect of shaft rotation on the hub roll moment balance response due to forward hub pitch moment loading, simulated BO105 hub mass.

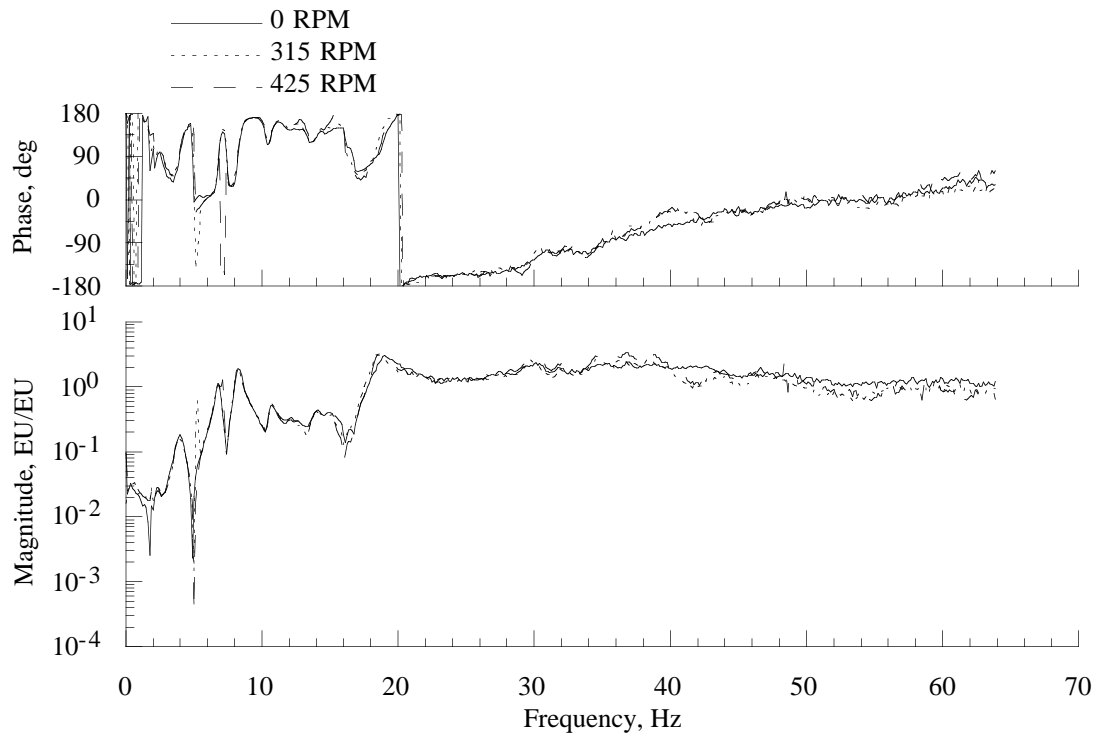


Figure 20(d). Effect of shaft rotation on the hub axial force balance response due to forward hub pitch moment loading, simulated BO105 hub mass.

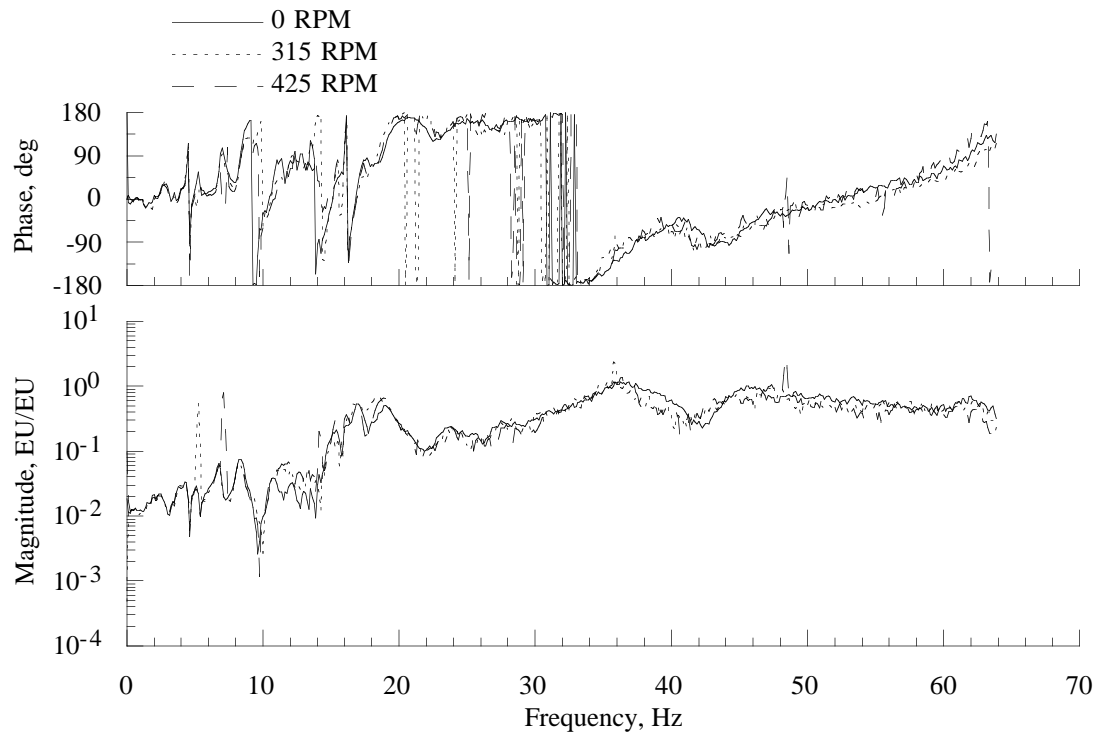


Figure 20(e). Effect of shaft rotation on the hub side force balance response due to forward hub pitch moment loading, simulated BO105 hub mass.

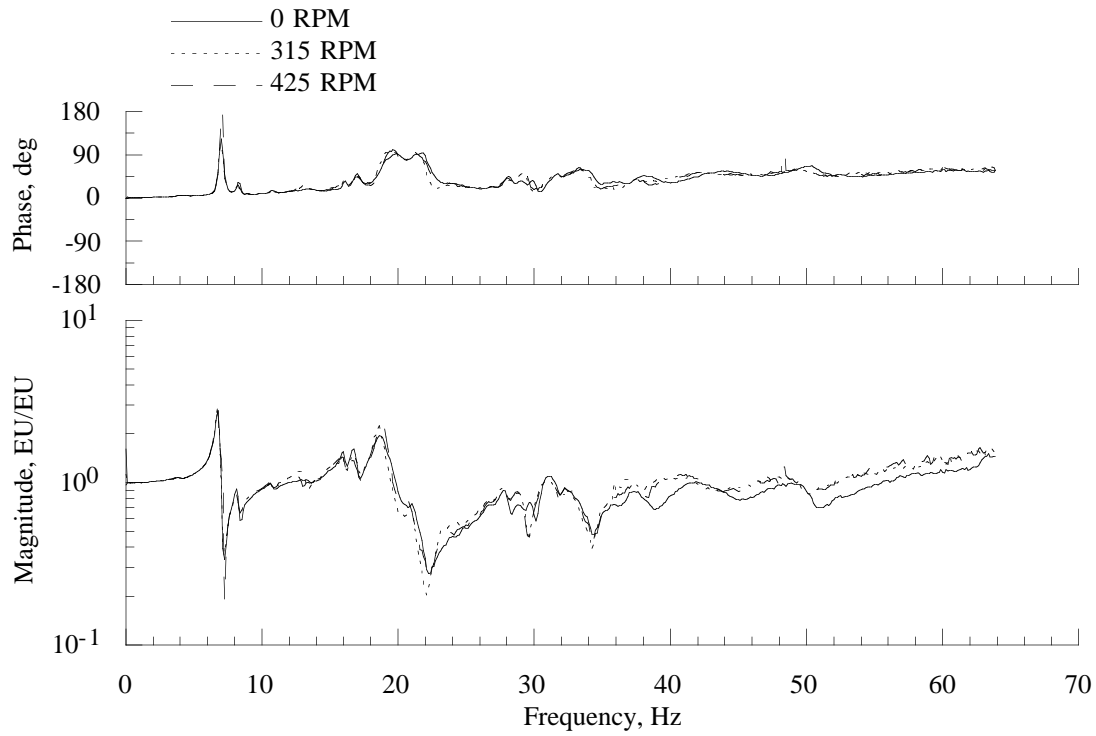


Figure 21(a). Effect of shaft rotation on the hub normal force balance response due to aft hub pitch moment loading, simulated BO105 hub mass.

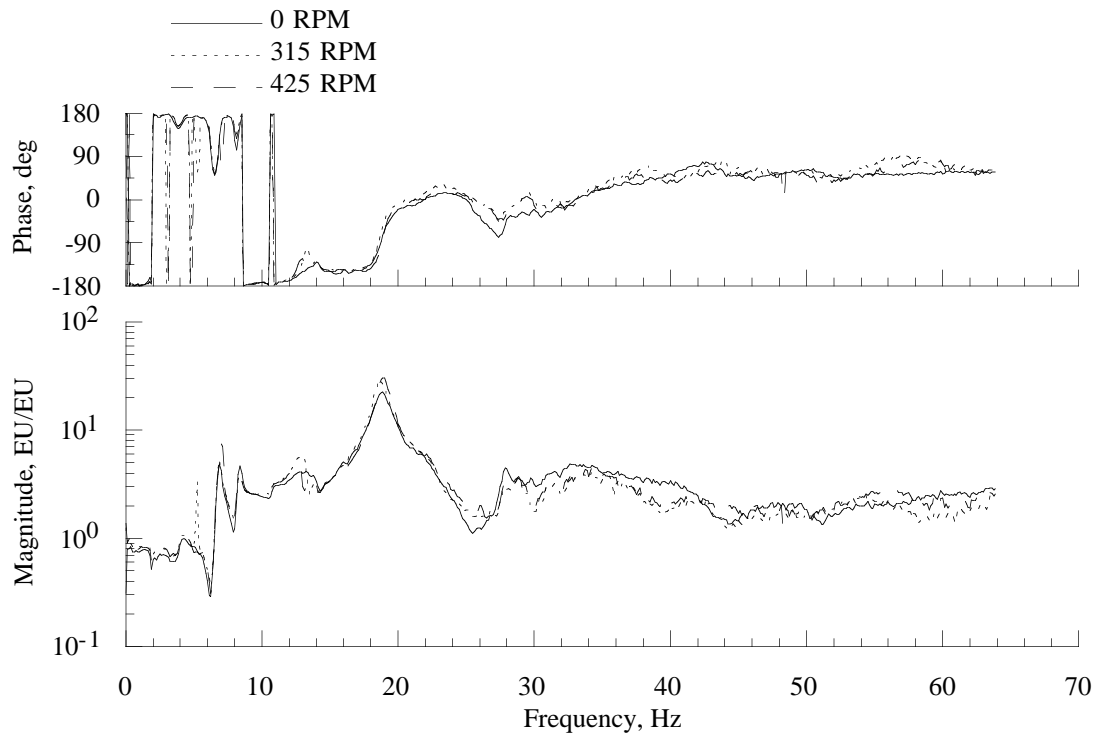


Figure 21(b). Effect of shaft rotation on the hub pitch moment balance response due to aft hub pitch moment loading, simulated BO105 hub mass.

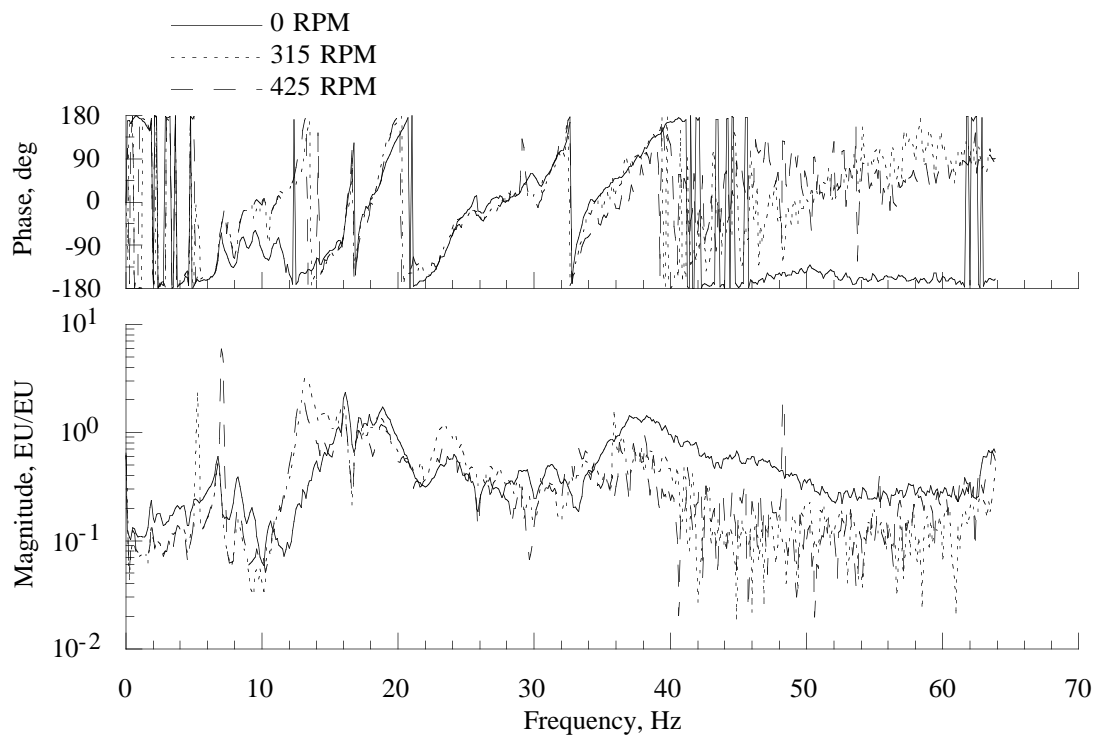


Figure 21(c). Effect of shaft rotation on the hub roll moment balance response due to aft hub pitch moment loading, simulated BO105 hub mass.

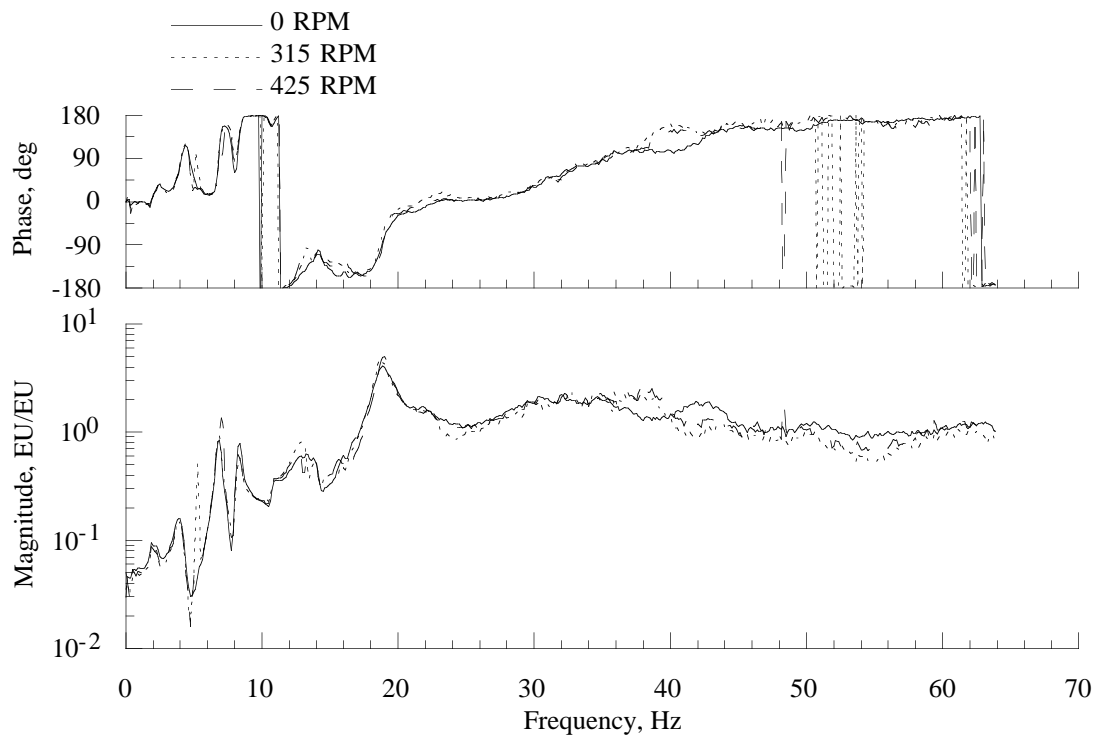


Figure 21(d). Effect of shaft rotation on the hub axial force balance response due to aft hub pitch moment loading, simulated BO105 hub mass.

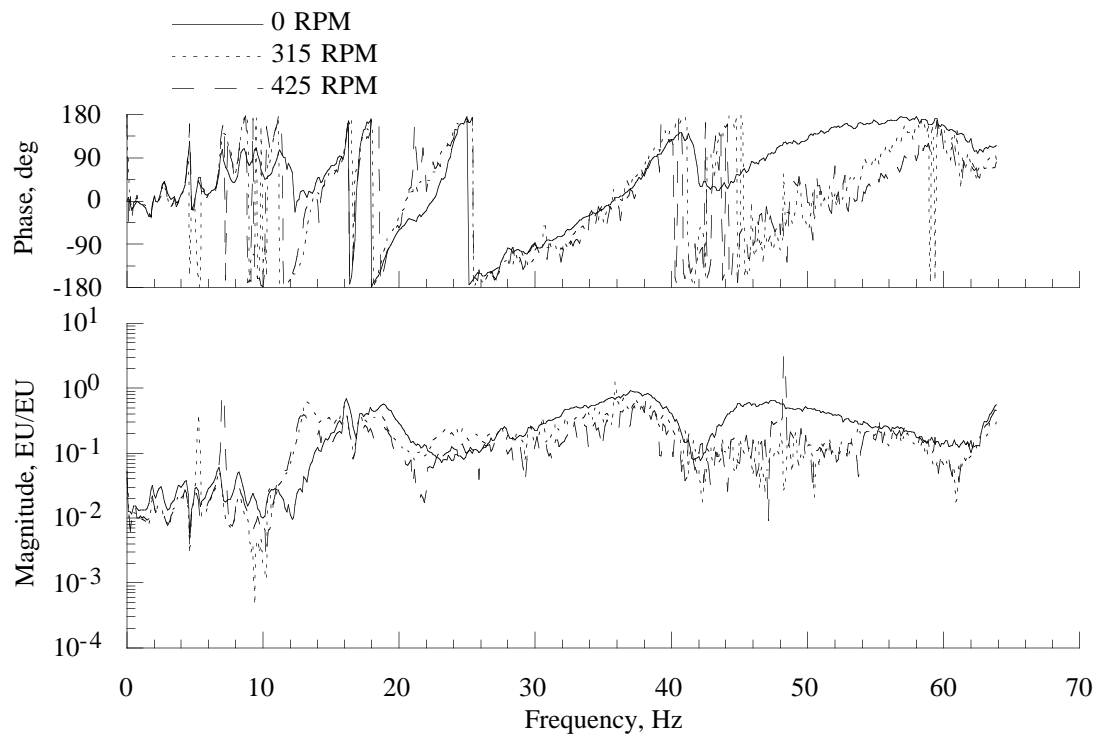


Figure 21(e). Effect of shaft rotation on the hub side force balance response due to aft hub pitch moment loading, simulated BO105 hub mass.

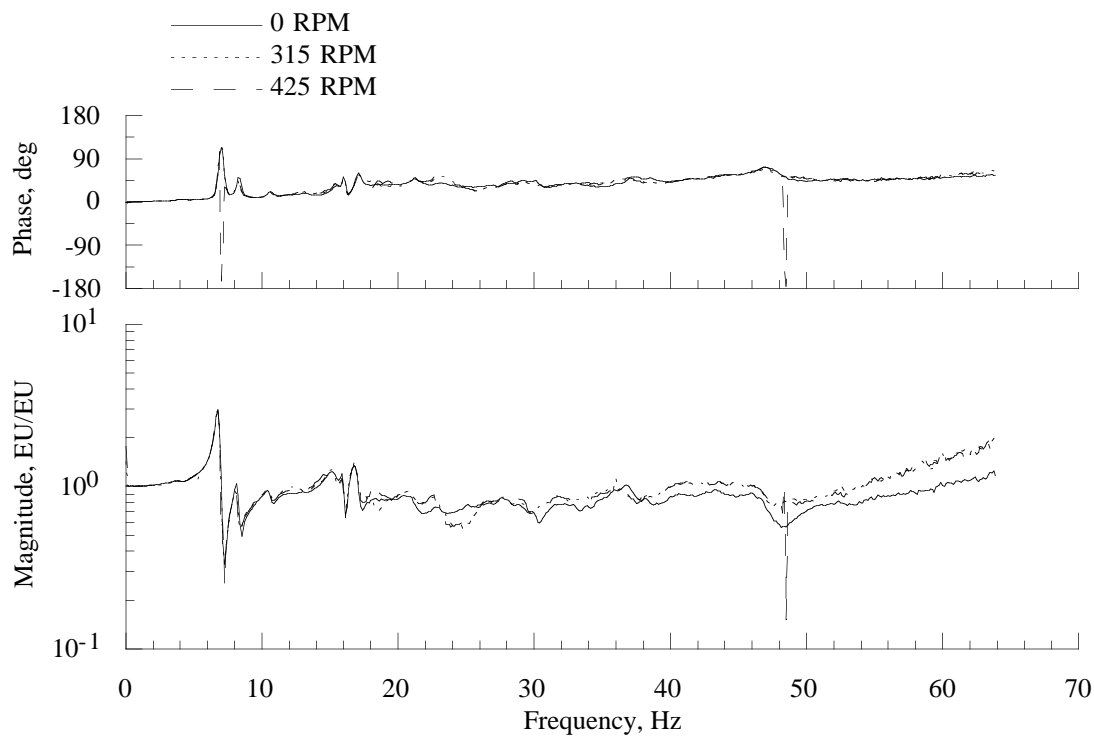


Figure 22(a). Effect of shaft rotation on the hub normal force balance response due to hub roll moment loading, simulated BO105 hub mass.

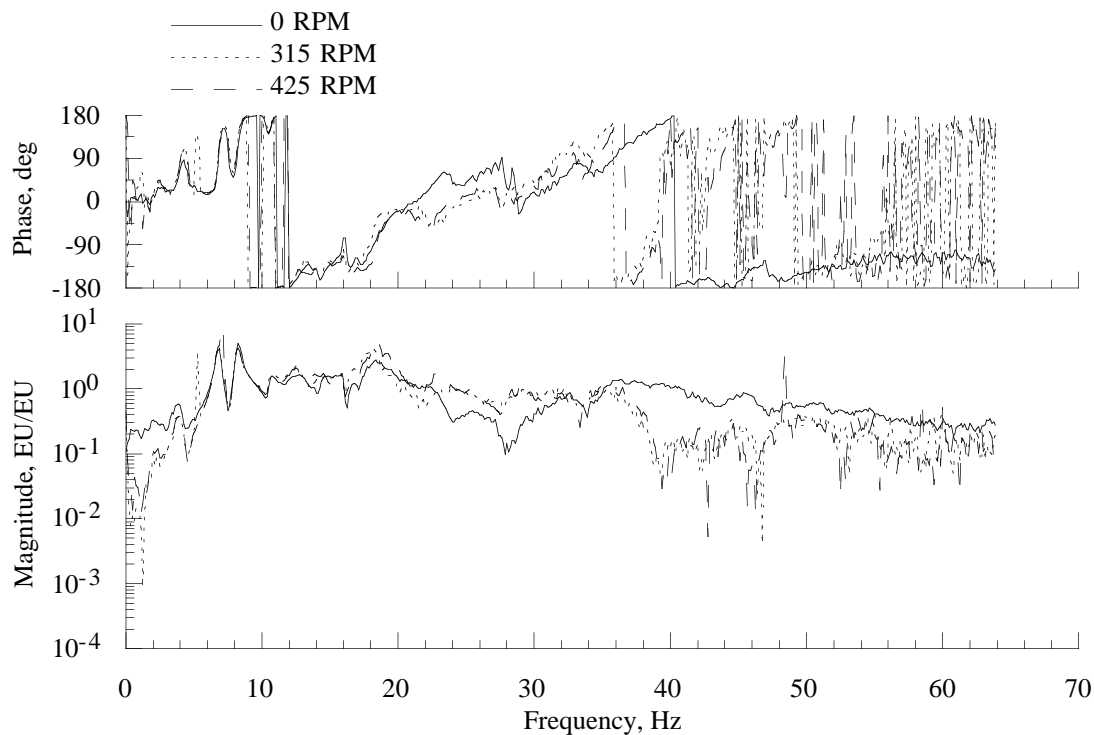


Figure 22(b). Effect of shaft rotation on the hub pitch moment balance response due to hub roll moment loading, simulated BO105 hub mass.

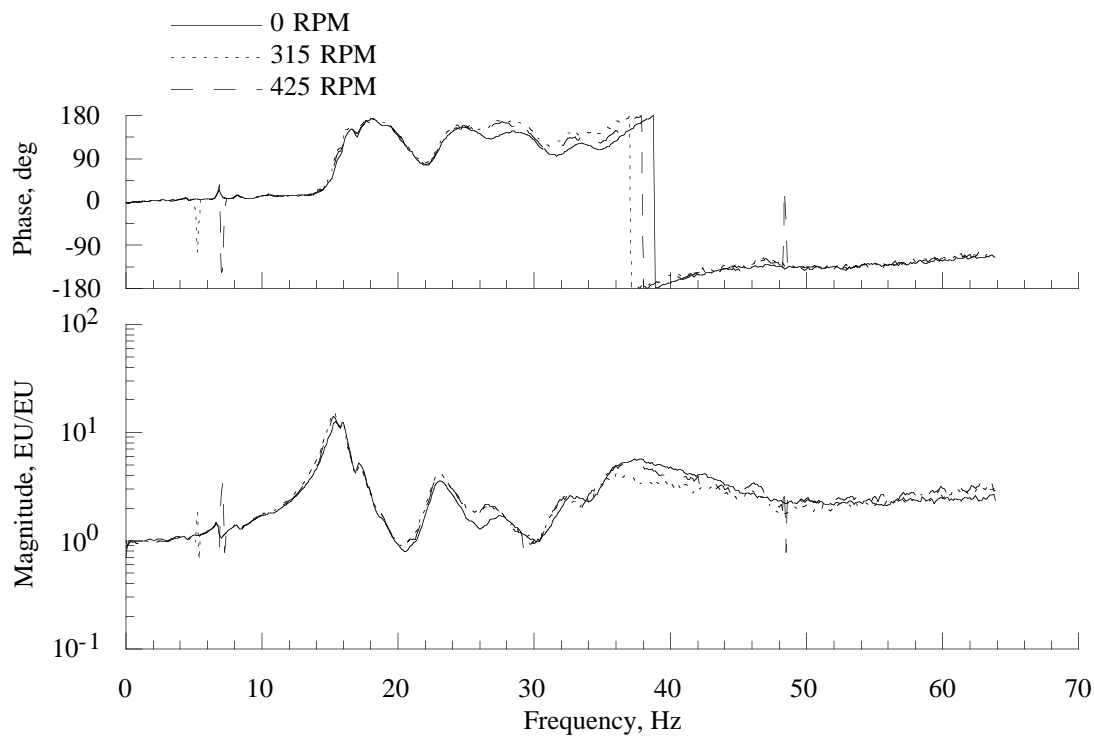


Figure 22(c). Effect of shaft rotation on the hub roll moment balance response due to hub roll moment loading, simulated BO105 hub mass.

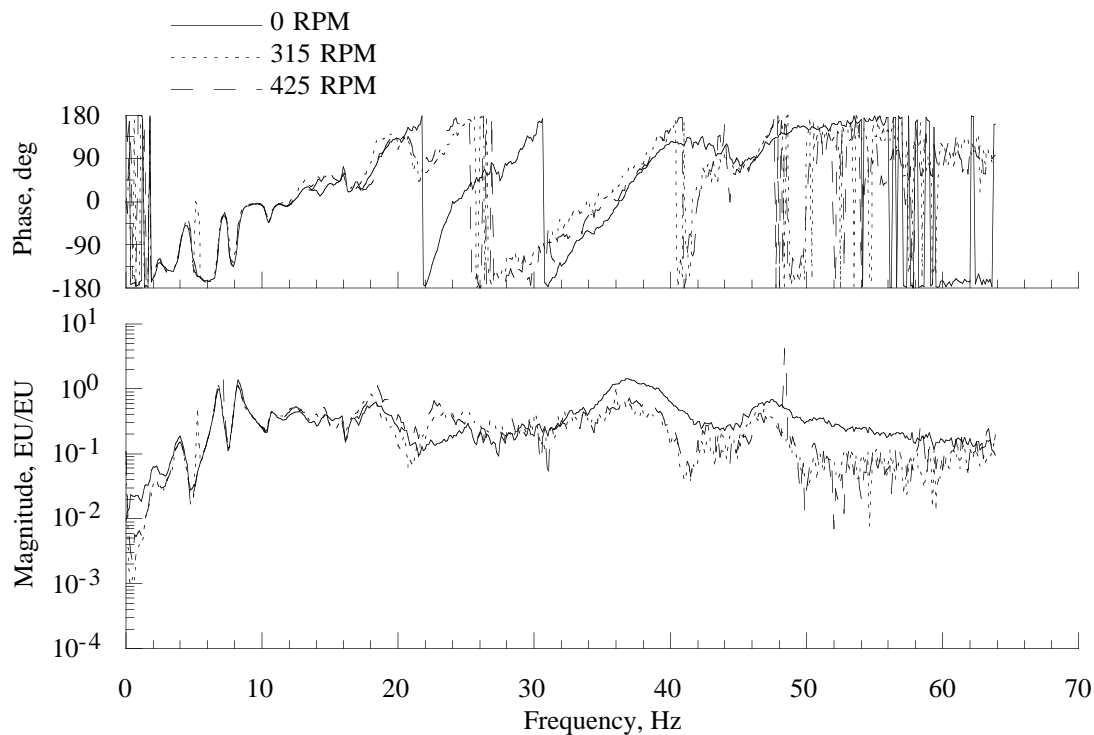


Figure 22(d). Effect of shaft rotation on the hub axial force balance response due to hub roll moment loading, simulated BO105 hub mass.

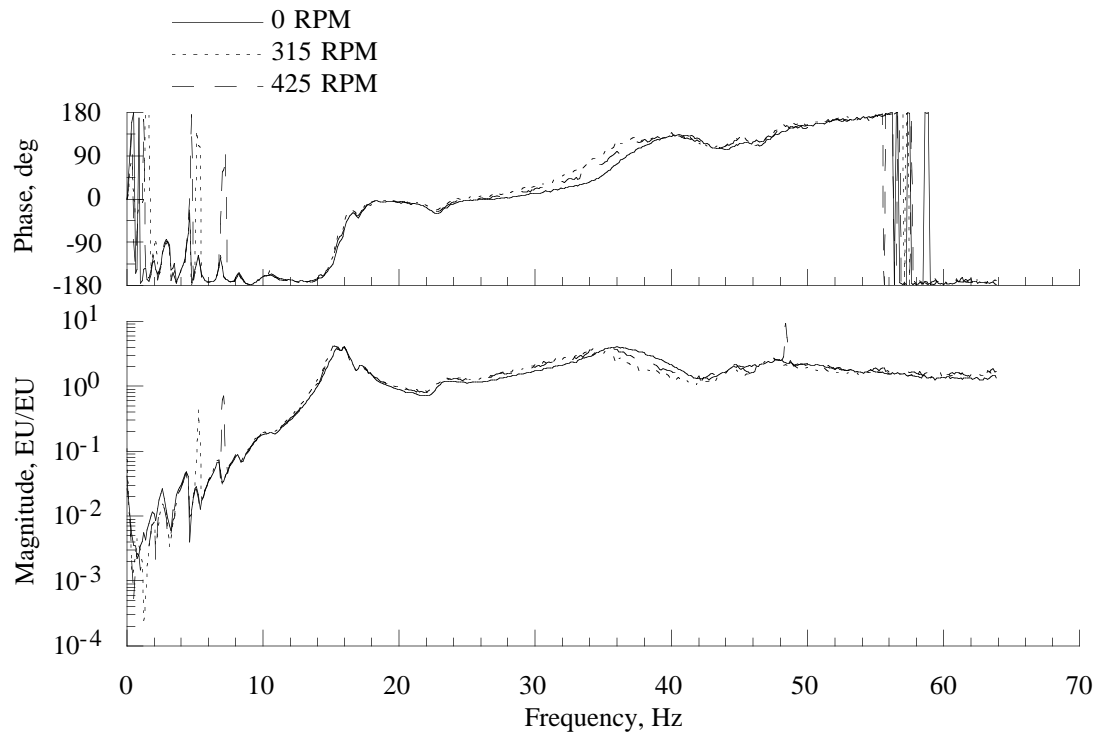


Figure 22(e). Effect of shaft rotation on the hub side force balance response due to hub roll moment loading, simulated BO105 hub mass.

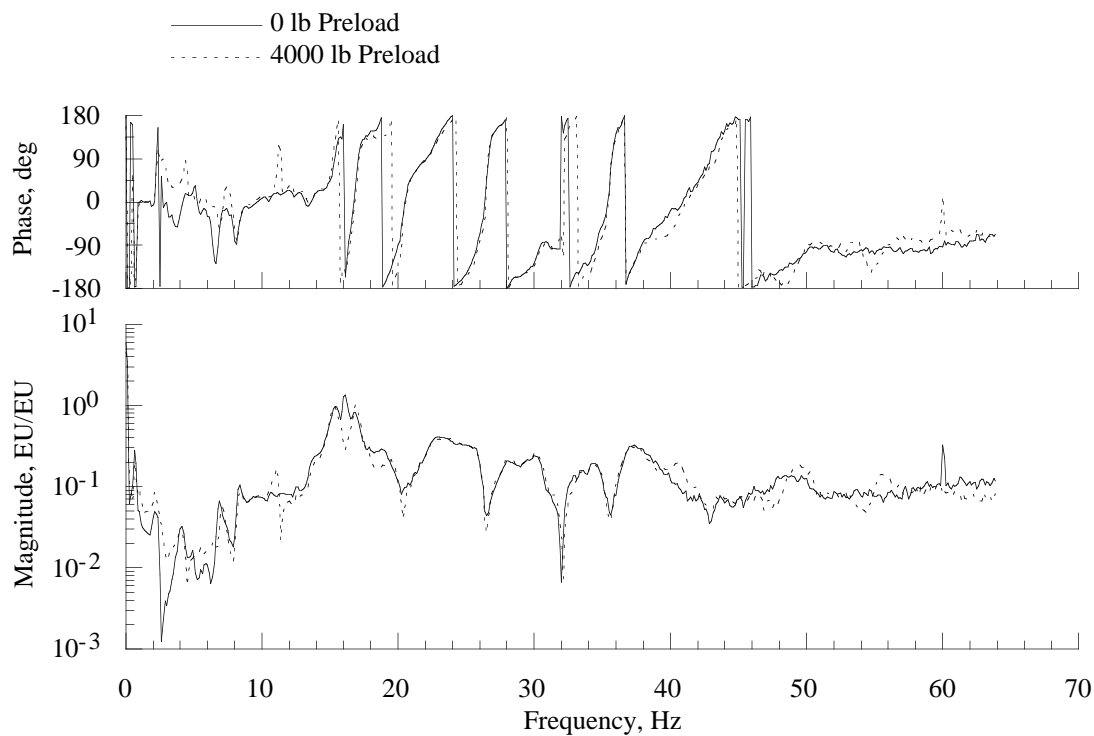


Figure 23(a). Effect of thrust preload on the hub normal force balance response due to hub side force loading, simulated BO105 hub mass.

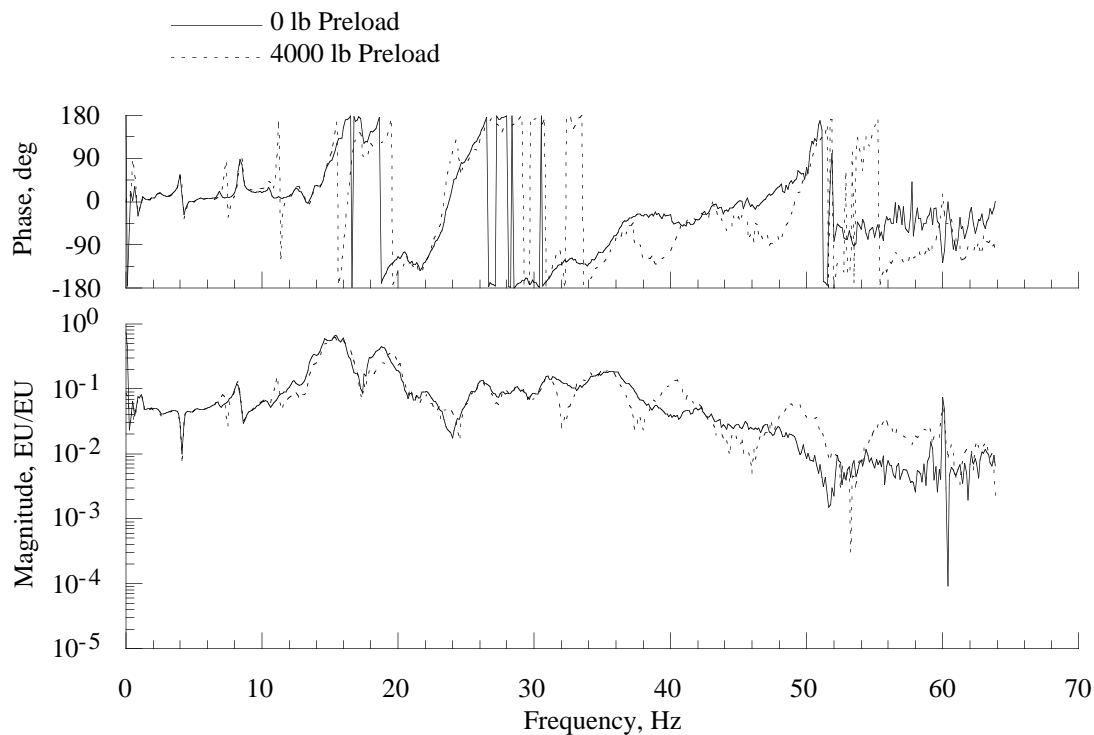


Figure 23(b). Effect of thrust preload on the hub pitch moment balance response due to hub side force loading, simulated BO105 hub mass.

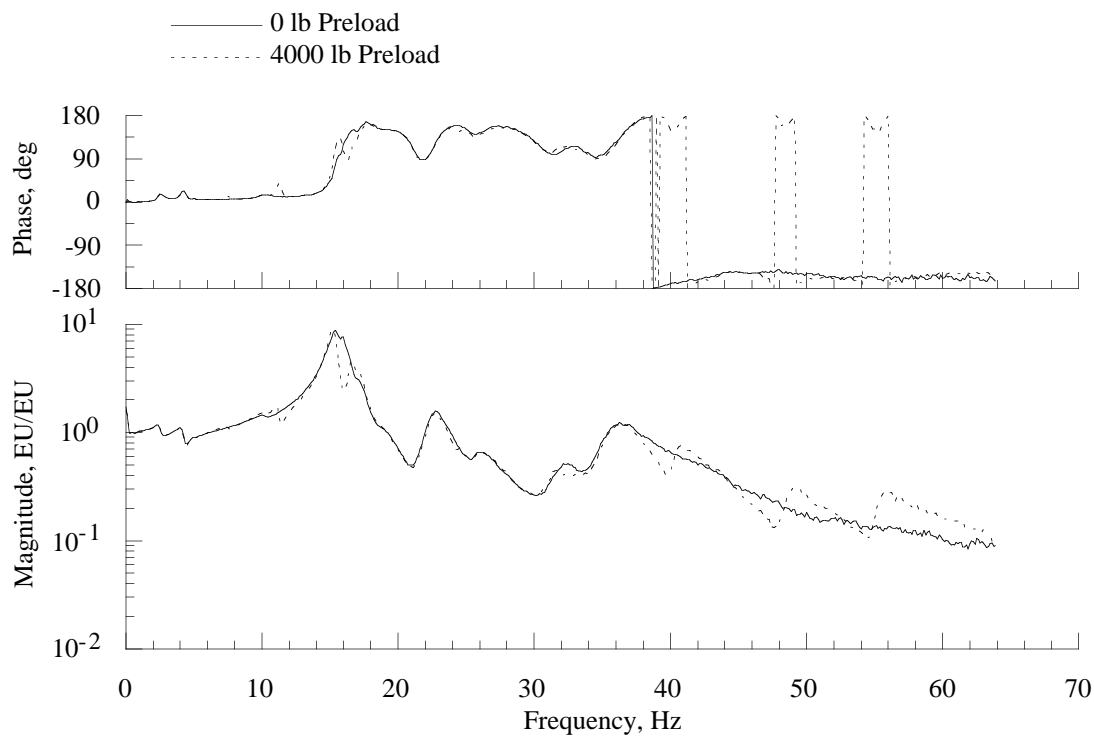


Figure 23(c). Effect of thrust preload on the hub roll moment balance response due to hub side force loading, simulated BO105 hub mass.

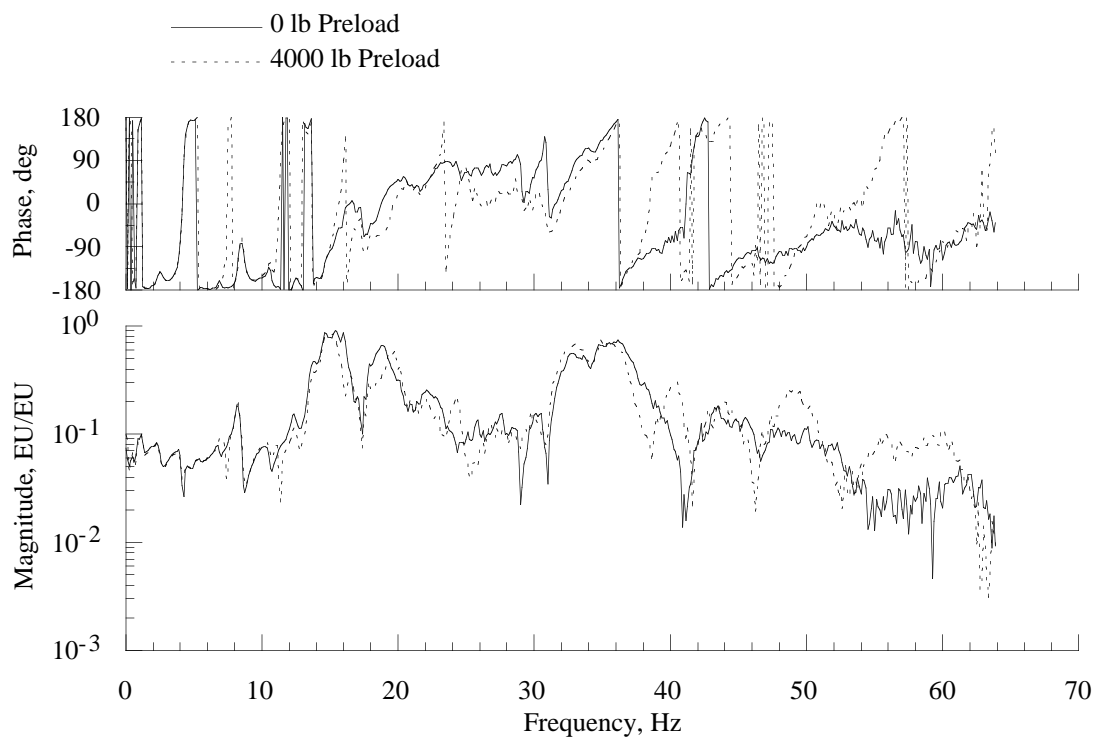


Figure 23(d). Effect of thrust preload on the hub axial force balance response due to hub side force loading, simulated BO105 hub mass.

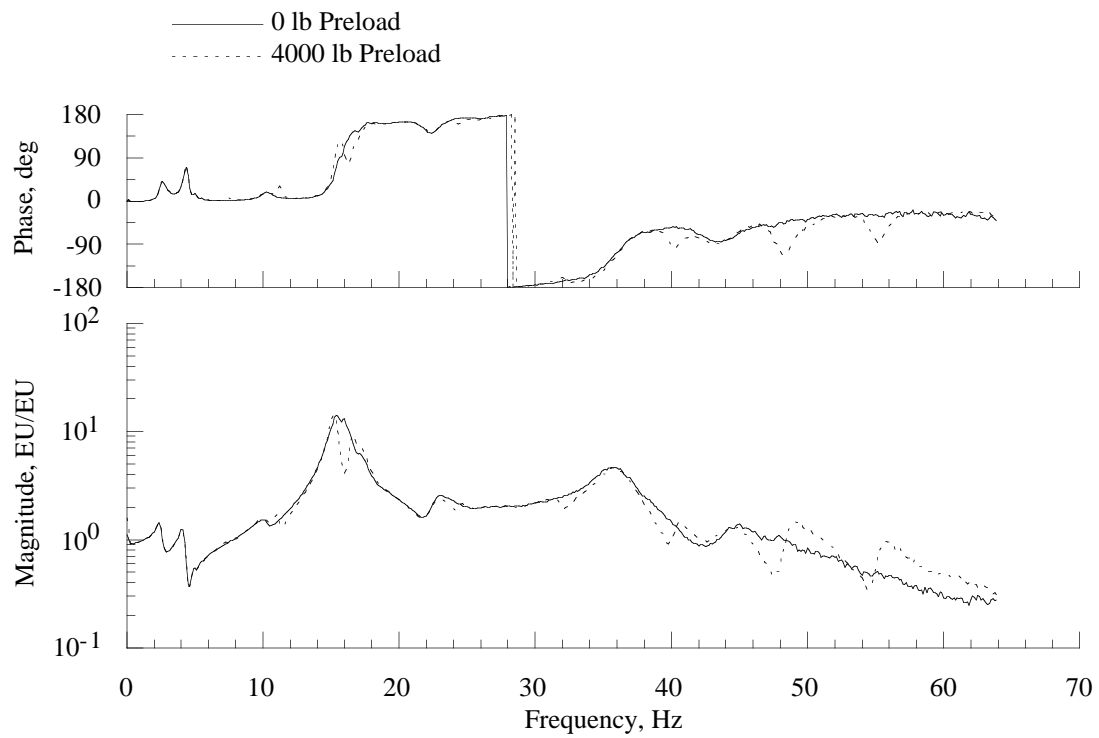


Figure 23(e). Effect of thrust preload on the hub side force balance response due to hub side force loading, simulated BO105 hub mass.

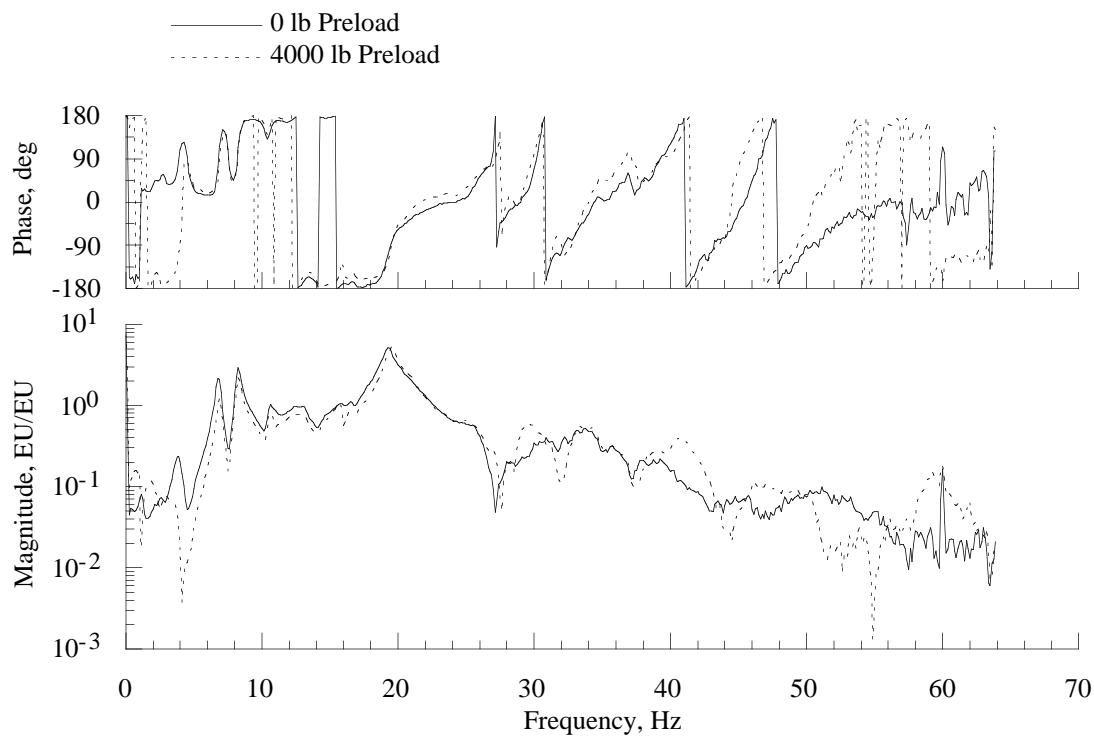


Figure 24(a). Effect of thrust preload on the hub normal force balance response due to hub axial force loading, simulated BO105 hub mass.

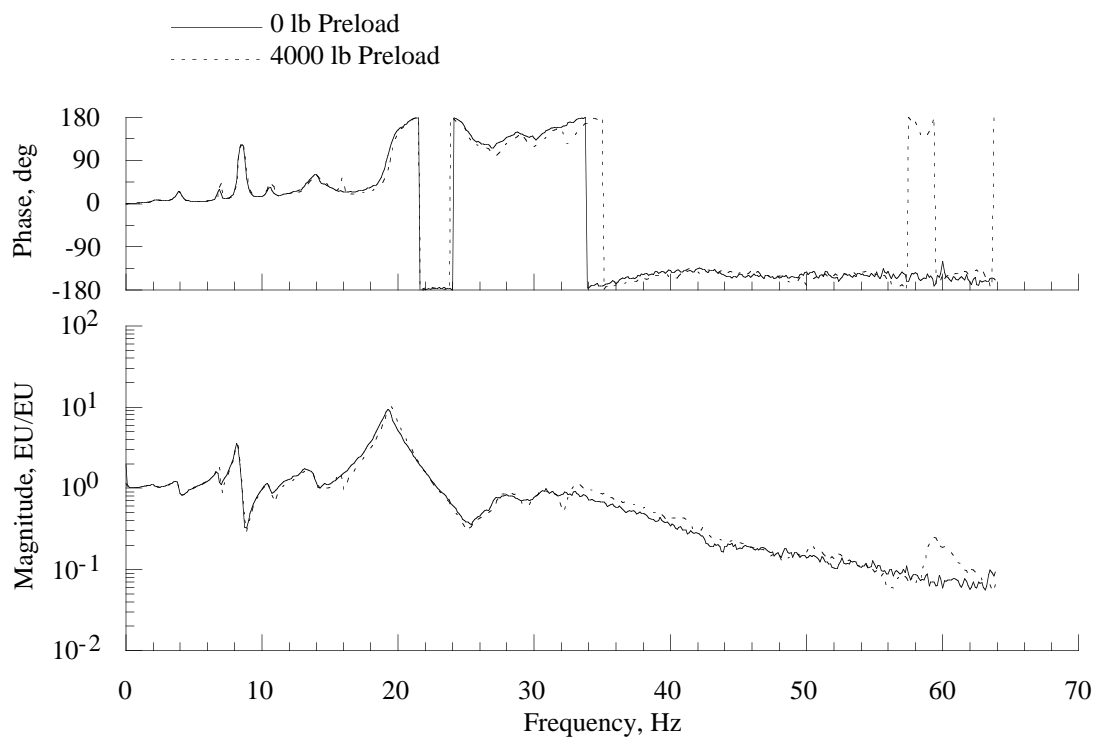


Figure 24(b). Effect of thrust preload on the hub pitch moment balance response due to hub axial force loading, simulated BO105 hub mass.

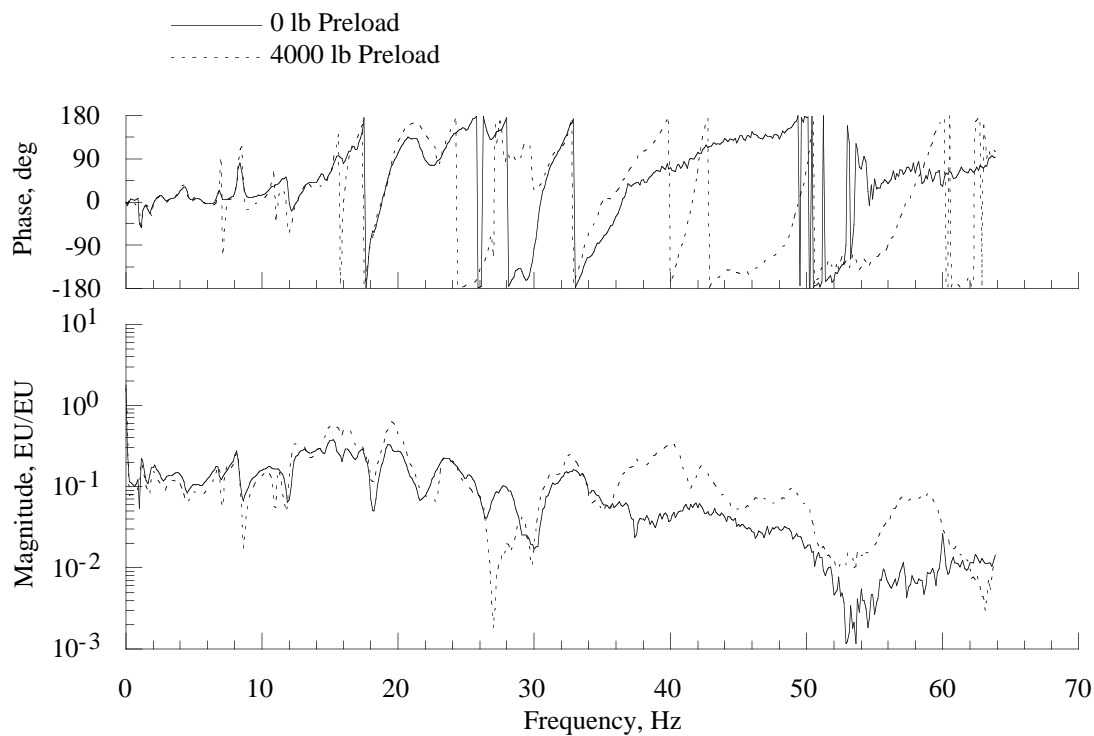


Figure 24(c). Effect of thrust preload on the hub roll moment balance response due to hub axial force loading, simulated BO105 hub mass.

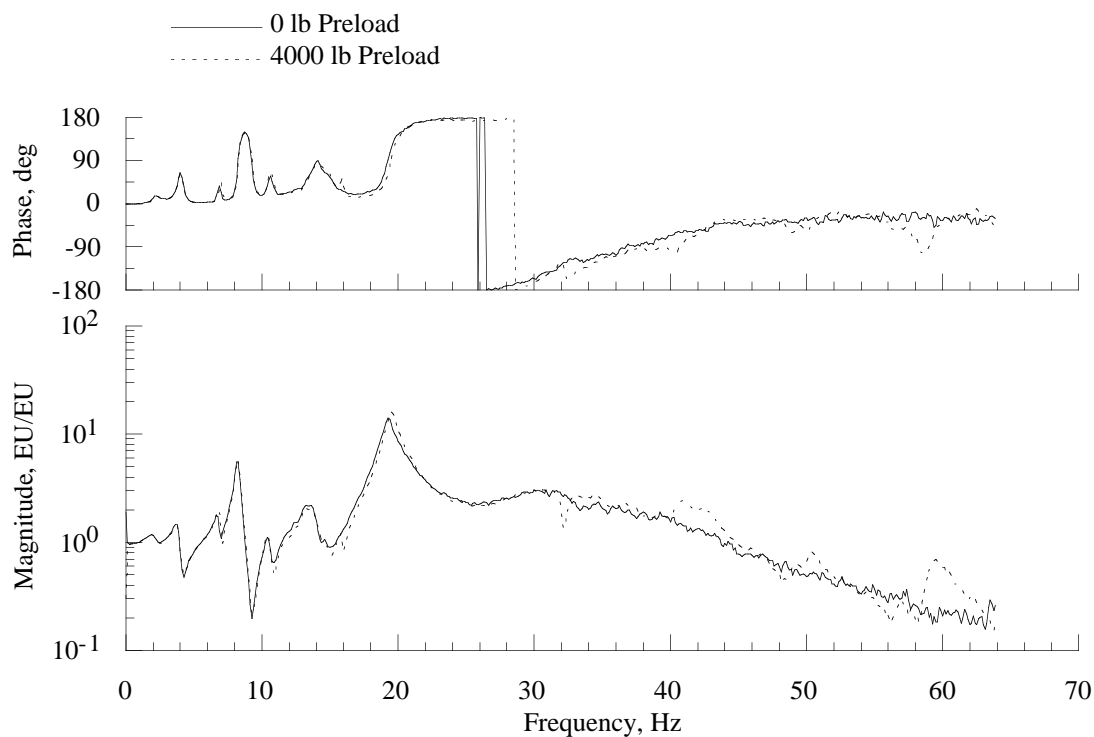


Figure 24(d). Effect of thrust preload on the hub axial force balance response due to hub axial force loading, simulated BO105 hub mass.

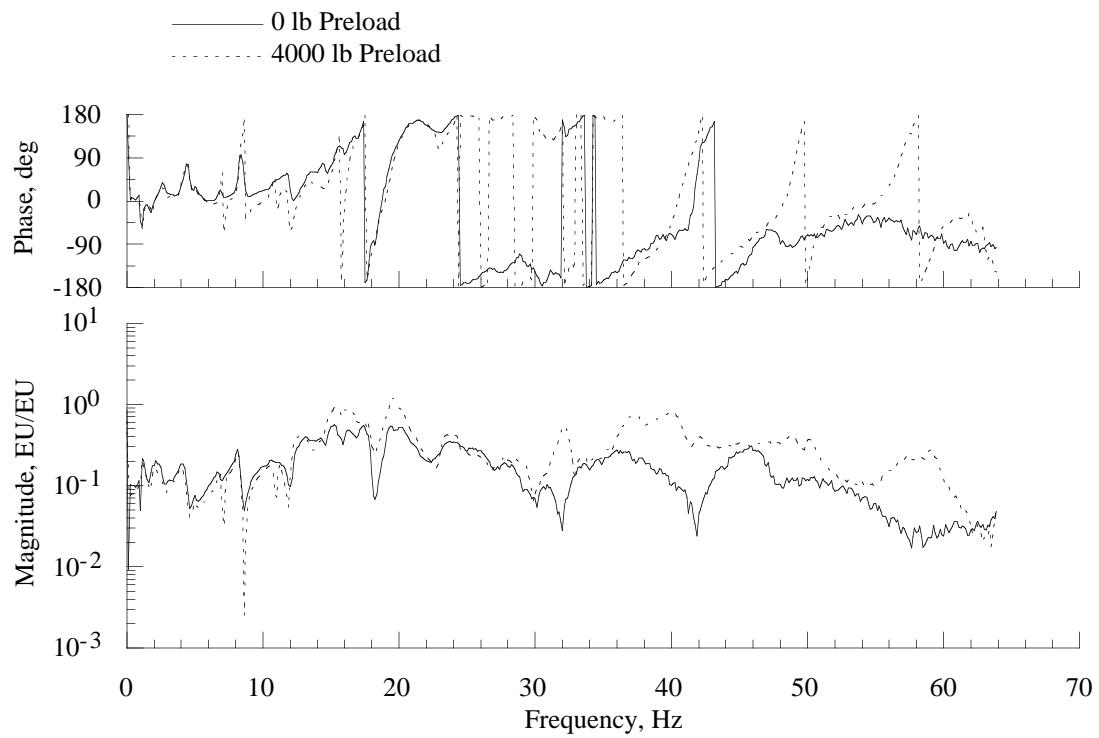


Figure 24(e). Effect of thrust preload on the hub side force balance response due to hub axial force loading, simulated BO105 hub mass.

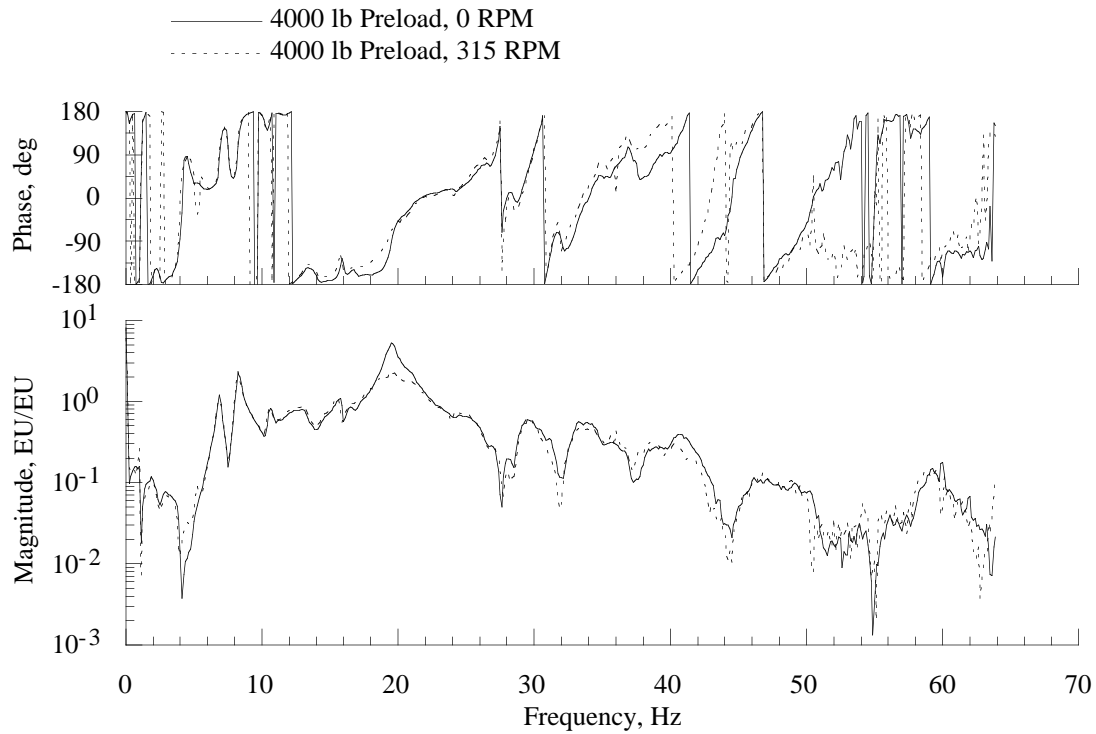


Figure 25(a). Effect of thrust preload with RPM variation on the hub normal force balance response due to hub axial force loading, simulated BO105 hub mass.

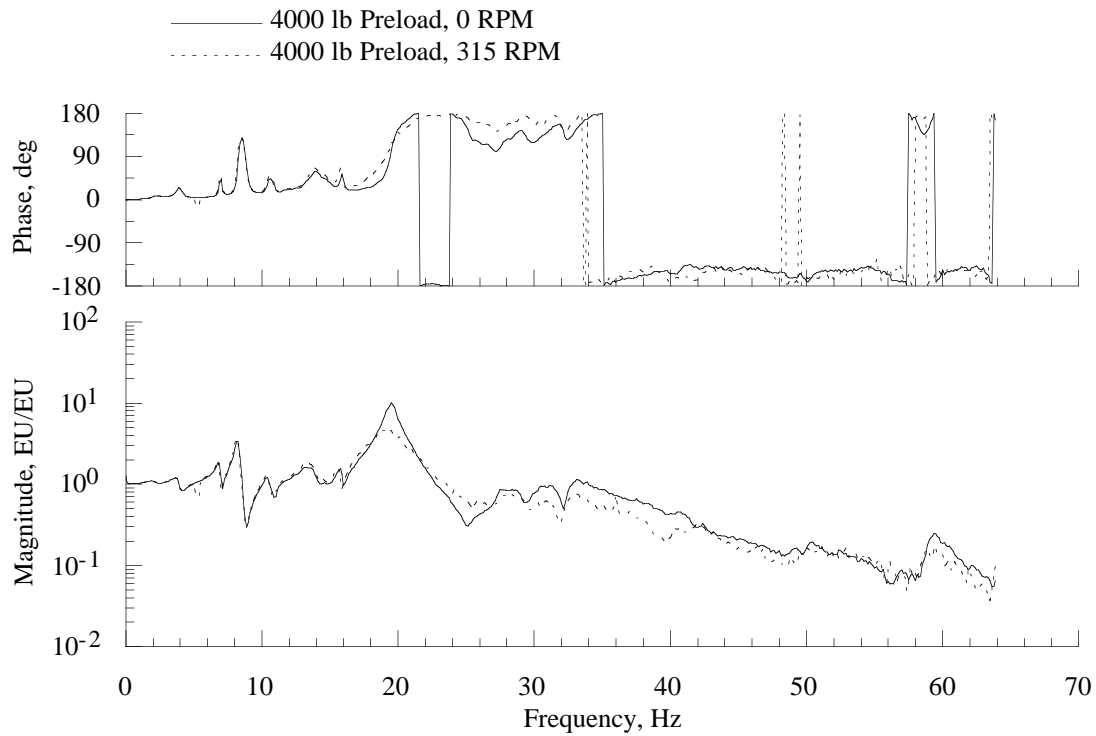


Figure 25(b). Effect of thrust preload with RPM variation on the hub pitch moment balance response due to hub axial force loading, simulated BO105 hub mass.

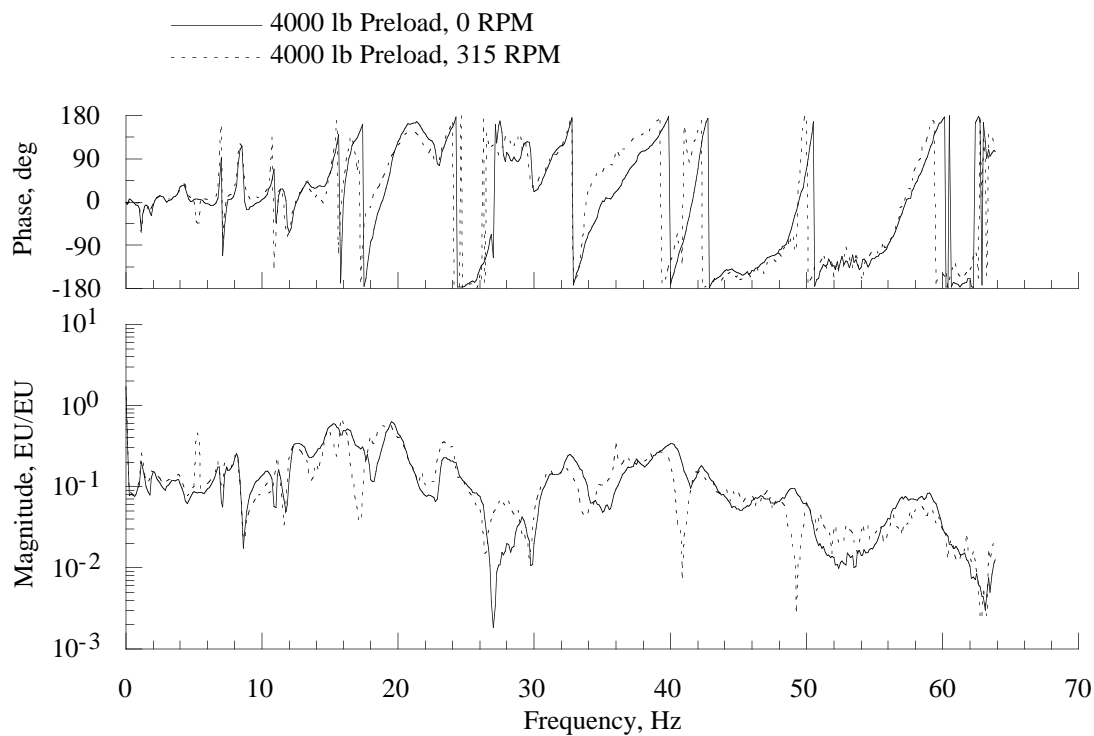


Figure 25(c). Effect of thrust preload with RPM variation on the hub roll moment balance response due to hub axial force loading, simulated BO105 hub mass.

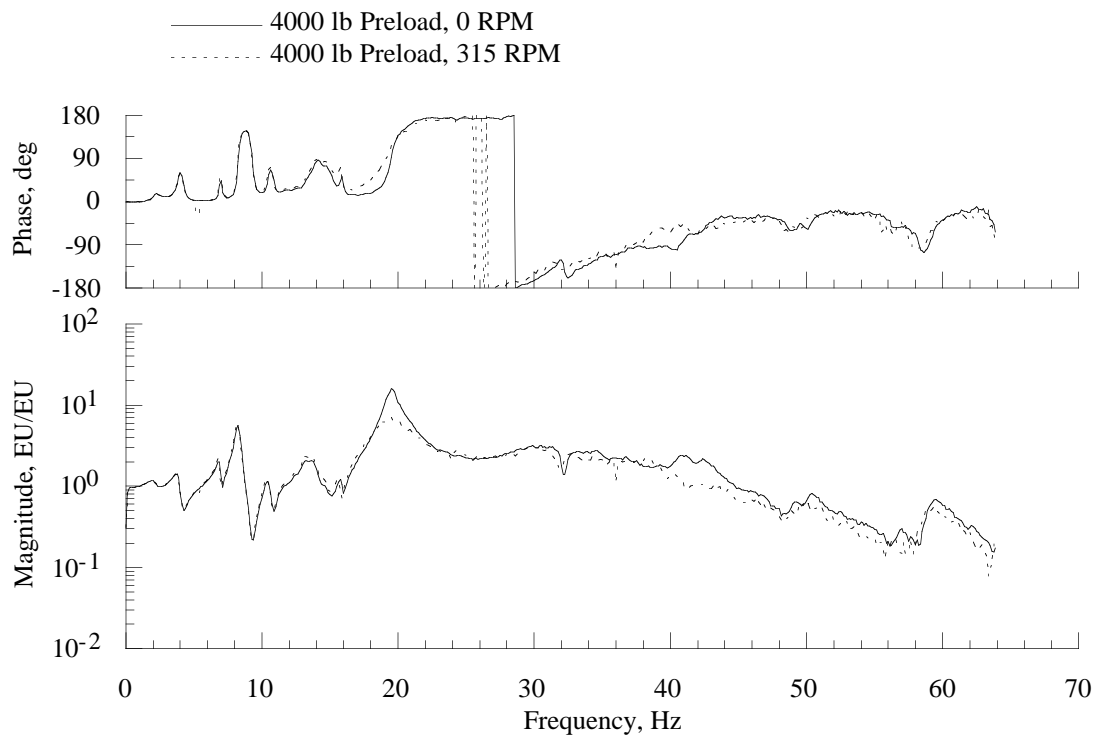


Figure 25(d). Effect of thrust preload with RPM variation on the hub axial force balance response due to hub axial force loading, simulated BO105 hub mass.

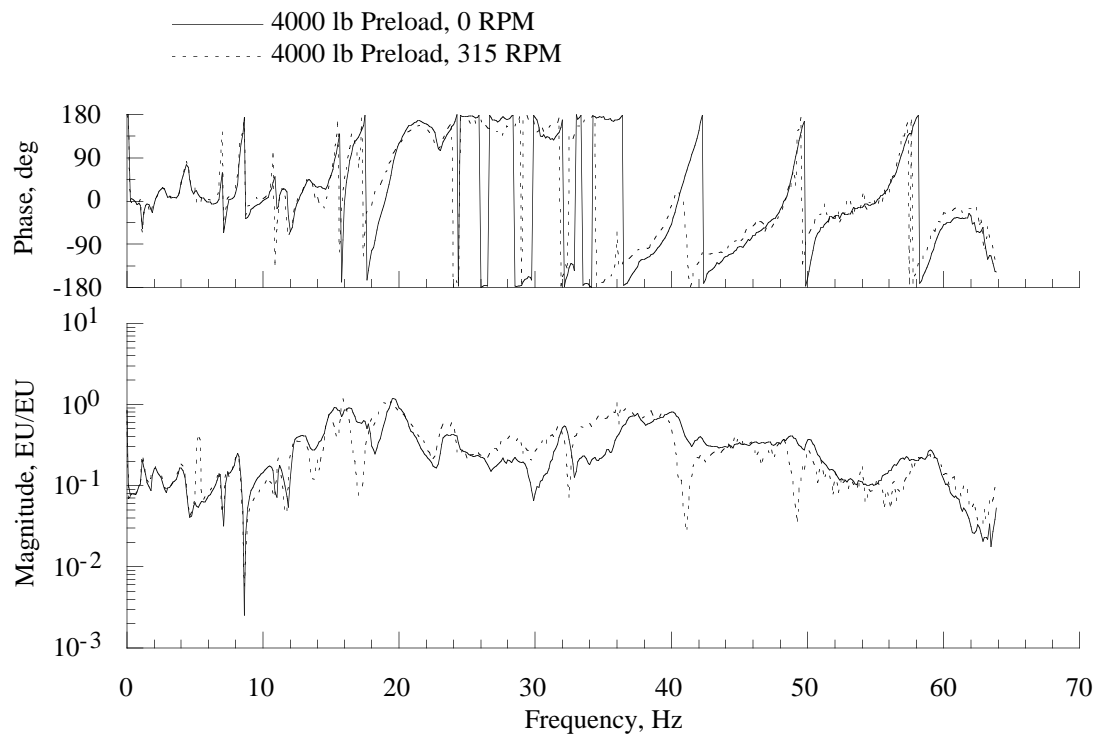


Figure 25(e). Effect of thrust preload with RPM variation on the hub side force balance response due to hub axial force loading, simulated BO105 hub mass.

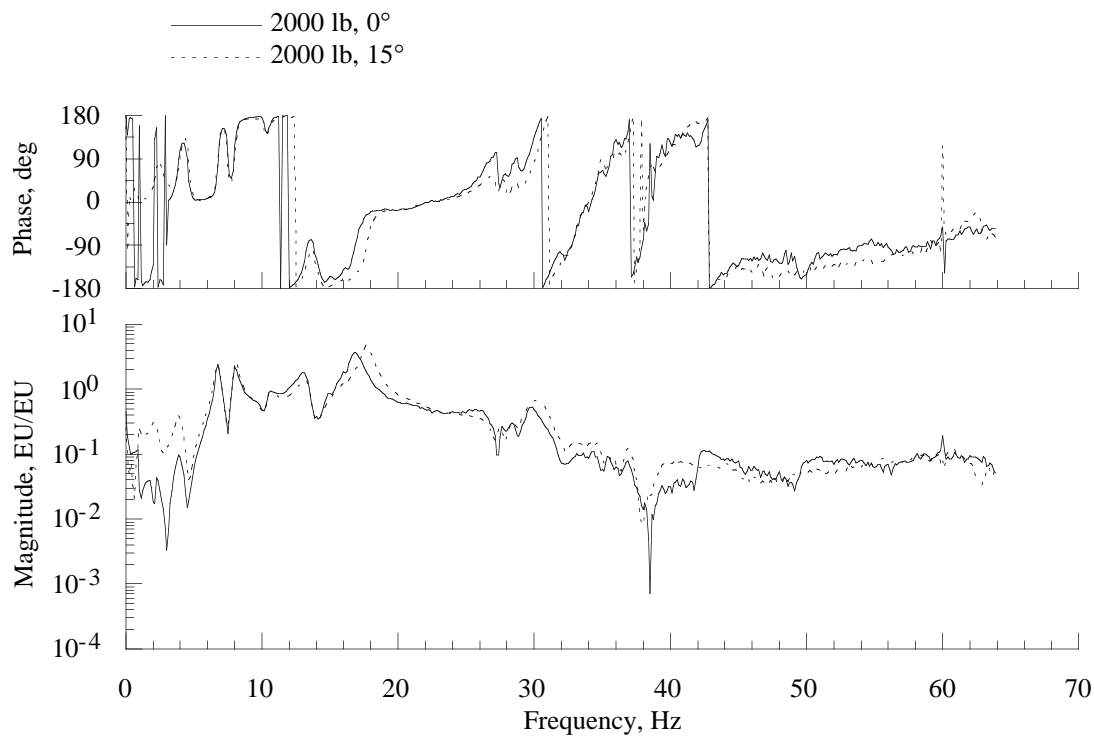


Figure 26(a). Comparison of thrust inclination preload on the hub normal force balance response due to hub axial force loading, simulated SBMR hub mass.

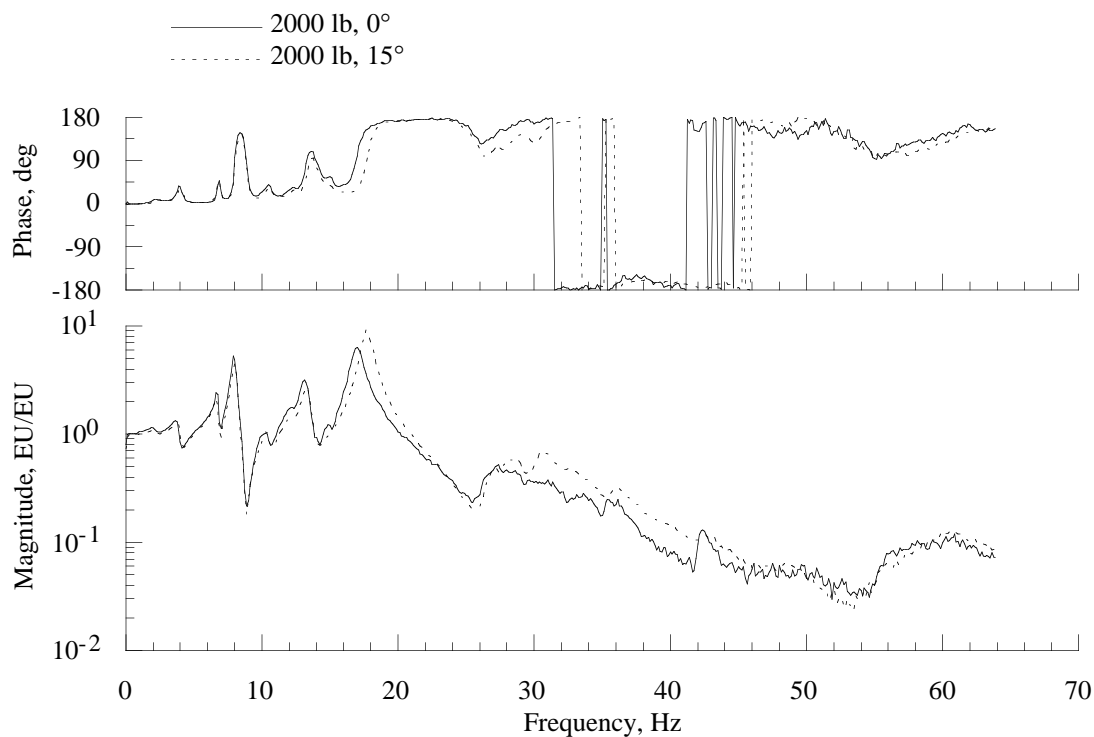


Figure 26(b). Comparison of thrust inclination preload on the hub pitch moment balance response due to hub axial force loading, simulated SBMR hub mass.

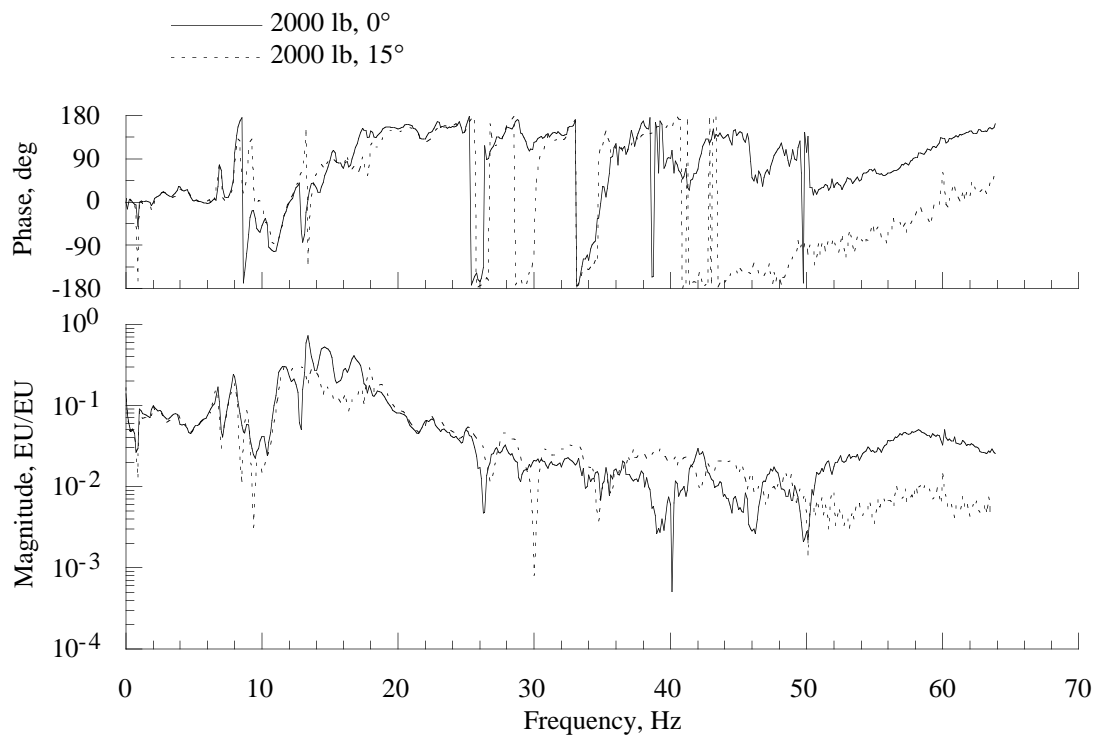


Figure 26(c). Comparison of thrust inclination preload on the hub roll moment balance response due to hub axial force loading, simulated SBMR hub mass.

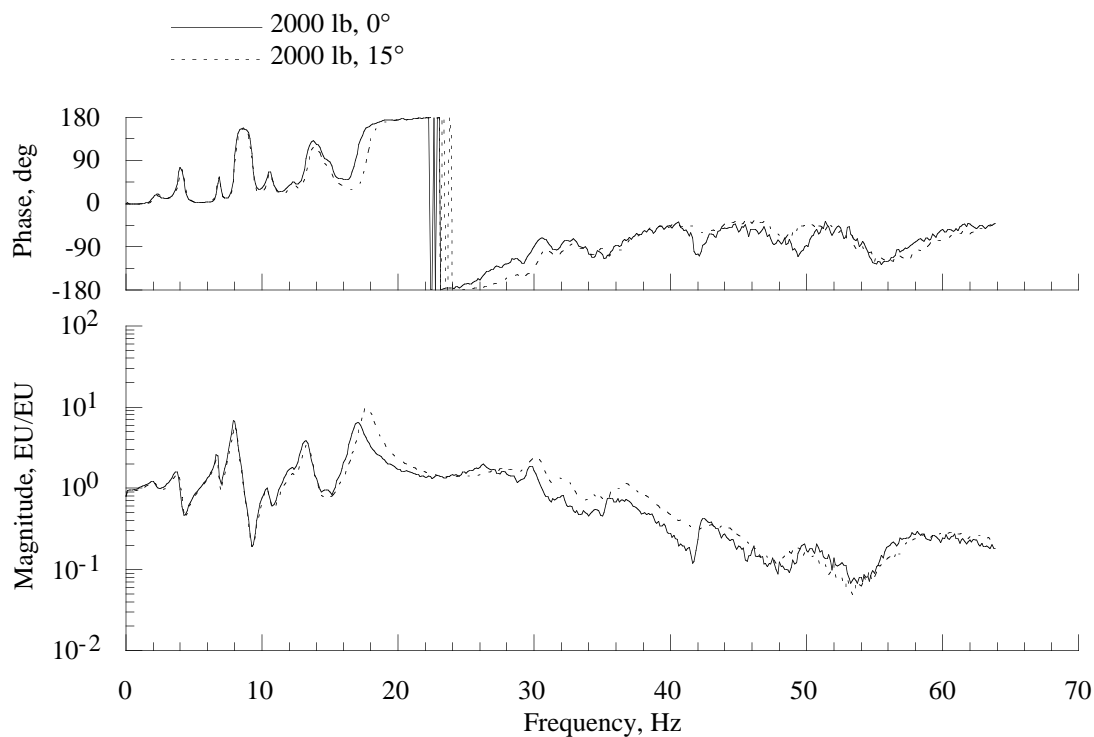


Figure 26(d). Comparison of thrust inclination preload on the hub axial force balance response due to hub axial force loading, simulated SBMR hub mass.

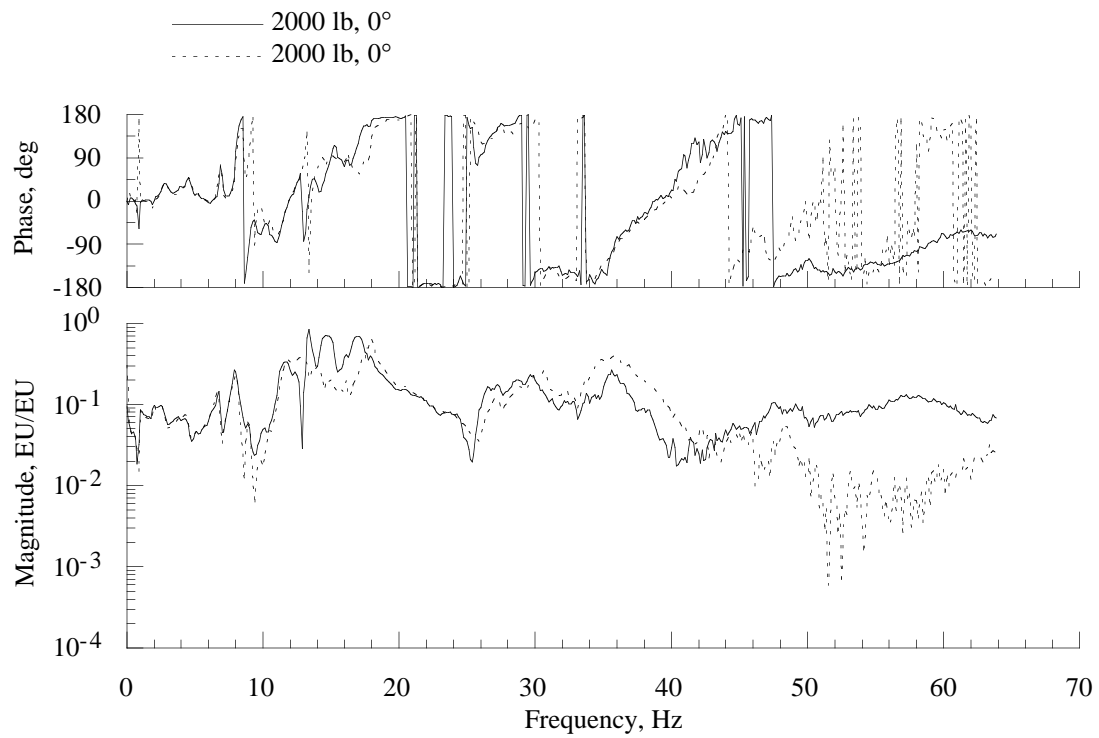


Figure 26(e). Comparison of thrust inclination preload on the hub side force balance response due to hub axial force loading, simulated SBMR hub mass.

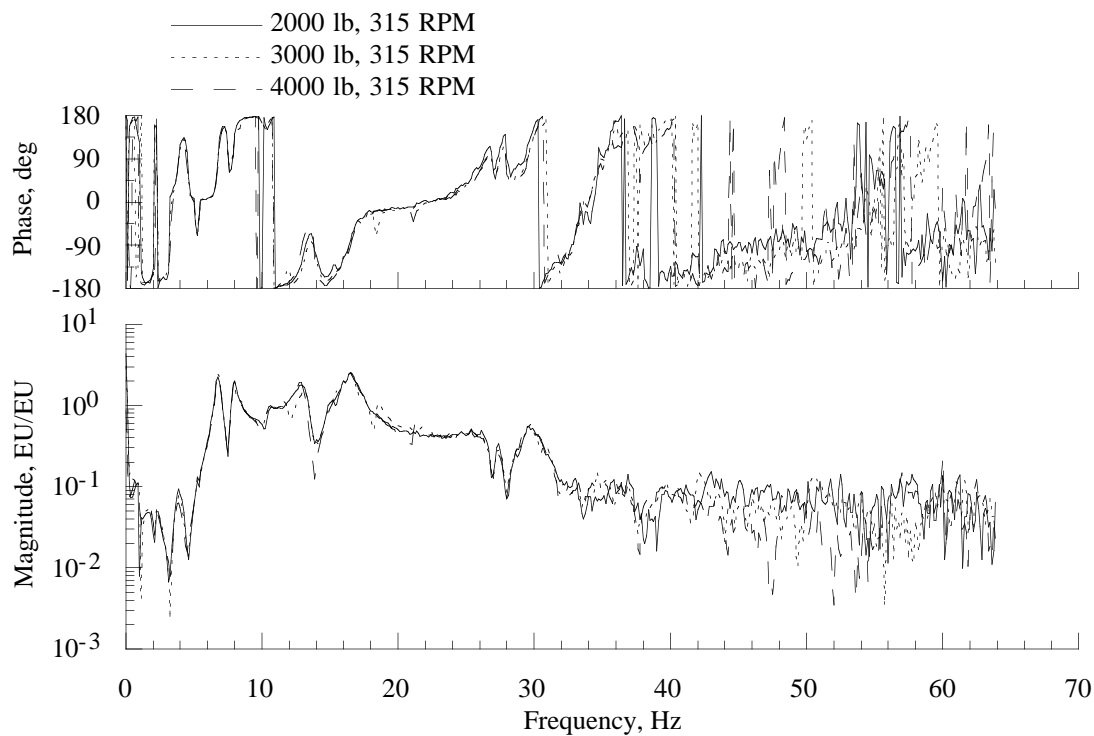


Figure 27(a). Comparison of variations in thrust preload with shaft rotation on the hub normal force balance response due to hub axial force loading, simulated SBMR hub mass.

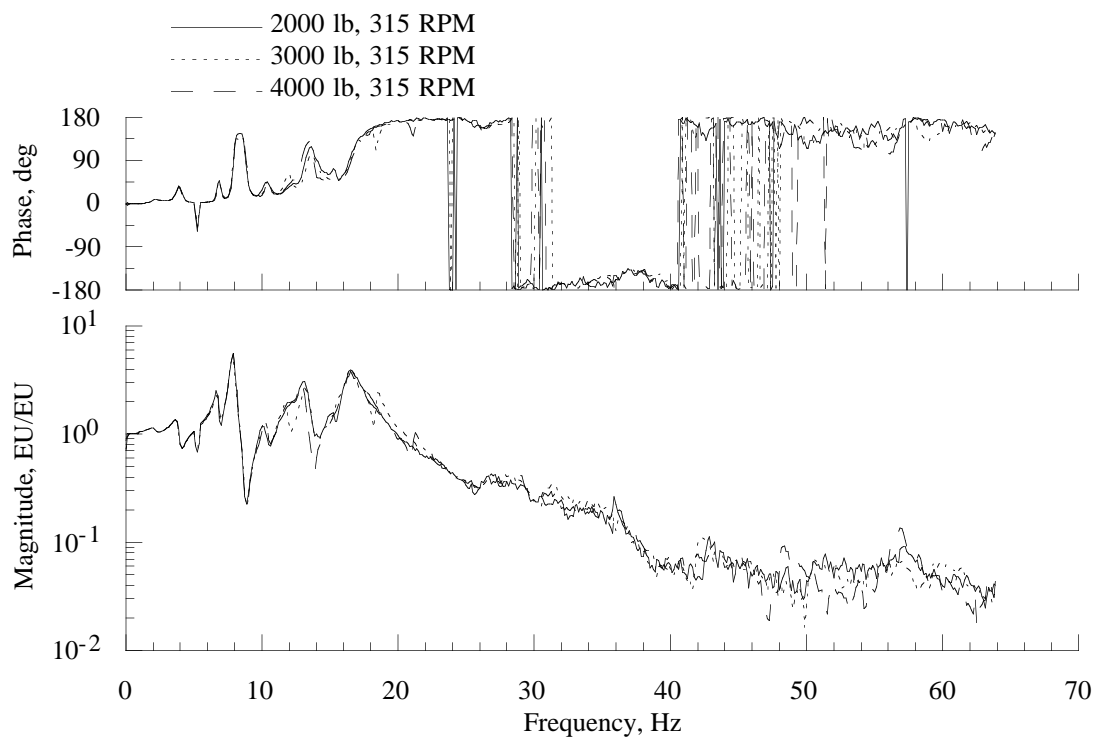


Figure 27(b). Comparison of variations in thrust preload with shaft rotation on the hub pitch moment balance response due to hub axial force loading, simulated SBMR hub mass.

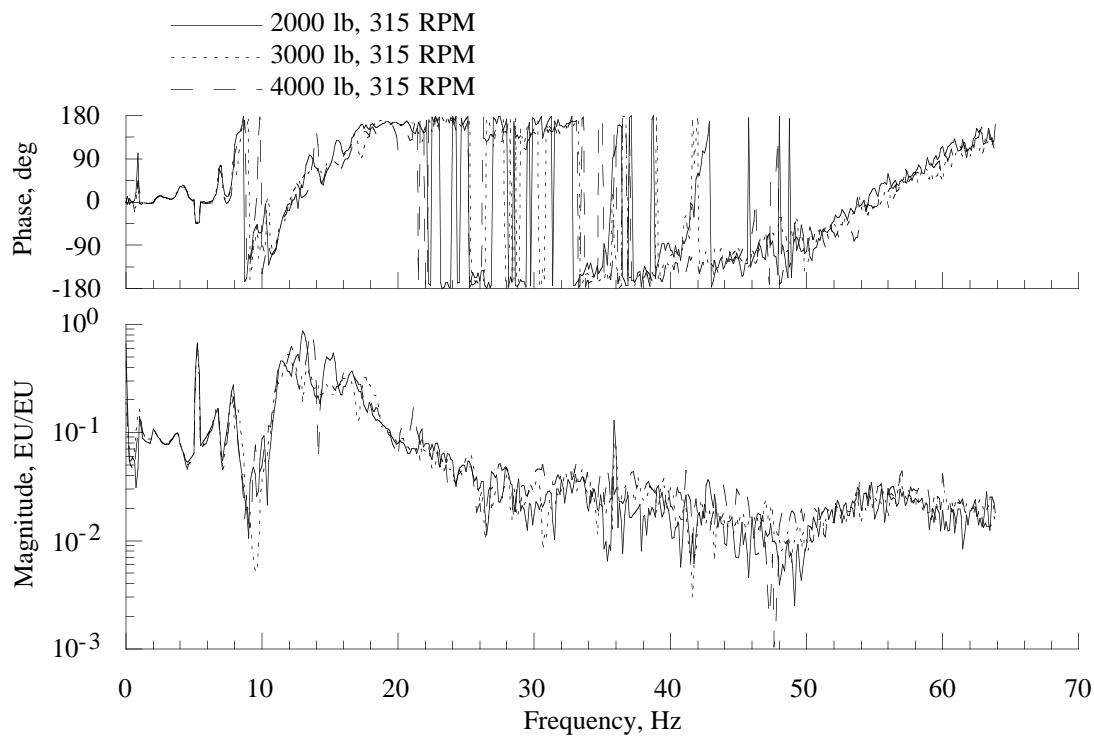


Figure 27(c). Comparison of variations in thrust preload with shaft rotation on the hub roll moment balance response due to hub axial force loading, simulated SBMR hub mass.

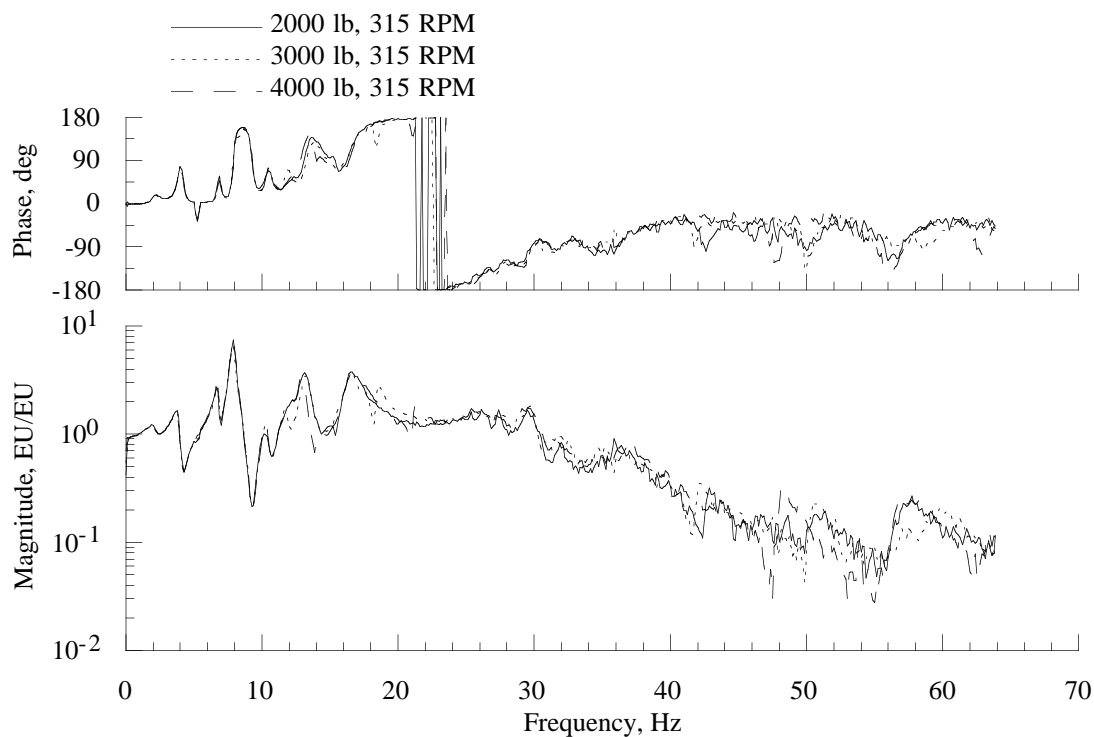


Figure 27(d). Comparison of variations in thrust preload with shaft rotation on the hub axial force balance response due to hub axial force loading, simulated SBMR hub mass.

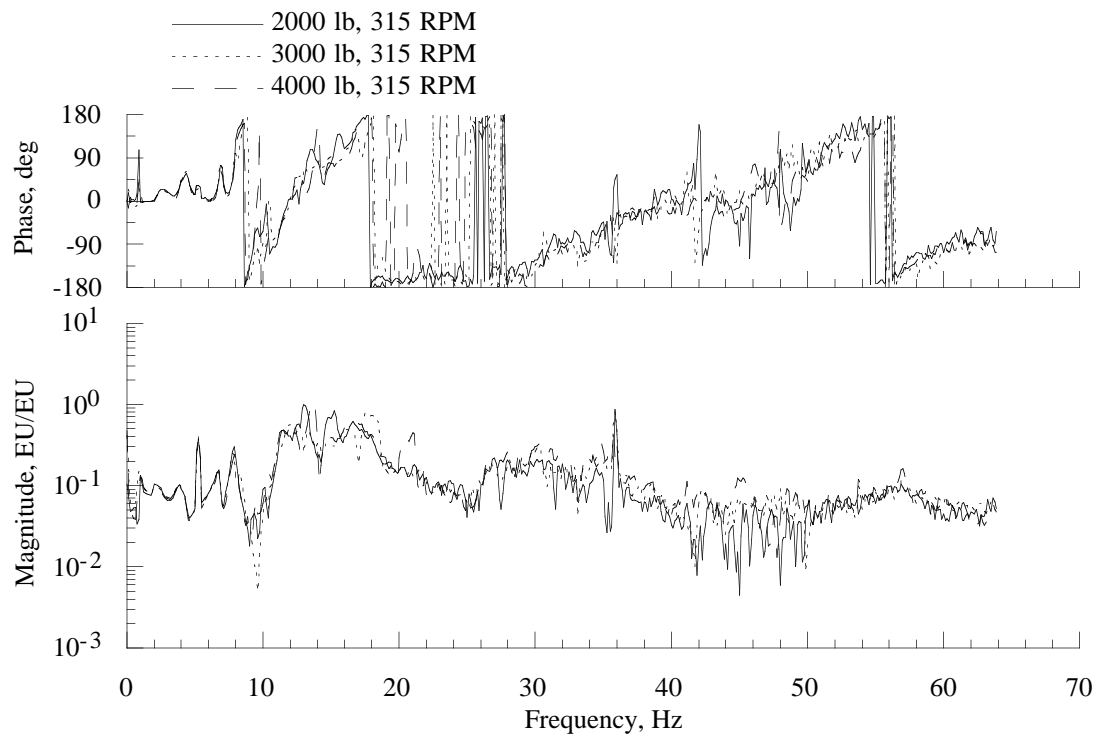


Figure 27(e). Comparison of variations in thrust preload with shaft rotation on the hub side force balance response due to hub axial force loading, simulated SBMR hub mass.

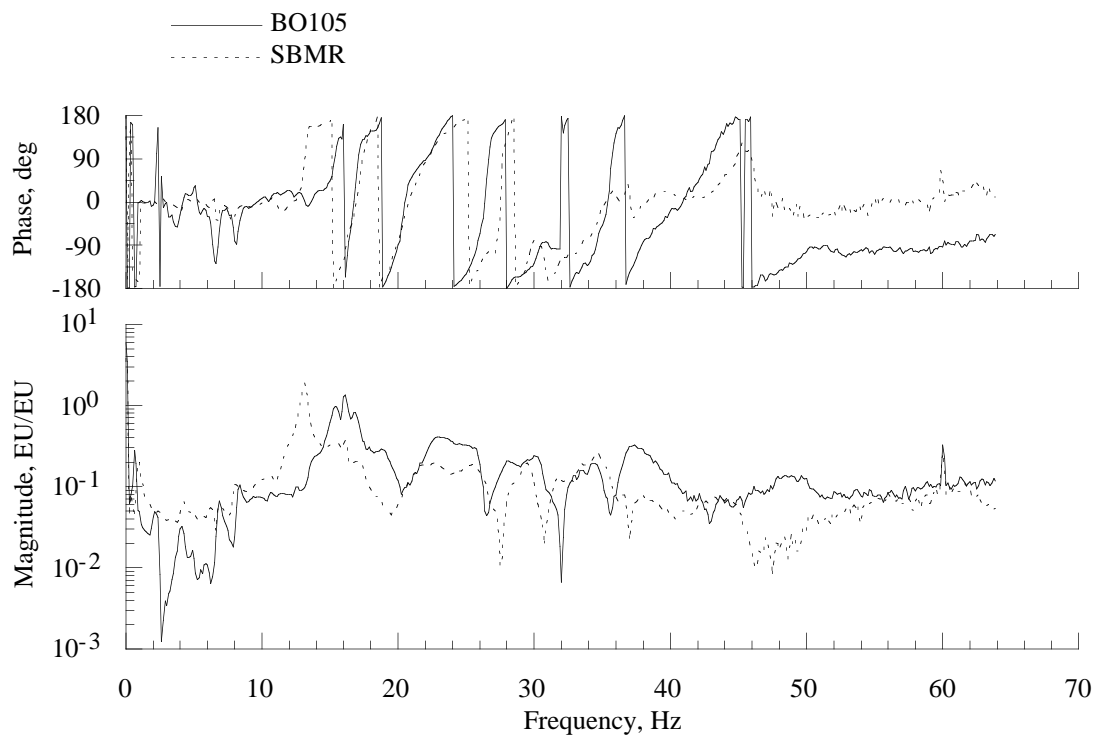


Figure 28(a). Effect of hub mass on the hub normal force balance response due to hub side force loading.

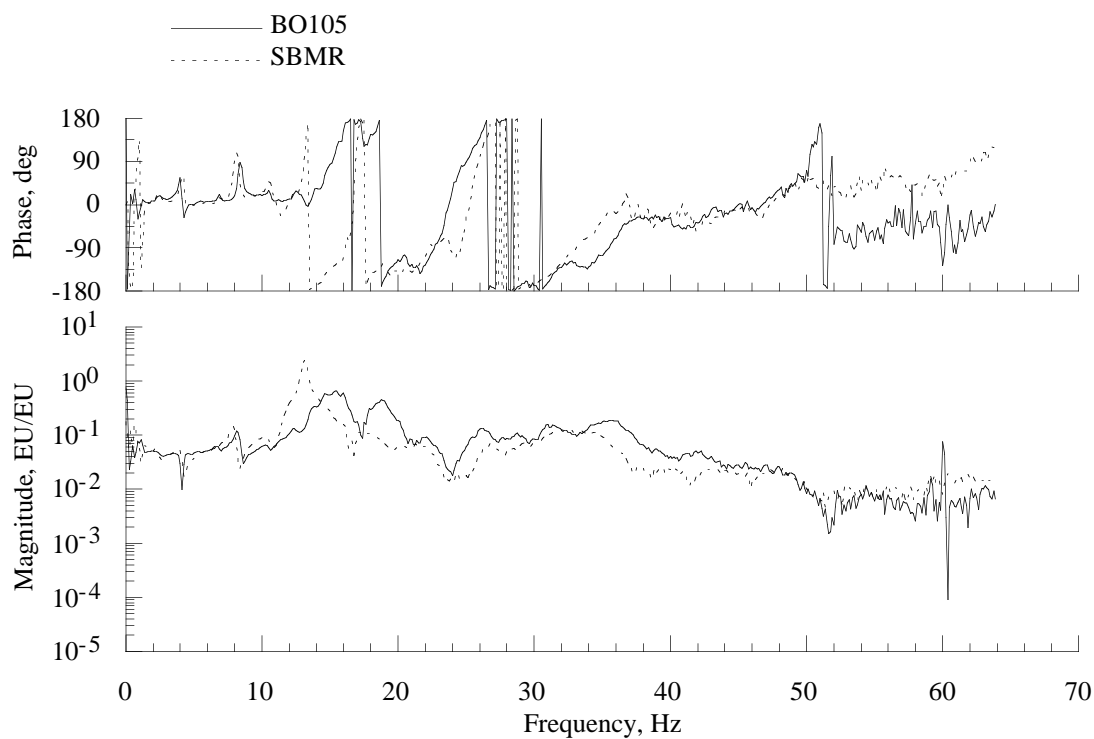


Figure 28(b). Effect of hub mass on the hub pitch moment balance response due to hub side force loading.

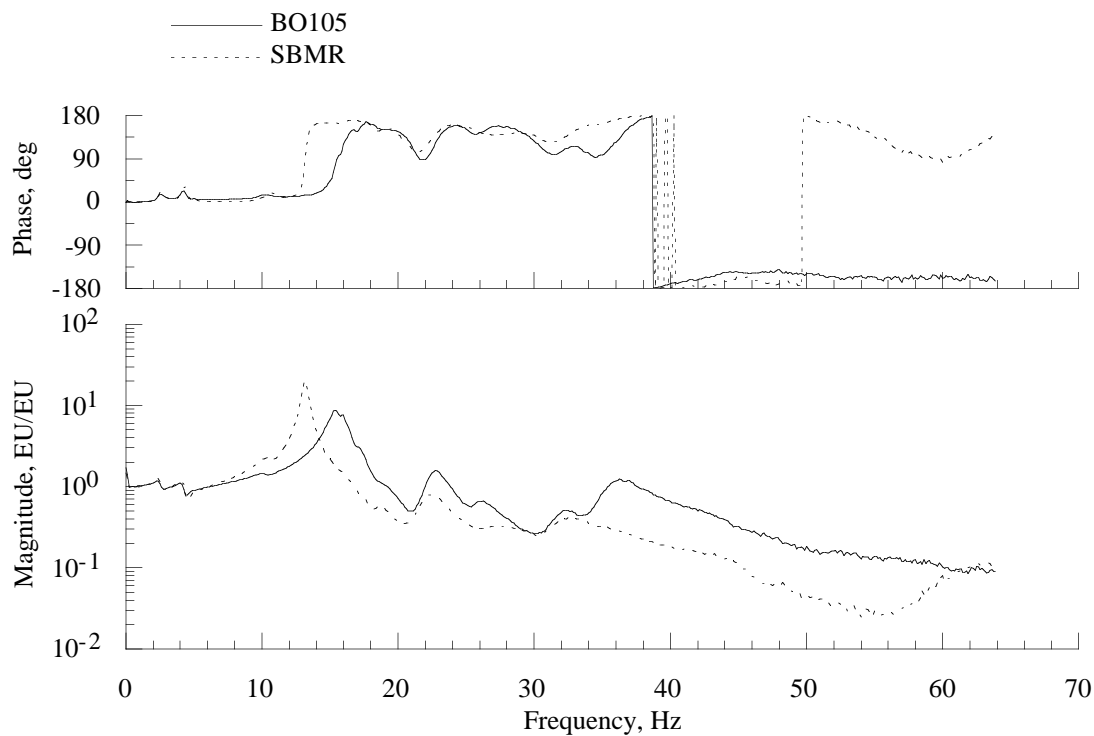


Figure 28(c). Effect of hub mass on the hub roll moment balance response due to hub side force loading.

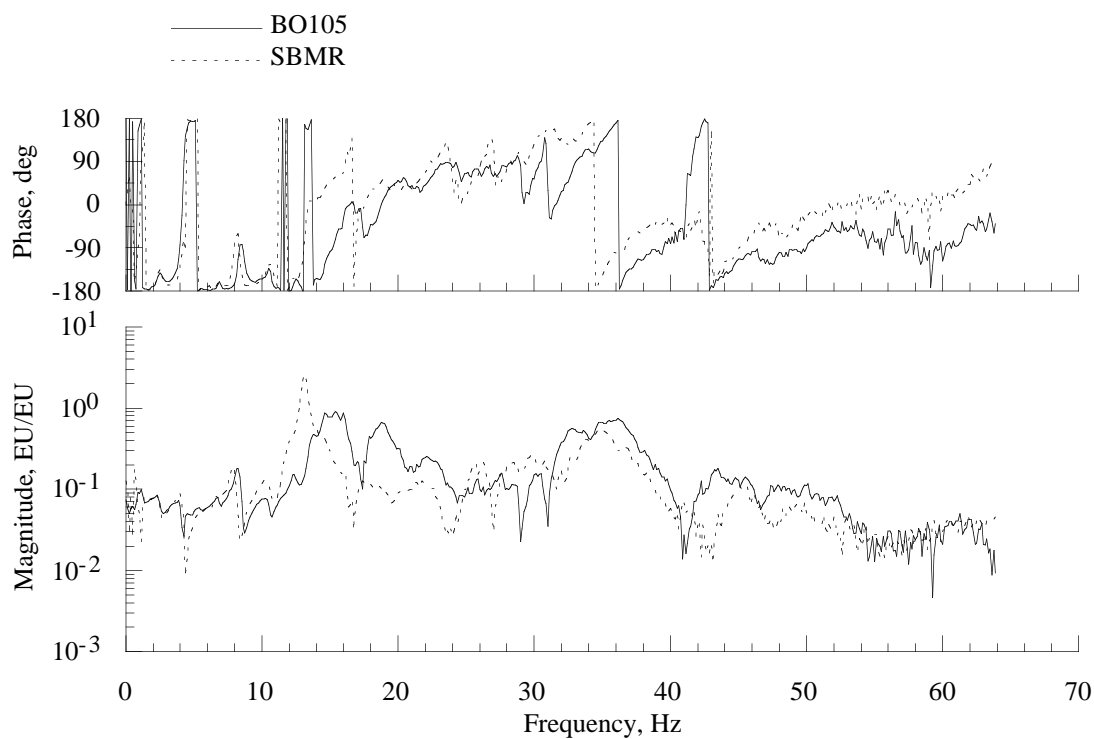


Figure 28(d). Effect of hub mass on the hub axial force balance response due to hub side force loading.

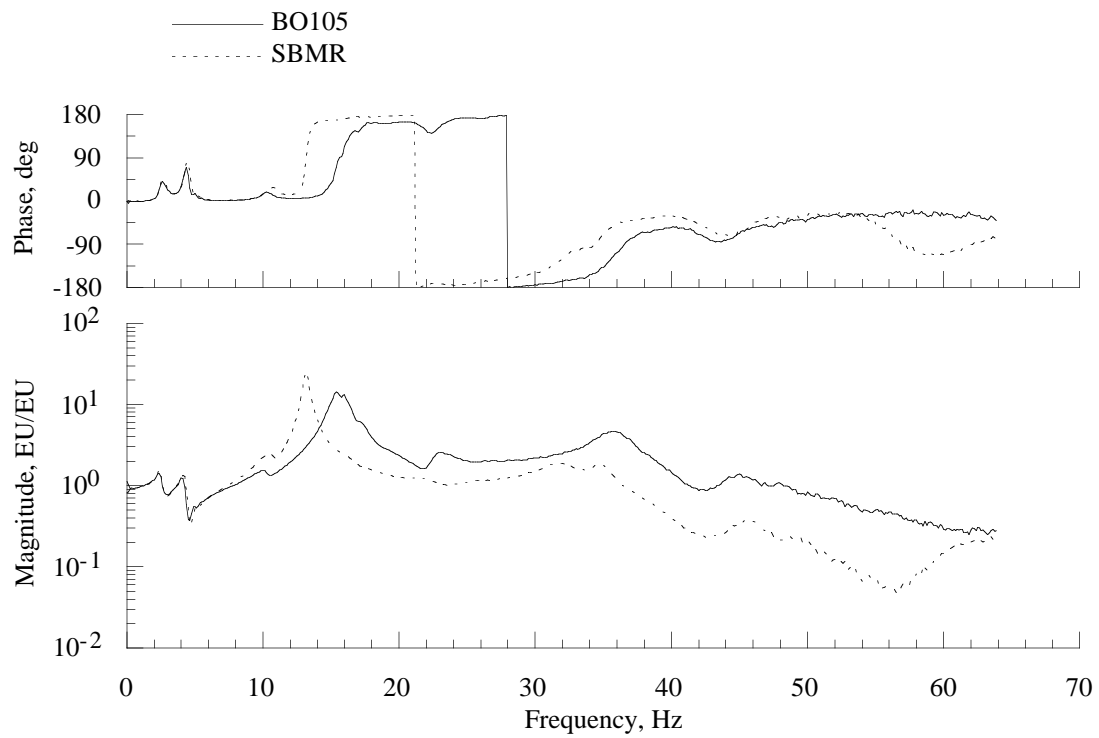


Figure 28(e). Effect of hub mass on the hub side force balance response due to hub side force loading.

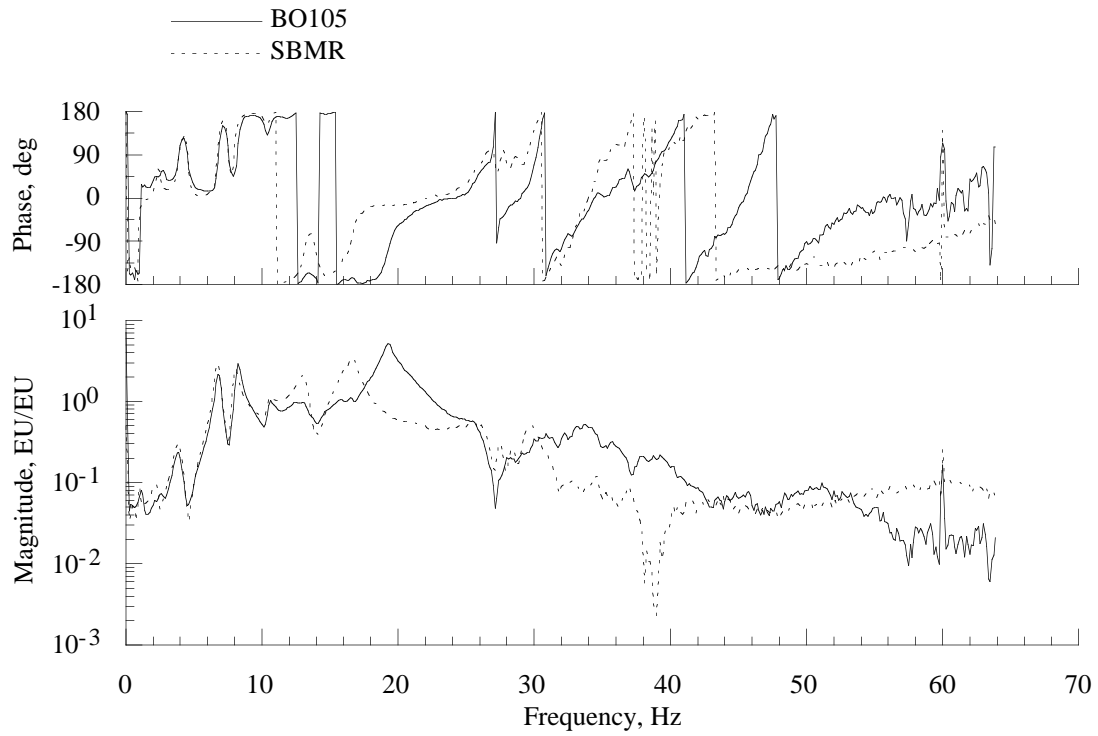


Figure 29(a). Effect of hub mass on the hub normal force balance response due to hub axial force loading.

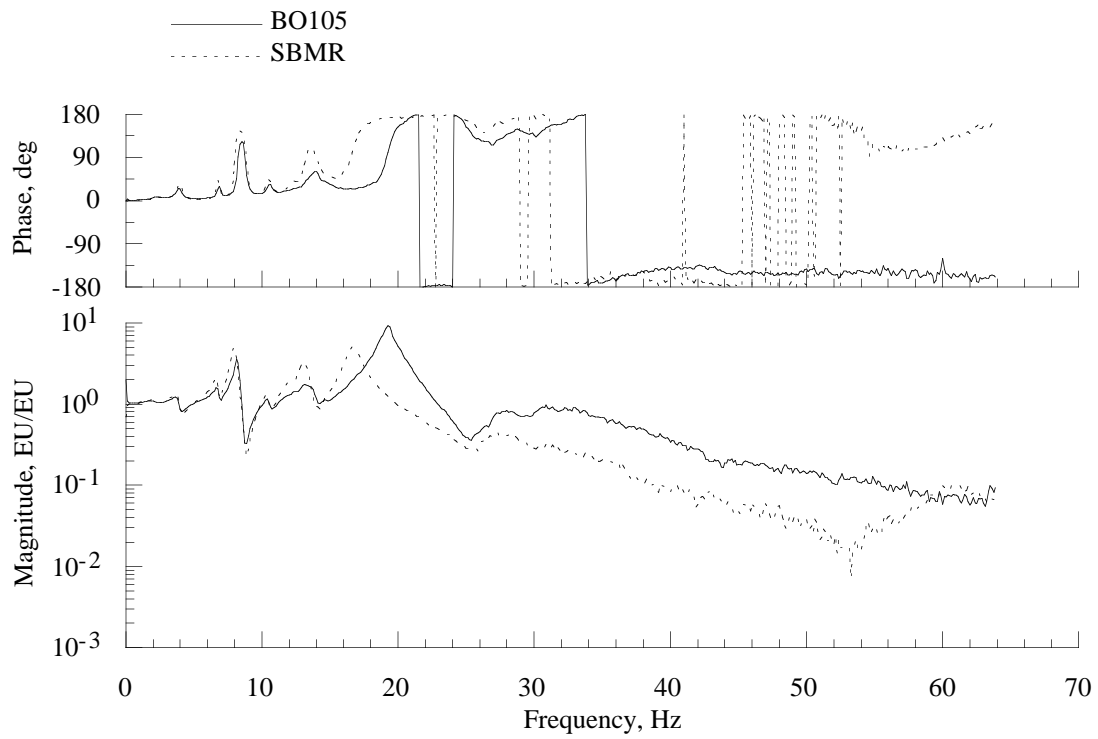


Figure 29(b). Effect of hub mass on the hub pitch moment balance response due to hub axial force loading.

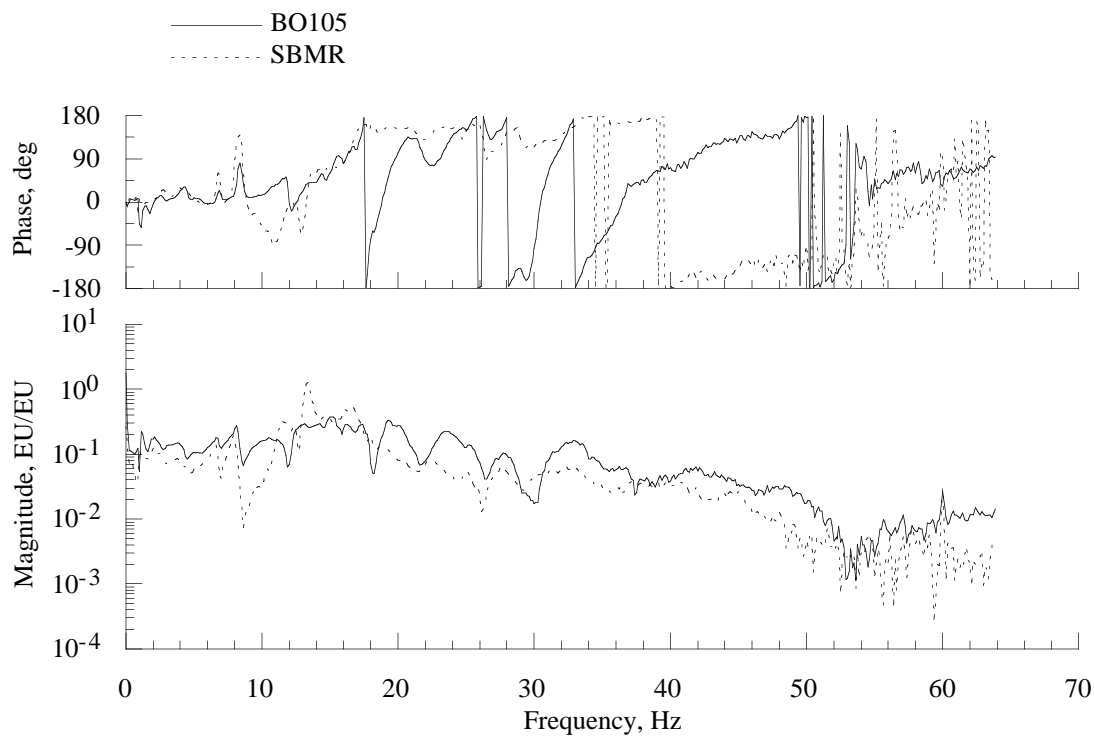


Figure 29(c). Effect of hub mass on the hub roll moment balance response due to hub axial force loading.

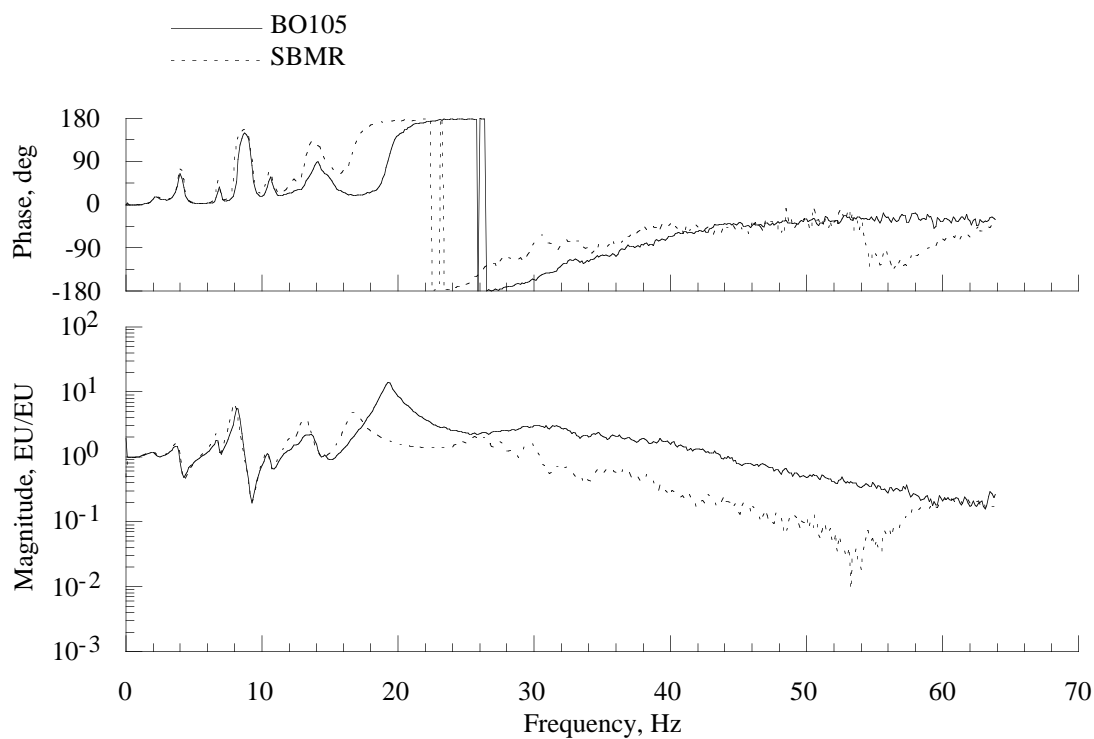


Figure 29(d). Effect of hub mass on the hub axial force balance response due to hub axial force loading.

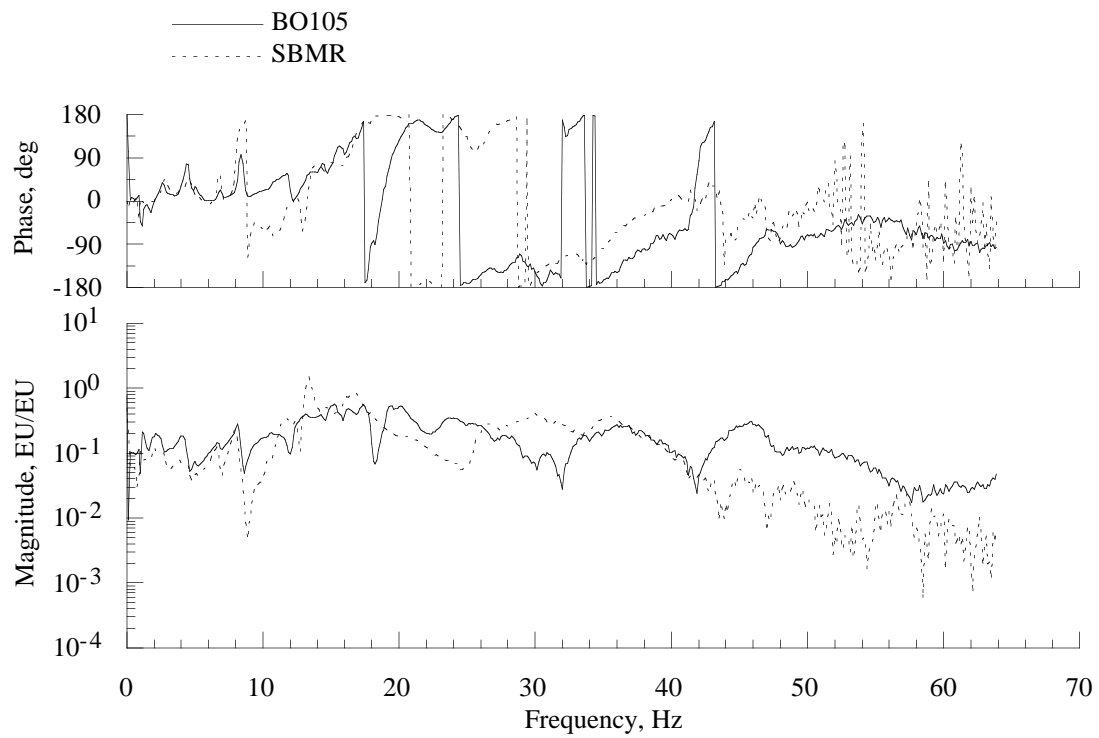


Figure 29(e). Effect of hub mass on the hub side force balance response due to hub axial force loading.

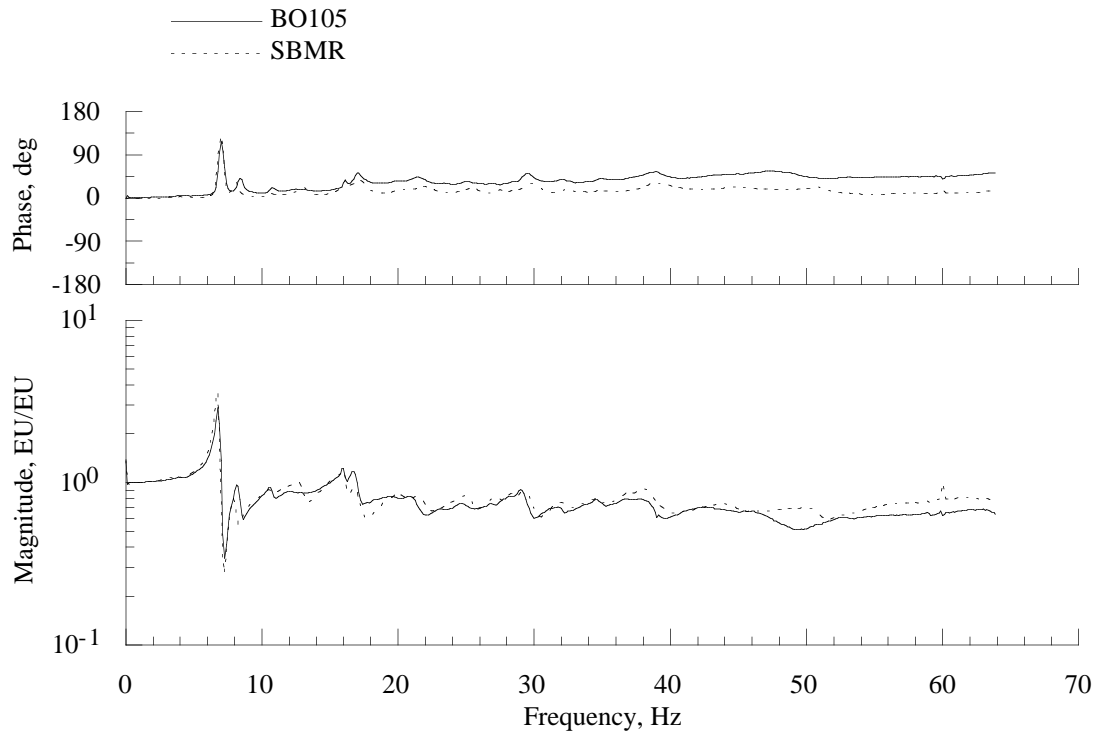


Figure 30(a). Effect of hub mass on the hub normal force balance response due to hub normal force loading.

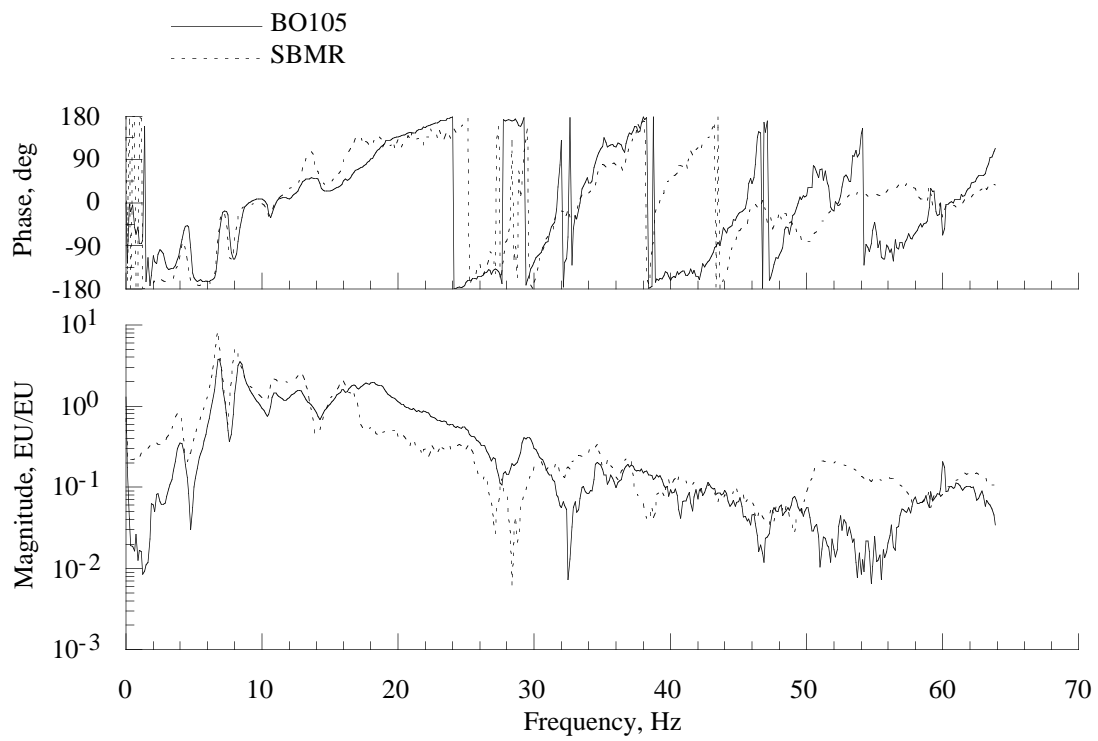


Figure 30(b). Effect of hub mass on the hub pitch moment balance response due to hub normal force loading.

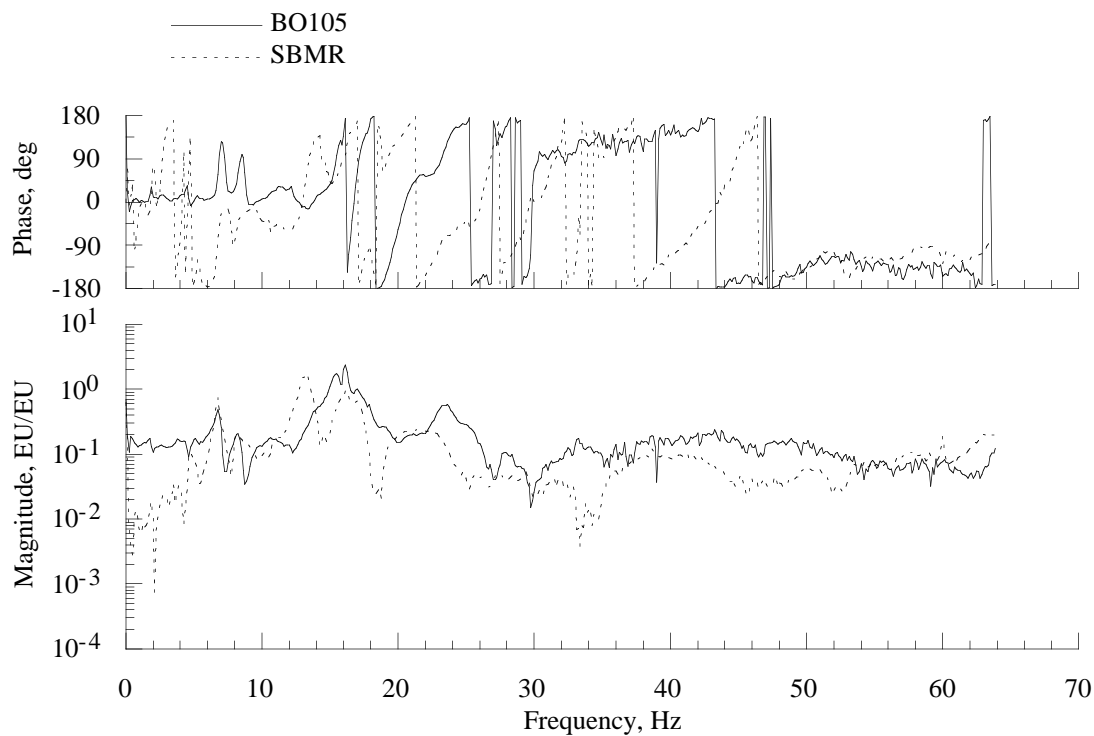


Figure 30(c). Effect of hub mass on the hub roll moment balance response due to hub normal force loading.

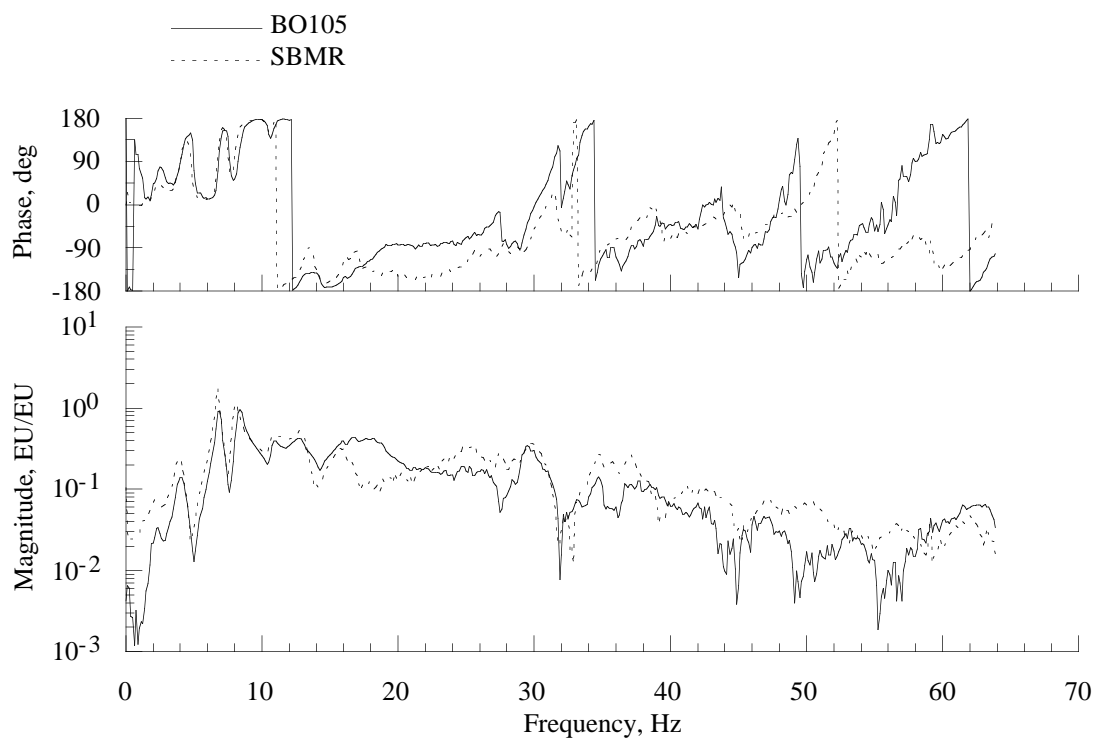


Figure 30(d). Effect of hub mass on the hub axial force balance response due to hub normal force loading.

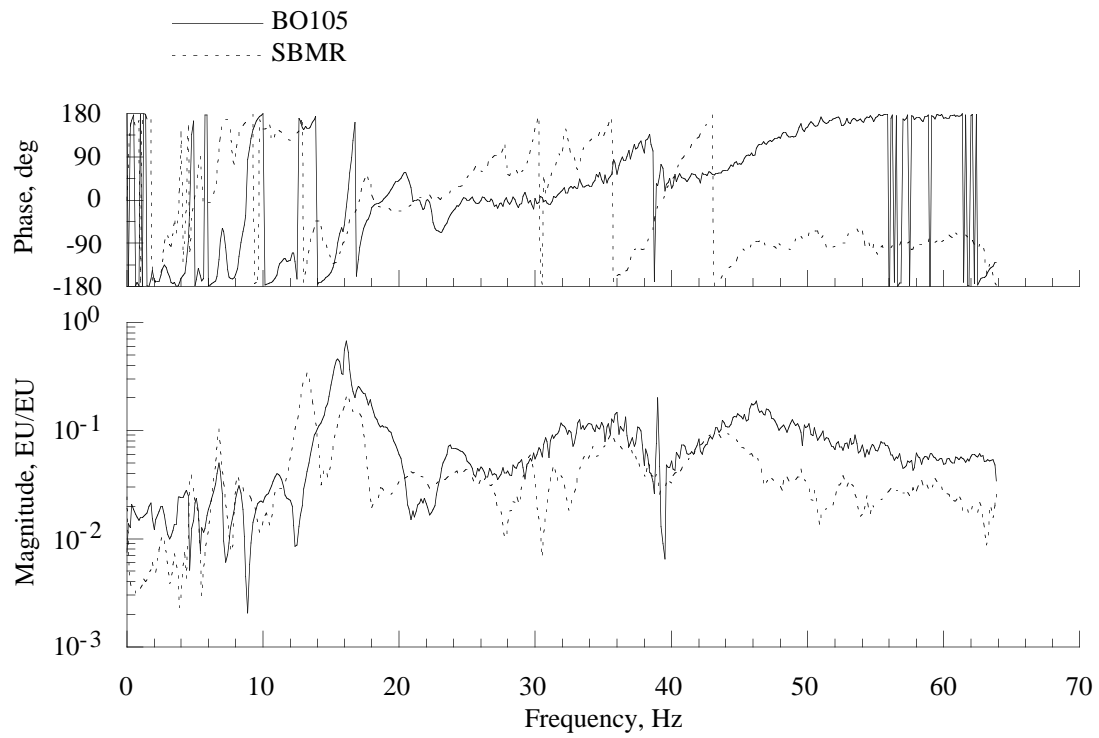


Figure 30(e). Effect of hub mass on the hub side force balance response due to hub normal force loading.

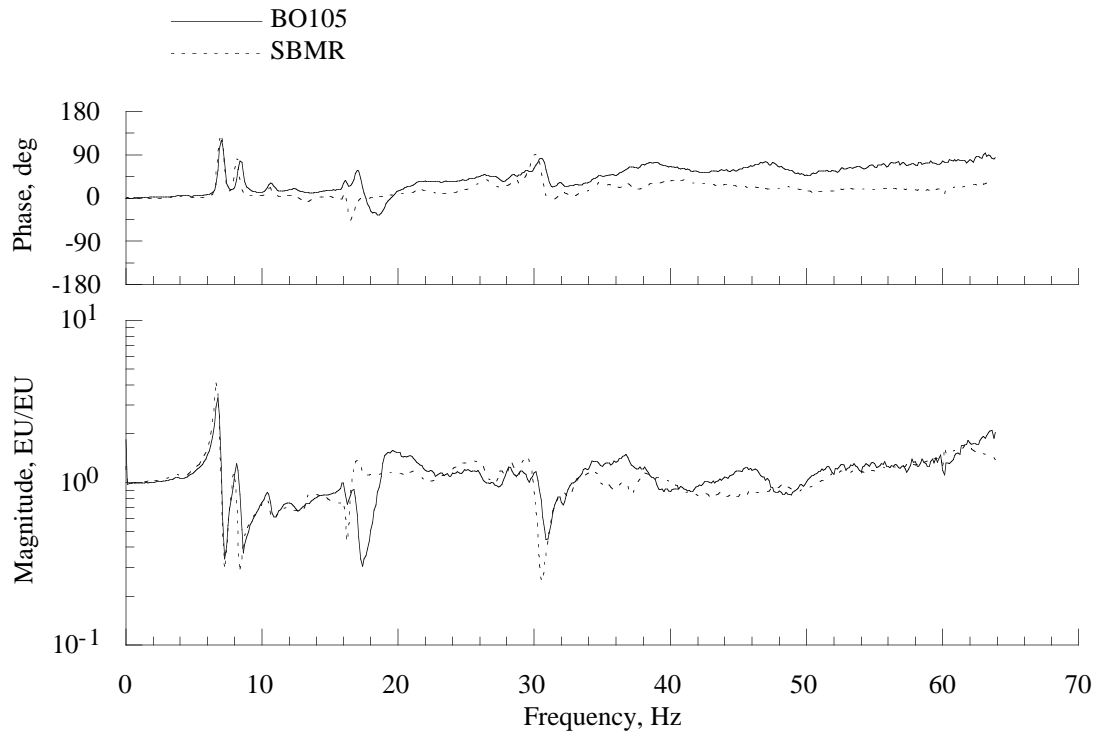


Figure 31(a). Effect of hub mass on the hub normal force balance response due to forward hub pitch moment loading.

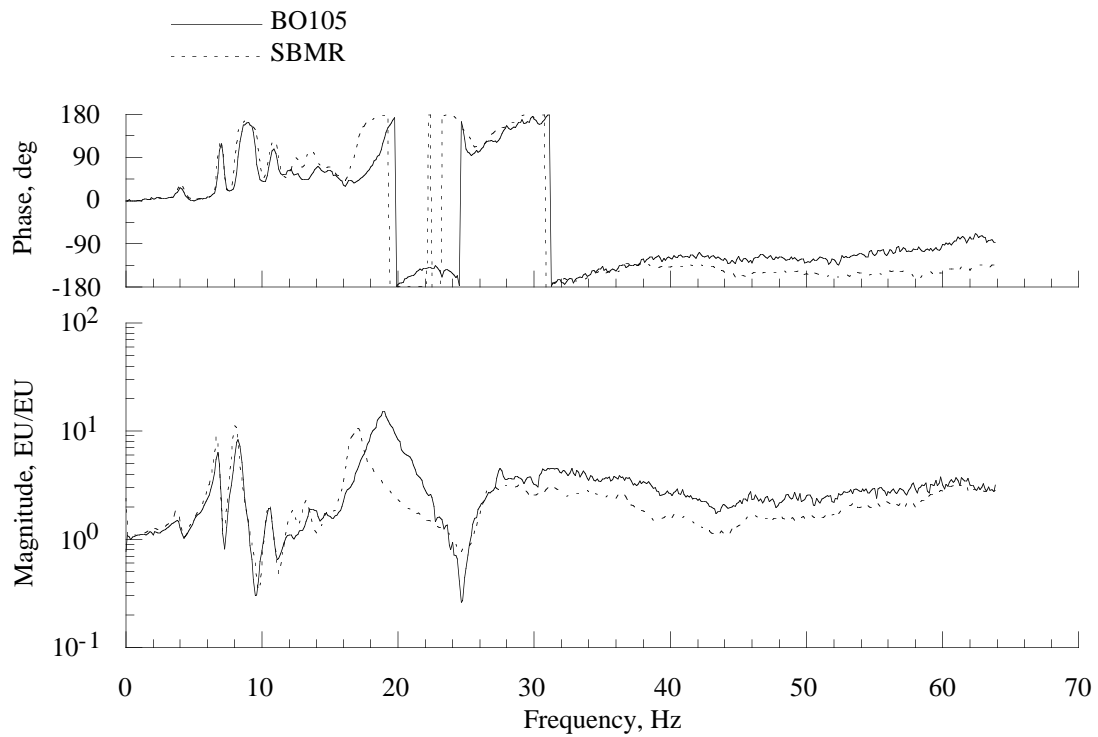


Figure 31(b). Effect of hub mass on the hub pitch moment balance response due to forward hub pitch moment loading.

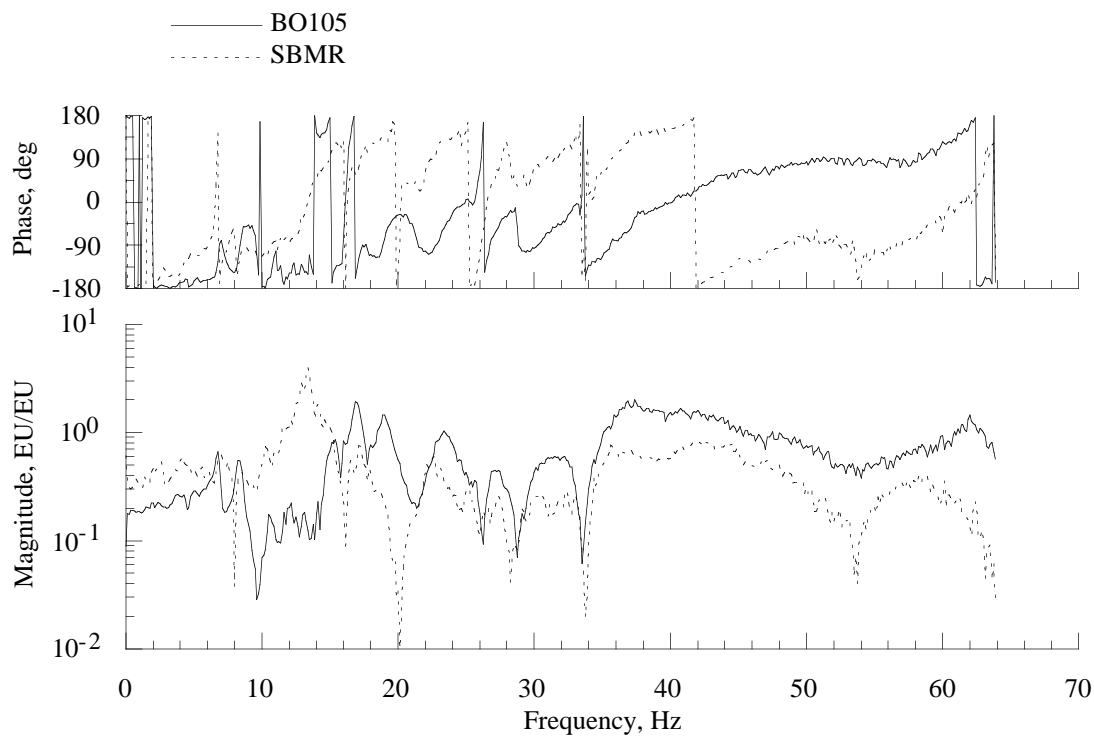


Figure 31(c). Effect of hub mass on the hub roll moment balance response due to forward hub pitch moment loading.

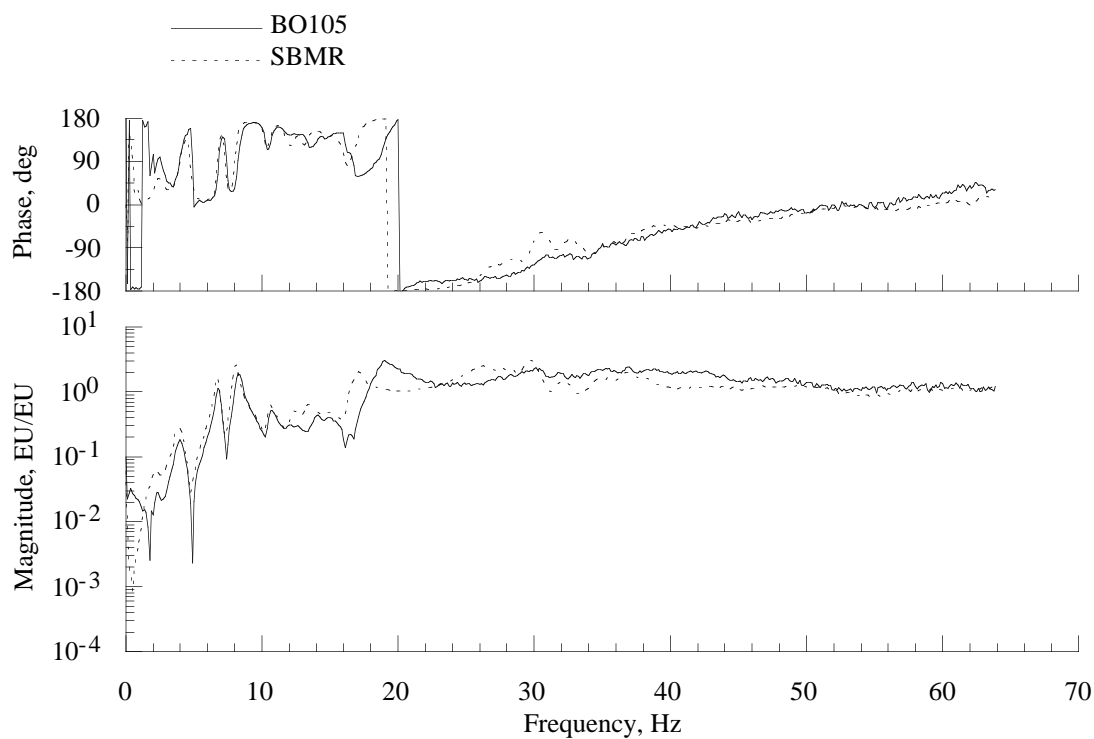


Figure 31(d). Effect of hub mass on the hub axial force balance response due to forward hub pitch moment loading.

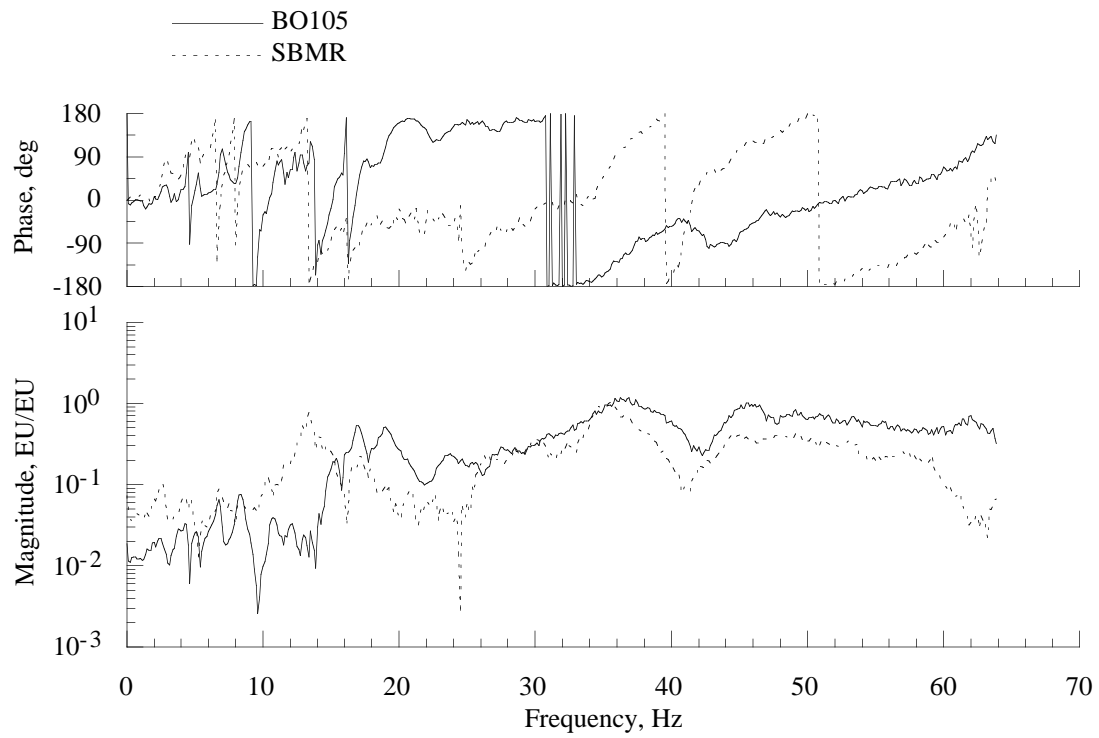


Figure 31(e). Effect of hub mass on the hub side force balance response due to forward hub pitch moment loading.

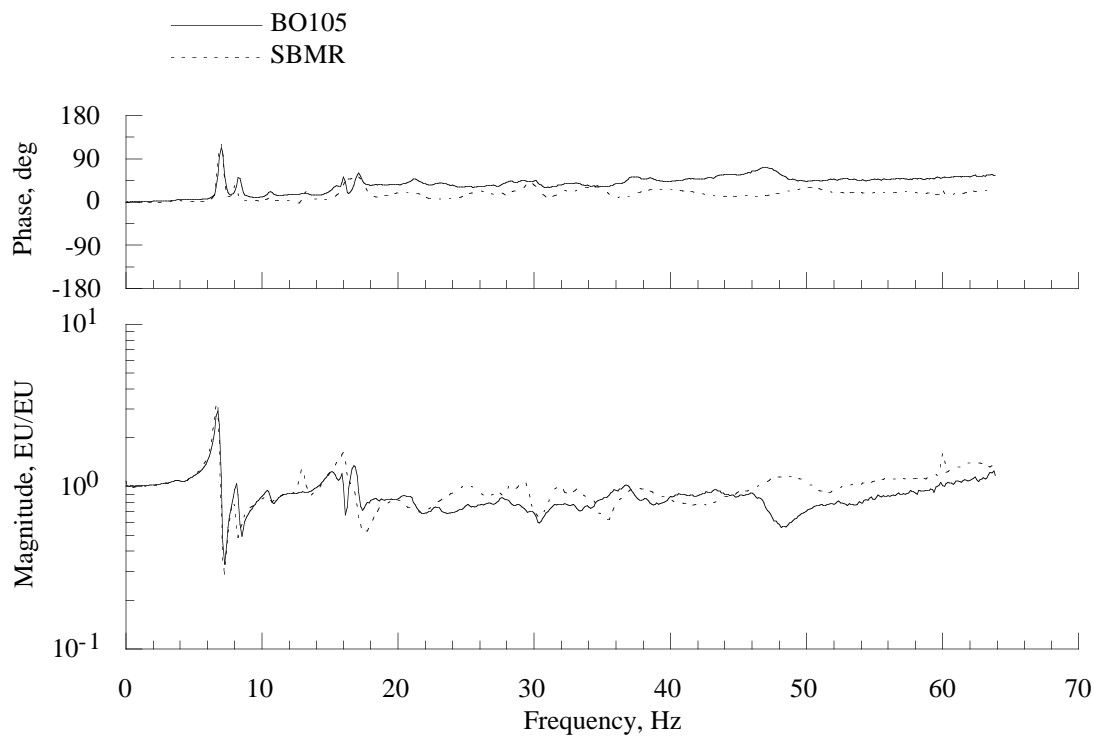


Figure 32(a). Effect of hub mass on the hub normal force balance response due to hub roll moment loading.

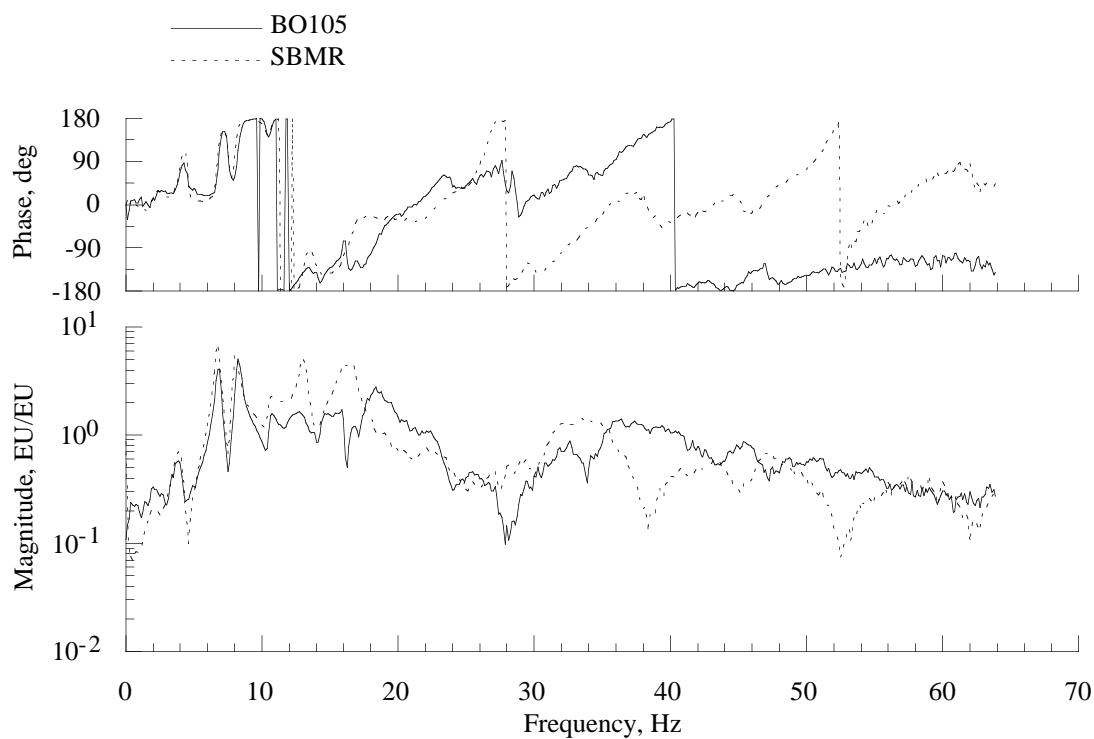


Figure 32(b). Effect of hub mass on the hub pitch moment balance response due to hub roll moment loading.

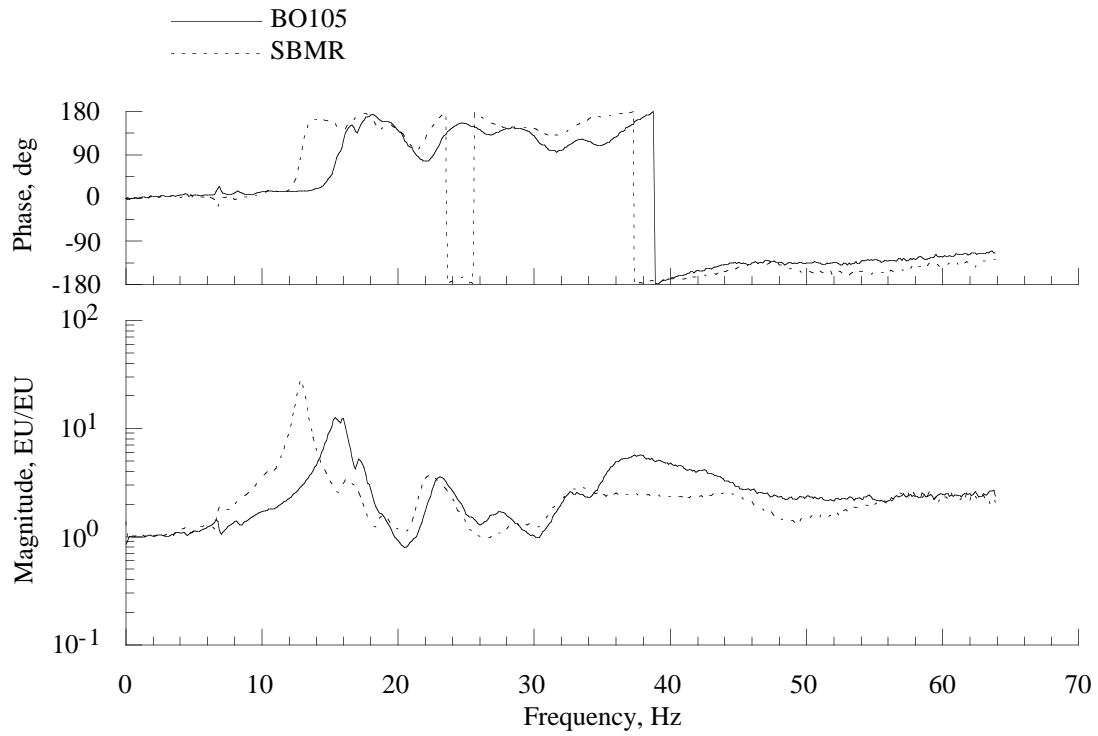


Figure 32(c). Effect of hub mass on the hub roll moment balance response due to hub roll moment loading.

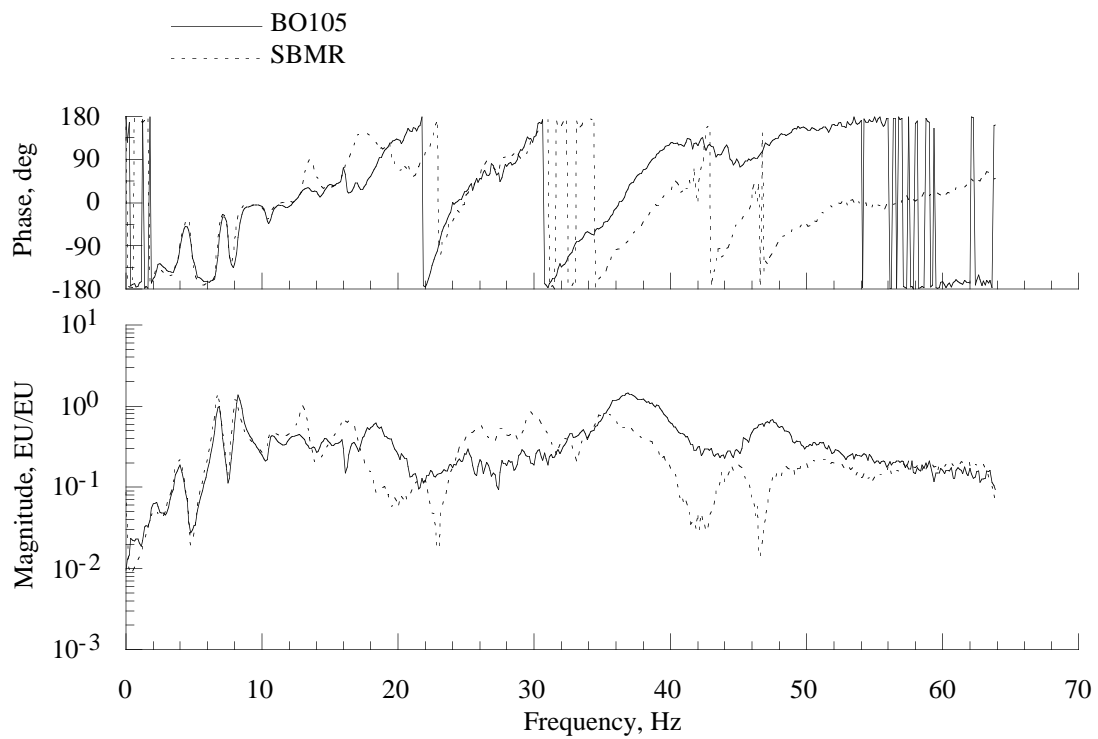


Figure 32(d). Effect of hub mass on the hub axial force balance response due to hub roll moment loading.

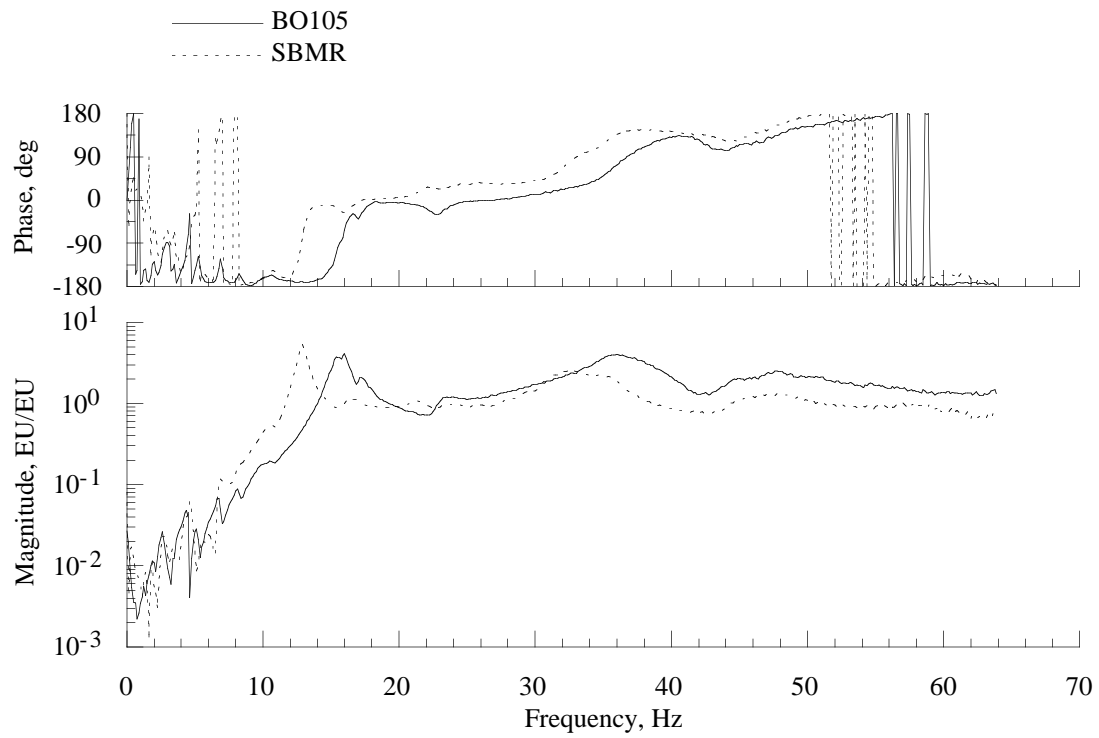


Figure 32(e). Effect of hub mass on the hub side force balance response due to hub roll moment loading.

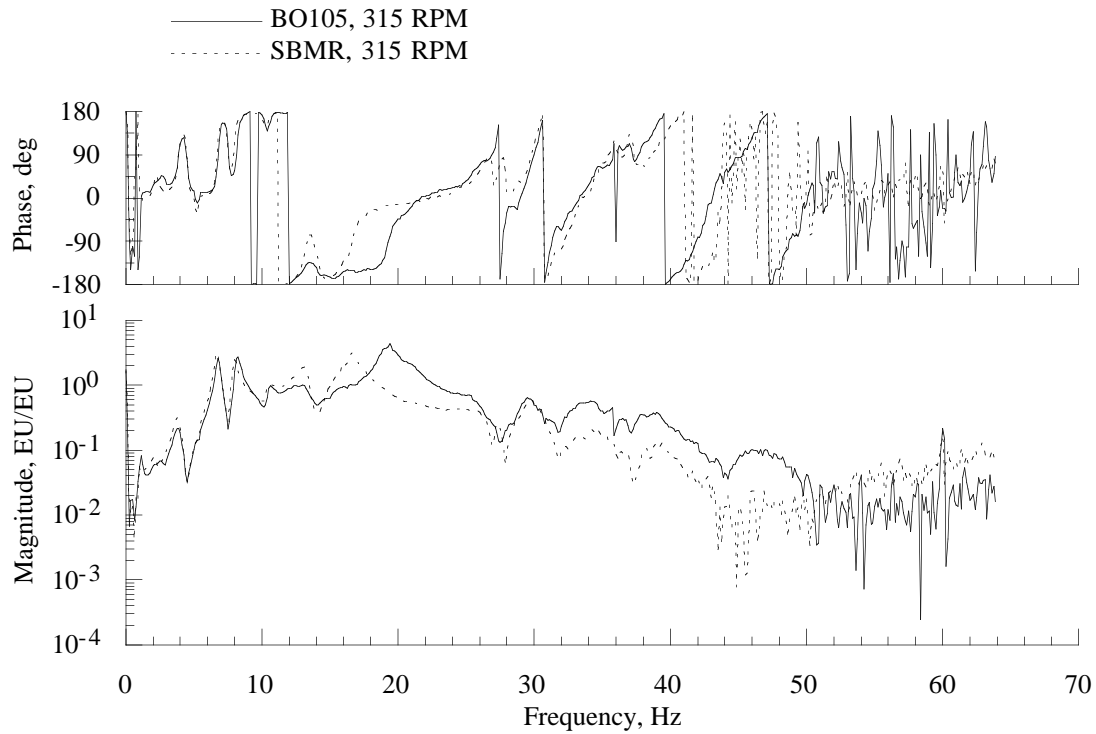


Figure 33(a). Comparison of hub mass variation with shaft rotation on the hub normal force balance response due to hub axial force loading.

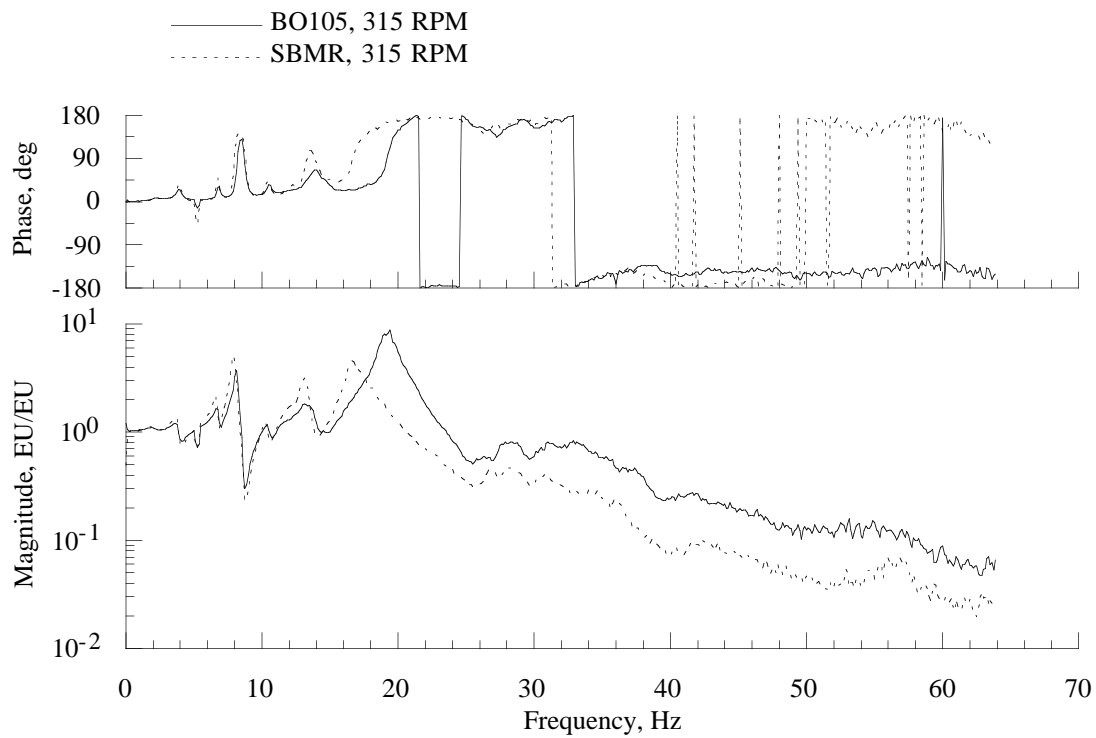


Figure 33(b). Comparison of hub mass variation with shaft rotation on the hub pitch moment balance response due to hub axial force loading.

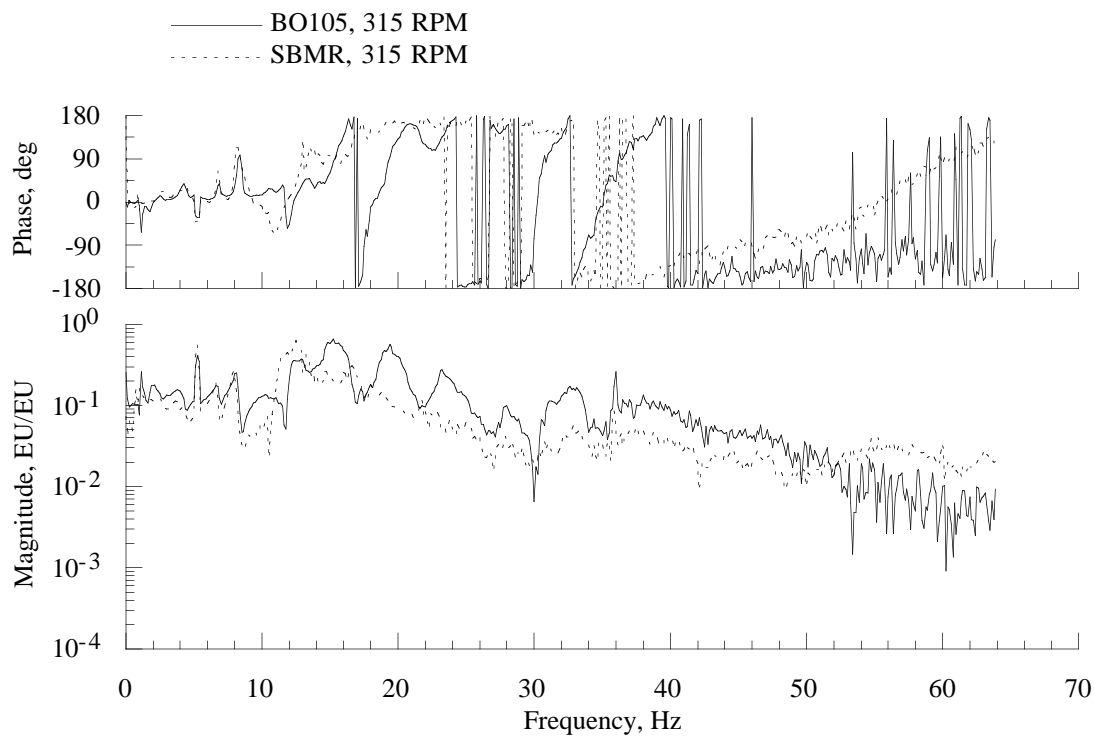


Figure 33(c). Comparison of hub mass variation with shaft rotation on the hub roll moment balance response due to hub axial force loading.

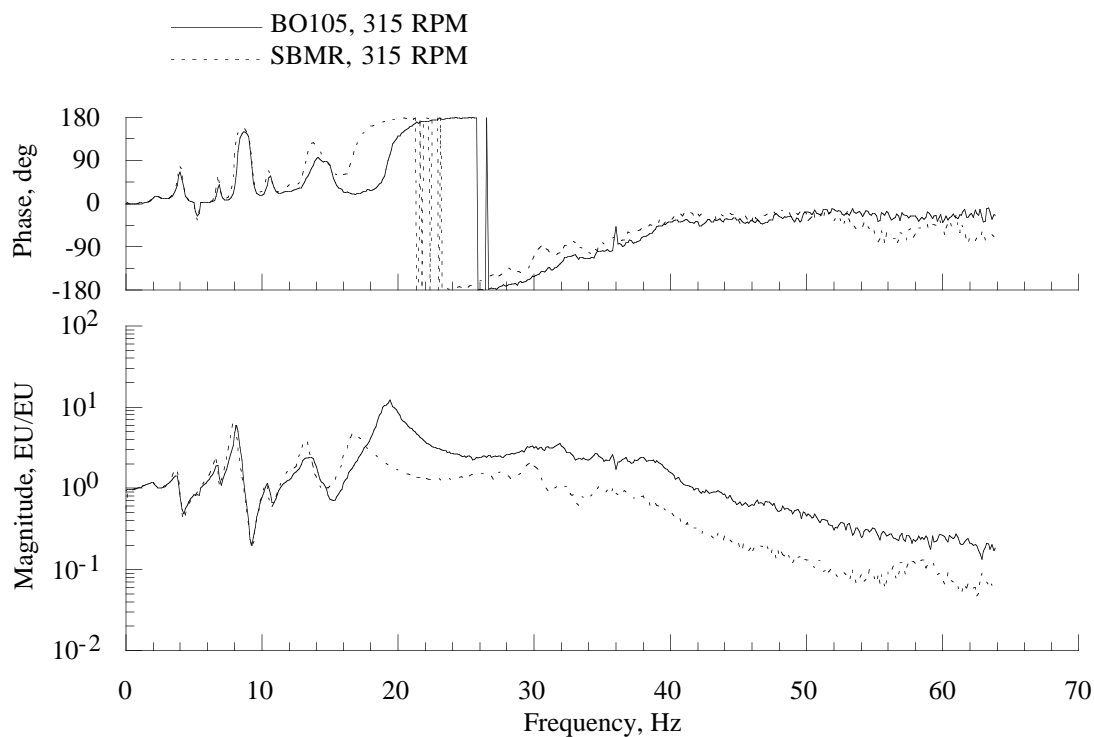


Figure 33(d). Comparison of hub mass variation with shaft rotation on the hub axial force balance response due to hub axial force loading.

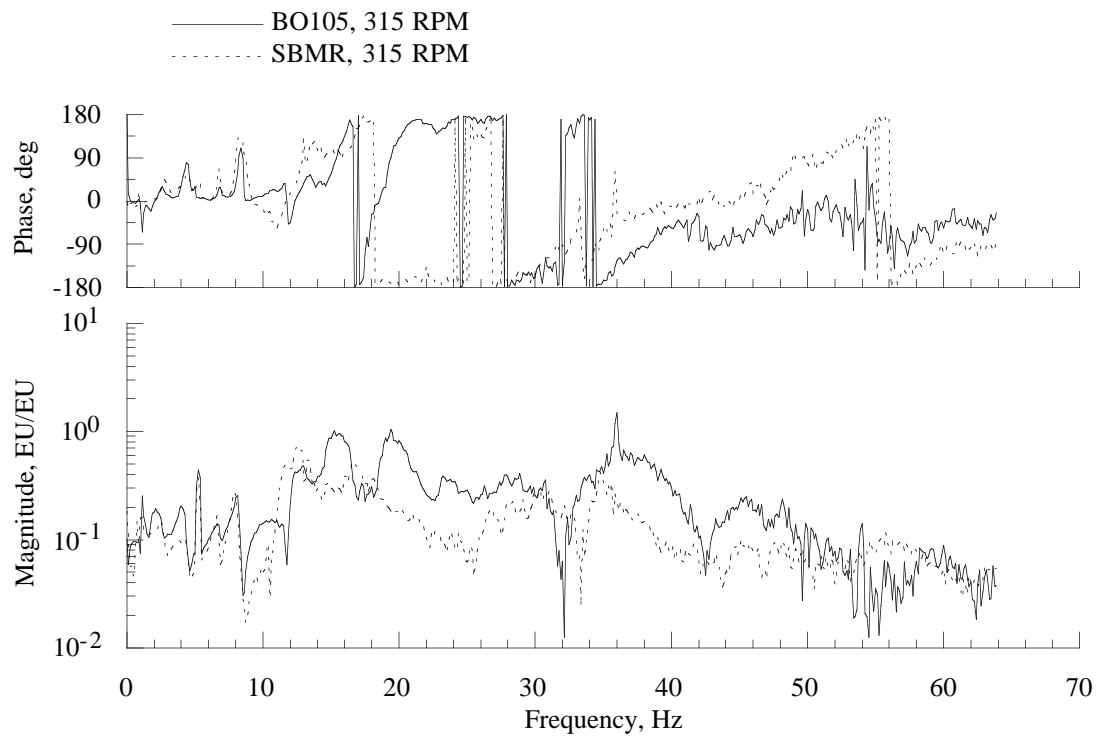


Figure 33(e). Comparison of hub mass variation with shaft rotation on the hub side force balance response due to hub axial force loading.

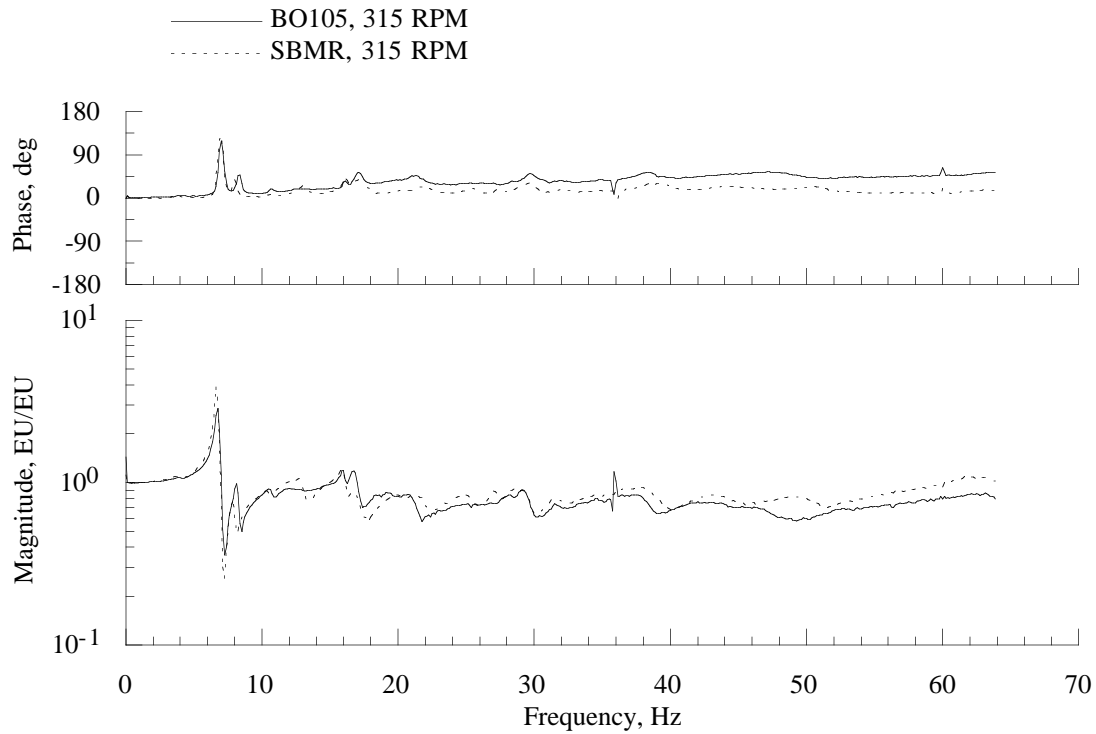


Figure 34(a). Comparison of hub mass variation with shaft rotation on the hub normal force balance response due to hub normal force loading.

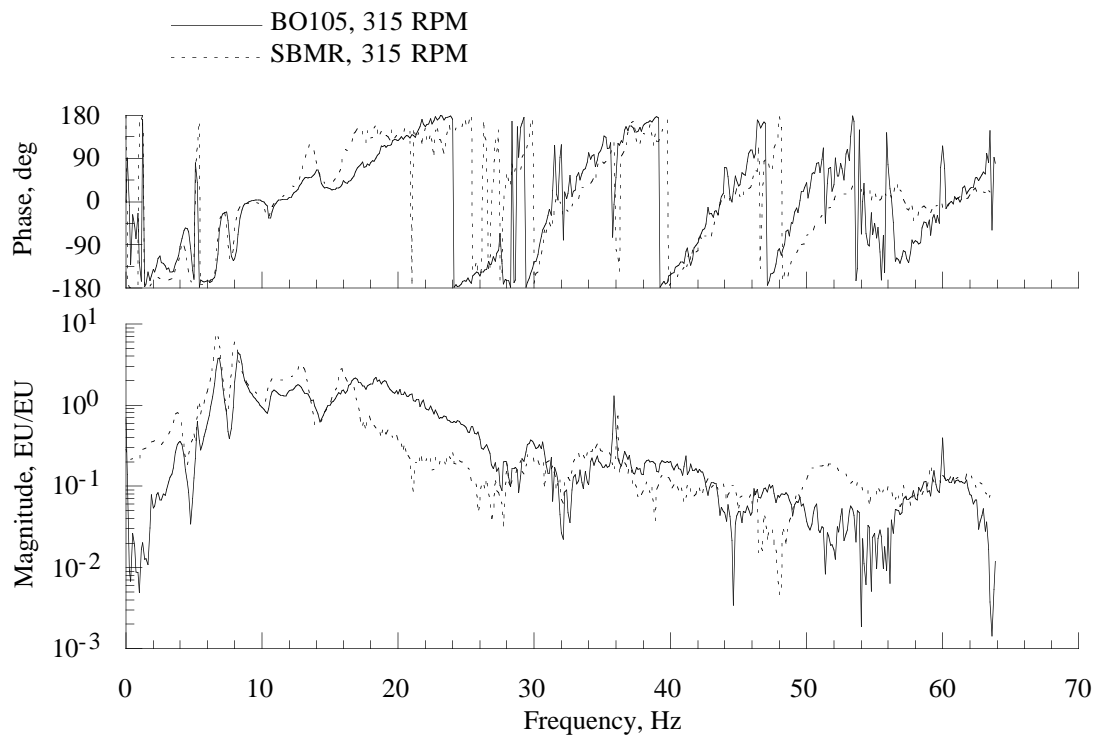


Figure 34(b). Comparison of hub mass variation with shaft rotation on the hub pitch moment balance response due to hub normal force loading.

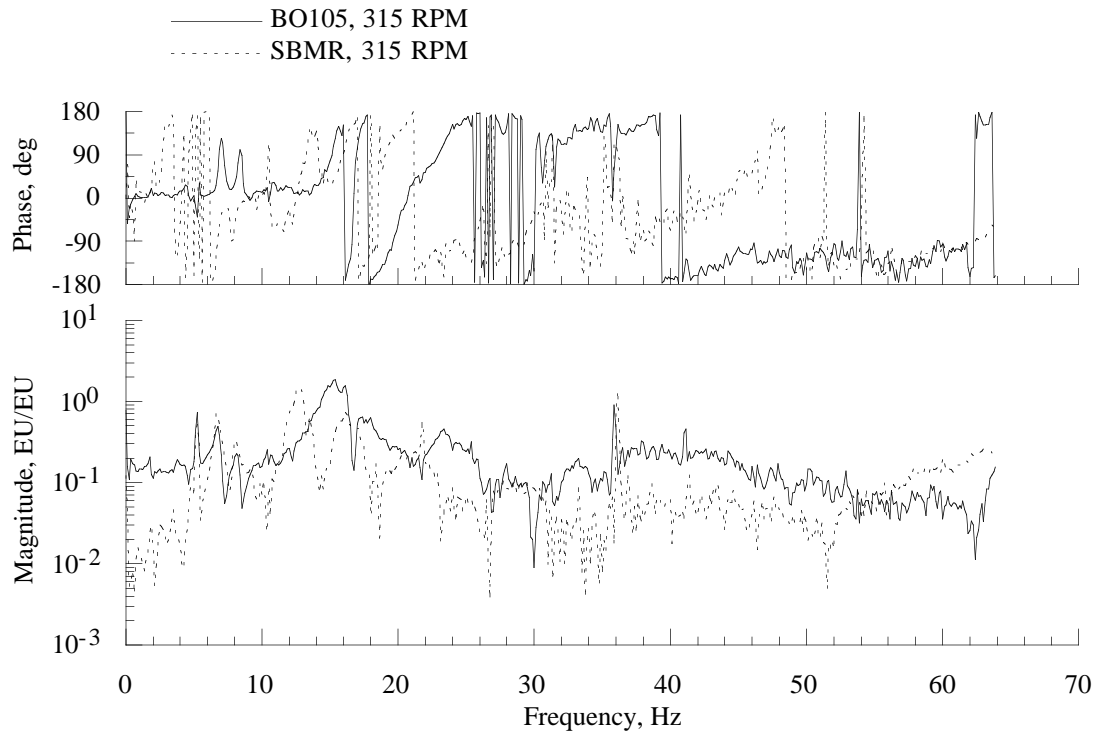


Figure 34(c). Comparison of hub mass variation with shaft rotation on the hub roll moment balance response due to hub normal force loading.

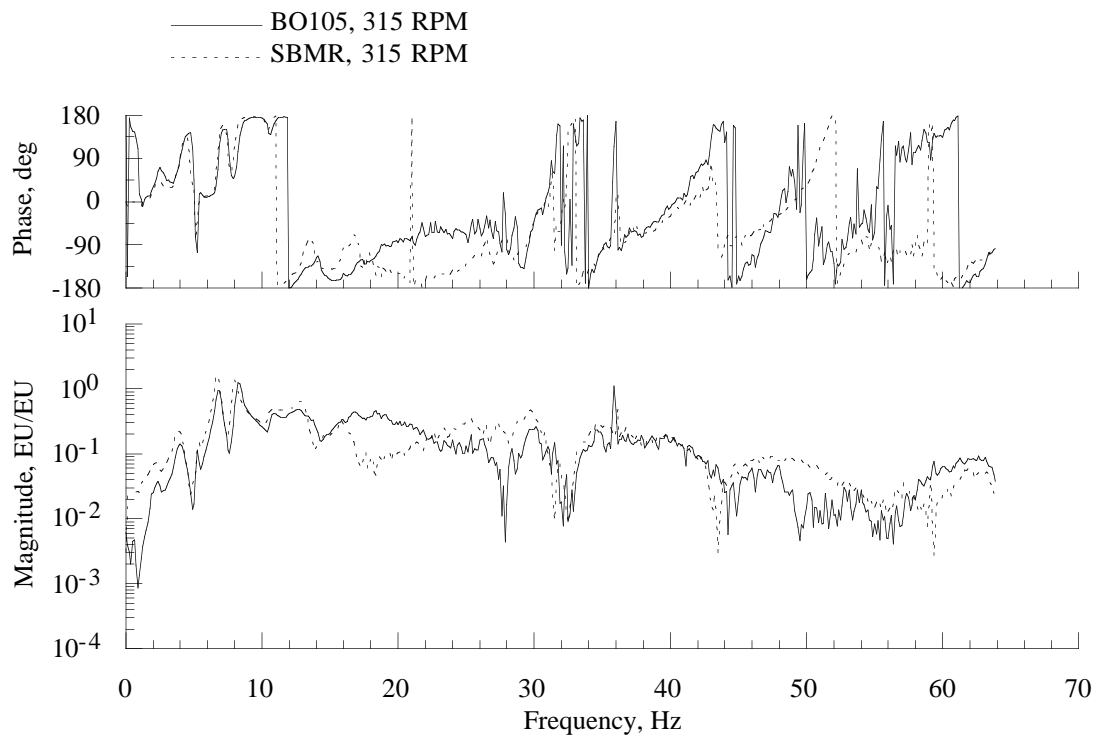


Figure 34(d). Comparison of hub mass variation with shaft rotation on the hub axial force balance response due to hub normal force loading.

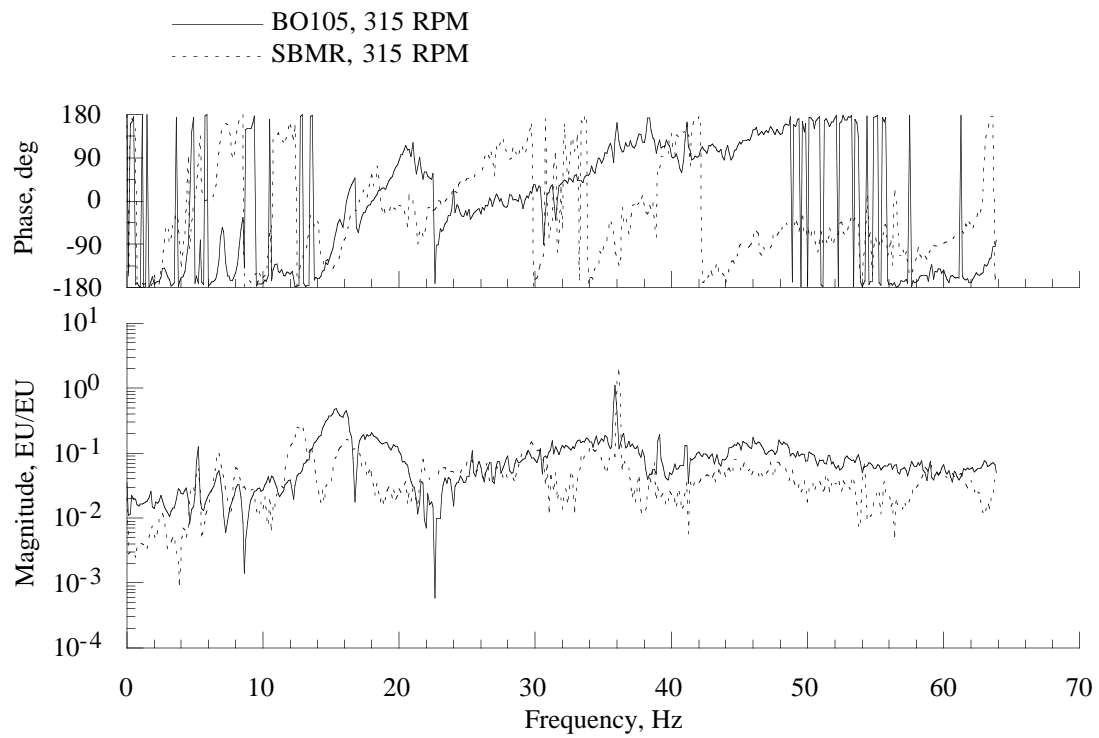


Figure 34(e). Comparison of hub mass variation with shaft rotation on the hub side force balance response due to hub normal force loading.

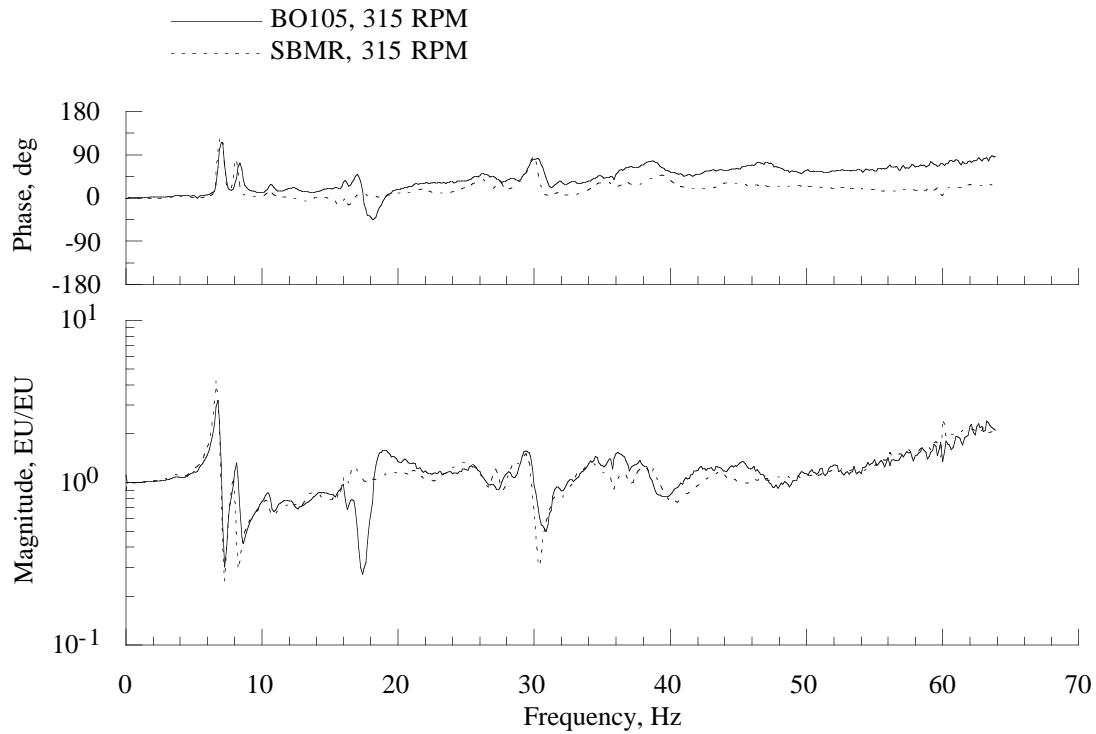


Figure 35(a). Comparison of hub mass variation with shaft rotation on the hub normal force balance response due to forward hub pitch moment loading.

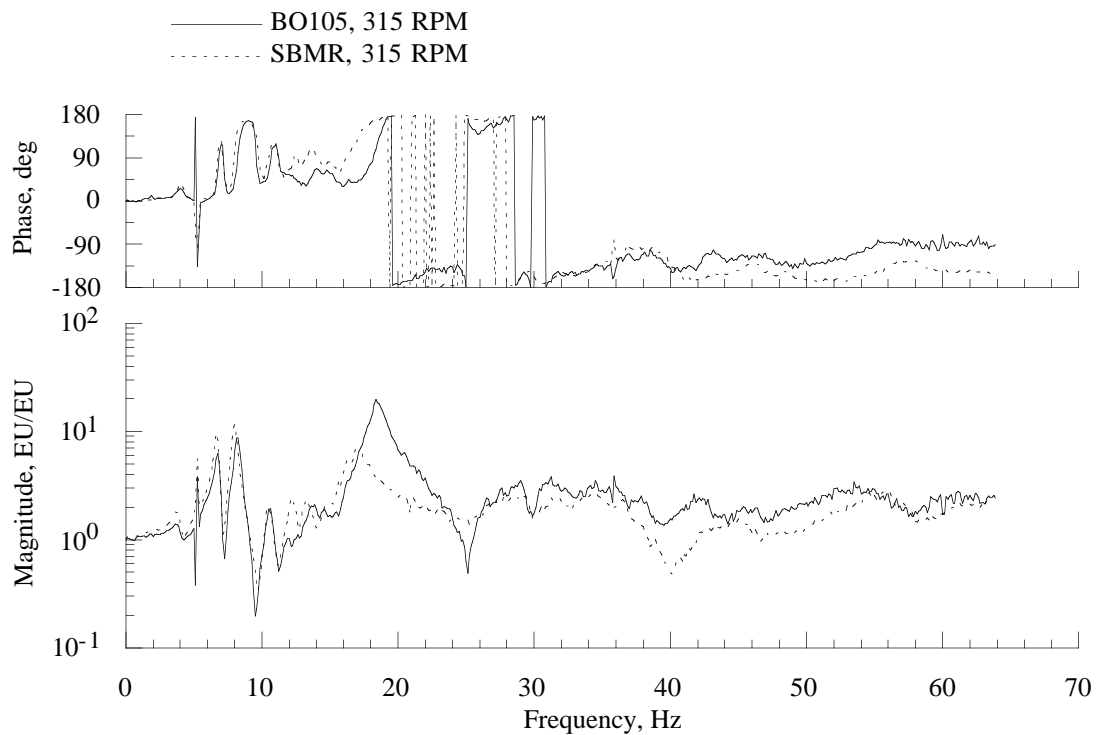


Figure 35(b). Comparison of hub mass variation with shaft rotation on the hub pitch moment balance response due to forward hub pitch moment loading.

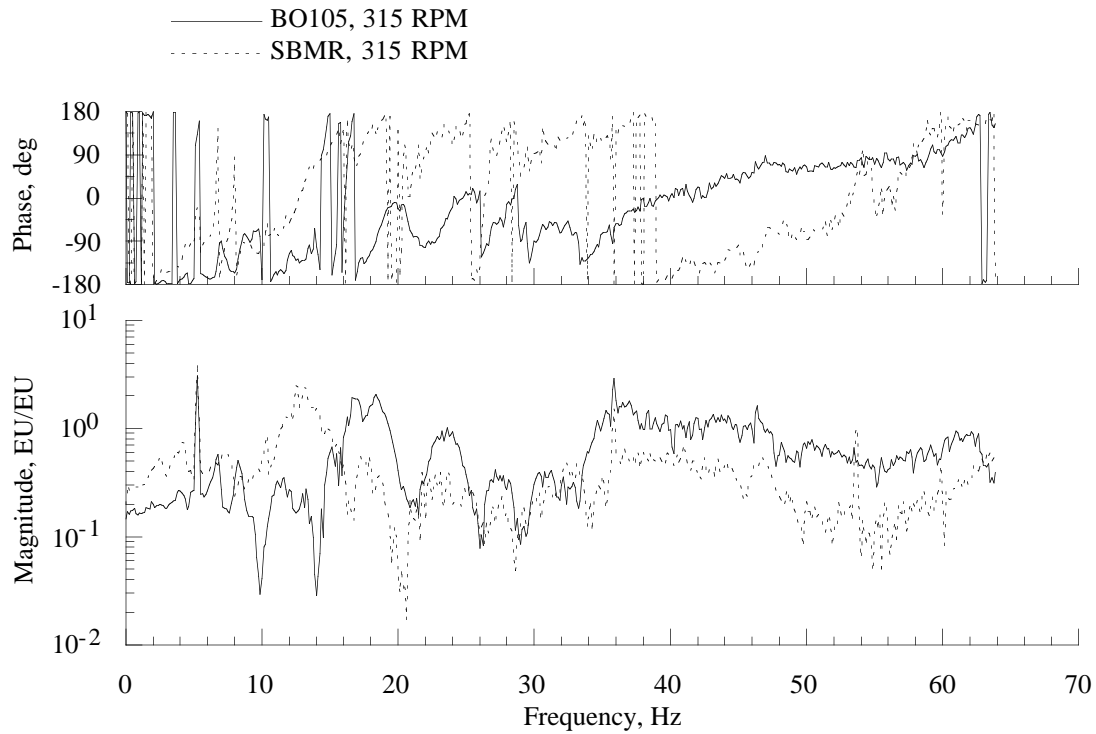


Figure 35(c). Comparison of hub mass variation with shaft rotation on the hub roll moment balance response due to forward hub pitch moment loading.

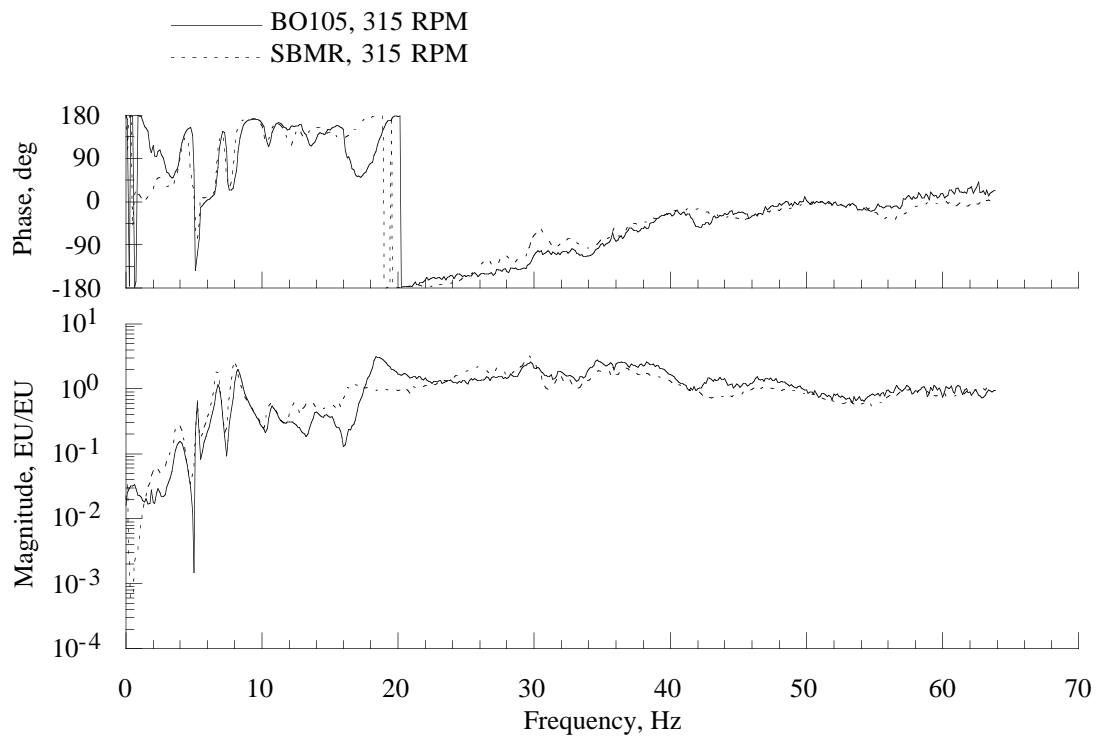


Figure 35(d). Comparison of hub mass variation with shaft rotation on the hub axial force balance response due to forward hub pitch moment loading.

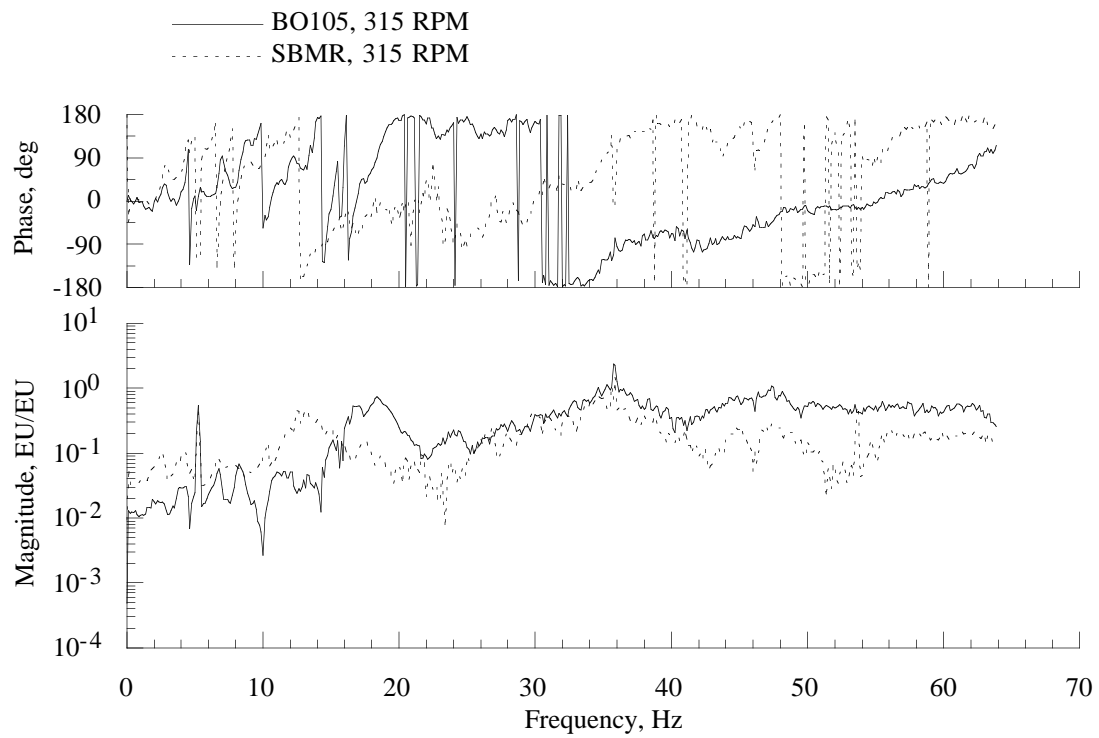


Figure 35(e). Comparison of hub mass variation with shaft rotation on the hub side force balance response due to forward hub pitch moment loading.

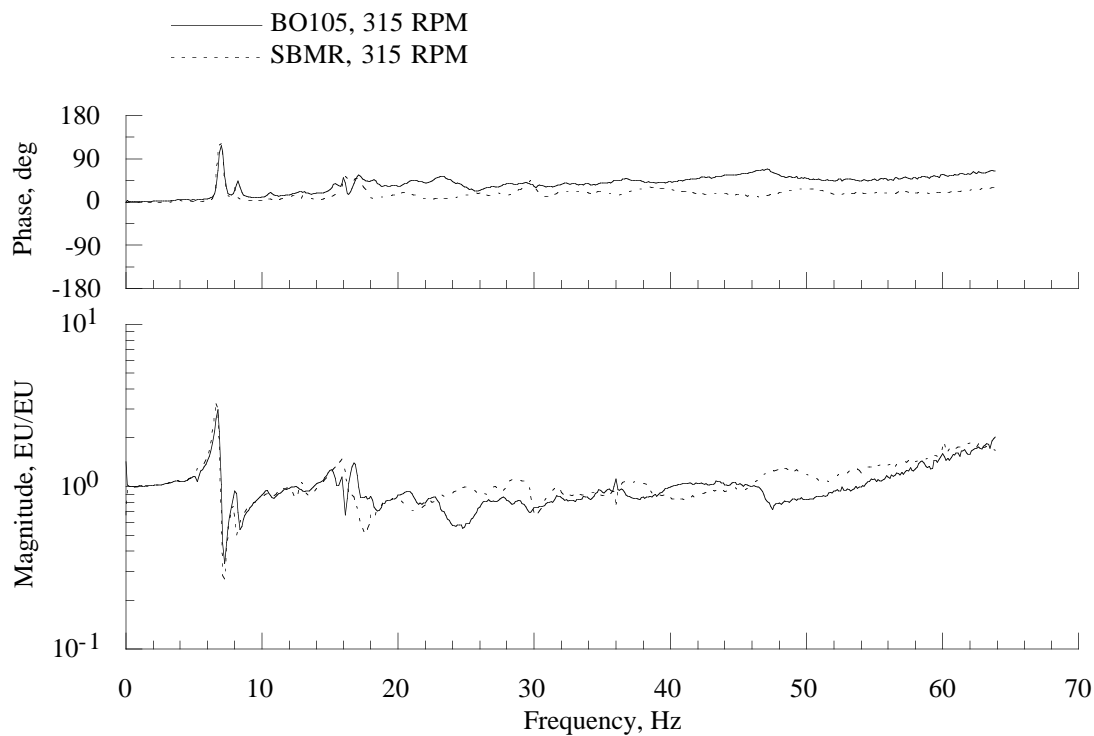


Figure 36(a). Comparison of hub mass variation with shaft rotation on the hub normal force balance response due to hub roll moment loading.

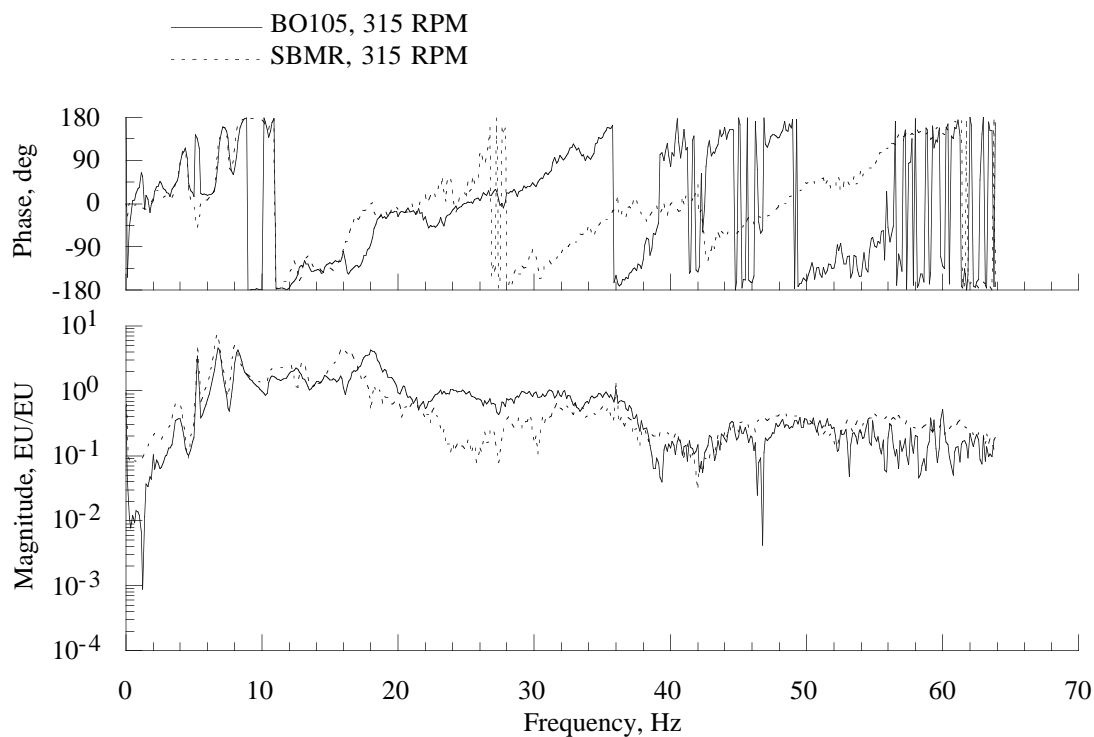


Figure 36(b). Comparison of hub mass variation with shaft rotation on the hub pitch moment balance response due to hub roll moment loading.

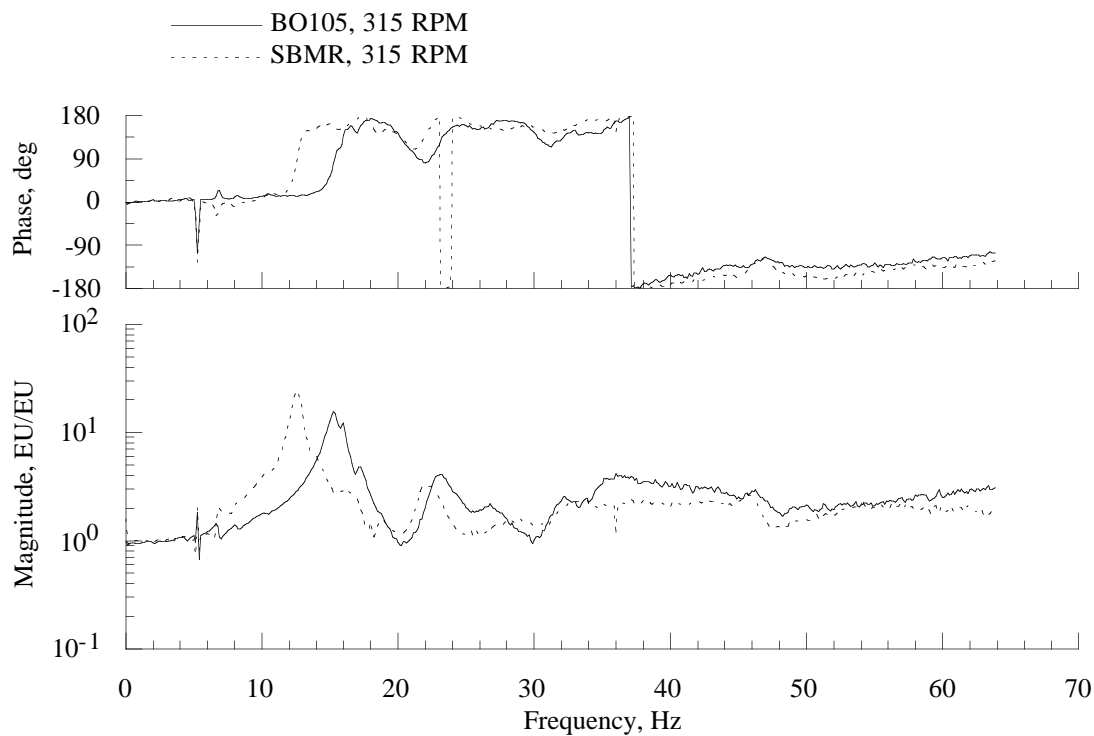


Figure 36(c). Comparison of hub mass variation with shaft rotation on the hub roll moment balance response due to hub roll moment loading.

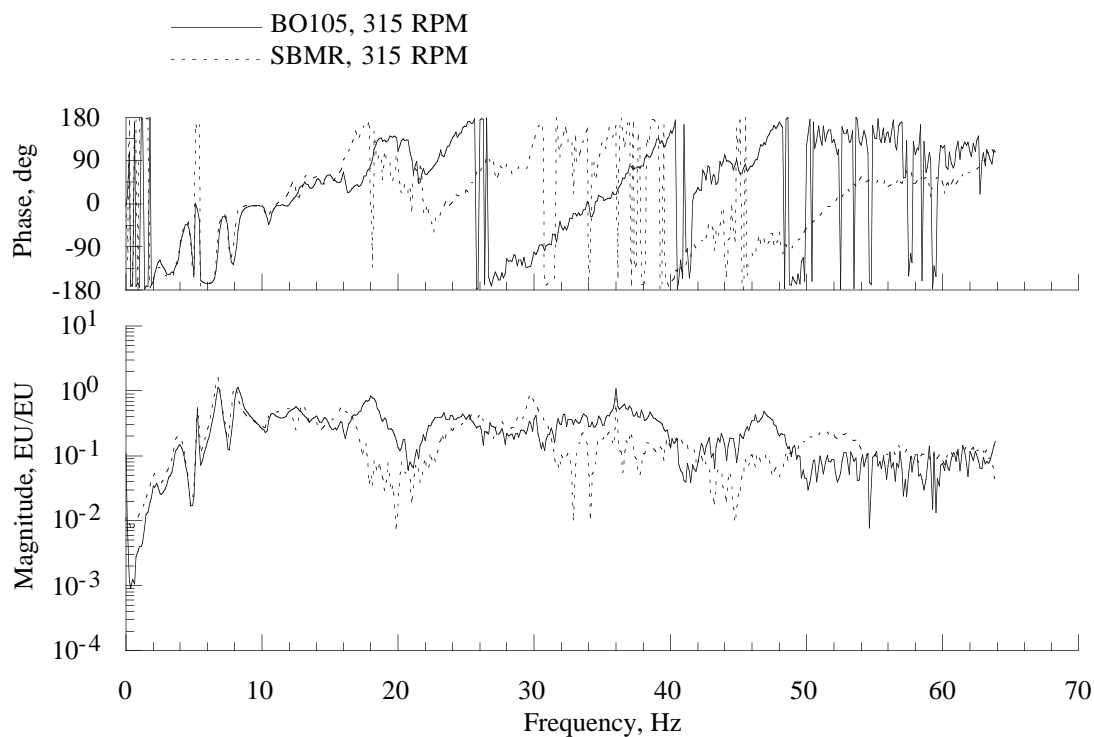


Figure 36(d). Comparison of hub mass variation with shaft rotation on the hub axial force balance response due to hub roll moment loading.

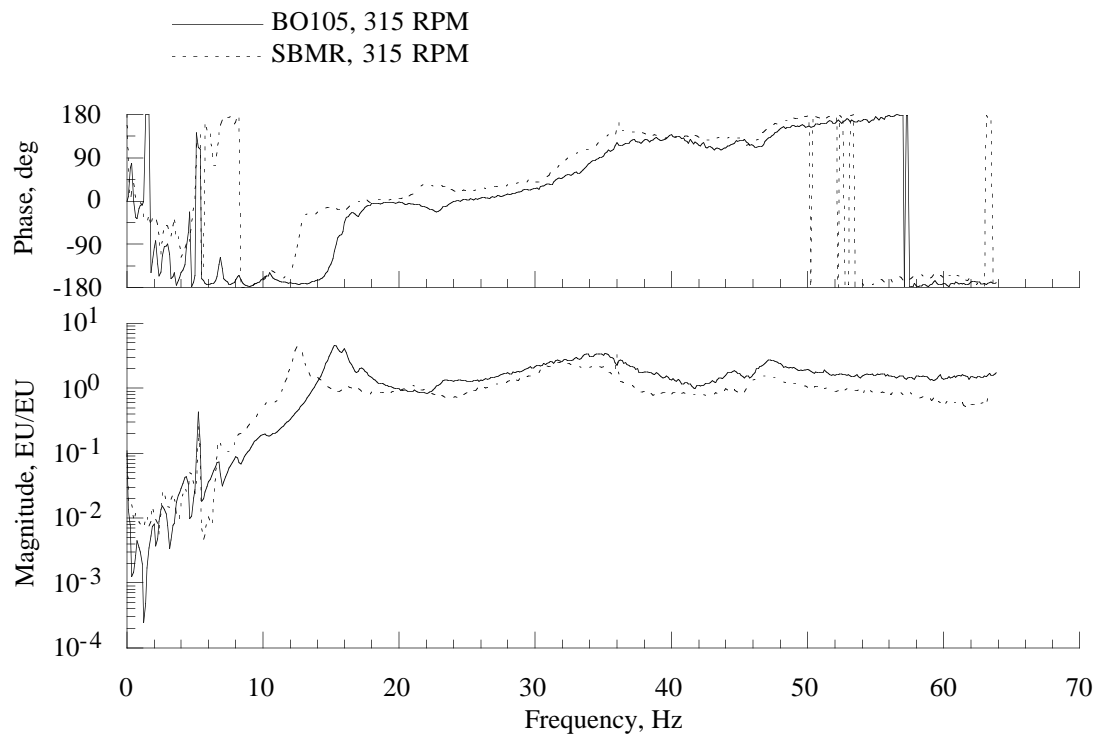


Figure 36(e). Comparison of hub mass variation with shaft rotation on the hub side force balance response due to hub roll moment loading.

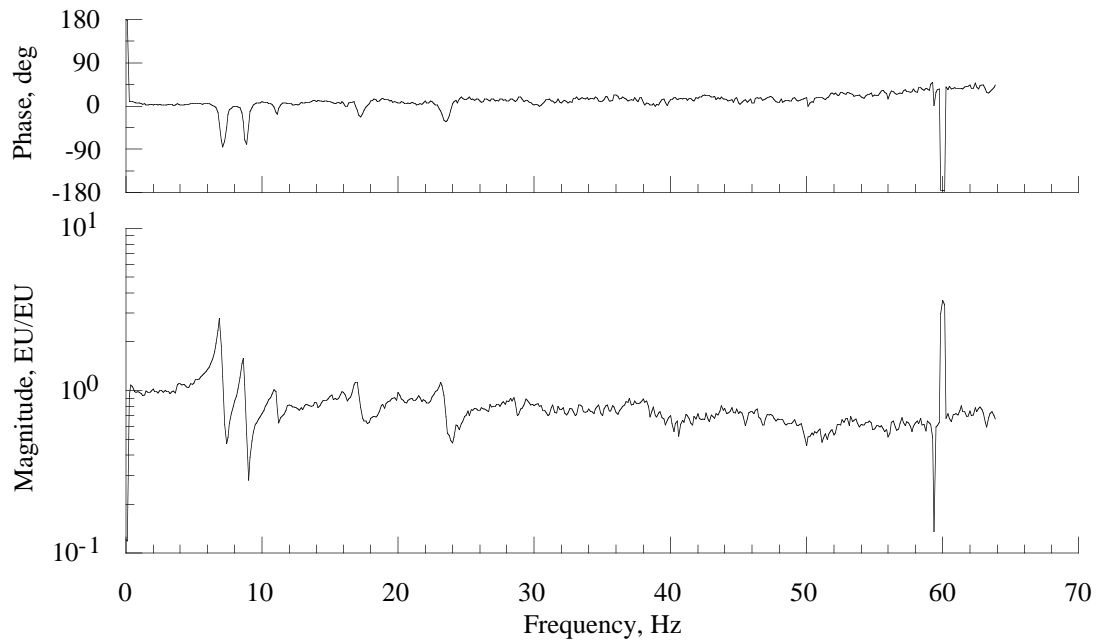


Figure 37(a). Hub normal force balance response due to push rod number 1 loading.

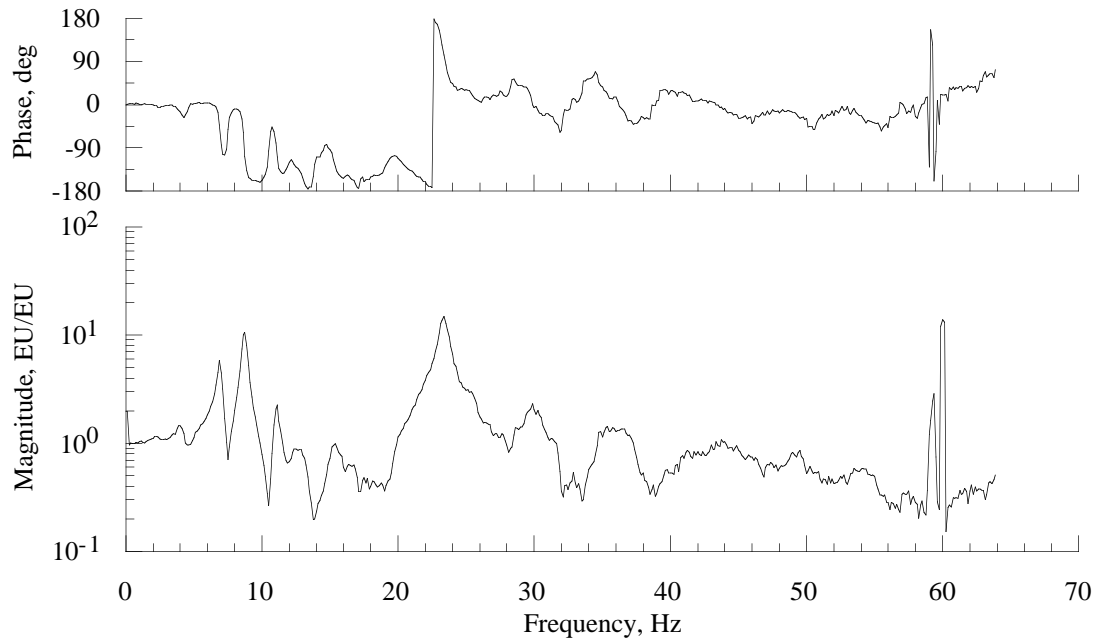


Figure 37(b). Hub pitch moment balance response due to push rod number 1 loading.

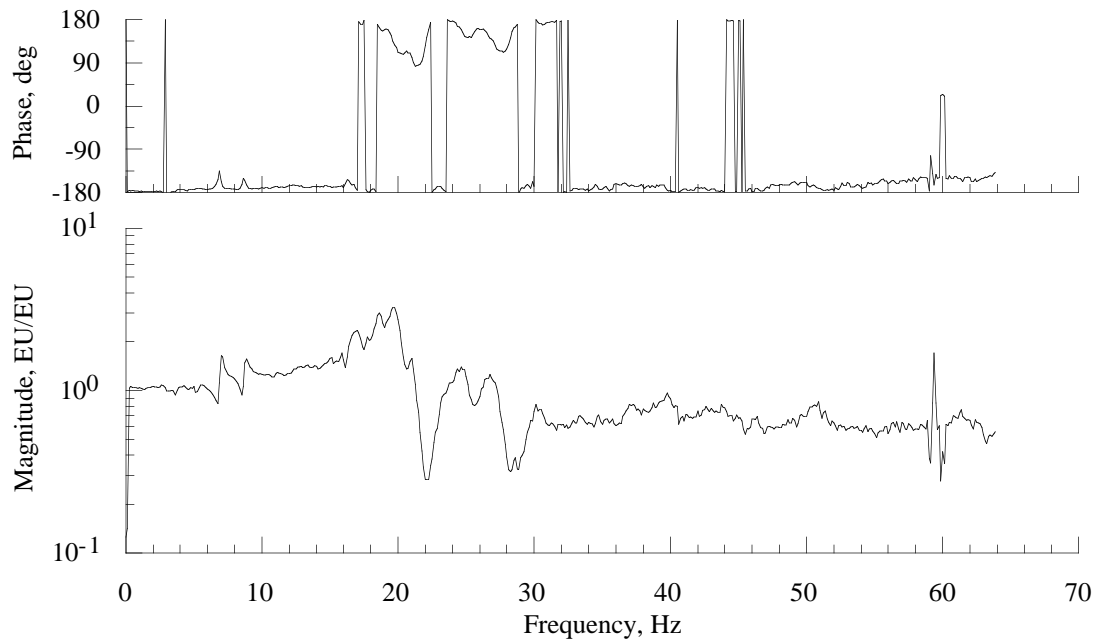


Figure 37(c). Hub roll moment balance response due to push rod number 1 loading.

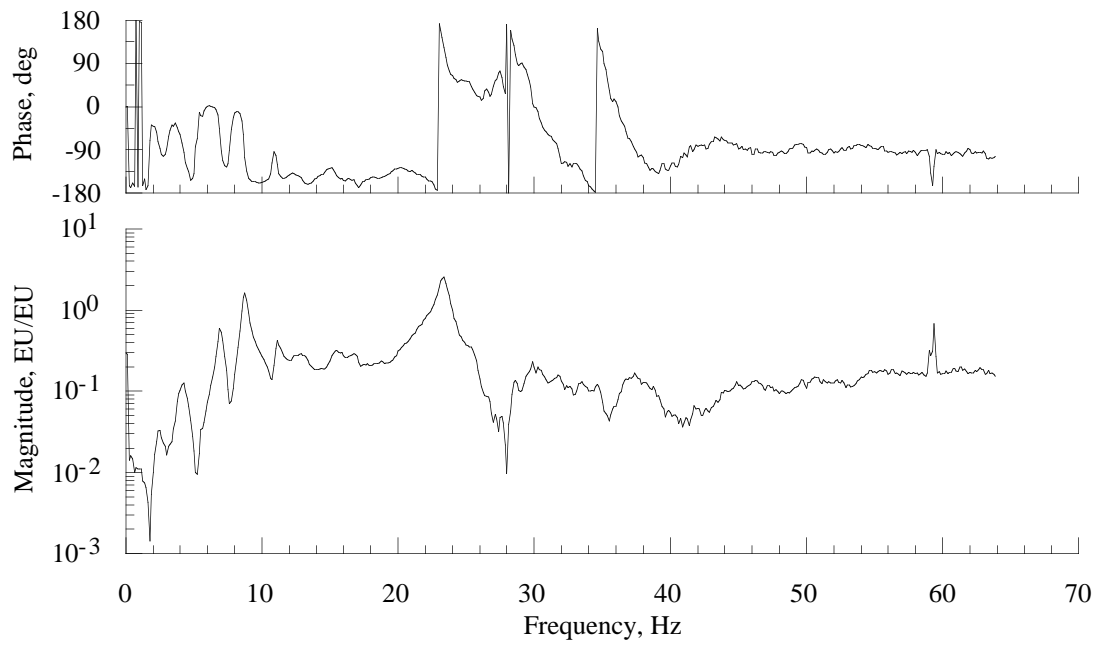


Figure 37(d). Hub axial force balance response due to push rod number 1 loading.

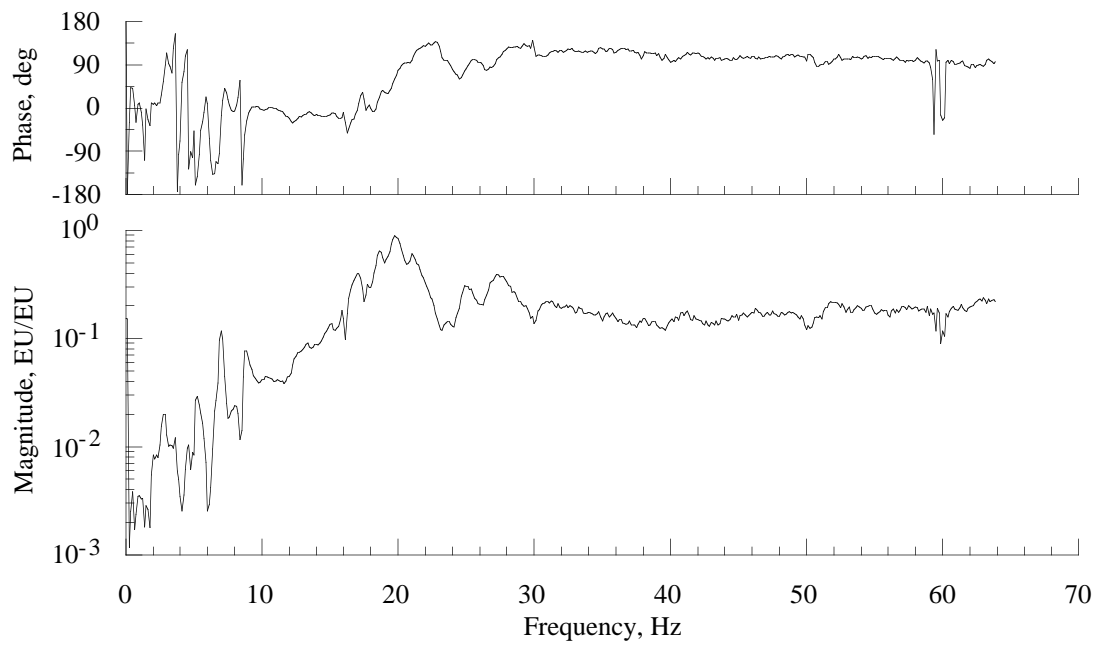


Figure 37(e). Hub side force balance response due to push rod number 1 loading.

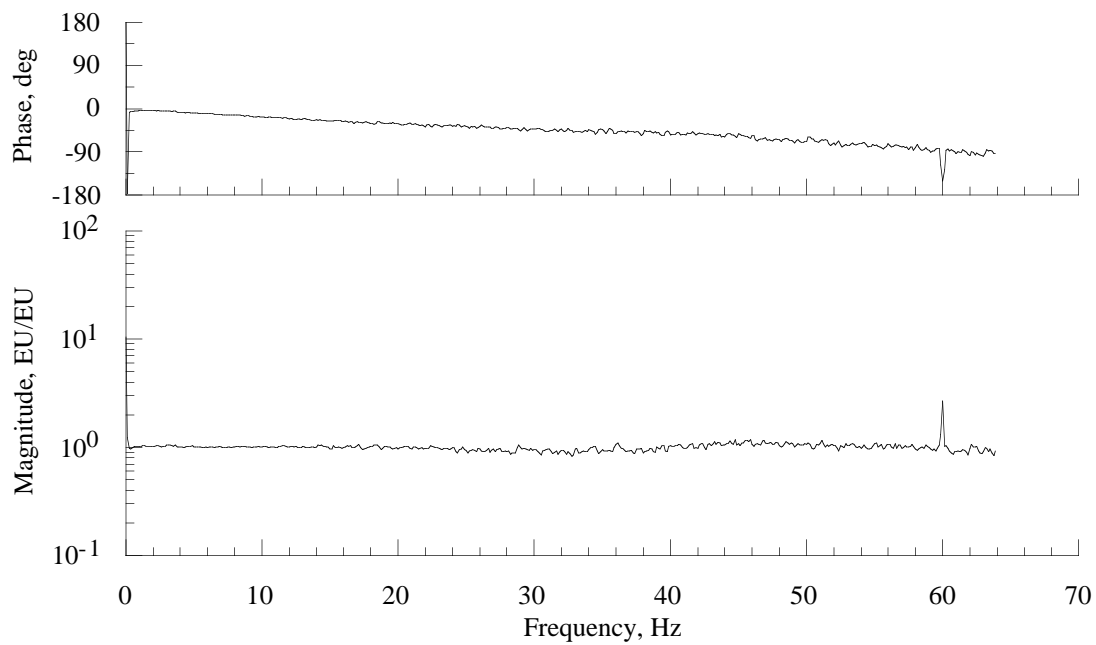


Figure 37(f). Push rod 1 response due to push rod number 1 loading.

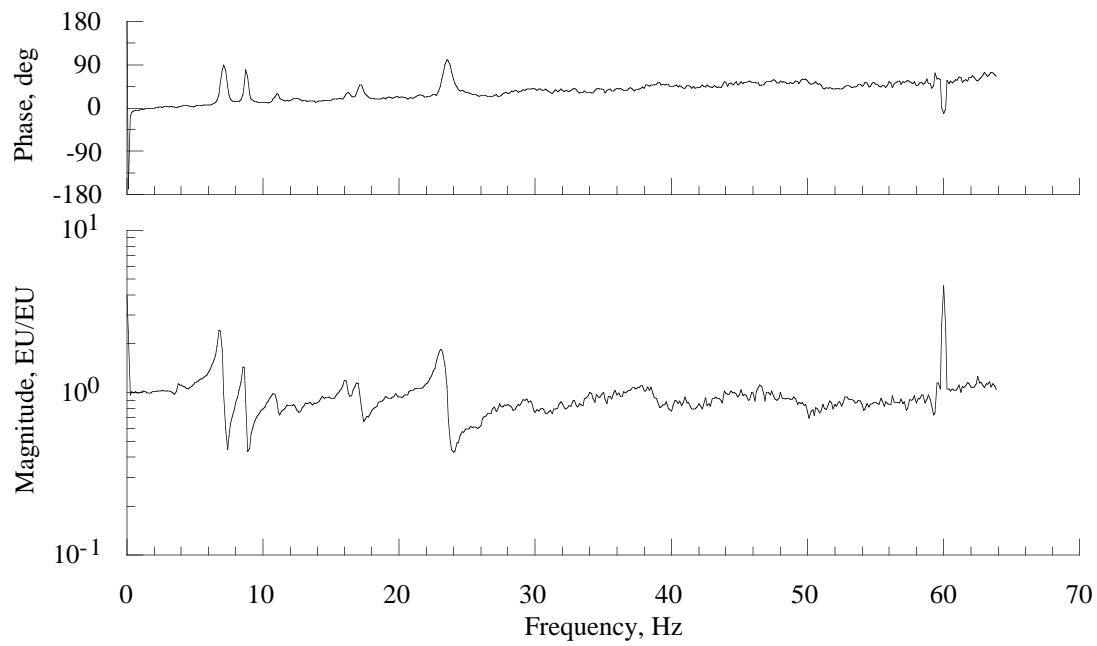


Figure 38(a). Hub normal force balance response due to push rod number 2 loading.

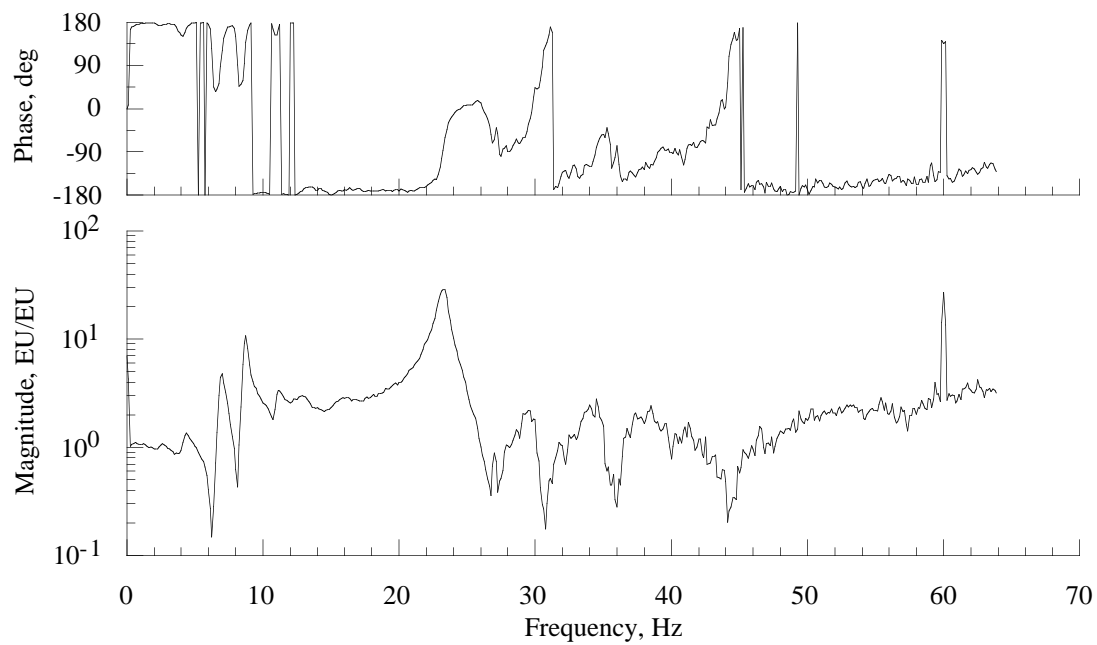


Figure 38(b). Hub pitch moment balance response due to push rod number 2 loading.

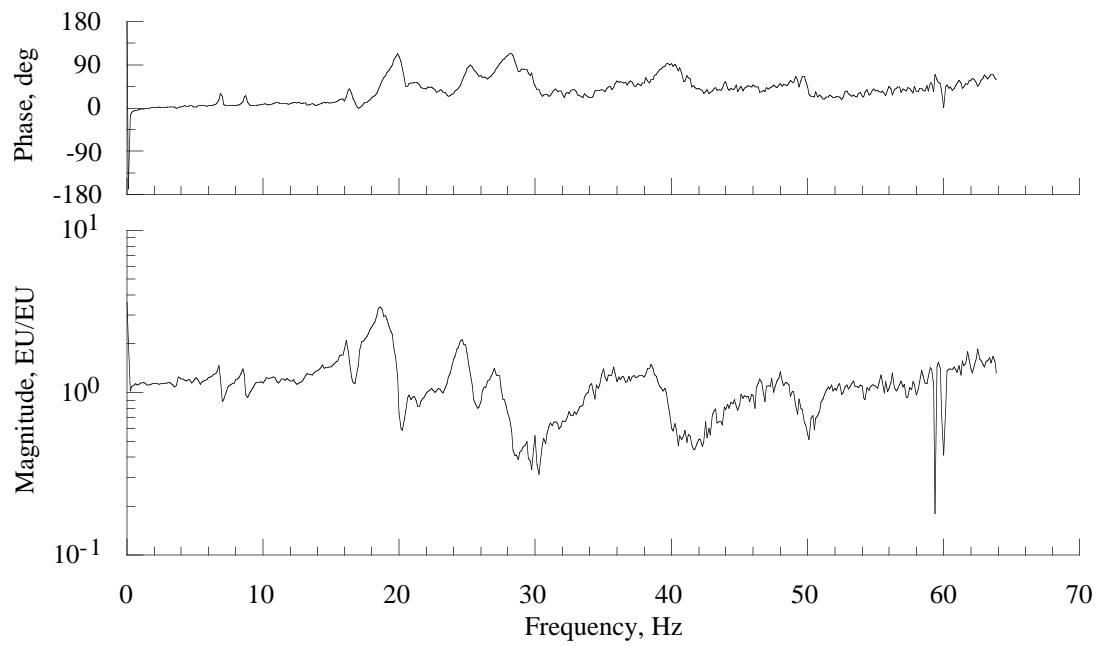


Figure 38(c). Hub roll moment balance response due to push rod number 2 loading.

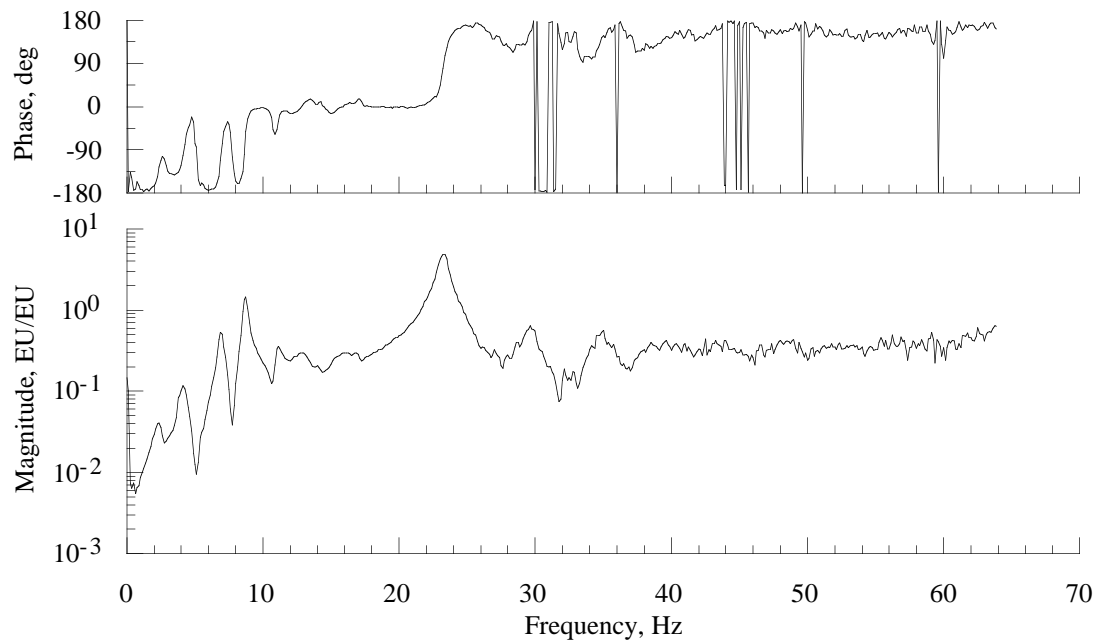


Figure 38(d). Hub axial force balance response due to push rod number 2 loading.

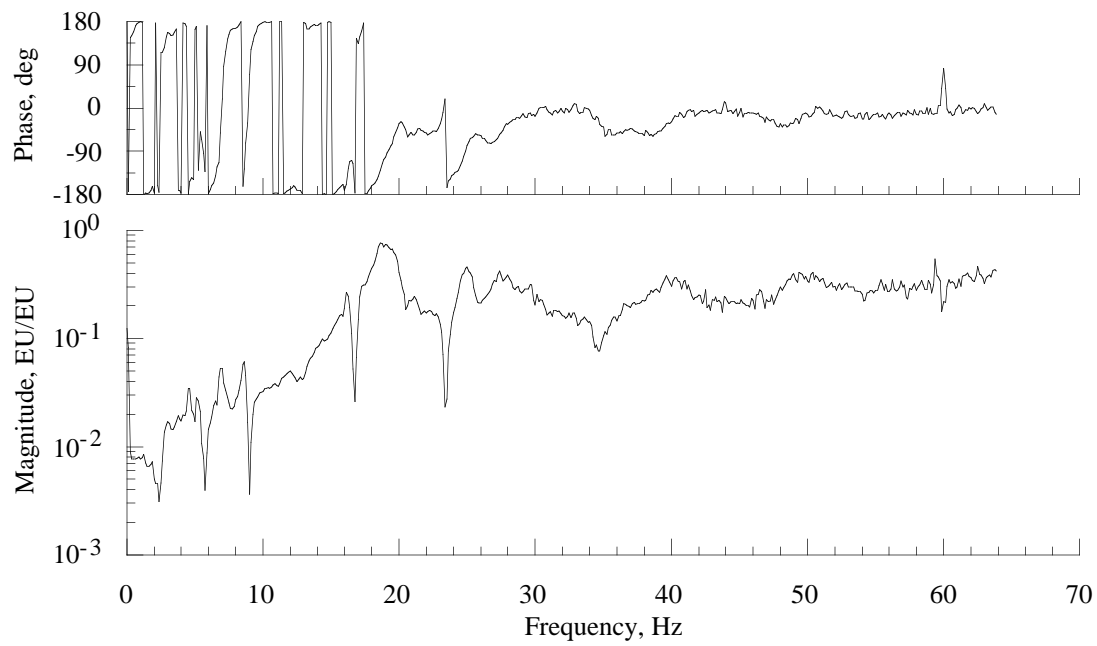


Figure 38(e). Hub side force balance response due to push rod number 2 loading.

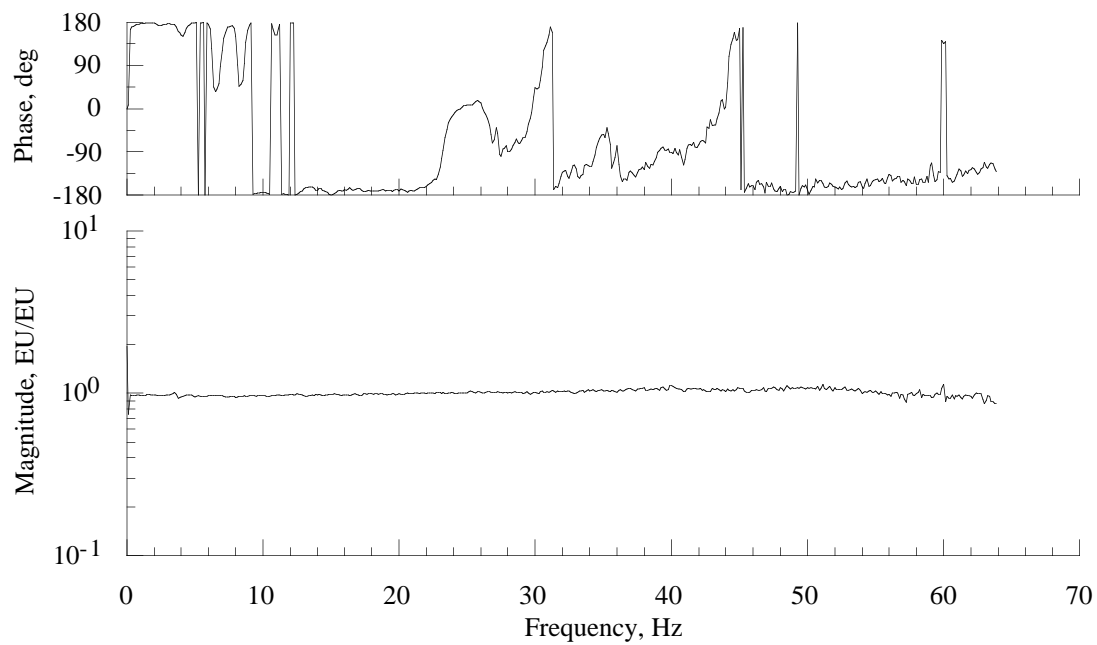


Figure 38(f). Push rod 2 response due to push rod number 2 loading.

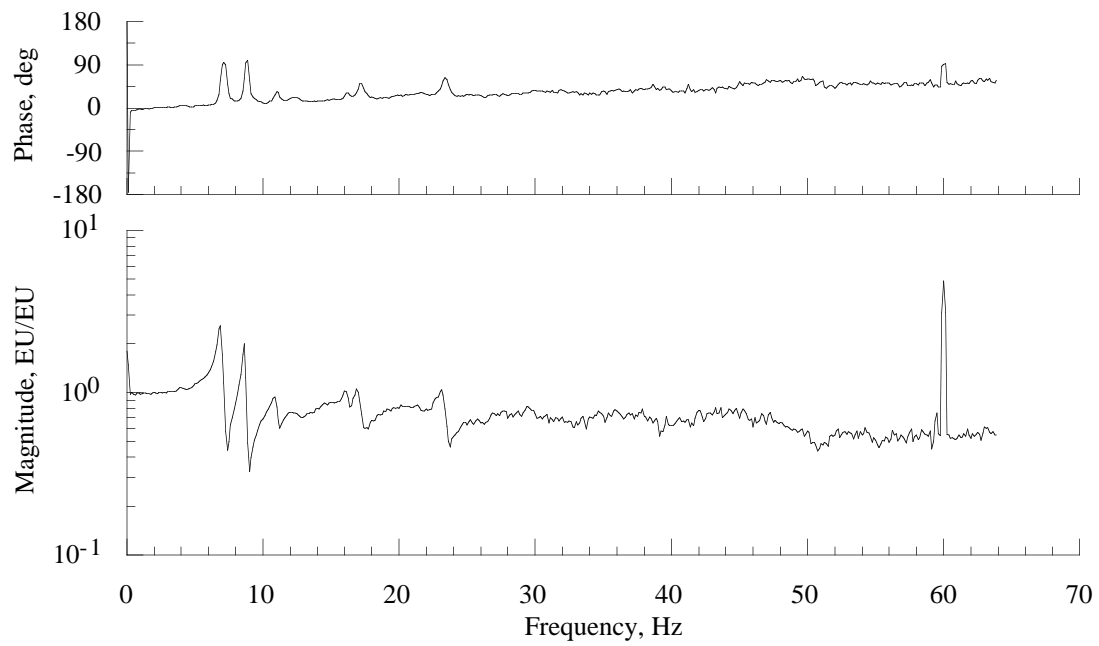


Figure 39(a). Hub normal force balance response due to push rod number 3 loading.

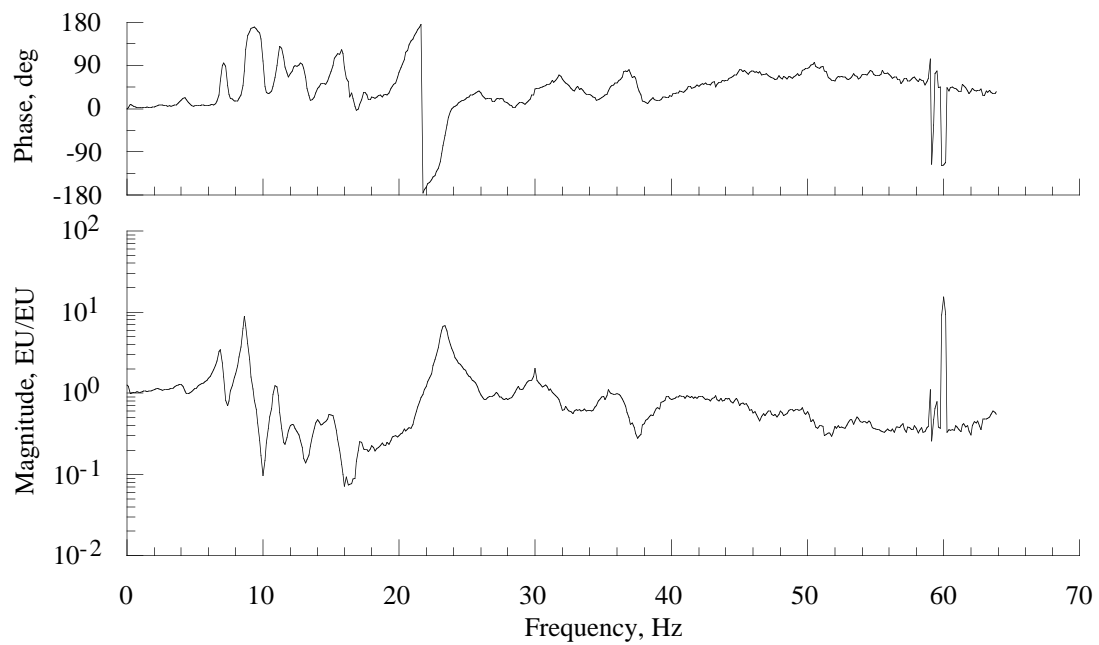


Figure 39(b). Hub pitch moment balance response due to push rod number 3 loading.

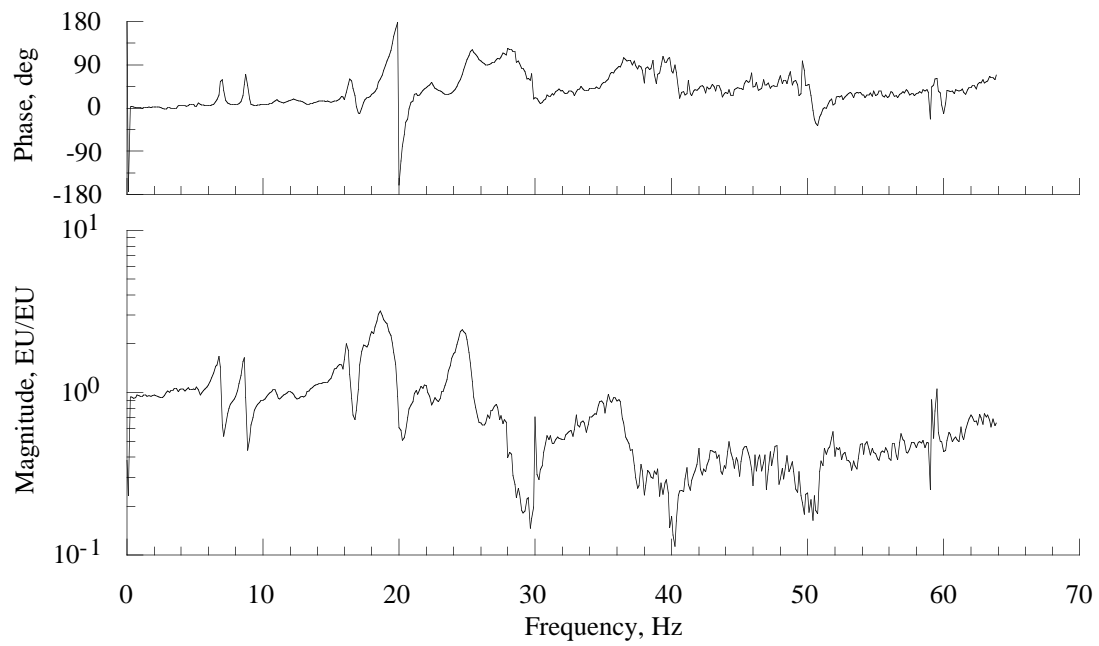


Figure 39(c). Hub roll moment balance response due to push rod number 3 loading.

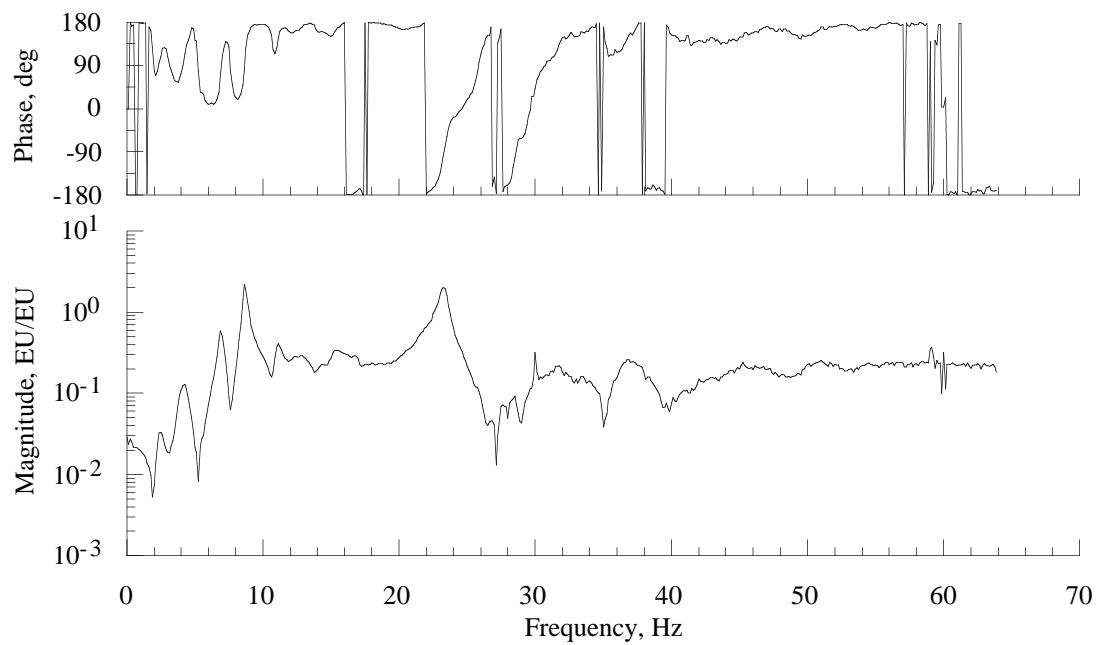


Figure 39(d). Hub axial force balance response due to push rod number 3 loading.

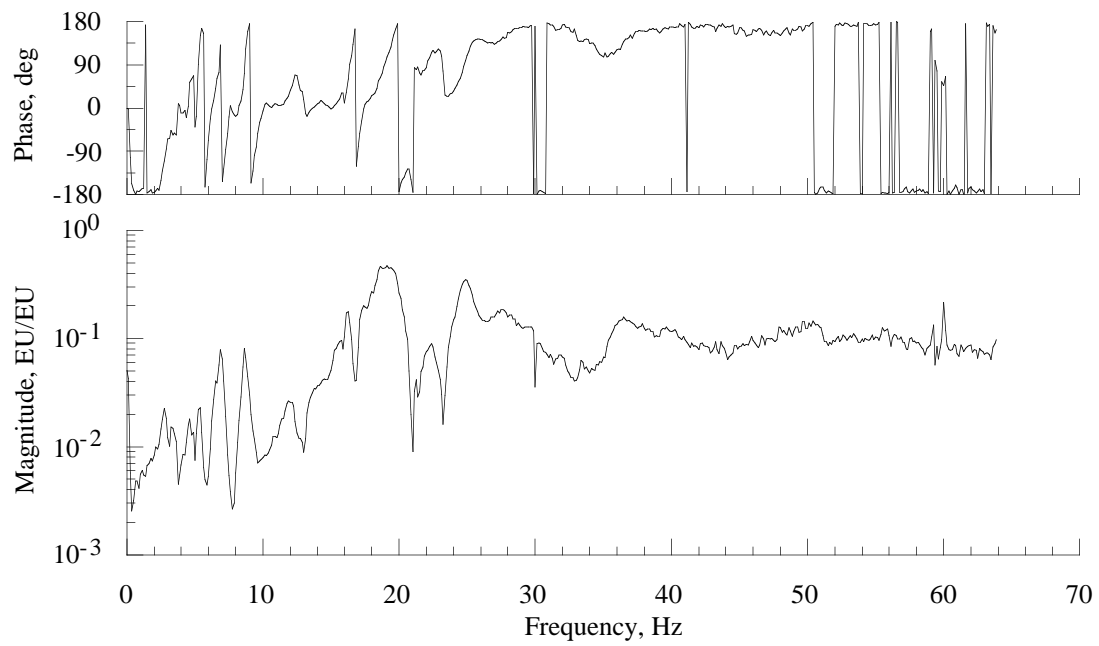


Figure 39(e). Hub side force balance response due to push rod number 3 loading.

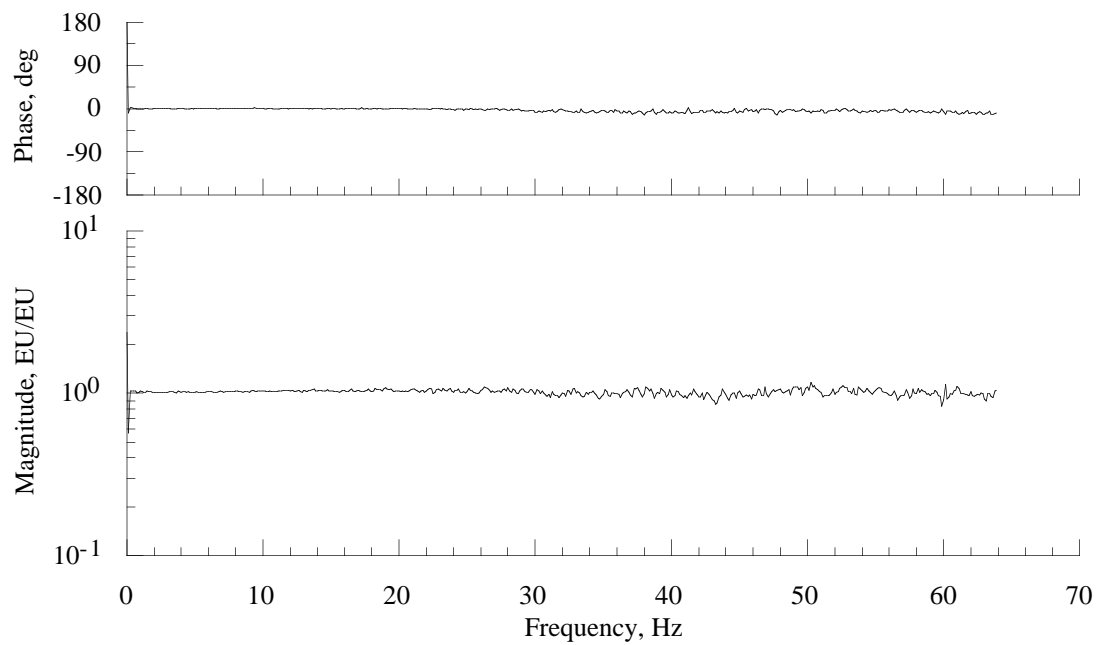


Figure 39(f). Push rod 3 response due to push rod number 3 loading.

REPORT DOCUMENTATION PAGE			Form Approved OMB No. 0704-0188	
Public reporting burden for this collection of information is estimated to average 1 hour per response, including the time for reviewing instructions, searching existing data sources, gathering and maintaining the data needed, and completing and reviewing the collection of information. Send comments regarding this burden estimate or any other aspect of this collection of information, including suggestions for reducing this burden, to Washington Headquarters Services, Directorate for Information Operations and Reports, 1215 Jefferson Davis Highway, Suite 1204, Arlington, VA 22202-4302, and to the Office of Management and Budget, Paperwork Reduction Project (0704-0188), Washington, DC 20503.				
1. AGENCY USE ONLY (Leave blank)		2. REPORT DATE April 1996		3. REPORT TYPE AND DATES COVERED Technical Memorandum
4. TITLE AND SUBTITLE Dynamic Calibration of the NASA Ames Rotor Test Apparatus Steady/Dynamic Rotor Balance			5. FUNDING NUMBERS 505-59-36	
6. AUTHOR(S) Randall L. Peterson and Johannes M. van Aken*				
7. PERFORMING ORGANIZATION NAME(S) AND ADDRESS(ES) Ames Research Center Moffett Field, CA 94035-1000			8. PERFORMING ORGANIZATION REPORT NUMBER A-961452	
9. SPONSORING/MONITORING AGENCY NAME(S) AND ADDRESS(ES) National Aeronautics and Space Administration Washington, DC 20546-0001			10. SPONSORING/MONITORING AGENCY REPORT NUMBER NASA TM-110393	
11. SUPPLEMENTARY NOTES Point of Contact: Randall L. Peterson, Ames Research Center, MS T-12B, Moffett Field, CA 94035-1000 (415) 604-5044 *Sterling Federal Systems, Inc., Palo Alto, California				
12a. DISTRIBUTION/AVAILABILITY STATEMENT Unclassified — Unlimited Subject Category 05			12b. DISTRIBUTION CODE	
13. ABSTRACT (Maximum 200 words) The NASA Ames Rotor Test Apparatus was modified to include a Steady/Dynamic Rotor Balance. The dynamic calibration procedures and configurations are discussed. Random excitation was applied at the rotor hub, and vibratory force and moment responses were measured on the steady/dynamic rotor balance. Transfer functions were computed using the load cell data and the vibratory force and moment responses from the rotor balance. Calibration results showing the influence of frequency bandwidth, hub mass, rotor RPM, thrust preload, and dynamic loads through the stationary push rods are presented and discussed.				
14. SUBJECT TERMS Rotor balance, Rotor loads, Balance calibration, Dynamic response			15. NUMBER OF PAGES 110	
			16. PRICE CODE A06	
17. SECURITY CLASSIFICATION OF REPORT Unclassified	18. SECURITY CLASSIFICATION OF THIS PAGE Unclassified	19. SECURITY CLASSIFICATION OF ABSTRACT	20. LIMITATION OF ABSTRACT	